DTU Nanotech
Department of Micro- and Nanotechnology

Electrokinetics of nanochannels and porous membranes with dynamic surface charges

Mathias Bækbo Andersen

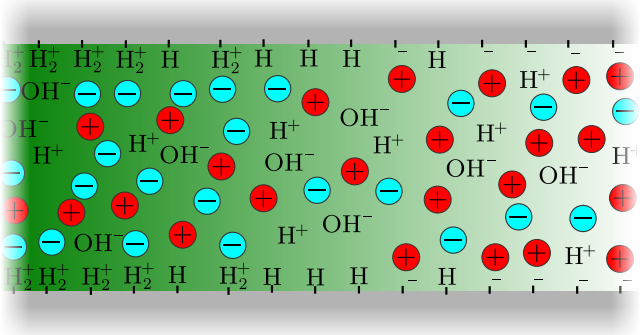

PhD thesis, 31 March 2012

Advisor: Prof Henrik Bruus

Technical University of Denmark
Department of Micro- and Nanotechnology
Building 345 East, DK-2800 Kongens Lyngby, Denmark
Phone +45 45255700, Fax +45 45887762
info@nanotech.dtu.dk
http://www.nanotech.dtu.dk
https://sites.google.com/site/baekbo

Abstract

The present thesis deals with fundamental aspects of mass-transport in the context of nanofluidics. One of the goals is to obtain a fundamental understanding of the working principles of nanofluidic mass-transport which can be applied in a macroscopic setting. To this end, we have developed a model framework that combines electrostatics, ionic transport, hydrodynamics, bulk solution equilibrium chemistry, and surface equilibrium chemistry. As detailed below, we use our model framework to analyze and interpret nanofluidic experiments and for theoretical predictions of novel nanofluidic phenomena.

First, we investigate how the surface dissociation constants and Stern layer capacitance depend on the local environment in terms of surface coating. Thus, we study the behavior of both bare and cyanosilane coated silica nanochannels subjected to two independent experiments. One experiment is particularly interesting because it relies on capillary filling, so it avoids the use of external forcing such as electric fields. Basically, during the filling of nanochannels by capillary action, the advancing electrolyte is titrated by deprotonation from the surface. This is observed using the pH-sensitive fluorescent dye fluorescein. The method relies on the large surface-to-volume ratio in the nanochannel and is thus a great example of a novel nanofluidic technique. Additionally, these measurements are complemented by current-monitoring in which an externally driven electro-osmotic (EO) flow velocity is used to estimate the zeta potential of the wall. Together, the two experiments provide independent data that are interpreted using our model framework. Solving the model self-consistently, while adjusting the low-value surface dissociation constant and the Stern capacitance, we obtain their dependence on the local surface condition in terms of surface coating.

Second, we investigate the streaming current resulting from an applied pressure difference in bare and surface-coated silica nanochannels. The channels have a low aspect ratio. Thus, we develop an effective boundary condition for the surface chemistry and apply our model in the 2-D cross section. Theoretically, we use our model to investigate the effects of corners in nanochannels on the electrochemical properties of the surface. As above, the streaming-current measurements are supplemented by current-monitoring data, and our model predicts

both streaming current and EO flow velocity using only parameters from the literature. Moreover, over 48 hours there is a steady rise in the streaming current which we ascribe to silica dissolution. Using our model, we estimate the dissolution rate as a function of buffer type and surface condition.

Third, in bare silica nanochannels, our model predicts a hitherto unnoticed minimum in the electrical conductance as the salt concentration decreases. Our model predicts the behavior of the minimum in the conductance for different conditions including CO_2 content, supporting buffer type, and nanochannel height. Notably, we find that the conductance minimum is mainly caused by hydronium ions, and in our case almost exclusively due to carbonic acid generated from the dissolution of CO_2 from the atmosphere. We carry out delicate experiments and measure the conductance of silica nanochannels as a function of decreasing salt concentration. The measurements conform with the model prediction, both for a pure salt buffer and a buffer with extra hydronium ions added, in this case through HCl. In any case, the model prediction is supported by the appearance of the conductance minimum in several independent studies in the literature.

Fourth, we use our model to predict a novel phenomenon called current-induced membrane discharge (CIMD) to explain over-limiting current in ion-exchange membranes. The model is based on dynamic surface charges in the membrane in equilibrium with the buffer. However, here we take the next step and consider strong out-of-equilibrium transport across the membrane. Our model predicts large pH variations in the electrodialysis system that in turn lowers the ion-selectivity of the membrane by protonation reactions. This opens up for significant over-limiting current. We use our model to investigate the dependence on reservoir concentration and pH. Even without fluid flow, CIMD predicts over-limiting current and even a suppression of the extended space charge layer and thus a suppression of the electro-osmotic instability. Future work will include comparison with experimental data which is a delicate procedure that requires much attention to the comparability between the conditions in the model and in the experiment.

Finally, we make a small digression and study induced-charge electro-osmosis (ICEO) and the validity of common EO slip formulae as a function of a finite Debye screening length and the system geometry (here the metal-strip height). The slip models are strictly only valid in the limit of a vanishing screening length. Compared to a full boundary-layer resolving model, we show surprisingly large deviations even for relatively thin screening layers. Both slip models are based on the classical Helmholtz–Smoluchowski expression, and while one assumes a static screening layer, the other takes surface conduction into account.

Resumé

Denne afhandling omhandler grundlæggende aspekter ved masse-transport i nanofluidik. Et af målene er at opnå en grundlæggende forståelse af de gældende principper for nanofluidisk masse-transport, som så kan anvendes i makroskopiske systemer. Til dette formål har vi udviklet en model der kombinerer elektrostatik, ion transport, hydrodynamik, ligevægtskemi i opløsning og ligevægtskemi på overflader. Som beskrevet nedenfor bruger vi vores model til at analysere og fortolke nanofluidik eksperimenter og til at lave teoretiske forudsigelser af nye nanofluidiske fænomener.

For det første undersøger vi hvordan ligevægtskonstanter og Stern-kapacitans afhænger af det lokale overfladeemiljø i form af overfladebelægning. Vi studerer både rene og cyanosilane-belagte silika nanokaneler i to uafhængige eksperimenter. Et eksperiment er særligt interessant, idet det bygger på kapillærfyldning, så brugen af eksterne drivfelter, såsom elektriske felter, undgås. Kort sagt bliver elektrolytten titreret af silika væggen under kapillærfyldningen. Vi observerer dette ved at anvende et pH-følsomt fluorescerende farvestof kaldet fluorescein. Metoden afhænger af det store overflade-til-volumen forhold i nanokanelen og er således et godt eksempel på en nyskabende nanofluidisk teknik. Disse kapillærfyldninger er derudover suppleret med strøm-overvågnings forsøg, hvori en eksternt drevet elektro-osmotisk (EO) strømning anvendes til at estimere zeta potentialet på væggen. Tilsammen giver de to eksperimenter uafhængig data, der fortolkes ved hjælp af vores model. Modellen løses selv-konsistent, medens værdien af ligevægtskonstanten og Stern kapacitansen optimeres. Således får vi belyst disse parametres afhængighed af den lokale tilstand på overfladen i form af overfladebelægning.

For det andet undersøger vi advektionsstrøm afledt af en påført trykforskel i rene og overfladebelagte silika nanokaneler. Kanalerne har et forhold mellem højde og bredde tæt på een. Vi har derfor udviklet en effektiv randbetingelse for overfladekemien og anvendt vores model i det 2-dimensionelle tværsnit. Vi bruger vores model til teoretisk at undersøge effekten af hjørner i nanokaneler på de elektrokemiske overfladeegenskaber. Som ovenfor er de advektionsstrømmålingerne suppleret med strøm-overvågnings forsøg og vores model forudsiger både advektionsstrømmen og EO strømningen kun ved brug af parametre fra litteraturen. Desuden er der i løbet af 48 timer en støt stigning i advektionsstrømmen,

som vi tilskriver opløsning af silikaen. Ved brug af vores model estimerer vi opløsningshastigheden som funktion af elektrolyt art og overfladetilstand.

For det tredje forudsiger vores model i rene silika nanokaneler et hidtil upåagtet minimum i den elektriske konduktans med faldende salt koncentration. Vores model forudsiger konduktansminimaets opførsel for forskellige forhold, herunder CO_2 indhold, elektrolyt art og højden af nanokanelen. Vi finder især at konduktansminimaet hovedsageligt er forårsaget af hydronium-ionerne, og i vores tilfælde næsten udelukkende på grund af kulsyren genereret fra opløsningen af CO_2 fra atmosfæren. Vi udfører fintfølende eksperimenter og måler konduktansen i silika nanokanelerne som funktion af faldende salt koncentration. Målingerne er i overensstemmelse med modellens forudsigelser, både for en ren salt elektrolyt og en elektrolyt med ekstra hydronium-ioner tilsat, i dette tilfælde gennem HCI. I alle tilfælde er modellens forudsigelser understøttet af forekomsten af konduktansminima i adskillige uafhængige undersøgelser i litteraturen.

For det fjerde bruger vi vores model til at forudsige et nyt fænomen kaldet strøm-induceret membran udledning (CIMD) som forklaring på over-begrænsende strøm i ionbyttermembraner. Modellen er baseret på dynamiske overfladeladninger i membranen i ligevægt med elektrolytten. Men her tager vi skridtet videre og undersøger stærk ikke-ligevægt transport igennem membranen. Vores model forudsiger store pH-variationer i elektrodialysesystemet, der nedsætter ionselektiviteten af membranen via protoneringsreaktioner. Dette åbner membranen op for betydelig over-begrænsende strøm. Vi bruger vores model til at undersøge afhængigheden af reservoir koncentration og pH. Selv uden væskestrøm forudsiger CIMD modellen over-begrænsende strøm og endda en undertrykkelse af det forlængede rumladningslag og dermed en undertrykkelse af den elektro-osmotiske ustabilitet. Det fremtidige arbejde vil omfatte sammenligning med eksperimentelle data, som er en delikat procedure, der kræver megen opmærksomhed med henblik på sammenligneligheden mellem betingelserne i modellen og i eksperimentet.

Endelig laver vi en lille sidebemærkning og studerer induceret-ladning elektro-osmose (ICEO) og gyldigheden af almindelige EO glide-hastighedsudtryk som funktion af en endelig Debye skærmningslængde og systemets geometri (her højden af metal-strimmelen). Glide-hastighedmodellerne er strengt taget kun gyldige i den grænse hvor skærmningslængden går mod nul. Sammenlignet med en grænselagsopløsende model viser vi overraskende store afvigelser, selv for relativt tynde skærmningslag. Begge glide-hastighedsmodeller er baseret på det klassiske Helmholtz–Smoluchowski udtryk, og medens den ene model antager et statisk skærmningslag, tager den anden model overfladestrøm i betragtning.

Preface

This thesis is submitted in partial fulfillment of the requirements for Degree of Doctor of Philosophy (PhD) at Technical University of Denmark (DTU). The work has been carried out at Department of Micro- and Nanotechnology (DTU Nanotech) in Theoretical Microfluidics Group (TMF) from April 2009 to March 2012. In the periods 16-21 November 2009, 14 March to 10 April 2010, 20-30 May 2010, 15 June to 31 July 2010, and 13-20 November 2010, I visited Professor Sumita Pennathur at University of California, Santa Barbara. In the periods 15 August to 11 September 2010 and 20 July to 20 September 2011, I visited Professor Martin Z. Bazant at Massachusetts Institute of Technology. The project was supervised by Professor Henrik Bruus at DTU Nanotech.

First, I would like to thank Henrik Bruus on both a professional and personal level. Professionally, Henrik has shown me how to be a great scientist, never loosing touch with the core disciplines while at the same time having fun. Personally, I appreciate the friendship and the moments shared together of which there are too many to mention here. At the same time, I would like to thank past and present members of TMF, in particular Misha Marie Gregersen, Kristian Lund Jensen, Jesper Toft Kristensen, and Christoffer Peder Nielsen for work on electrokinetics, and Søren Vedel, Kåre Hartvig Jensen, and Kasper Kristensen for being great office buddies. In general, my colleagues at DTU Nanotech have all together provided a good and friendly atmosphere thereby making it joyful to work on a demanding PhD project.

I would also like to thank my good colleagues at UC Santa Barbara. Professor Sumita Pennathur, especially for our work on nanochannels, the many visits I have had to her Nanolab, and for her catching enthusiasm and warm hospitality. At the same time, I would like to thank past and present people related to the UCSB Nanolab, particularly Jared Frey for our work on nanochannels, and for helping us with everything from finding a house in Santa Barbara to doing a great barbecue. Also, my thanks go to Jaydeep P. Bardhan, Andrew Crumrine, and Deep Shah. Furthermore, I thank Professor Carl Meinhart and Gaurav Soni, mainly for our work on induced-charged electro-osmosis and our meetings in our house in Santa Barbara.

Moreover, I would like to thank Professor Martin Z. Bazant, in particular

for our work on ion-selective membranes and for my visits to his group. At the same time, I would like to thank past and present members of Martin's group, especially Ali Mani for our interaction, my visit to Stanford University, and for inviting me to a Postdoctoral position. Also, my thanks go to Daosheng Deng and Juhyun Song.

Next, I am very thankful to P. M. Biesheuvel, particularly for our work on ion-selective membranes, the many emails exchanged, and for our meetings at University of Twente and in Leiden. In the same regard, I would like to thank Michiel van Soestbergen.

It is very important for me to mention that the extensive collaboration with foreign colleagues would not have been possible without the generous support from the Danish Ministry of Science, Technology and Innovation in the form of the EliteForsk Travel Stipend. I am very grateful and proud to have received this honor.

Last, but not least, I would like to give a very special thank to my family and friends for their love and support. In particular, my wife Maria Fernanda Gallegos Molina, my father and mother Mogens Bækbo Andersen and Pia Larsen, my sister Nina Bækbo Andersen, and my friends and study buddies Rune Barnkob and Morten Siwertsen.

Kongens Lyngby, 31 March 2012

Mathias Bækbo Andersen

Contents

List of Figures

List of Tables

List of Main Symbols, Constants, and Acronyms

Symbol	Description	Unit/value/definition
a_i	Ionic activity	
AFM	Atomic force microscope	
b_i	Backward reaction rate constant	$\mathrm{m^3\,s^{-1}}$ ($\mathrm{M\,s^{-1}}$)
c_i	Concentration (molar)	$\mathrm{M} = \mathrm{mol\,L^{-1}}$
$c_{⊖}$	Standard-state reference concentration	$1\,\mathrm{M}$
C_s	Stern surface capacitance	$\mathrm{F\,m^{-2}}$
C_i	Surface capacitance	$\mathrm{F\,m^{-2}}$
CIMD	Current-induced membrane discharge	
d	Dimensionality	
D_i	Diffusion coefficient	$\mathrm{m^2\,s^{-1}}$
Da_i	Damköhler number (diffusion-to-reaction time)	$L^2/(D_i\tau_{\mathrm{reac},i})$
e	Elementary charge	$1.602 \times 10^{-19}\,\mathrm{C}$
$\boldsymbol{E}$	Electric field vector	
EDL	Electric double layer	
EO	Electro-osmotic	
EOI	Electro-osmotic instability	
f_i	Forward reaction rate constant	$\mathrm{m^3\,s^{-1}}$ ($\mathrm{M\,s^{-1}}$)
$\boldsymbol{f}$	Force density vector	$\mathrm{N\,m^{-3}}$
FEM	Finite element method	
$\boldsymbol{i}_\mathrm{el}$	Electrical current density vector	$\mathrm{A\,m^{-2}}$
I	Ionic strength	$\mathrm{m^{-3}}$ (or M)
I_el	Electrical current	A
ICEO	Induced-charge electro-osmosis	
$\boldsymbol{J}$	Flux vector	$\mathrm{m^{-2}\,s^{-1}}$
k_B	Boltzmann constant	$1.381 \times 10^{-23}\,\mathrm{J\,K^{-1}}$
k_p	Ionic hindrance factor	
K_i	Dissociation constant	
K_w	Water self-ionization constant	10^{-14} (at 298 K)
L	Characteristic length scale	m
n_i	Concentration (particle number)	$\mathrm{m^{-3}}$
N_A	Avogadro constant	$6.022 \times 10^{23}\,\mathrm{mol^{-1}}$
OLC	Over-limiting current	
p	Pressure	Pa
Pe_i	Péclet number (advection-to-diffusion mass transport)	$v_0 L/D_i$
$\mathrm{p}K_i$	Dissociation constant	
$\boldsymbol{r}$	Position vector	m
R_i	Reaction production term	$\mathrm{m^{-3}\,s^{-1}}$

Continued on next page

Symbol	Description	Unit/value/definition
Re	Reynolds number	$v_0 L/\nu$
RMS	Root mean square	
	(inertial-to-viscous forces)	
SDL	Stagnant diffusion layer	
St	Strouhal number	$L/(v_0\tau)$
	(flow-to-unsteady time)	
T	Temperature	298 K
	(unless mentioned otherwise)	
$\boldsymbol{T}$	Maxwell electrical stress tensor	$\mathrm{Pa} = \mathrm{N\,m^{-2}}$
$\boldsymbol{u}_i$	Average ionic velocity vector	$\mathrm{m\,s^{-1}}$
$\boldsymbol{v}$	Velocity field vector	$\mathrm{m\,s^{-1}}$
v_{hs}	Helmholtz–Smoluchowski slip velocity	$\mathrm{m\,s^{-1}}$
v_0	Characteristic velocity scale	$\mathrm{m\,s^{-1}}$
$V_{\mathrm{T}} = k_{\mathrm{B}}T/e$	Thermal voltage	25.7 mV (at 298 K)
$\boldsymbol{x}$	Position vector	m
Z	Valence	
α	Ionization degree	
γ	Surface tension	$\mathrm{N\,m^{-1}} = \mathrm{J\,m^{-2}}$
Γ_i	Surface concentration	$\mathrm{m^{-2}}$
δ_{ij}	Kronecker delta	
ϵ_{p}	Porosity	
ε_0	Vacuum permittivity	$8.854 \times 10^{-12}\,\mathrm{F\,m^{-1}}$
ε_{r}	Relative permittivity	
ζ	Zeta (shear-plane) surface potential	V
η	Dynamic viscosity	Pa s
θ	Surface group charge sign	
λ_{D}	Debye screening length	m
μ_i	Ionic mobility	$\mathrm{m^2\,s^{-1}\,V^{-1}}$
$\bar{\mu}_i$	Electrochemical potential	J
$\mu_i^{\ominus}$	Standard-state ionic energy	J
ν	Kinematic viscosity	$\mathrm{m^2\,s^{-1}}$
ρ_{el}	Electrical charge density	$\mathrm{C\,m^{-3}}$
ρ_{m}	Mass density	$\mathrm{kg\,m^{-3}}$
σ	Surface charge density	$\mathrm{C\,m^{-2}}$
$\boldsymbol{\sigma}$	Viscous stress tensor	$\mathrm{Pa} = \mathrm{N\,m^{-2}}$
τ	Characteristic unsteady time scale	s
$\tau_{\mathrm{reac},i}$	Characteristic reaction time scale	s
ϕ	Electrical potential	V
∂_i	Partial derivative	

Chapter 1

Introduction

We give specific introductions to each chapter, thus the introduction below is of a general character.

1.1 Nanofluidics and ion-selective membranes

The study of ionic species and charged surfaces has traditionally been done in the context of colloids [1–4] and membrane science [5–7]. In relation to this, the recent advent of micro- and nanofluidics has lead to precise control of the fluid-confining micro-geometry along with a multitude of small-scale measurement and detection techniques [8–15].

Some of the technologies that have enabled nanofluidics are the atomic force microscope (AFM), the scanning tunneling microscope (STM), fluorescent microscopy, the electron, x-ray, and ion-beam lithographs, and new micromaching techniques like soft lithography, nanoimprint lithography, injection molding, and bottom-up assembly methods [10]. Thus, the field of colloid and membrane science is experiencing a renaissance in the micro-nano-fluidic context. Figure 1.1 shows some of the classical scientific fields that are related to nanofluidics [10].

Excellent reviews of the diverse possibilities within nanofluidics are given in Refs. [10, 16–21]. In particular, current research in nanofluidics include energy harvesting [22–28], surface-charge governed transport [29–35], entropic-trap studies of proteins and DNA [36–42], pre-concentration, ion-enrichment and ion-depletion, deionization, desalination, and water purification [43–53], non-linear electrical nanofluidic elements e.g. diodes and rectifiers [54–65], separation of ions, nanoparticles, and biomolecules [66–70], significant effects of fluid slip [71–73], amplified pH effects [74–76], streaming current [77–79], capillary phenomena [80, 81], ion-ion correlations [82], and biosensing and single-molecule studies [83, 84].

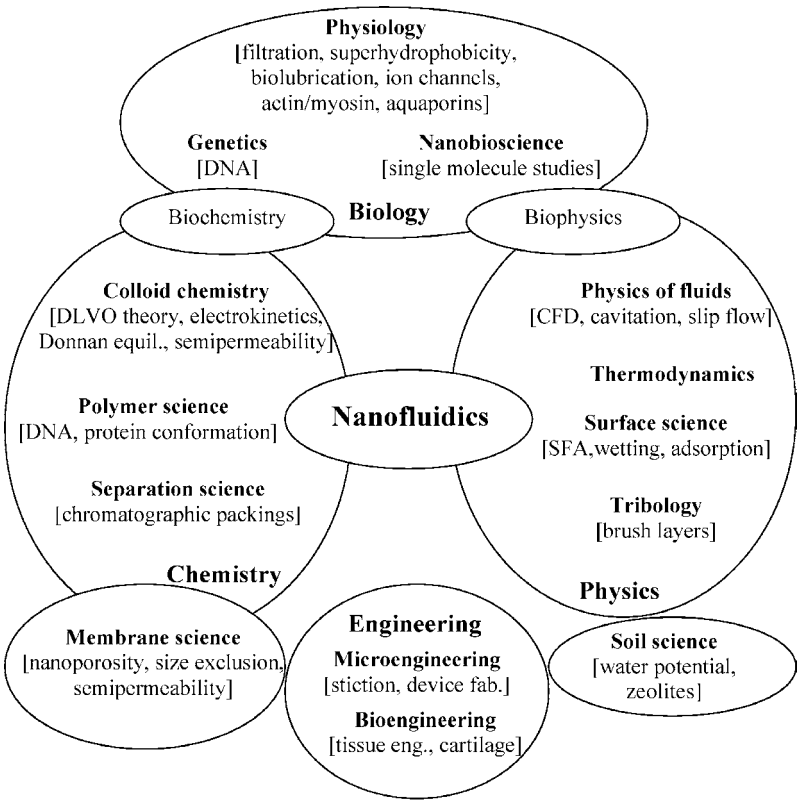

Figure 1.1: This thesis strives to expand the fundamental understanding of nanofluidics which is related to many other scientific disciplines within physics, chemistry, and biology such as membrane science, separation science, nanobioscience, soil science, genetics, *etc.* Figure adapted from Eijkel *et al.* [10].

The prevalent extensive literature from fields like colloid and membrane science is a huge advantage and provides an excellent basis for nanofluidics. However, at the same time, surprises must be expected due to the greater control and detectability of nanofluidics. A challenge is therefore to test and expand upon the previous knowledge using the novel and powerful possibilities of nanofluidics.

Especially the understanding of ion-selective membranes may benefit from nanofluidic studies. Ion-selective membranes are used for many purposes including ion-exchange and desalination [7, 85], electrophysiology [86], and fuel cells [87, 88]. An ion-selective membrane can be viewed as a huge macroscopic bundle of nanochannels, connected chaotically in parallel and series. More precisely, ion-selective membranes are made up of networks of entangled polymers in between which there is a microscopic pore space.

The similarities between ion-selective membranes and nanochannels are many. One of the great potentials of nanofluidics is to use its controlled setting to obtain a fundamental understanding of the working principles on the microscopic level. This understanding can then be applied on the macroscopic level of the ion-selective membrane. This is an advantage, in particular whenever a macroscopic throughput is desirable as in e.g. desalination (water purification). It would

be unfeasible to fabricate billions upon billions of fine nanochannels running in parallel, but instead straight forward to use a macroscopic piece of ion-selective membrane. Thus, this is exactly one of the main motivations for this thesis; to obtain a fundamental understanding of the working principles of nanofluidic mass-transport which can be applied in a macroscopic setting.

1.2 Outline of the thesis

The thesis is naturally build around my five research papers listed in Section 1.3.1. However, in the dissertation I have rephrased the papers and given a combined presentation emphasizing the connections between the various parts of my work. The actual papers are enclosed in Chapters B to F. The chapter by chapter contents are as follows.

Chapter 2: Basic theory We summarize the basic theory that constitute the common denominator of our work. The topics covered include electrostatics, ionic transport, electrochemical equilibrium, hydrodynamics, bulk solution chemistry, and surface chemistry. Throughout the thesis we will refer back to this chapter to avoid unnecessary repetition of the theory. However, where it serves a purpose in terms of clarity we restate equations and expressions as needed.

Chapter 3: Numerical techniques The fields of nanofluidics and ion-selective membranes consist of the coupling of several different physical phenomena, as mentioned above. In terms of mathematical modeling, this leads to several coupled and non-linear partial differential equations. To the degree it is feasible, we always conduct analytical studies, but when they become intractable we resort to numerical analysis. To this end we use the finite-element-method (FEM) software `COMSOL` (version 3.5a) and the scientific software `Matlab`. Thus, in this chapter we touch briefly upon the basic concepts of FEM and how it is implemented using the weak form (the Galerkin method).

Chapter 4: Nanochannels: Surface-dependent thermodynamic constants We apply our model of bulk and surface chemistry coupled via Boltzmann distributed ions. We do this in bare and cyanosilane coated nanochannels and compare our model against two independent types of experiments. We adjust the low-value surface dissociation constant and the Stern layer capacitance and obtain good agreement with the experimentally measured zeta potential and capillary dark-to-bright length-ratio (interpretable as the surface charge density).

Chapter 5: Nanochannels: Streaming current and wall dissolution We apply our model to 2D nanochannels where we model the surface chemistry by an effective boundary condition along the perimeter of the channel cross-section. We use the previously found values for the adjustable parameters and obtain good agreement between the model and the experimentally measured zeta potential and

streaming current. Thus verified, we use the model together with the measured transient increase in streaming current over 48 hours to predict dissolution rates in silica nanochannels.

Chapter 6: Nanochannels: Conductance and CO_2 in dilute electrolytes We use our model to predict a conductance minimum in nanochannels filled with dilute electrolytes. Our model shows that hydronium is responsible for the minimum, and further shows that dissolved carbonic acid from atmospheric CO_2 plays an essential role in this regard. We perform experiments that conform with the model predictions. Furthermore, we point out several independent studies in the literature where the conductance minimum has been experimentally measured.

Chapter 7: Membranes: Over-limiting current We apply our model framework to ion-selective membranes and predict a new mechanism for over-limiting current (OLC) called current-induced membrane discharge (CIMD). Our model shows that OLC can be due to a chemically induced loss of ion-selectivity even in the absence of fluid flow. Our model even predicts that the extended space charge layer responsible for the electro-osmotic instability (EOI) is suppressed. Thus, CIMD is a fundamentally new mechanism offering an alternative explanation for OLC, and also predicts other important consequences such as the loss of ion-selectivity of the membrane.

Chapter 8: ICEO: finite Debye-length effects We digress a bit from dynamic surface charge and look at the effect of a finite Debye length in induced-charge electro-osmosis. We do this by comparing two common slip-velocity models to a full boundary-layer resolving model. The slip models are strictly only valid in the limit of a vanishing Debye length and we show that they deviate surprisingly much from the full model even at relatively thin screening layers.

Chapter 9: Conclusion and outlook We summarize our work and offer some directions for future research.

1.3 Publications during the PhD studies

During my studies I have published four peer reviewed journal papers (a fifth submitted) and two peer reviewed conference proceedings (a third and fourth submitted), and I have presented my work at several international conferences.

1.3.1 Peer reviewed journal publications

- **M. B. Andersen**, M. van Soestbergen, A. Mani, H. Bruus, P. M. Biesheuvel, and M. Z. Bazant, *Current-induced membrane discharge* (submitted to Phys Rev Lett on 29 Feb 2012 `http://arxiv.org/abs/1202.6448`). Enclosed in Chapter E.

- **M. B. Andersen**, J. Frey, S. Pennathur, and H. Bruus, *Surface-dependent chemical equilibrium constants and capacitances in bare and 3-cyanopropyldimethylchlorosilane coated silica nanochannels*, J Colloid Interface Sci **353**, 301 (2011). Enclosed in Chapter B.
- **M. B. Andersen**, H. Bruus, J. P. Bardhan, and S. Pennathur, *Streaming current and wall dissolution over 48 h in silica nanochannels*, J Colloid Interface Sci **360**, 262 (2011). Enclosed in Chapter C.
- K. L. Jensen, J. T. Kristensen, A. M. Crumrine, **M. B. Andersen**, H. Bruus, and S. Pennathur, *Hydronium-dominated ion transport in carbon-dioxide-saturated electrolytes at low salt concentrations in nanochannels*, Phys Rev E **83**, 056307 (2011). Enclosed in Chapter D.
- M. M. Gregersen, **M. B. Andersen**, G. Soni, C. Meinhart, and H. Bruus, *Numerical analysis of finite debye-length effects in induced-charge electro-osmosis*, Phys Rev E 79, 066316 (2009). Enclosed in Chapter F.

1.3.2 Peer reviewed conference contributions

- **M. B. Andersen**, M. van Soestbergen, A. Mani, H. Bruus, P. M. Biesheuvel, and M. Z. Bazant, *Current-induced membrane discharge and over-limiting current in ion-selective membranes,* ICREA symposium 2012 "Nanofluidics, Colloids, and Membranes", Barcelona, Spain, 16-18 July 2012 (submitted).
- C. P. Nielsen, **M. B. Andersen**, and H. Bruus, *Numerical method for separating length scales in microchannels containing non-ideal ion-selective membranes and extended space-charge layers,* ICREA symposium 2012 "Nanofluidics, Colloids, and Membranes", Barcelona, Spain, 16-18 July 2012 (submitted).
- A. M. Crumrine, D. Shah, **M. B. Andersen**, H. Bruus, and S. Pennathur, *Nanofluidic carbon-dioxide sensor using nanoscale hydronium-dominated ion transport theory*, MEMS 2011, IEEE 24th International Conference on MEMS, pp. 944-947 Cancun, Mexico, 23-27 January 2011.
- **M. B. Andersen**, J. Frey, S. Pennathur, and H. Bruus, *Concentration dependence of stern layer capacitances and surface equilibrium constants in silica-based nanofluidic channels*, μTAS 2010, The 14th international conference on miniaturized systems for chemistry and life sciences, pp. 1409-1411, Groningen, The Netherlands, 3-7 October 2010.

1.3.3 Other scientific contributions

- **M. B. Andersen**, H. Bruus, A. Mani, and M. Z. Bazant, *Concentration polarization and desalination in nanochannels: Effect of surface charge dynamics*, 64th Annual Meeting of the American Physical Society's Division of Fluid Dynamics, Baltimore, Maryland, USA, 20-22 November 2011.

- **M. B. Andersen**, H. Bruus, *The effect of silane-coating on silica nanochannels*, Annual meeting of the Danish Physical Society, Nyborg Strand, Denmark, 21-22 June 2011.
- **M. B. Andersen**, H. Bruus, J. Frey, and S. Pennathur, *Electrochemical surface properties of bare- and silanecoated silica nanochannels*, 63rd Annual Meeting of the American Physical Society's Division of Fluid Dynamics, Long Beach, California, USA, 21-23 November 2010.
- **M. B. Andersen**, J. Frey, S. Pennathur, and H. Bruus, *Investigation of the solid/liquid interface of coated silica nanochannels during capillary filling*, 9th International Conference on Electrokinetic Phenomena, Turku, Finland, 6-10 June 2010.
- **M. B. Andersen**, and H. Bruus, *Concentration polarization effects in nanochannel induced-charge electro-osmosis*, 62nd Annual Meeting of the American Physical Society's Division of Fluid Dynamics, Minneapolis, Minnesota, USA, 22-24 November 2009.
- **M. B. Andersen**, and H. Bruus, *Numerical analysis of analyte transport across un-biased electrodes in nanochannels*, Gordon Research Conference on the Physics and Chemistry of Microfluidics, Barga, Italy, 28 June-3 July 2009.
- **M. B. Andersen**, and H. Bruus, *Theoretical analysis of electrokinetic analyte transport in nano-slits*, Annual meeting of the Danish Physical Society Nordic Meeting, Technical University of Denmark, Denmark, 16-18 June 2009.

Chapter 2

Basic theory

2.1 Notation

Due to traditions in the literature we use two notations for concentration: n in units of m^{-3} and c in units of $\mathrm{M} = \mathrm{mol\,L}^{-1}$. The relation between the two notations is $n = 1000\,N_\mathrm{A}\,c$. Furthermore, for notational simplicity, when working with the log of concentration $\mathrm{p}X = -\log_{10}(c_X/c_\ominus)$ and with acid dissociation constants

$$K_\mathrm{A} = \frac{c_\mathrm{A} c_\mathrm{H}}{c_\mathrm{HA} c_\ominus} \qquad (\mathrm{p}K_\mathrm{A} = -\log_{10} K_\mathrm{A}) \tag{2.1}$$

we will often leave out the standard-state scaling factor $c_\ominus = 1\,\mathrm{M}$, unless noted otherwise. We use the short-hand notation $\frac{\partial}{\partial i} = \partial_i$ for partial derivatives and typeset vectors (tensors) in boldface. Occasionally, we will use the Einstein summation convention where summing over repeated indices is implied. For notational simplicity we use H^+ instead of $\mathrm{H_3O}^+$ as the chemical symbol for the hydronium ion. Also, we refer to the hydronium ion H^+ and the hydroxyl ion OH^- under one as "water ions".

2.2 Electrostatics

Electrodynamic phenomena are described by Maxwell's equations where we neglect magnetic effects and thus deal with a purely electrostatic problem. This is described by the Poisson equation which relates the electrostatic potential ϕ to the electrical space charge density ρ_el [14, 89, 90],

$$-\boldsymbol{\nabla} \cdot (\varepsilon \boldsymbol{\nabla} \phi) = \rho_\mathrm{el}, \tag{2.2}$$

in which $\varepsilon = \varepsilon_\mathrm{r}\varepsilon_0$ is the dielectric permittivity. ε_r is the relative permittivity and $\varepsilon_0 = 8.854 \times 10^{-12}\,\mathrm{F\,m}^{-1}$ is the vacuum permittivity. The electrical charge

density is related to the sum of all ion concentrations n_i,

$$\rho_{\mathrm{el}} = e \sum_i Z_i n_i, \tag{2.3}$$

where $e = 1.602 \times 10^{-19}\,\mathrm{C}$ is the elementary charge and Z_i is the valence of ion i. The electric field $\boldsymbol{E}$ is defined as the negative gradient of the electrostatic potential $\boldsymbol{E} = -\boldsymbol{\nabla}\phi$ and the ionic strength I of the electrolyte is defined as

$$I = \frac{1}{2} \sum_i Z_i^2 n_i. \tag{2.4}$$

We undertake a dimensional analysis of the Poisson equation by scaling position with the characteristic length L, electric potential with the thermal voltage $V_{\mathrm{T}} = k_{\mathrm{B}}T/e$ ($\approx 25.7\,\mathrm{mV}$ at $25\,^{\circ}\mathrm{C}$), and concentration with the bulk ionic strength I_{b} ("bulk" explained below). We assume a constant dielectric permittivity in the domain of interest and get (a tilde denotes a dimensionless quantity)

$$\left(\frac{\lambda_{\mathrm{D}}}{L}\right)^2 \tilde{\nabla}^2 \tilde{\phi} = -\sum_i Z_i \tilde{n}_i \tag{2.5}$$

where

$$\lambda_{\mathrm{D}} = \sqrt{\frac{\varepsilon k_{\mathrm{B}} T}{2\, e^2 I_{\mathrm{b}}}} \tag{2.6}$$

is the Debye screening length in which $k_{\mathrm{B}} = 1.381 \times 10^{-23}\,\mathrm{J\,K^{-1}}$ is the Boltzmann constant, and T is the temperature. For a binary $Z{:}Z$ electrolyte of bulk concentration n_{b} the ionic strength reduces to $I_{\mathrm{b}} = Z^2 n_{\mathrm{b}}$ and the Debye length to $\lambda_{\mathrm{D}} = \sqrt{\varepsilon k_{\mathrm{B}} T / \left[2\,(Ze)^2 n_{\mathrm{b}}\right]}$.

We are interested in aqueous (monovalent) electrolytes at standard laboratory conditions for which we can write the screening length as $\lambda_{\mathrm{D}} \approx (c_{\mathrm{b}}/\mathrm{M})^{-\frac{1}{2}} \times 0.3\,\mathrm{nm}$ (note the use of c_{b} indicating that the unit of concentration is M) and thus for a typical electrolyte concentration of $10^{-2}\,\mathrm{M}$ the Debye length is $\lambda_{\mathrm{D}} \approx 3\,\mathrm{nm}$.

For microsystems with a typical length scale L in the range $10^3\,\mathrm{nm}$ to $10^6\,\mathrm{nm}$ the factor $(\lambda_{\mathrm{D}}/L)^2$ multiplying the Laplacian in Eq. (2.5) becomes very small, on the order of 10^{-6} to 10^{-3}, in any case much smaller than unity. Thus, the left-hand-side in Eq. (2.5) is close to zero and the electroneutrality condition becomes

$$\sum_{i=1}^{N} Z_i n_i = 0. \tag{2.7}$$

However, in thin sheaths, or boundary layers, close to interfaces and boundaries the so-called electric double layer (EDL) may form. This electrically charged layer decays over a distance given by the Debye length λ_{D} and the EDL is therefore especially significant in micro- and nanofluidics. Thus, the term "bulk" is referring to the region (immediately) outside the EDL (in an asymptotic sense). The EDL relates to many important phenomena including ion selectivity [5–7, 91], streaming potential, electroviscous effect, EO flow, electrophoresis [14, 92, 93], and ICEO [94].

2.3 Ionic transport

The equation expressing mass conservation of the ionic species is [93, 95]

$$\frac{\partial n_i}{\partial t} + \boldsymbol{\nabla} \cdot \boldsymbol{J}_i = R_i, \tag{2.8}$$

in which $\boldsymbol{J}_i$ is the flux and R_i is the production term. We deal with the production term later. Generally, the flux is related to the average ion velocity $\boldsymbol{u}_i$,

$$\boldsymbol{J}_i = n_i \boldsymbol{u}_i. \tag{2.9}$$

The multicomponent diffusion equation relates the average ion velocity to the driving force and the friction with other ions [95, 96],

$$n_i \boldsymbol{\nabla} \bar{\mu}_i = k_\mathrm{B} T \sum_j \frac{n_i n_j}{n_\mathrm{tot} \mathcal{D}_{ij}} \left(\boldsymbol{u}_j - \boldsymbol{u}_i \right), \tag{2.10}$$

where $\bar{\mu}_i$ is the electrochemical potential, n_tot is the sum of all concentrations (including the solvent), and $\mathcal{D}_{ij}$ is a diffusion coefficient describing the interaction of species i and j. The electrochemical potential consists of entropic and electrostatic energies [14, 93, 95],

$$\bar{\mu}_i = \mu_i^\ominus + k_\mathrm{B} T \ln a_i + Z_i e \phi, \tag{2.11}$$

where $\mu_i^\ominus$ is a standard-state reference energy and a_i is the activity. The activity relates to the concentration through the activity coefficient γ_i, $a_i = \gamma_i c_i / c_\ominus$, in which $c_\ominus = 1\,\mathrm{M}$ is a standard-state reference concentration [97].

We are interested in ideal solutions (implying dilute solutions) whereby we can approximate the activity coefficient with unity, $\gamma_i = 1$. In this case ion-ion interactions vanish whereby the expression for the flux simplifies and it is possible to identify three terms: diffusion, electromigration, and advection. The flux-expression is also known as the Nernst–Planck equation [14, 93, 95],

$$\boldsymbol{J}_i = D_i \left(-\boldsymbol{\nabla} n_i - \frac{Z_i}{V_\mathrm{T}} n_i \boldsymbol{\nabla} \phi \right) + n_i \boldsymbol{v}, \tag{2.12}$$

where D_i is the diffusion coefficient and $\boldsymbol{v}$ is the solvent velocity.

We find the electrical current density $\boldsymbol{i}_\mathrm{el}$ carried by the ions by multiplying $\boldsymbol{J}_i$ with the ionic charge and summing,

$$\boldsymbol{i}_\mathrm{el} = e \sum_i Z_i \boldsymbol{J}_i. \tag{2.13}$$

In the special case where the contribution to the current from diffusion and advection is negligible we obtain Ohm's law,

$$\boldsymbol{i}_\mathrm{el} = \sigma_\mathrm{el} \boldsymbol{E}, \tag{2.14}$$

where

$$\sigma_{\mathrm{el}} = e \sum_i Z_i \mu_i n_i \tag{2.15}$$

is the electrical conductivity and we have used the Einstein equation [98],

$$\mu_i = Z_i \frac{D_i}{V_{\mathrm{T}}}, \tag{2.16}$$

to relate the ionic mobility μ_i (at infinite dilution) to the diffusivity.

We carry out a dimensional analysis by scaling length with L, concentration with $n_{i,\mathrm{b}}$, fluid velocity with v_0, time with the unsteady time-scale τ, production with $n_{i,\mathrm{b}}/\tau_{\mathrm{reac},i}$ ($\tau_{\mathrm{reac},i}$ being the characteristic reaction time) and Eq. (2.8) becomes

$$Pe_i \, St \, \frac{\partial \tilde{n}_i}{\partial \tilde{t}} + \tilde{\boldsymbol{\nabla}} \cdot \left(-\tilde{\boldsymbol{\nabla}} \tilde{n}_i - Z_i \tilde{n}_i \tilde{\boldsymbol{\nabla}} \tilde{\phi} + Pe_i \, \tilde{n}_i \tilde{\boldsymbol{v}} \right) = Da_i \, \tilde{R}_i, \tag{2.17}$$

where $Pe_i = v_0 L / D_i$ is the Péclet number (mass transport by advection to mass transport by diffusion), $St = L/(v_0 \tau)$ is the Strouhal number (the flow time scale to the unsteady time scale), and $Da_i = L^2/(D_i \tau_{\mathrm{reac},i})$ is the Damköhler number (characteristic time for diffusion to the characteristic reaction time for chemical reaction).

Typically, microsystems have a length scale $L \lesssim 10^{-5}\,\mathrm{m}$, flows with velocity scale $v_0 \lesssim 10^{-4}\,\mathrm{m\,s^{-1}}$, and ions with diffusion coefficient $D \sim 10^{-9}\,\mathrm{m^2\,s^{-1}}$. In this case $Pe \lesssim 1$, where $Pe \sim 1$ indicates that advection could be significant and $Pe \ll 1$ indicates that advection is negligible. Also, for long time scales (steady-state) $\tau \to \infty$, the Strouhal number vanishes $St \to 0$ whereby we can neglect the unsteady term. Moreover, in quasi-equilibrium chemistry the reactions occur instantaneously corresponding to a short reaction time $\tau_{\mathrm{reac},i} \to 0$ and thus a large Damköhler number $Da \to \infty$. This limit leads to the condition $R_i = 0$ which we use in Section 2.6 where we discuss the chemistry in more detail.

2.4 Electrochemical equilibrium

With no fluid flow (or a low Péclet number $Pe \ll 1$) and the system at electrochemical equilibrium (uniform electrochemical potential) the flux is zero and diffusion must balance electromigration whereby Eq. (2.12) leads to the Boltzmann distribution of the ions,

$$n_i = n_{i,\mathrm{b}} \exp\left[-\frac{Z_i(\phi - \phi_{\mathrm{b}})}{V_{\mathrm{T}}} \right], \tag{2.18}$$

where $n_{i,\mathrm{b}}$ and ϕ_{b} are reference (bulk) levels for the concentration and electric potential, respectively. When $\phi = \phi_{\mathrm{b}}$ then $n_i = n_{i,\mathrm{b}}$. We apply the Boltzmann

distribution in the Poisson equation Eq. (2.2) and obtain the Poisson–Boltzmann equation,

$$\nabla^2\phi = -\frac{e}{\varepsilon}\sum_i Z_i n_{i,\mathrm{b}} \exp\left[-\frac{Z_i(\phi-\phi_\mathrm{b})}{V_\mathrm{T}}\right]. \tag{2.19}$$

In the special case of a planer wall with surface normal along the z-coordinate we can integrate Eq. (2.19) once to obtain

$$\left(\frac{\mathrm{d}\phi}{\mathrm{d}z}\right)^2 = 2\frac{k_\mathrm{B}T}{\varepsilon}\sum_i n_{i,\mathrm{b}}\left\{\exp\left[-\frac{Z_i(\phi-\phi_\mathrm{b})}{V_\mathrm{T}}\right] - \exp\left[-\frac{Z_i(\phi^*-\phi_\mathrm{b})}{V_\mathrm{T}}\right]\right\}, \tag{2.20}$$

where ϕ^* is the reference potential where $\mathrm{d}\phi/\mathrm{d}z = 0$.

Immediately at the charged wall bounding the electrolyte, at the plane of viscous shear (also called the slip-plane), we define the zeta potential ζ relative to ϕ_b. The surface charge density σ is related to the normal derivative of the potential [14, 89, 90],

$$-\frac{\sigma}{\varepsilon} = \boldsymbol{n}\cdot\boldsymbol{\nabla}\phi, \tag{2.21}$$

and we have the freedom to define $\phi_\mathrm{b} = \phi^*$. Then, Eq. (2.20) becomes the Grahame equation [3, 99],

$$\sigma^2 = 2\,\varepsilon k_\mathrm{B}T\sum_i n_{i,\mathrm{b}}\left[\exp\left(-\frac{Z_i\zeta}{V_\mathrm{T}}\right) - 1\right], \tag{2.22}$$

which for a binary $Z{:}Z$ electrolyte simplifies to

$$\sigma = \frac{\varepsilon}{\lambda_\mathrm{D}}\frac{2\,V_\mathrm{T}}{Z}\sinh\left(\frac{Z\zeta}{2\,V_\mathrm{T}}\right), \tag{2.23}$$

which in the Debye–Hückel limit of small surface potentials $Z\zeta/(2\,V_\mathrm{T}) \ll 1$ simplifies to $\sigma = \zeta\,\varepsilon/\lambda_\mathrm{D}$.

For a binary $Z{:}Z$ electrolyte we rewrite Eq. (2.20) [assuming $z > 0$ and thus $\mathrm{sgn}(\mathrm{d}\phi/\mathrm{d}z) = -\,\mathrm{sgn}(\phi)$] [4],

$$\frac{\mathrm{d}\phi}{\mathrm{d}z} = -\frac{2}{Z}\frac{V_\mathrm{T}}{\lambda_\mathrm{D}}\sinh\left(\frac{Z\phi}{2\,V_\mathrm{T}}\right), \tag{2.24}$$

which we integrate to obtain the Gouy–Chapman solution [14],

$$\phi = \frac{4\,V_\mathrm{T}}{Z}\tanh^{-1}\left[\tanh\left(\frac{Z\zeta}{4\,V_\mathrm{T}}\right)\exp\left(-\frac{z}{\lambda_\mathrm{D}}\right)\right], \tag{2.25}$$

which in the Debye–Hückel limit of small surface potentials $Z\zeta/(4\,V_\mathrm{T}) \ll 1$ simplifies to $\phi = \zeta\exp\left(-z/\lambda_\mathrm{D}\right)$. We apply this result in Eq. (2.18) which upon expansion yields $n_\pm = n_\mathrm{b}\left[1 \mp Z\zeta\exp\left(-z/\lambda_\mathrm{D}\right)/V_\mathrm{T}\right]$.

2.5 Hydrodynamics

The equation for mass conservation of the fluid is [14, 93]

$$\frac{\partial \rho_\mathrm{m}}{\partial t} + \boldsymbol{\nabla} \cdot (\rho_\mathrm{m} \boldsymbol{v}) = 0, \tag{2.26}$$

where ρ_m is the mass density of the fluid. For incompressible fluids the mass density following a fluid particle is constant, $D\rho_\mathrm{m}/Dt = 0$, ($\mathrm{D}/\mathrm{D}t = \partial/\partial t + \boldsymbol{v} \cdot \boldsymbol{\nabla}$ is the material derivative) and the equation for conservation of mass becomes

$$\boldsymbol{\nabla} \cdot \boldsymbol{v} = 0. \tag{2.27}$$

The equations for the conservation of momentum are the Navier–Stokes equations [14, 93, 100],

$$\rho_\mathrm{m} \frac{Dv_i}{Dt} = -\partial_i p + \partial_j \sigma_{ij} + f_i, \tag{2.28}$$

where the indices run over the three spatial coordinates x, y, and z. Moreover, p is the pressure,

$$\sigma_{ij} = \eta \left[\partial_j v_i + \partial_i v_j - (\beta - 1)\, \delta_{ij} \partial_k v_k\right] \tag{2.29}$$

is the viscous stress tensor, f_i is a force density, β is a dimensionless viscosity ratio, and δ_{ij} is the Kronecker delta. β relates to effects of compressibility. The force density f_i could be due to gravity $\rho_\mathrm{m} g_i$, buoyancy $(\partial \rho_\mathrm{m}/\partial T)\, \Delta T\, g_i$, and electrical stresses $\partial_j T_{ij}$, where

$$T_{ij} = \varepsilon \left\{ E_i E_j - \frac{1}{2} \left[1 - \frac{\rho_\mathrm{m}}{\varepsilon} \left(\frac{\partial \varepsilon}{\partial \rho_\mathrm{m}} \right)_T \right] E_k E_k\, \delta_{ij} \right\} \tag{2.30}$$

is the Maxwell stress tensor. We take the divergence of the Maxwell stress tensor and write out the three resulting terms: the Coulomb force $\rho_\mathrm{el} E_i$, the dielectric force $-\frac{1}{2} E_k E_k \partial_i \varepsilon$, and the electrostriction $\frac{1}{2} \partial_i \left[\rho_\mathrm{m} \left(\partial \varepsilon / \partial \rho_\mathrm{m}\right)_T E_k E_k\right]$ [101–103].

For single-phase incompressible Newtonian fluids at isothermal conditions, and no gradients in the electrical permittivity, the viscous stress tensor reduces to

$$\sigma_{ij} = \eta \left(\partial_j v_i + \partial_i v_j\right), \tag{2.31}$$

and the Navier–Stokes equations become [14]

$$\rho_\mathrm{m} \frac{D\boldsymbol{v}}{Dt} = -\boldsymbol{\nabla} p + \eta \nabla^2 \boldsymbol{v} + \rho_\mathrm{el} \boldsymbol{E}. \tag{2.32}$$

To further reduce the equations we undertake a dimensional analysis by scaling position with L, velocity with the electrokinetic velocity scale $v_0 = \varepsilon V_\mathrm{T}^2/(\eta L)$, pressure with $p_0 = \varepsilon \left(V_\mathrm{T}/L\right)^2$ and time with τ. We rewrite the electric force

density term $\rho_{\mathrm{el}}\boldsymbol{E} = \varepsilon\nabla^2\phi\boldsymbol{\nabla}\phi$, and scale the electrical potential with the thermal voltage V_{T}. Thus, the scaled Navier–Stokes equations become

$$Re\left[St\,\frac{\partial\tilde{\boldsymbol{v}}}{\partial\tilde{t}} + \left(\tilde{\boldsymbol{v}}\cdot\tilde{\boldsymbol{\nabla}}\right)\tilde{\boldsymbol{v}}\right] = -\tilde{\boldsymbol{\nabla}}\tilde{p} + \tilde{\nabla}^2\tilde{\boldsymbol{v}} + \tilde{\nabla}^2\tilde{\phi}\tilde{\boldsymbol{\nabla}}\tilde{\phi}, \tag{2.33}$$

in which $Re = v_0 L/\nu$ is the Reynolds number (inertial force to viscous force) [14, 93]. The kinematic viscosity $\nu = \eta/\rho_{\mathrm{m}}$ has unit of $\mathrm{m^2\,s^{-1}}$ whereby it resembles a "diffusion coefficient" for momentum.

Typically, aqueous solutions in microsystems have $\nu \sim 10^{-6}\,\mathrm{m^2\,s^{-1}}$, a length scale $L \lesssim 10^{-5}\,\mathrm{m}$, and a velocity scale $v_0 \lesssim 10^{-4}\,\mathrm{m\,s^{-1}}$. In this case $Re \lesssim 10^{-3}$, and for long time scales (steady-state) $\tau \to \infty$ the Stouhal number vanishes $St \to 0$. Hence, the left-hand-side in Eq. (2.33) is negligible. Re-dimensionalization then yields the most general form of the Navier–Stokes equations used in this thesis,

$$\boldsymbol{0} = -\boldsymbol{\nabla}p + \eta\nabla^2\boldsymbol{v} + \rho_{\mathrm{el}}\boldsymbol{E}, \tag{2.34}$$

also known as the Stokes equations.

2.5.1 Helmholtz–Smoluchowski slip

We assume an electric field E_x, tangential to a charged surface, acting on the charge density in the equilibrium EDL (with associated equilibrium potential ϕ_{eq}), thereby giving rise to a tangential velocity v_x. Furthermore, we assume $\lambda_{\mathrm{D}}/L \ll 1$ and that tangential pressure gradients are negligible, and Stokes equations Eq. (2.34) simplify to a balance between tangential viscous and electrical stresses, $0 = \eta\partial_z^2 v_x - \varepsilon E_x \partial_z^2\phi_{\mathrm{eq}}$ (z being the surface-normal coordinate). This equation is readily integrated subject to the no-slip condition $v_x(z=0) = 0$ and the condition that v_x remains finite for all z. The resulting tangential velocity,

$$v_x = \varepsilon\zeta(\phi/\zeta - 1)E_x/\eta, \tag{2.35}$$

approaches the limiting Helmholtz–Smoluchowski velocity v_{hs} asymptotically as $z \to \infty$ (on the "inner" scale of λ_{D}),

$$v_{\mathrm{hs}} = -\frac{\varepsilon\zeta}{\eta}E_x. \tag{2.36}$$

Seen from the "outer" macroscopic scale the surface appears to have a slip velocity of v_{hs}.

2.6 Bulk solution chemistry

We summarize the review of equilibrium chemistry for microfluidic electrokinetics by Persat *et al.* [97, 104, 105]. We define pH in terms of the activity of the hydronium ion, $\mathrm{pH} \equiv -\log_{10} a_{\mathrm{H}}$, which for dilute solutions simplifies to

$$\mathrm{pH} \equiv -\log_{10}\frac{c_{\mathrm{H}}}{c_{\ominus}}. \tag{2.37}$$

We remind that the H^+- and OH^- ions are referred to under one as "water ions".

We describe the chemistry of the water ions, and any additional ions in the electrolyte, by the proton dissociation reaction,

$$HA + H_2O \underset{b_A}{\overset{f_A}{\rightleftharpoons}} A^- + H_3O^+, \tag{2.38}$$

where HA is the undissociated molecule, H_20 is the water molecule, A^- is the dissociated molecule, and f_A and b_A are the forward and backward reaction rate constants, respectively. If the rate constants are large in the sense of a small reaction time scale $\tau_{\mathrm{reac,A}} \ll 1$, and thus a large Damköhler number $Da \gg 1$ (cf. Section 2.3), then the reaction will be maintained at equilibrium and the production term vanishes,

$$R_A = f_A a_{HA} a_{H_2O} - b_A a_A a_H = 0. \tag{2.39}$$

This leads to the condition of chemical equilibrium and the definition of the acid dissociation constant K_A,

$$\frac{a_A a_H}{a_{HA} a_{H_2O}} = \frac{f_A}{b_A} = K_A. \tag{2.40}$$

K_A is also referred to as "equilibrium constant" and is also given as $pK_A = -\log_{10} K_A$. For ideal solutions the activity of the water molecule is constant and defined to be unity, $a_{H_2O} \equiv 1$, and Eq. (2.40) simplifies to

$$K_A = \frac{c_A c_H}{c_{HA} c_\ominus}. \tag{2.41}$$

In general, the dissociation constant depends on ionic strength and temperature, but we neglect such effects unless noted otherwise.

In particular, for the water ions the reaction Eq. (2.38) is known as self-ionization and is always present in aqueous electrolytes,

$$H_2O + H_2O \underset{b_w}{\overset{f_w}{\rightleftharpoons}} OH^- + H_3O^+, \tag{2.42}$$

where the subscript "w" refers to "water ions". The equilibrium condition becomes

$$\frac{c_{OH} c_H}{c_\ominus^2} = \frac{f_w}{b_w} = K_w, \tag{2.43}$$

in which $K_w = 10^{-14}$ at 25 °C. For notational simplicity we omit $c_\ominus$ in what follows.

Aside from the self-ionization, dissociation reactions can be introduced purposefully e.g. through a buffer to control the pH (especially relevant in biological work). The reactions can also appear unintentionally e.g. due to the absorbtion of

CO_2 from the atmosphere which is subsequently transformed into carbonic acid H_2CO_3 (more about this in Chapter 6).

We want to write all chemical reactions as acid dissociations (i.e. with a H^+ on the right-hand-side of the chemical reaction) since this facilitates a straightforward and general mathematical treatment (explained below).

In this regard, we account for base reactions, $BOH \rightleftharpoons B^+ + OH^-$, by rewriting them to acidic form,

$$B^+ + \frac{1}{2}H_{2(g)} \rightleftharpoons B + H^+. \tag{2.44}$$

Moreover, we account for the presence of a chemically inert salt by the addition of the corresponding amount of acid and base i.e. 1 mM of KCL is modeled as 1 mM of HCl and 1 mM of KOH, and 1 mM Na_2HPO_4 is modeled as 2 mM NaOH and 1 mM H_3PO_4.

It is convenient with a systematic scheme for the complex situation where the electrolyte consists of multiple ionic species correlating to each other through acid dissociation reactions. We introduce the concept of a chemical "family" X containing the reactions $X^Z \rightleftharpoons X^{Z-1} + H^+$, $Z = n_X + 1, n_X + 2, n_X, \ldots, p_X$, where n_X and p_X is the minimum and maximum valence, respectively. As an example, the family of phosphoric acid X=H_3PO_4 consists of the four members $X^{3-} = PO_4^{3-}$, $X^{2-} = HPO_4^{2-}$, $X^- = H_2PO_4^-$, and $X^0 = H_3PO_4$. Using the general notation, all the dissociation reactions within a family are

$$X^{p_X} \rightleftharpoons X^{p_X-1} + H^+, \qquad K_{X,p_X-1}, \tag{2.45a}$$
$$X^{p_X-1} \rightleftharpoons X^{p_X-2} + H^+, \qquad K_{X,p_X-2}, \tag{2.45b}$$
$$\ldots \tag{2.45c}$$
$$X^{n_X+1} \rightleftharpoons X^{n_X} + H^+, \qquad K_{X,n_X\cdot}, \tag{2.45d}$$

while chemical equilibrium for each individual reaction is

$$K_{X,Z} = \frac{c_{X,Z}c_H}{c_{X,Z+1}}, \tag{2.46}$$

and mass conservation for the entire family is

$$c_X = \sum_{Z=n_X}^{p_X} c_{X,Z}, \tag{2.47}$$

where c_X is the total (analytical) concentration of the family.

For electroneutral conditions (see also Section 2.2) the total charge from all ionic species must vanish,

$$\sum_X \sum_{Z=n_X}^{p_X} Z c_{X,Z} + c_H - \frac{K_w}{c_H} = 0, \tag{2.48}$$

where c_{H} is taken out of the sum due to its special significance. Note the notation: the outer sum runs over the chemical families while the inner sum runs over the valences within each family.

Within each chemical family it is possible to relate the concentration of each charge state Z to that of the neutral state and that of the hydronium ion,

$$K_{\mathrm{X},0}K_{\mathrm{X},1}K_{\mathrm{X},2}\dots K_{\mathrm{X},Z-1} = \frac{c_{\mathrm{X},0}}{c_{\mathrm{X},1}}\frac{c_{\mathrm{X},1}}{c_{\mathrm{X},2}}\dots\frac{c_{\mathrm{X},Z-1}}{c_{\mathrm{X},Z}}c_{\mathrm{H}}^{Z} \tag{2.49a}$$

$$= \frac{c_{\mathrm{X},0}}{c_{\mathrm{X},Z}}c_{\mathrm{H}}^{Z}, \tag{2.49b}$$

which we rewrite in terms of $c_{\mathrm{X},Z}$,

$$c_{\mathrm{X},Z} = c_{\mathrm{X},0}L_{\mathrm{X},Z}c_{\mathrm{H}}^{Z}, \tag{2.50}$$

where

$$L_{\mathrm{X},Z} = \begin{cases} \prod_{Z'=Z}^{-1} K_{\mathrm{X},Z'} & Z < 0 \\ 1 & Z = 0\,. \\ \prod_{Z'=0}^{Z-1} K_{\mathrm{X},Z'}^{-1} & Z > 0 \end{cases} \tag{2.51}$$

Furthermore, applying Eq. (2.50) in the family mass conservation Eq. (2.47) yields $c_{\mathrm{X},0}$, which upon reinsertion in Eq. (2.50) leads to

$$c_{\mathrm{X},Z} = c_{\mathrm{X}}\, g_{\mathrm{X},Z}, \tag{2.52}$$

in which

$$g_{\mathrm{X},Z} = L_{\mathrm{X},Z}c_{\mathrm{H}}^{Z}\left(\sum_{Z=n_{\mathrm{X}}}^{p_{\mathrm{X}}} L_{\mathrm{X},Z}c_{\mathrm{H}}^{Z}\right)^{-1}. \tag{2.53}$$

We apply Eq. (2.52) in the electroneutrality condition Eq. (2.48) and obtain an algebraic equation for c_{H},

$$\sum_{\mathrm{X}}\sum_{Z=n_{\mathrm{X}}}^{p_{\mathrm{X}}} Z c_{\mathrm{X}}\, g_{\mathrm{X},Z} + c_{\mathrm{H}} - \frac{K_{\mathrm{w}}}{c_{\mathrm{H}}} = 0. \tag{2.54}$$

This equation can be solved for c_{H} e.g. numerically in an iterative process.

Once the hydronium-ion concentration is determined, the concentration of all other ionic species are given by Eq. (2.52). We note that Eq. (2.54) can be rewritten to polynomial form and solved efficiently as shown by Persat *et al.* [97]. In Chapter A.3 we include their `Matlab` "ITPCalculator" script (available at `http://microfluidics.stanford.edu`) with slight modifications according to our implementation.

2.6.1 Ionic transport and chemical equilibrium

Below we summarize how to account for transport of ionic species in chemical equilibrium. For each chemical family the assumption of a large Damköhler number reduces the $p_\mathrm{X} - n_\mathrm{X} = N_\mathrm{X}$ ionic transport equations Eq. (2.8) to $N_\mathrm{X} - 1$ conditions of chemical equilibrium Eq. (2.41), to which the condition of mass conservation is added in order to balance the number of unknowns with the number of equations. An exception to this scheme is the water ions; c_OH is given in terms of c_H by the water self-ionization equilibrium Eq. (2.43) and c_H by the electroneutrality condition Eq. (2.54).

However, during transport, the concentrations are no longer uniform in space. We find the effective flux equations that take chemical equilibrium into account by utilizing that the total production $\sum_{Z=n_\mathrm{X}}^{p_\mathrm{X}} R_Z$ within a family must vanish [104, 106–108]. An exception to this rule is the water ions, more about that below. Thus, we sum the individual transport equations in Eq. (2.8) within each family and obtain the effective transport equation for the analytical concentration n_X without production term,

$$\frac{\partial n_\mathrm{X}}{\partial t} + \boldsymbol{\nabla} \cdot [-\boldsymbol{\nabla} (D_\mathrm{X} n_\mathrm{X}) - \mu_\mathrm{X} n_\mathrm{X} \boldsymbol{\nabla}\phi + n_\mathrm{X} \boldsymbol{v}] = 0, \tag{2.55}$$

where the effective diffusivity D_X and effective mobility μ_X are given as [107, 108]

$$D_\mathrm{X} = \sum_{Z=n_\mathrm{X}}^{p_\mathrm{X}} g_{\mathrm{X},Z} D_{\mathrm{X},Z}, \qquad \mu_\mathrm{X} = \sum_{Z=n_\mathrm{X}}^{p_\mathrm{X}} g_{\mathrm{X},Z} \mu_{\mathrm{X},Z}. \tag{2.56}$$

The electrical potential constitutes a new variable in the system and requires an accompanying equation.

If the transport occurs without generation of electrical space charge then the water ions are determined by the electroneutrality condition Eq. (2.54), and the electrical potential is determined by conservation of the total current as shown in Bercovici *et al.* [107].

If the transport happens with generation of electrical space charge, as in electrodialysis systems at over-limiting current Chapter 7, then the water ions are determined by an effective flux equation as shown in Section 7.2.1.3, and the electrical potential is determined by the Poisson equation Eq. (2.2). This is the case in Chapter 7 where we study over-limiting current in ion-selective membranes.

2.7 Surface chemistry

Below we summarize selected parts of the theory of surface chemistry [4]. We start by presenting one of the simplest surface chemistry models, the "two-layer model", which introduces acid dissociation reactions on the surface. Next, we extend this to the "four-layer model" which introduces adsorption of metal ions onto the charged surface groups, so-called site-binding.

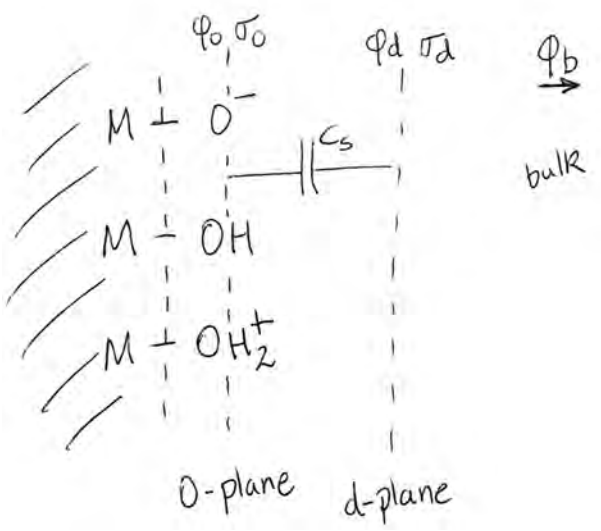

Figure 2.1: Sketch of the two-layer surface chemistry model.

2.7.1 Two-layer model

We assume the surface consists of surface groups which are either charge neutral MOH, negatively charged $\mathrm{MO^-}$, or positively charged $\mathrm{MOH_2^+}$, see Fig. 2.1. These surface groups are in an acid dissociation equilibrium with the hydronium ion $\mathrm{H_0^+}$ at the 0-plane (the plane of the mean position of the hydronium ion when reacting),

$$\mathrm{MOH} \rightleftharpoons \mathrm{MO^-} + \mathrm{H_0^+}, \tag{2.57a}$$
$$\mathrm{MOH_2^+} \rightleftharpoons \mathrm{MOH} + \mathrm{H_0^+}, \tag{2.57b}$$

described in equilibrium by

$$K_{\mathrm{MO}} = \frac{\Gamma_{\mathrm{MO}} c_{\mathrm{H},0}}{\Gamma_{\mathrm{MOH}}}, \tag{2.58a}$$
$$K_{\mathrm{MOH_2}} = \frac{\Gamma_{\mathrm{MOH}} c_{\mathrm{H},0}}{\Gamma_{\mathrm{MOH_2}}}, \tag{2.58b}$$

where K_i is the dissociation constant and Γ_i is the surface concentration of group i. For silica $\mathrm{p}K_{\mathrm{SiO}} \approx 6.8$ [109] and $\mathrm{p}K_{\mathrm{SiOH_2}} \approx -1.9$ [110], indicating that for neutral pH ≈ 7 the amount of positively charged surface groups is negligible and Eq. (2.57b) can be ignored. However, if the pH is sufficiently low this approximation is not valid and Eq. (2.57b) needs to be considered.

The local concentration of ion i at the surface j-plane is related to its bulk counterpart through the Boltzmann factor,

$$c_{i,j} = c_{i,\mathrm{b}} \exp\left(-Z_i \frac{\phi_j - \phi_{\mathrm{b}}}{V_{\mathrm{T}}}\right). \tag{2.59}$$

In the case of the hydronium ion this leads to,

$$c_{\mathrm{H},0} = c_{\mathrm{H,b}} \exp\left(-\frac{\phi_0 - \phi_\mathrm{b}}{V_\mathrm{T}}\right). \tag{2.60}$$

When the surface concentration of positive and negative groups are equal, $\Gamma_{\mathrm{MO}} = \Gamma_{\mathrm{MOH_2}}$, the surface is said to be at the "point of zero charge" (PZC). At this condition we get from Eq. (2.58) that the pH at the 0-plane is the average of the dissociation constants,

$$\mathrm{pH}_{0,\mathrm{pzc}} = \frac{\mathrm{p}K_{\mathrm{MO}} + \mathrm{p}K_{\mathrm{MOH_2}}}{2}. \tag{2.61}$$

Using the Boltzmann relation in Eq. (2.60) the pH in the bulk at the PZC becomes

$$\mathrm{pH}_{\mathrm{b,pzc}} = \mathrm{pH}_{0,\mathrm{pzc}} + \frac{\phi_0 - \phi_\mathrm{b}}{V_\mathrm{T}} \log_{10}(\mathrm{e}), \tag{2.62}$$

where $\log_{10}(\mathrm{e}) \approx 0.43$. For a characteristic value of $\phi_0 - \phi_\mathrm{b} \approx -100\,\mathrm{mV}$ the correction in the bulk to $\mathrm{pH}_{0,\mathrm{pzc}}$ is -2 units.

The total amount of surface sites Γ_{tot} is conserved,

$$\Gamma_{\mathrm{MOH}} + \Gamma_{\mathrm{MO}} + \Gamma_{\mathrm{MOH_2}} = \Gamma_{\mathrm{tot}}, \tag{2.63}$$

which we rewrite using Eq. (2.58),

$$\Gamma_{\mathrm{MOH}} = \Gamma_{\mathrm{tot}} \left(1 + \frac{K_{\mathrm{MO}}}{c_{\mathrm{H},0}} + \frac{c_{\mathrm{H},0}}{K_{\mathrm{MOH_2}}}\right)^{-1}. \tag{2.64}$$

The surface charge density σ_0 at the 0-plane is related to the surface concentration of charged surface groups,

$$\begin{aligned} \sigma_0 &= e\left(\Gamma_{\mathrm{MOH_2}} - \Gamma_{\mathrm{MO}}\right) \\ &= e\left(\frac{c_{\mathrm{H},0}}{K_{\mathrm{MOH_2}}} - \frac{K_{\mathrm{MO}}}{c_{\mathrm{H},0}}\right)\Gamma_{\mathrm{MOH}}. \end{aligned} \tag{2.65}$$

We assume zero charge between the 0- and d-plane which thus act as capacitor plates, and the potential difference between the planes is linearly related to the surface charge density through the Stern capacitance [3, 4, 14, 93, 95],

$$C_\mathrm{s}\left(\phi_0 - \phi_\mathrm{d}\right) = \sigma_0. \tag{2.66}$$

Any charge imbalance will be canceled quickly by the mobile ions and we thus require electroneutrality between the surface 0-plane and the diffuse layer d-plane,

$$\sigma_0 + \sigma_\mathrm{d} = 0. \tag{2.67}$$

Using Eqs. (2.60), (2.64), and (2.65) together with Grahame's equation Eq. (2.22) (where $\sigma = -\sigma_\mathrm{d}$ and $\zeta = \phi_\mathrm{d}$), the two equations Eqs. (2.66) and (2.67) are closed

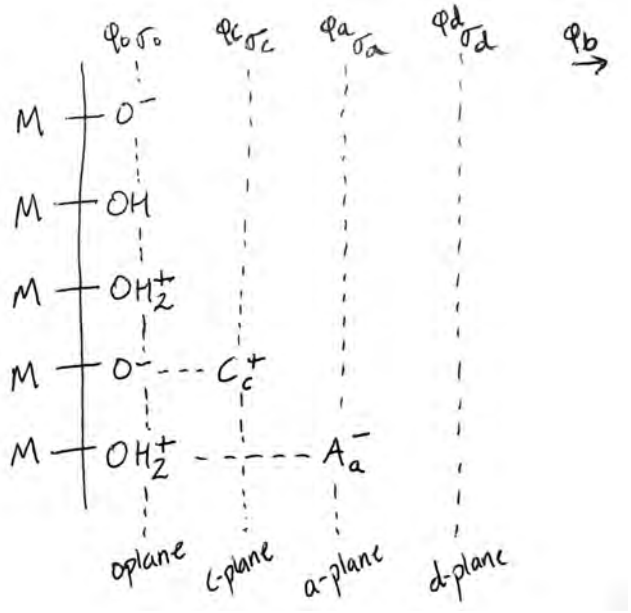

Figure 2.2: Sketch of the four-layer surface chemistry model.

in terms of the two surface potentials ϕ_0 and ϕ_d, and thus constitute the two-layer model.

Unfortunately, the system is rarely analytically tractable due to the many non-linear terms and a numerical solution is therefore often required. As is often seen in the literature we express the surface charge density in terms of the surface concentrations,

$$\sigma_0 = e\Gamma_\mathrm{tot}\left(\frac{c_{\mathrm{H},0}}{K_{\mathrm{MOH_2}}} - \frac{K_\mathrm{MO}}{c_{\mathrm{H},0}}\right)\left(1 + \frac{K_\mathrm{MO}}{c_{\mathrm{H},0}} + \frac{c_{\mathrm{H},0}}{K_{\mathrm{MOH_2}}}\right)^{-1}. \tag{2.68}$$

We note that the two-layer model couples to the local bulk electrolyte concentrations $c_{i,\mathrm{b}}$ through the Boltzmann factors in Eq. (2.60) and through Grahame's equation Eq. (2.22).

2.7.2 Four-layer model

We expand the two-layer model to additionally take into account site-binding i.e. the electrostatic adsorption of charged monovalent (metal) ions onto charged surface groups of opposite charge sign [111–114], see Fig. 2.2.

The negatively charged surface groups are in equilibrium with the cations $\mathrm{C_c^+}$ at the c-plane (the plane of the mean position of the cations when binding) and the positively charged surface groups with the anions $\mathrm{A_a^-}$ at the a-plane (the plane of the mean position of the anions when binding),

$$\mathrm{MO^-C^+} \rightleftharpoons \mathrm{MO^-} + \mathrm{C_c^+}, \tag{2.69a}$$
$$\mathrm{MOH_2^+A^-} \rightleftharpoons \mathrm{MOH_2^+} + \mathrm{A_a^-}. \tag{2.69b}$$

These reactions are described by the equilibrium equations

$$K_{\mathrm{MOC}} = \frac{\Gamma_{\mathrm{MO}} c_{\mathrm{C,c}}}{\Gamma_{\mathrm{MOC}}}, \tag{2.70a}$$

$$K_{\mathrm{MOH_2A}} = \frac{\Gamma_{\mathrm{MOH_2}} c_{\mathrm{A,a}}}{\Gamma_{\mathrm{MOH_2A}}}. \tag{2.70b}$$

The concentration of cations $c_{\mathrm{C,c}}$ at the c-plane and anions $c_{\mathrm{A,a}}$ at the a-plane are related to their bulk counterparts, $c_{\mathrm{C,b}}$ and $c_{\mathrm{A,b}}$, though the Boltzmann relation Eq. (2.59) and the surface potential at the c-plane ϕ_{c} and at the a-plane ϕ_{a},

$$c_{\mathrm{C,c}} = c_{\mathrm{C,b}} \exp\left(-\frac{\phi_{\mathrm{c}} - \phi_{\mathrm{b}}}{V_{\mathrm{T}}}\right), \tag{2.71a}$$

$$c_{\mathrm{A,a}} = c_{\mathrm{A,b}} \exp\left(\frac{\phi_{\mathrm{a}} - \phi_{\mathrm{b}}}{V_{\mathrm{T}}}\right). \tag{2.71b}$$

Conservation of the five types of surface sites becomes

$$\Gamma_{\mathrm{MOH}} + \Gamma_{\mathrm{MO}} + \Gamma_{\mathrm{MOH_2}} + \Gamma_{\mathrm{MOC}} + \Gamma_{\mathrm{MOH_2A}} = \Gamma_{\mathrm{tot}}, \tag{2.72}$$

which we rewrite using the equilibrium conditions Eqs. (2.58) and (2.70),

$$\Gamma_{\mathrm{MOH}} = \Gamma_{\mathrm{tot}} \left(1 + \frac{K_{\mathrm{MO}}}{c_{\mathrm{H,0}}} + \frac{c_{\mathrm{H,0}}}{K_{\mathrm{MOH_2}}} + \frac{K_{\mathrm{MO}}}{c_{\mathrm{H,0}}} \frac{c_{\mathrm{C,c}}}{K_{\mathrm{MOC}}} + \frac{c_{\mathrm{H,0}}}{K_{\mathrm{MOH_2}}} \frac{c_{\mathrm{A,a}}}{K_{\mathrm{MOH_2A}}}\right)^{-1}. \tag{2.73}$$

The surface charge density at the 0-plane has additional contributions from the positive and negative parts of the site-binding complexes $\mathrm{MO^-C^+}$ and $\mathrm{MOH_2^+A^-}$. The surface charge density at the c-plane σ_{c} and a-plane σ_{a} are related to the surface concentration of $\mathrm{MO^-C^+}$ and $\mathrm{MOH_2^+A^-}$, respectively,

$$\begin{aligned}\sigma_0 &= e\left(\Gamma_{\mathrm{MOH_2}} - \Gamma_{\mathrm{MO}} + \Gamma_{\mathrm{MOH_2A}} - \Gamma_{\mathrm{MOC}}\right) \\ &= e\left(\frac{c_{\mathrm{H,0}}}{K_{\mathrm{MOH_2}}} - \frac{K_{\mathrm{MO}}}{c_{\mathrm{H,0}}} + \frac{c_{\mathrm{H,0}}}{K_{\mathrm{MOH_2}}} \frac{c_{\mathrm{A,a}}}{K_{\mathrm{MOH_2A}}} - \frac{K_{\mathrm{MO}}}{c_{\mathrm{H,0}}} \frac{c_{\mathrm{C,c}}}{K_{\mathrm{MOC}}}\right) \Gamma_{\mathrm{MOH}},\end{aligned} \tag{2.74a}$$

$$\begin{aligned}\sigma_{\mathrm{c}} &= e\Gamma_{\mathrm{MOC}} \\ &= e \frac{K_{\mathrm{MO}}}{c_{\mathrm{H,0}}} \frac{c_{\mathrm{C,c}}}{K_{\mathrm{MOC}}} \Gamma_{\mathrm{MOH}},\end{aligned} \tag{2.74b}$$

$$\begin{aligned}\sigma_{\mathrm{a}} &= -e\Gamma_{\mathrm{MOH_2A}} \\ &= -e \frac{c_{\mathrm{H,0}}}{K_{\mathrm{MOH_2}}} \frac{c_{\mathrm{A,a}}}{K_{\mathrm{MOH_2A}}} \Gamma_{\mathrm{MOH}}.\end{aligned} \tag{2.74c}$$

The Stern capacitor model Eq. (2.66) is expanded using the zero-charge-between-planes assumption to include the c- and a-plane, thus introducing the capacitances C_1 (between the 0- and c-plane), C_2 (between the c- and a-plane), and C_3 (between the a- and d-plane),

$$C_1\left(\phi_0 - \phi_{\mathrm{c}}\right) = \sigma_0, \tag{2.75a}$$

$$C_2\left(\phi_{\mathrm{c}} - \phi_{\mathrm{a}}\right) = -\left(\sigma_{\mathrm{a}} + \sigma_{\mathrm{d}}\right), \tag{2.75b}$$

$$C_3\left(\phi_{\mathrm{a}} - \phi_{\mathrm{d}}\right) = -\sigma_{\mathrm{d}}. \tag{2.75c}$$

The electroneutrality condition Eq. (2.67) is extended by the c- and a-plane surface charge densities,

$$\sigma_0 + \sigma_\mathrm{c} + \sigma_\mathrm{a} + \sigma_\mathrm{d} = 0. \tag{2.76}$$

Using Eqs. (2.60), (2.71), (2.73), and (2.74) together with Grahame's equation Eq. (2.22) (where $\sigma = -\sigma_\mathrm{d}$ and $\zeta = \phi_\mathrm{d}$), the four equations Eqs. (2.75) and (2.76) are closed with respect to the four surface potentials ϕ_0, ϕ_c, ϕ_a, and ϕ_d, and thus constitute the four-layer model.

As already mentioned, the equations are rarely analytically tractable due to the many non-linear terms and are therefore often solved numerically. As in Eq. (2.68) we use the electroneutrality condition to express the (total) surface charge density in terms of the surface concentrations,

$$\begin{aligned} -\sigma_\mathrm{d} =& \sigma_0 + \sigma_\mathrm{c} + \sigma_\mathrm{a} \\ =& e\Gamma_\mathrm{tot} \left(\frac{c_{\mathrm{H},0}}{K_{\mathrm{MOH_2}}} - \frac{K_\mathrm{MO}}{c_{\mathrm{H},0}} \right) \times \\ & \left(1 + \frac{K_\mathrm{MO}}{c_{\mathrm{H},0}} + \frac{c_{\mathrm{H},0}}{K_{\mathrm{MOH_2}}} + \frac{K_\mathrm{MO}}{c_{\mathrm{H},0}} \frac{c_{\mathrm{C,c}}}{K_\mathrm{MOC}} + \frac{c_{\mathrm{H},0}}{K_{\mathrm{MOH_2}}} \frac{c_{\mathrm{A,a}}}{K_{\mathrm{MOH_2A}}} \right)^{-1}. \end{aligned} \tag{2.77}$$

Finally, we mention that there exist many possible extensions of the two- and four-layer models. More planes of adsorption and different types of surface complexes can be introduced . It is also known that the presence of a divalent ion D^{2-} can change the sign of the surface charge density through the site-binding reaction [115–117],

$$\mathrm{MOH_2^+D^{2-}} \rightleftharpoons \mathrm{MOH_2^+} + \mathrm{D_d^{2-}}, \tag{2.78}$$

which shifts the surface charge density from positive to negative. Surfactants might also influence the surface chemistry and in chapters 4 and 5 we include such a molecule (cyanosilane) in our analysis.

Chapter 3

Numerical techniques

The field of nanofluidics is a multiphysics coupling of electrostatics, electrochemical transport of multiple ionic species, and fluid dynamics. The corresponding mathematical framework consists of many coupled and non-linear partial differential equations and non-trivial boundary conditions. We analyze this both by analytical and numerical means.

For the numerical analysis we resort to the FEM software `COMSOL` (version 3.5a) and the programming environment software `Matlab`. Using such programs allows us to focus more on the actual physics than the numerics.

Below we give a short introduction to the finite element method and illustrate basic parts of its usage [118–120]. We do not go into detail about the exact numerical solution procedures, as that is outside our scope.

3.1 The finite element method

The finite element method has several advantages compared to other numerical schemes including: (i) applicability to any field problem, (ii) little geometric

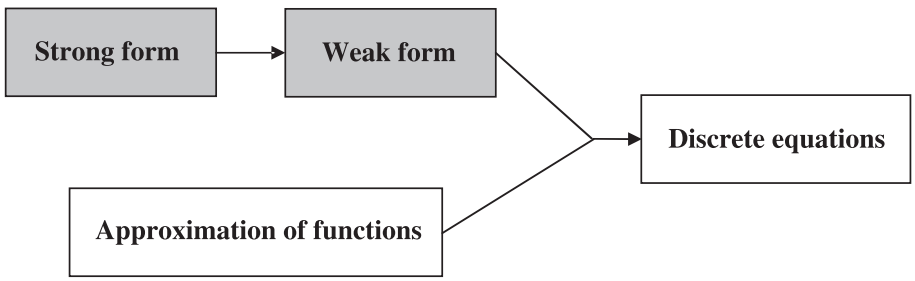

Figure 3.1: A conceptual breakdown of the FEM analysis. Adapted form Fish and Belytschko [119].

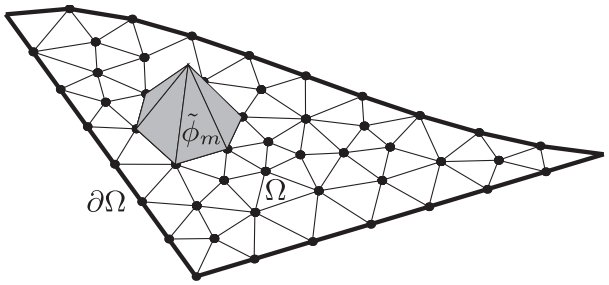

Figure 3.2: A finite element basis function in a finite element mesh. Adapted from Olesen [121].

restriction on the computational domain (curved boundaries *etc.*), (iii) little restriction on the boundary conditions, (iv) little restriction on material properties (may even vary within elements), (v) problems described by different mathematical equations can be combined, (vi) easy to mesh and re-mesh as required by the problem.

In some numerical methods, e.g. the finite difference scheme, it is possible to write down the algebraic equations directly from the partial differential equations. This is not the case in FEM where additional steps are needed. As shown in Fig. 3.1 we conceptually break down the finite element analysis in four parts [119]: the strong form, the weak form, approximation of functions, and the discrete equations.

Once the method to obtain the discrete equations is understood the actual FEM analysis is carried out in five steps [119]: (i) preprocessing/meshing (subdivision of the domain into finite elements), (ii) formulating the equations for the elements, (iii) assembling the full system of equations from the element equations, (iv) solving the equations, and (v) postprocessing. Below we present an excerpt from our work in Ref. [79] about the FEM weak form implementation in `COMSOL`.

3.2 The weak form in `COMSOL`

3.2.1 Introduction: mesh and test functions

The most common partial differential equations in theoretical physics has the form of the divergence of some generalized flux equal to a generalized source term. As the flux is often the gradient of some generalized driving potentials, we end up with the classical second-order partial differential equations.

In the FEM scheme, these equations are solved by introducing a mesh on the computational domain Ω with a finite number M of elements $m = 1, 2, 3, ..., M$. Each element is assigned a test function $\tilde{\phi}_m$ (which is also a basis function, thus the Galerkin method), which differs from zero only in that particular element, see Fig. 3.2. A given field $\phi(\boldsymbol{r})$ is represented by a linear combination of basis

functions with coefficients ϕ_m,

$$\phi(\boldsymbol{r}) = \sum_{m=1}^{M} \phi_m \tilde{\phi}_m(\boldsymbol{r}) \tag{3.1}$$

In the weak form, a given differential equation in the continuous space is transformed into M equations, one for each coefficient ϕ_m, by multiplying it by each of the test functions, integrating over the domain, and demanding that all integrals should be zero. In the following we illustrate the method with specific examples.

3.2.2 The Poisson equation in weak form

As example, we consider the Poisson equation, given in strong form in Eq. (2.2), which in weak form becomes

$$\int_\Omega \tilde{\phi}_m(\boldsymbol{r}) \left\{ \boldsymbol{\nabla} \cdot [\varepsilon \boldsymbol{\nabla} \phi(\boldsymbol{r})] + \rho_{\mathrm{el}}(\boldsymbol{r}) \right\} \mathrm{d}V = 0, \quad m = 1, 2, \ldots, M. \tag{3.2}$$

Here $\mathrm{d}V$ is the volume integration element. For brevity, we suppress in the following the test function index m as well as the spatial coordinate $\boldsymbol{r}$.

It turns out to be advantageous to transform the second order derivatives into first order. Thus, we use Gauss's theorem to integrate by parts Eq. (3.2),

$$\int_{\partial\Omega} \tilde{\phi}\, \boldsymbol{n} \cdot (\varepsilon \boldsymbol{\nabla} \phi) \, \mathrm{d}a - \int_\Omega \left[\left(\boldsymbol{\nabla} \tilde{\phi} \right) \cdot (\varepsilon \boldsymbol{\nabla} \phi) - \tilde{\phi}\, \rho_{\mathrm{el}} \right] \mathrm{d}V = 0, \tag{3.3}$$

where $\mathrm{d}a$ is the surface integration element with outward normal vector $\boldsymbol{n}$. In COMSOL the integrals for each test function is carried out automatically, and the answer is stored in a large matrix, where each entry corresponds to a contribution from a specific part of the domain or the boundary.

3.2.3 Boundary conditions

The coefficient to $\tilde{\phi}$ on the boundary is seen from Eq. (3.3) to be the normal derivative $\boldsymbol{n} \cdot (\varepsilon \boldsymbol{\nabla} \phi)$. One therefore imposes a given Neumann condition $\boldsymbol{n} \cdot (\varepsilon \boldsymbol{\nabla} \phi) = N(\boldsymbol{r})$ on the boundary by substitution of the term,

$$\int_{\partial\Omega} \tilde{\phi}\, N(\boldsymbol{r}) \, \mathrm{d}a - \int_\Omega \left[\left(\boldsymbol{\nabla} \tilde{\phi} \right) \cdot (\varepsilon \boldsymbol{\nabla} \phi) - \tilde{\phi}\, \rho_{\mathrm{el}} \right] \mathrm{d}V = 0. \tag{3.4}$$

It is more tricky to impose a Dirichlet condition $\phi = D(\boldsymbol{r})$ on the boundary. In this case the normal derivative on the boundary is free to vary such that the imposed Dirichlet boundary condition indeed is fulfilled. This case therefore requires the introduction of an auxiliary field $f(\boldsymbol{r})$ on the boundary, the so-called Lagrange multiplier, together with its associated test function $\tilde{f}(\boldsymbol{r})$, and one writes

$$\int_{\partial\Omega} \left\{ \tilde{\phi} f + \tilde{f} \, [D(\boldsymbol{r}) - \phi] \right\} \mathrm{d}a - \int_\Omega \left[\left(\boldsymbol{\nabla} \tilde{\phi} \right) \cdot (\varepsilon \boldsymbol{\nabla} \phi) - \tilde{\phi}\, \rho_{\mathrm{el}} \right] \mathrm{d}V = 0. \tag{3.5}$$

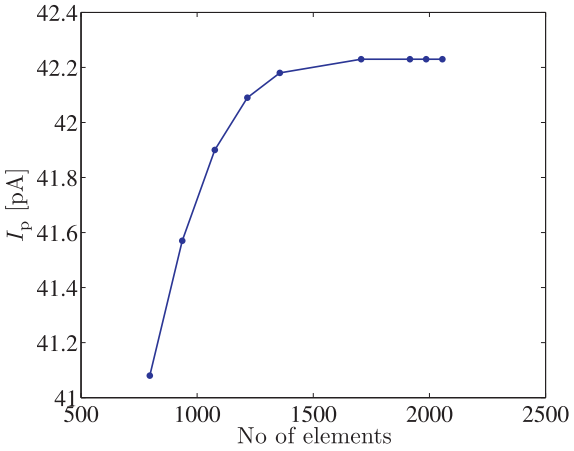

Figure 3.3: Mesh convergence test showing the convergence of the streaming current I_p as the number of elements is increased. Adapted from our paper [79].

In this formulation, the test function $\tilde{f}$ of the Lagrange multiplier only exists on the boundary, and therefore its coefficient $[D(\boldsymbol{r})-\phi]$ is forced to be zero for any converged solution of the problem. On the other hand, the coefficient $f(\boldsymbol{r})$ to the potential test function $\tilde{\phi}$ is a dependent variable, which through $\boldsymbol{\nabla}\tilde{\phi}$ couples to the terms of the volume integral. Since this coefficient is also the normal derivative of the potential, we find that it has been determined as $\boldsymbol{n}\cdot[\varepsilon\boldsymbol{\nabla}\phi] = f$ for a converged solution.

COMSOL is set up for implementing partial differential equations in the weak form given by Eqs. (3.4) and (3.5): A volume integral containing (i) the gradient of the test functions, which relates to the divergence of the flux or the Laplace term in Eq. (3.2), and (ii) a term containing the test functions, which relates to source terms in (3.2), and finally (iii) a boundary integral containing test functions, which relates to the boundary conditions, and perhaps also a term containing a Lagrange multiplier test function $\tilde{f}$.

COMSOL has a build-in automated mesh generator which provides the user with complete control of the mesh including how fine the mesh should be and in which parts of the domain. It is always important to be critical towards numerical results and we perform different checks including mesh convergence tests.

As an example, Fig. 3.3 shows the convergence of the streaming current with increasing number of elements in the finite element mesh (related to the work in Chapter 5). In our numerical simulations we therefore make sure to use meshes with a sufficiently high amount of elements to resolve the problem to within the necessary accuracy.

Chapter 4

Nanochannels: Surface-dependent thermodynamic constants

This study was carried out together with Professor Sumita Pennathur and her student Jared Frey, UC Santa Barbara. The following is my personal presentation of our work in Chapter B where additional details may be found.

4.1 Introduction

Theory of electrokinetic phenomena in micro- and nanofluidics is particularly successful in describing systems with electrolytes of few and inert ions (like aqueous KCl solutions) and constant surface charge or surface potential at the wall. However, it is less successful in describing more complex systems [19, 21, 122, 123]. Especially the understanding of fundamental properties of the solid-liquid interaction needs to be improved. In relation to this, a complicating factor when measuring the fundamental properties in micro- and nanofluidic systems is the disturbance induced by the applied field. For example, measurements of the surface-charge governed conductance across ion-selective media (see Chapter D) can be affected by the appearance of ion-concentration polarization.

Here, we make use of a novel method, originally shown by Janssen *et al.* [74], that relies on capillary filling and thus avoids the use of externally applied fields. Moreover, the method is unique to nanofluidics because it relies on the large surface-to-volume ratio. The method is fairly simple and constitute an excellent platform for the assessments of the electrochemical properties of surfaces such as silicon dioxide.

We extend the previous investigation using our unified model which couples the equilibrium chemistry of the bulk and the surface through Boltzmann distributed ions. Furthermore, we investigate both bare and surface-coated nanochannels.

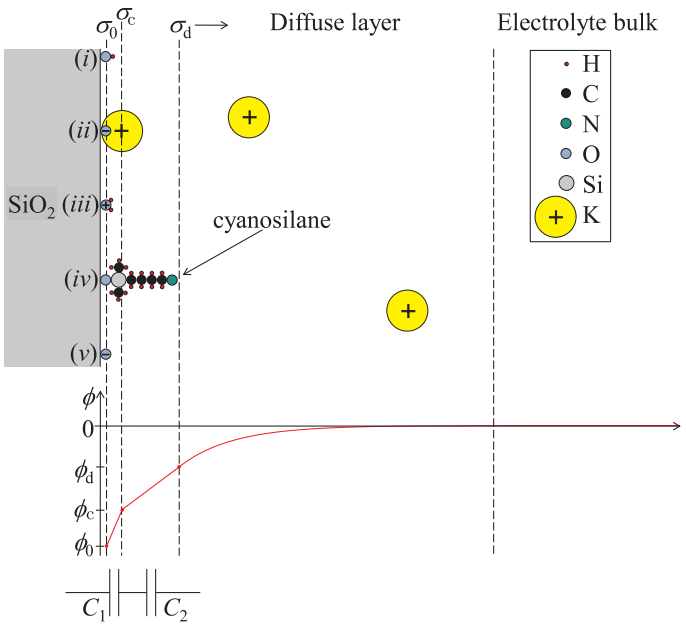

Figure 4.1: Sketch of the solid-liquid interface showing the five surface complexes and the three interfacial planes with associated surface charge σ_i and surface potential ϕ_i $i = 0, \mathrm{c}, \mathrm{d}$. Figure adapted from our paper [76].

4.2 Model

We consider long and flat nanochannels with non-overlapping screening layers and use a 1D description of the solid-liquid interface, see Fig. 4.1.

4.2.1 Surface chemistry

The electrolyte consists of aqueous potassium phosphate salt KH_2PO_4. The silica nanochannel has negative surface charge leading us to neglect anion surface adsorption, but to still account for potassium cation adsorption and the formation of the surface complex SiO^-K^+. Hence, we employ a simplified version of the four-layer model presented in Section 2.7.2 called the triple-layer model. The absence of adsorption of anions effectively corresponds to the limit where the dissociation constant for anion adsorbtion goes to infinity,

$$K_{\mathrm{SiOH_2A}} \to \infty, \tag{4.1}$$

whereby the surface concentration of the $SiOH_2^+A^-$ group goes to zero,

$$\Gamma_{\mathrm{SiOH_2A}} \to 0. \tag{4.2}$$

Thus, for the surface chemistry we consider the silanol dissociation reactions,

$$\mathrm{SiOH_2^+} \rightleftharpoons \mathrm{SiOH} + \mathrm{H_0^+}, \tag{4.3a}$$
$$\mathrm{SiOH} \rightleftharpoons \mathrm{SiO^-} + \mathrm{H_0^+}, \tag{4.3b}$$

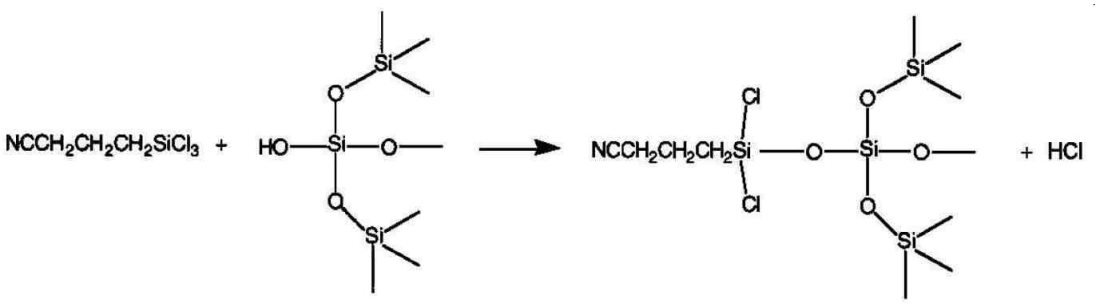

Figure 4.2: Coating reaction between a cyanosilane molecule and a silanol surface group and the additional product HCl. Adapted from Gelest [124].

and the site-binding reaction between the negative silanol groups and the positive potassium cation,

$$\mathrm{SiO^-K^+} \rightleftharpoons \mathrm{SiO^-} + \mathrm{K_c^+}. \tag{4.4}$$

The three surface reactions above are described by the dissociation constants $\mathrm{p}K_{\mathrm{SiOH_2}}$, $\mathrm{p}K_{\mathrm{SiO}}$, and $\mathrm{p}K_{\mathrm{SiOK}}$, respectively.

The triple-layer model contains only two surface capacitances between the three charged surface planes,

$$C_1\left(\phi_0 - \phi_\mathrm{c}\right) = \sigma_0, \tag{4.5a}$$

$$C_2\left(\phi_\mathrm{c} - \phi_\mathrm{d}\right) = -\sigma_\mathrm{d}. \tag{4.5b}$$

With these modifications to the four-layer model in Section 2.7.2 the surface chemistry of the triple-layer model is described in the limit of zero anion adsorption [Eqs. (4.1) and (4.2)] by the capacitor relations Eq. (4.5), the surface charge densities Eq. (2.74), the Boltzmann distributions Eqs. (2.71a) and (2.60), and the electroneutrality condition Eq. (2.76).

Additionally, we coat the channels with 3-cyanopropyldimethylchlorosilane (cyanosilane) which binds to the neutral silanol group SiOH as shown in Fig. 4.2. We incorporate this molecule in the model by adjusting the total number of surface sites Γ_tot. This is a reasonable approach as we know from other studies [125, 126] that cyanosilane forms a fully wettable, slightly hydrophilic, stable monolayer on the surface where it occupies $\approx 25\,\%$ of the sites.

Due to the presence of the cyanosilane molecule we do not assume that the surface capacitances C_1 and C_2 and the surface dissociation constant $\mathrm{p}K_{\mathrm{SiOH_2}}$ are constant but allow them to vary with the surface composition (bare or coated).

4.2.2 Bulk solution chemistry

For the bulk chemistry we employ the theory in Section 2.6 in the form of Eq. (2.54) implemented in a `Matlab` using a modified version of the ITPCalculator script [97, 105], see Chapter A.3. The electroneutrality assumption is

Table 4.1: List of the chemical family X, the valence Z, the reaction, the dissociation constant $\mathrm{p}K_{\mathrm{X},Z}$, the diffusion constant $D_{\mathrm{X},Z}$, and the electrophoretic mobility $\mu_{\mathrm{X},Z}$. Table adapted from our paper [76].

X	Z	Reaction				$\mathrm{p}K^a_{\mathrm{X},Z}$	$D^b_{\mathrm{X},Z}$ $[10^{-9}\ \frac{\mathrm{m}^2}{\mathrm{s}}]$	$\mu^b_{\mathrm{X},Z}$ $[10^{-9}\ \frac{\mathrm{m}^2}{\mathrm{s\,V}}]$
H_3PO_4	-1	H_3PO_4	$\rightleftharpoons$	$H_2PO_4^-$	$+H^+$	2.15	0.959	-37.3
	-2	$H_2PO_4^-$	$\rightleftharpoons$	HPO_4^{2-}	$+H^+$	7.21	0.759	-59.1
	-3	HPO_4^{2-}	$\rightleftharpoons$	PO_4^{3-}	$+H^+$	12.33	0.824	-96.2
$C_{20}H_{12}O_5$	1	$C_{20}H_{10}O_5H_3^+$	$\rightleftharpoons$	$C_{20}H_{10}O_5H_2$	$+H^+$	2.22[c]	0.57[d]	22.0[d]
	-1	$C_{20}H_{10}O_5H_2$	$\rightleftharpoons$	$C_{20}H_{10}O_5H^-$	$+H^+$	4.34[c]	0.64[e]	-25.0[e]
	-2	$C_{20}H_{10}O_5H^-$	$\rightleftharpoons$	$C_{20}H_{10}O_5^{2-}$	$+H^+$	6.68[c]	0.502[e]	-39.5[e]
KOH	1	$K^+ + \frac{1}{2}H_{2(g)}$	$\rightleftharpoons$	K	$+H^+$	14.0	1.96	76.2
NaOH	1	$Na^+ + \frac{1}{2}H_{2(g)}$	$\rightleftharpoons$	Na	$+H^+$	14.0	1.33	51.9
H_2O	1						9.311[f]	362.4[f]
	-1	H_2O	$\rightleftharpoons$	OH^-	$+H^+$	14.0	5.273[f]	-205.2[f]
SiOH	1	$SiOH_2^+$	$\rightleftharpoons$	SiOH	$+H_0^+$	-1.9[g]		
	-1	SiOH	$\rightleftharpoons$	SiO^-	$+H_0^+$	6.8[g]		
SiOK	-1	SiO^-K^+	$\rightleftharpoons$	SiO^-	$+K_c^+$	-0.06[g]		

[a]For acids $\mathrm{p}K_{\mathrm{X},Z}$ values are at infinite dilution and at 25 °C from Persat *et al.* [97] unless otherwise stated. [b]$D_{\mathrm{X},Z}$ values and $\mu_{\mathrm{X},Z}$ (signed) values at infinite dilution at 25 °C from Lide [127] unless otherwise stated. [c]$\mathrm{p}K_{\mathrm{A}}$ values at infinite dilution and at 25 °C from Smith *et al.* [128]. [c]Estimate. [e]$\mu_{\mathrm{X},Z}$ values from Persat *et al.* [97] with $D_{\mathrm{X},Z}$ values calculated from these using $D_{\mathrm{X},Z} = \mu_{\mathrm{X},Z} k_{\mathrm{B}} T/(Ze)$. [f]Here $Z = 1$ represents H^+ and $Z = -1$ represents OH^-. [g]For bare silica: SiOH [109, 110] and SiOK [129].

valid since we solve for the ion concentration in the large reservoirs and the ions are Boltzmann distributed. Furthermore, the screening layer is on the order of 1 nm which is negligible compared to the nanochannel height on the order of 150 nm.

We consider in the bulk the presence of phosphoric acid (the buffer)

$$H_3PO_4 \rightleftharpoons H_2PO_4^- + H^+, \tag{4.6a}$$
$$H_2PO_4 \rightleftharpoons HPO_4^{2-} + H^+, \tag{4.6b}$$
$$HPO_4 \rightleftharpoons PO_4^{3-} + H^+, \tag{4.6c}$$

of fluorescein (the dye)

$$C_{20}H_{10}O_5H_3^+ \rightleftharpoons C_{20}H_{10}O_5H_2 + H^+, \tag{4.7a}$$
$$C_{20}H_{10}O_5H_2 \rightleftharpoons C_{20}H_{10}O_5H^- + H^+, \tag{4.7b}$$
$$C_{20}H_{10}O_5H^- \rightleftharpoons C_{20}H_{10}O_5^{2-} + H^+, \tag{4.7c}$$

of potassium hydroxide and sodium hydroxide

$$K^+ + \frac{1}{2}H_{2(g)} \rightleftharpoons K + H^+, \tag{4.8a}$$

$$Na^+ + \frac{1}{2}H_{2(g)} \rightleftharpoons Na + H^+, \tag{4.8b}$$

and of water ions

$$H_2O \rightleftharpoons OH^- + H^+. \tag{4.9}$$

The dissociation constant for all reactions along with the diffusivity and mobility for all ionic species are summarized in Table 4.1.

4.3 Experiments

4.3.1 Chemicals

In short, the potassium phosphate KH_2PO_4 electrolyte of concentration 10 mM, 30 mM, 50 mM, 100 mM and 383 mM was titrated to pH 7.2 using a 1 M potassium hydroxide KOH solution to ensure similar conditions for the pH-sensitive fluorescein molecule. The relatively high buffer concentration results in a small Debye screening length in the range 0.3 nm to 2 nm.

Figure 4.3 shows that the only fluorescent charge state $Z = -2$ of fluorescein is dominant above pH 6 to 7 and negligible below pH 5 to 6. To validate the pH-dependence of the fluorescent effects we used as control marker the pH-insensitive fluorescent molecule Alexa Fluor 488. Standard experimental precautions were taken to ensure reproducible experiments. Details are given in our paper [76] enclosed in Chapter B.

4.3.2 Experimental setup and procedure

The sketch in Fig. 4.4 and the photo in Fig. A.3 shows the inverted epifluorescent microscopy setup used for recoding the capillary filling. In short, a mercury (Hg) arc lamp emitted light which was filtered to 488 nm and focused onto the chip using a 10× objective. The remitted light was focused back through the 10× objective and through a 532 nm filter before it was finally focused by a 0.5× demagnifying lens into the CCD camera which recorded the images onto a computer.

Platinum wires were used for electrical connection to the reservoirs (not relevant during the capillary filling experiments).

4.3.3 Design and fabrication

The chip design followed that in Refs. [130, 131] while the fabrication follows that by Pennathur *et al.* [66]. Figure A.1(a) shows the chip design of 12 parallel

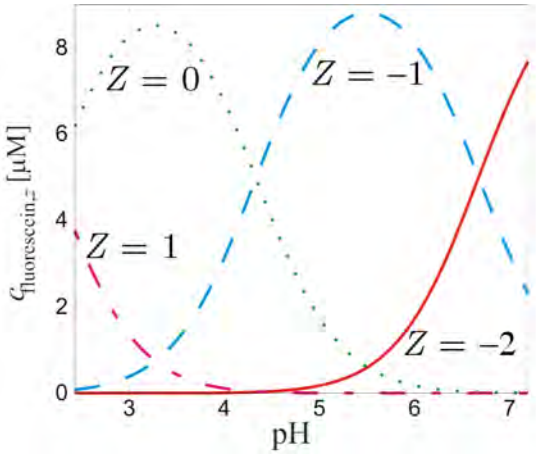

Figure 4.3: The dependence of the concentration of the charge states $Z = -2, -1, 0$, and 1 of the Fluorescein molecule on the supporting buffer pH. Only $Z = -2$ is fluorescent with an optical emission wavelength at 521 nm. Figure adapted from our paper [76].

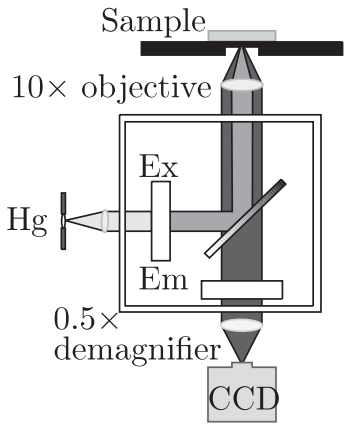

Figure 4.4: Sketch of the inverted microscopy setup showing the mercury lamp (Hg), the excitation filter (Ex) the 10× objective, the sample, the emission filter (Em), the 0.5× demagnifier, and the CCD camera. Figures adapted from our paper [76].

nanochannels of depth 115 nm, 145 nm and 195 nm (depending on the wafer production batch), of length 5 cm, and of width 5 µm, 10 µm, 15 µm, 20 µm, 30 µm and 40 µm (two channels of each width), with etched ruler markings in increments of 100 µm along the channels. Both ends of the nanochannels were connected to 1.6 µm deep inlet microchannels measuring 2 mm by 5 mm which were further connected to circular inlet reservoirs of the same depth and with a diameter of 5 mm.

4.3.4 Surface coating and cleaning

In approximately half of the experiments we used surface coated channels. The coating molecule was 3-cyanopropyldimethylcholorsilane and the exact coating and cleaning procedures are given in our paper [76].

In short, the nanochannels were coated by drying them on a hotplate after which they were filled by capillary action with 0.1 M cyanosilane in an acetonitrile solution. After the initial filling the solution were driven through the channels by EO flow and subsequently stored overnight in the same solution. Finally, the channels were rinsed and stored in ethanol solution.

4.3.5 Surface characterization

We studied the effect of surface coating using AFM measurements in the inlet reservoirs on bare and coated chips and found the surface roughness to be 0.3 nm and 0.7 nm, respectively [see Fig. A.1(b)].

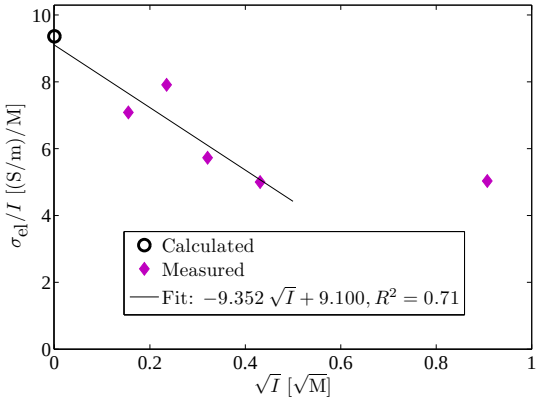

Figure 4.5: Kohlrausch plot of the dependence of the molar conductivity σ_{el}/I on the square root of the ionic strength I showing measured data points (filled purple rhombi) along with their linear regression (black curve), and the theoretical prediction at infinite dilution (open black circle). Figure adapted from our paper [76].

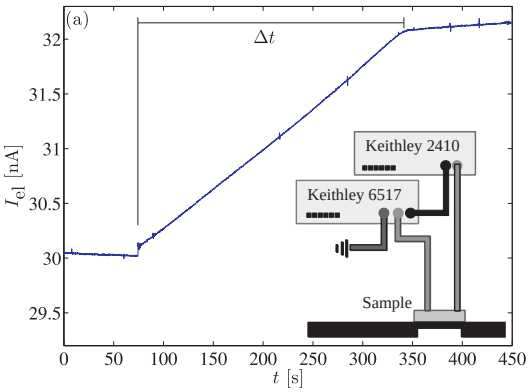

Figure 4.6: Determination of the zeta potential by transient measurement of the current I_{el} to get the electro-osmotic flow flushing time Δt across the nanochannels [132]. The sketch shows the experimental setup. Figure adapted from our paper [76].

By depositing 10 µL of de-ionized water on bare and coated silica glass slides we measured a contact angle of 32° and 75°, respectively [see Fig. A.1(c) and (d)].

4.3.6 Kohlrausch buffer characterization

We characterized the buffer by measuring its electrical conductivity σ_{el}, given theoretically in Eq. (2.15) in the limit of infinite dilution.

The empirical square-root law of Kohlrausch states that for concentrated electrolytes (though not too concentrated) the molar conductivity σ_{el}/I depends linearly on the square root of the ionic strength I. Figure 4.5 shows such a Kohlrausch plot for our electrolyte along with the theoretical result at infinite dilution. For the four lowest values of the ionic strength Kohlrausch's law holds, and when extrapolated to zero (infinite dilution) there is good agreement with the theoretical result.

We note that for dilute solutions of strong electrolytes the Debye–Hückel–Onsager theory makes it possible to derive the square root law by taking ion-ion interactions into account.

4.3.7 Zeta potential by current-monitoring

We measured the zeta potential ζ in the channels using the current-monitoring technique described by Sze *et al.* [132].

First, we introduced into the channels the buffer with a concentration slightly

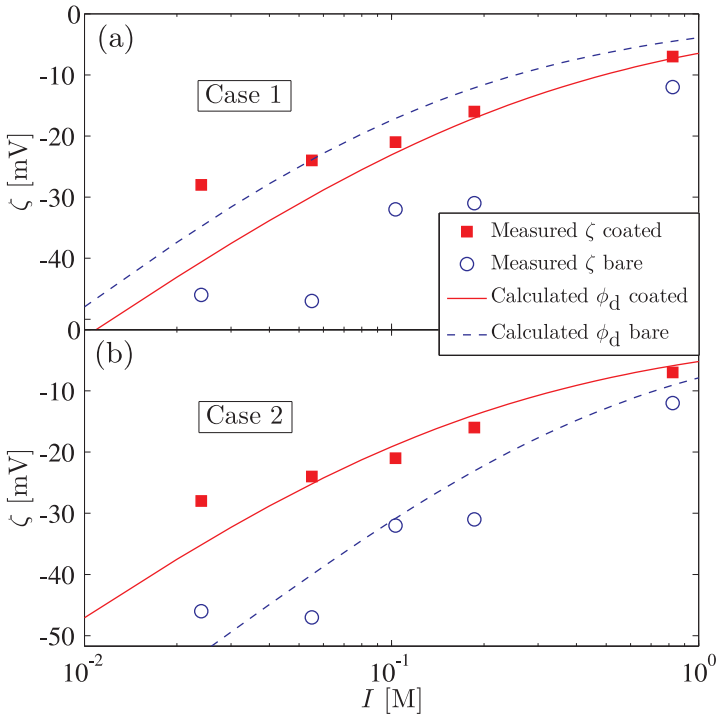

Figure 4.7: The dependence of the zeta potential ζ on the ionic strength I in bare (dashed curves and open circles, blue color) and cyanosilane coated (full curves filled squares, red color) nanochannels, either measured (symbols) or predicted (curves), for the "Case 1" [panel(a)] and "Case 2" [panel(b)]. Figure adapted from our paper [76].

lower than the target concentration. We applied an electric field $\Delta V/L$ along the channels and measured the resulting electrical current $I_{\rm el}$ over time until it stabilized.

Then, we depleted the reservoir upstream of the channels and filled it with the buffer of the target concentration and applied the electric field. The measured current increased in time, as shown in Fig. 4.6, due to the displacement of the low-conductivity buffer by the high (the displacement being due to advection by the EO flow). When all of the low-conductivity buffer had left the channels the current stabilized at a new higher level.

We then estimated the electro-osmotic flow velocity as the length of the channels L by the time Δt for displacement and equated that to the Helmholtz–Smoluchowski expression Eq. (2.36) to obtain the zeta potential,

$$\zeta = \frac{L}{\Delta t}\left(\frac{\varepsilon}{\eta}\frac{\Delta V}{L}\right)^{-1}. \tag{4.10}$$

We identify the zeta potential with the surface potential at the d-plane, i.e. $\zeta = \phi_{\rm d}$.

Figure 4.7 shows that the measured (symbols) zeta potential decreases in magnitude with increasing ionic strength, in agreement with the literature [133].

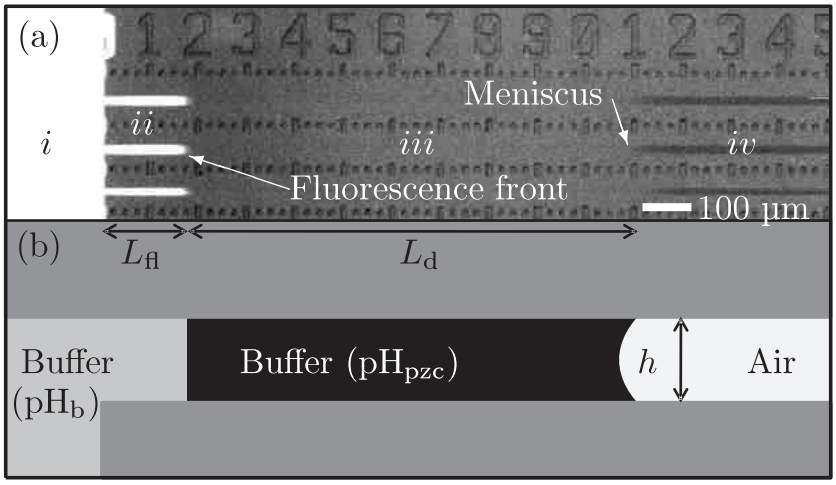

Figure 4.8: (a) Top-down image of the capillary filling in three nanochannels showing (*i*) strong signal in the reservoir, (*ii*) strong signal in the high-pH bright zone, (*iii*) low signal in the low-pH dark zone, and (*iv*) no signal in the air-filled zone. (b) Side-view sketch of the image in (a). Figure adapted from our paper [76].

The two panels show the same experimental data but two different theoretical results (curves) for the two cases "Case 1" and "Case 2", respectively. Case 1 and Case 2 are explained below.

For now, we note that the agreement between the experimental data and the theory is better in Case 2.

4.3.8 Capillary filling

The balance of surface tension and gravity leads to the capillary length $l_{\mathrm{cap}} = \sqrt{\gamma/(\rho g)}$, in which γ is the surface tension (for clean water at 25 °C the surface tension with air is $\gamma \approx 72\,\mathrm{mN\,m^{-1}}$ leading to a capillary length of $l_{\mathrm{cap}} \approx 2\,\mathrm{mm}$).

Furthermore, a contact angle θ below 90° (hydrophilic) leads to a curved meniscus and a Young–Laplace pressure drop pulling the electrolyte into the flat high-aspect ratio nanochannel of height h and width w. As the electrolyte advances into the channel the hydraulic resistance increases and the length L of the liquid column becomes proportional to the square root of time,

$$L = \sqrt{\frac{\gamma\, h\, \cos\theta}{3\,\eta}\, t}, \tag{4.11}$$

which is the Washburn relation [134].

Janssen *et al.* [74] originally showed the following phenomenon. We added a small amount of the pH-sensitive dye fluorescein to the electrolyte and observed during the capillary filling a bisection of the advancing electrolyte into a fluorescent zone near the entrance and a non-fluorescent zone near the meniscus front, see Fig. 4.8. The transition in the fluorescent signal between the two zones was remarkably sharp and only became diffuse at later times into the experiment.

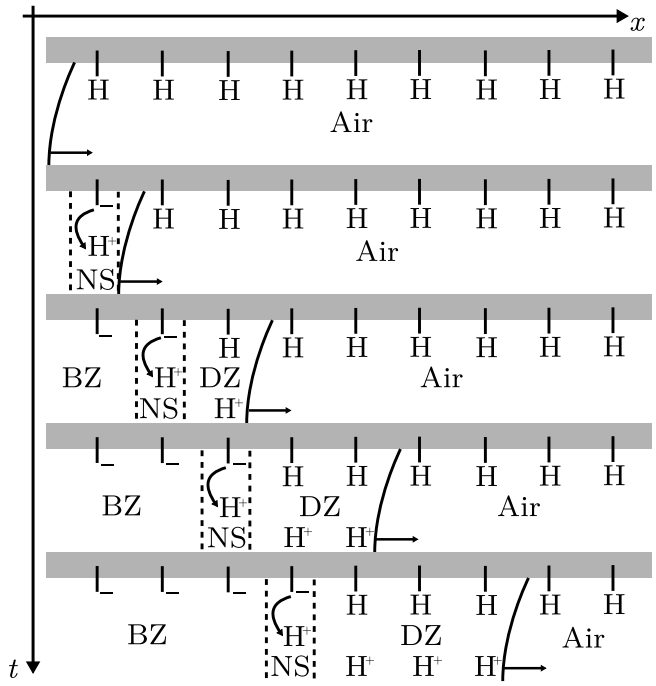

Figure 4.9: Cartoon of the capillary filling process showing the equilibrium zones bright (BZ), dark (DZ), and air-filled (Air), and the non-equilibrium slice (NS).

The explanation is that the silica surface deprotonates (releases protons) into the solution thereby lowering the pH below the point where the fluorescent signal is quenched.

The nanochannel can be thought of as divided into three distinct equilibrium zones and one thin non-equilibrium cross-sectional slice, see Fig. 4.9. One equilibrium zone is the air-filled zone (Air) ahead of the advancing electrolyte column with an electrically neutral surface consisting almost exclusively of the silanol group SiOH. Another equilibrium zone is in the dark zone (DZ) of the electrolyte with the same electrically neutral surface as in the air-filled zone and thus with $\mathrm{pH}_{\mathrm{pzc}}$ in the electrolyte. The final equilibrium zone is in the fluorescent bright zone (BZ) where a considerable fraction of the surface is deprotonated and consists of the negatively charged silanol group SiO^-. Squeezed between the fluorescent bright and dark equilibrium zones is a thin cross-sectional non-equilibrium slice (NS) where deprotonation occurs.

During the transient capillary filling we continuously measured the lengths of the bright fluorescent L_{fl} and dark L_{d} zones. Figure 4.10 shows that the Washburn square-root-of-time law holds for the combined length $L_{\mathrm{fl}} + L_{\mathrm{d}}$ as well as for the individual lengths L_{fl} and L_{d}. Combined with the sharp bright-dark transition this confirms that advection dominates in the axial direction while diffusion across the small height is fast enough together with rapid chemical reactions to ensure height-wise equilibrium (c.f. the thinness of the non-equilibrium slice). Moreover, the ratio $L_{\mathrm{d}}/L_{\mathrm{fl}}$ is constant in time during the capillary filling.

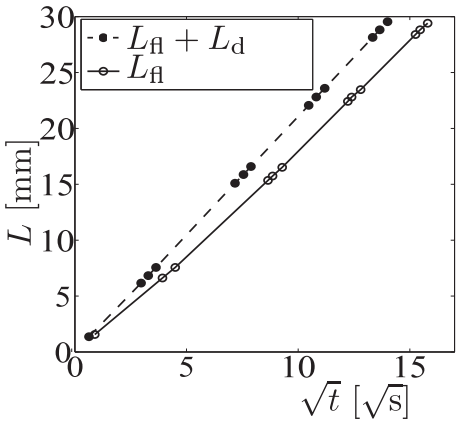

Figure 4.10: Experimental data (not all data points shown) showing the position of the meniscus $L_{\mathrm{fl}} + L_{\mathrm{d}}$ and of the fluorescent front L_{fl} against the square root of time $\sqrt{t}$, showing linear Washburn correlation. Figure adapted from our paper [76].

We can relate $L_{\mathrm{d}}/L_{\mathrm{fl}}$ to the surface charge in the following manner. The amount per area $\Gamma_{\mathrm{H}}^{\mathrm{rel}}$ of protons that has been released from the surface is related to the total amount $N_{\mathrm{H}}^{\mathrm{rel}}$ of protons released by the surface area $2\,(w+h)\,L_{\mathrm{fl}}$ in the fluorescent bright zone of the electrolyte column,

$$N_{\mathrm{H}}^{\mathrm{rel}} = 2\,(w+h)\,L_{\mathrm{fl}}\Gamma_{\mathrm{H}}^{\mathrm{rel}}. \tag{4.12}$$

At the same time, the amount $N_{\mathrm{H}}^{\mathrm{abs}}$ of protons absorbed by the volume whL_{d} of the electrolyte in the dark zone is related to the concentration B_s of protons needed to titrate the electrolyte from $\mathrm{pH_b}$ to $\mathrm{pH_{pzc}}$,

$$N_{\mathrm{H}}^{\mathrm{abs}} = whL_{\mathrm{d}}B_s, \tag{4.13}$$

in which

$$B_s = \sum_{\mathrm{X}} \sum_{Z=n_{\mathrm{X}}}^{p_{\mathrm{X}}} Z\left(c_{\mathrm{X},Z}^{\mathrm{pzc}} - c_{\mathrm{X},Z}^{\mathrm{b}}\right). \tag{4.14}$$

The amount of protons released must equal the amount absorbed which leads to the expression

$$\Gamma_{\mathrm{H}}^{\mathrm{rel}} = B_s \frac{h}{2\,(1+h/w)} \frac{L_{\mathrm{d}}}{L_{\mathrm{fl}}}. \tag{4.15}$$

Finally, as the initial dry surface consists almost exclusively of the neutral silanol group SiOH the surface charge at the 0-plane must arise due to the release of protons, $\sigma_0 = -e\Gamma_{\mathrm{H}}^{\mathrm{rel}}$, which leads to a relation between the experimentally measured length ratio $L_{\mathrm{d}}/L_{\mathrm{fl}}$ and the theoretically determined surface charge σ_0,

$$\frac{L_{\mathrm{d}}}{L_{\mathrm{fl}}} = -\frac{2\,(1+h/w)}{eB_s h}\sigma_0. \tag{4.16}$$

Table 4.2: Case 1: using $C_2 = 0.20\,\mathrm{F\,m^{-2}}$ from the literature for both bare and coated surfaces. Case 2: varying C_2 with surface composition. Also shown are the fitted values of C_1 and $\mathrm{p}K_{\mathrm{SiOH_2}}$ and the calculated values of R^2, C_s, and $\mathrm{pH_{pzc}}$. Table adapted from our paper [76].

Case	Surface	Set	Fitted		Calculated		
		$C_2\,(\mathrm{F\,m^{-2}})$	$C_1\,(\mathrm{F\,m^{-2}})$	$\mathrm{p}K_{\mathrm{SiOH_2}}$	R^2	$C_\mathrm{s}\,(\mathrm{F\,m^{-2}})$	$\mathrm{pH_{pzc}}$
1	bare	0.20	0.69	−1.03	0.81	0.16	2.9
1	coated	0.20	15.47	−0.54	0.40	0.20	3.1
2	bare	0.80	0.77	−1.61	0.80	0.39	2.6
2	coated	0.15	13.47	−0.29	0.40	0.15	3.3

4.3.9 Parametric model investigation

Using Eqs. (4.14) and (4.16) we investigate the response of the variables $L_\mathrm{d}/L_\mathrm{fl}$, ϕ_d, σ_0, and σ_d on the ionic strength and on the parameters C_1, C_2, $\mathrm{p}K_{\mathrm{SiOK}}$, $\mathrm{p}K_{\mathrm{SiOH_2}}$, $\mathrm{p}K_{\mathrm{SiO}}$, and Γ_tot, see Fig. A.5. We note that C_1 and $\mathrm{p}K_{\mathrm{SiOH_2}}$ have the largest impact on $L_\mathrm{d}/L_\mathrm{fl}$ while C_2 has the largest impact on ϕ_d. Consequently, below where we fit the model to the experimental data we use C_1, C_2 and $\mathrm{p}K_{\mathrm{SiOH_2}}$ as adjustable parameters.

4.4 Results

We fit the model to the length ratio $L_\mathrm{d}/L_\mathrm{fl}$ from 43 individual capillary filling experiments by varying the surface capacitance C_1 and the surface dissociation constant $\mathrm{p}K_{\mathrm{SiOH_2}}$. We take other parameters from the literature with those related to chemistry given in Table 4.1 and others being the total site density for the bare surface $\Gamma_\mathrm{tot} = 4.6 \times 10^{18}\,\mathrm{m^{-2}}$ [135] (thus $\Gamma_\mathrm{tot} = 3.45\,\mathrm{m^{-2}}$ for the coated surface), $\varepsilon_\mathrm{r} = 78$, and $T = 25\,^\circ\mathrm{C}$.

Furthermore, we make the distinction of two cases regarding the surface capacitance C_2. Case 1 is when C_2 is taken to be $0.2\,\mathrm{F\,m^{-2}}$, irrespective of the surface condition [129]. However, even though Case 1 leads to good agreement in terms of $L_\mathrm{d}/L_\mathrm{fl}$ it reproduces the zeta potential poorly, see Fig. 4.7(a). Thus, we introduce Case 2 where we remedy the ϕ_d/ζ mismatch by varying C_2 with the surface composition leading to $C_2^\mathrm{bare} = 0.8\,\mathrm{F\,m^{-2}}$ for the bare surface and $C_2^\mathrm{coated} = 0.15\,\mathrm{F\,m^{-2}}$ for the coated surface.

Table 4.2 summarizes the results for the two cases and states explicitly the goodness-of-fit parameter R^2, the total Stern layer capacitance $C_\mathrm{s} = (C_1^{-1} + C_2^{-1})^{-1}$, and $\mathrm{pH_{pzc}}$ [note that $\mathrm{pH_{pzc}}$ through Eq. (2.61) relates to the dissociation constant $\mathrm{p}K_{\mathrm{SiOH_2}}$]. In the following we focus on the results obtained using Case 2.

Figure 4.11 shows that the length ratio $L_\mathrm{d}/L_\mathrm{fl}$ decreases with ionic strength I and increases from the bare to the coated surface. For the coated surface there is

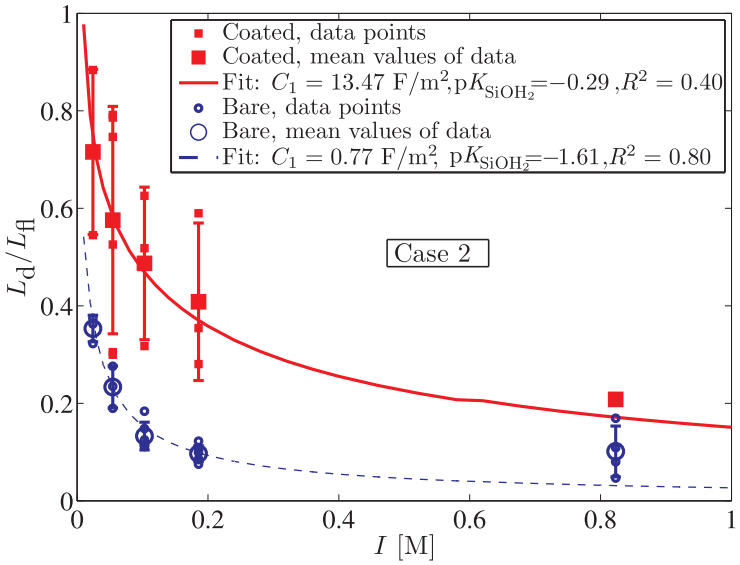

Figure 4.11: The dependence of the dark-to-fluorescent length ratio L_d/L_{fl} on the ionic strength I in bare (dashed curves and open circles, blue color) and cyanosilane coated (full curves filled squares, red color) nanochannels, either measured (symbols) or predicted (curves), for "Case 2". Figure adapted from our paper [76].

a larger spread in the measurements (symbols) reflecting that those experiments were more difficult to perform.

The decreasing trend of L_d/L_{fl} with I relates to Eq. (4.16) and the fact that the titration concentration B_s increases faster with ionic strength than σ_0 (see Fig. 4.12).

It is more surprising that L_d/L_{fl} increases in the coated channels. The naive expectation is that the decrease in surface sites Γ_{tot} through Eq. (2.77) leads to a smaller surface charge and thus by Eq. (4.16) to a smaller L_d/L_{fl}.

In bare channels we find a dissociation constant $pK_{SiOH_2} = -1.61$ and a Stern capacitance $C_s = 0.39\,\mathrm{F\,m^{-2}}$ corresponding fairly well with the literature values of -1.9 [110, 136] and $0.17\,\mathrm{F\,m^{-2}}$ [129]. The difference may be due to the use of different types of electrolytes as pointed out in Refs. [137, 138]. Our results therefore suggest that the presence of cyanosilane on the surface increases both the capacitance C_1 (from $0.77\,\mathrm{F\,m^{-2}}$ to $13.47\,\mathrm{F\,m^{-2}}$) and the dissociation constant pK_{SiOH_2} (from -1.61 to -0.29).

We use our model Case 2 results to further interpret the electrochemical properties of the solid-liquid interface. Figure 4.12 shows the dependence of the surface potentials and surface charge densities on the ionic strength (a similar figure for Case 1 is given in Fig. A.2).

Panel (a) reveals that the large increase in C_1 leads to a smaller potential difference between the 0- and c-plane. Furthermore, the 0-plane potential ϕ_0 is almost independent of both the ionic strength and the surface condition.

Panel (b) shows large increases in the magnitude of σ_0 and σ_c with both ionic

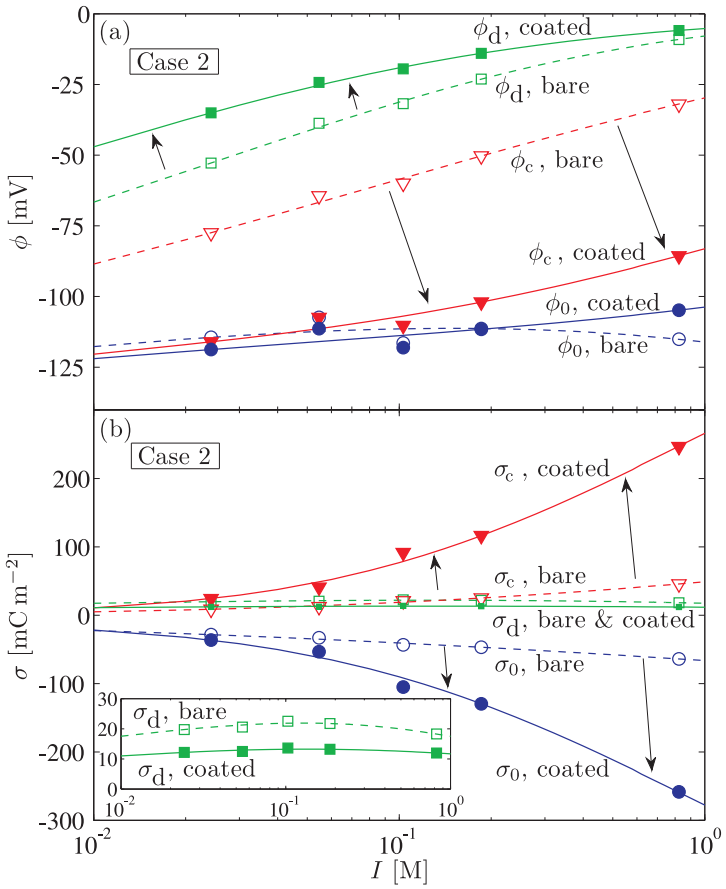

Figure 4.12: The dependence of the potential ϕ_i (top panel) and surface charge density σ_i (bottom panel) on the ionic strength I in bare (dashed curves and open symbols) and cyanosilane coated (full curves filled symbols) nanochannels for parameters corresponding to Case 2. The inset in the bottom panel is a zoom to better show σ_d. Figure adapted from our paper [76].

strength and surface coating. The inset is a zoom on the diffuse-layer surface charge density σ_d and reveals that it varies little with the ionic strength and drops with surface coating. The predicted diffuse-layer surface charge density in bare channels $\sigma_d \approx 20\,\mathrm{mC\,m^{-2}}$ compares reasonably well with the $25\,\mathrm{mC\,m^{-2}}$ found by Schoch *et al.* [139], but is somewhat lower than the $60\,\mathrm{mC\,m^{-2}}$ found by Stein *et al.* [29]. The discrepancy might be due to the use of different types of electrolytes [137, 138].

Figure 4.13 shows that in bare channels (dashed lines, open symbols) there is little variation in the surface concentrations Γ_i with ionic strength. This is in contrast to the coated channels (full lines, filled symbols) where the surface concentration of the neutral silanol group SiOH decreases and that of the metal complex SiOK increases, both significantly. This implies that in coated channels almost all deprotonated silanol groups SiO^- adsorb a cation K^+ to form the metal complex SiOK.

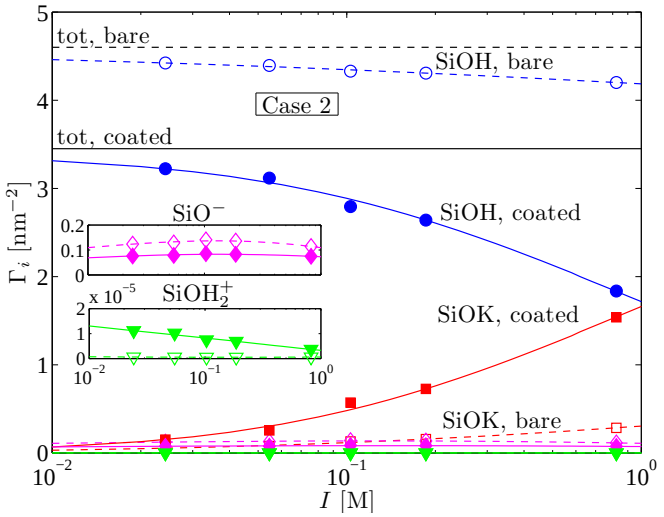

Figure 4.13: The dependence of the surface concentration Γ_i on ionic strength I in bare (dashed curves and open symbols) and cyanosilane coated (full curves and filled symbols) channels for parameters corresponding to "Case 2". Figure adapted from our paper [76].

Furthermore, the insets show that the surface concentration of positive silanol groups $SiOH_2^+$ is significantly larger in coated channels (though still small) and that the surface concentration of negative silanol groups SiO^- varies little with ionic strength and drops with surface coating.

In conclusion, we have investigated the solid-liquid interface in bare and cyanosilane coated silica nanochannels. Our model combines the equilibrium chemistry of the surface and the bulk. The experiments were two-fold consisting of capillary filling and current-monitoring. The capillary filling experiments utilized the novel technique by Janssen *et al.* [74] relying on the transient deprotonation of the silica surface and avoiding the use of any external driving fields. We fit our model to the experimental data and find that the surface capacitances C_1 and C_2 and the surface dissociation constant pK_{SiOH_2} depend on the surface condition (either bare or coated). Our model allows us to investigate and predict the electrochemical composition of the solid-liquid interface which can aid in the design of nanofluidic systems.

Future work in this direction could investigate the influence of varying the pH and of other surface coatings.

Chapter 5

Nanochannels: Streaming current and wall dissolution

This study was carried out together with Professor Sumita Pennathur, UC Santa Barbara, and Jaydeep P. Bardhan, Rush University Medical Center. The following is my personal presentation of our work in Chapter C where additional details may be found.

5.1 Introduction

Silica is abundant and widely used for micro- and nanofabrication, partly due to its properties and its history as the material of choice in the semi-conductor industry. There is evidence that silica dissolves at small, but finite, dissolution rates when in contact with aqueous solutions [140–143]. The order of magnitude of this dissolution rate, around $0.01\,\mathrm{nm\,min^{-1}}$ or $5\,\mu\mathrm{m\,year^{-1}}$, suggests that it is of significance in nanoscale structures.

Consequently, it is important to investigate ways, e.g. by surface coating, to prohibit the dissolution to ensure long-term stability and functionality of nanofluidic systems. Here, we study the dissolution effect by measuring over 48 h the increase in the streaming current at constant applied pressure. We consider nanochannels ranging from low to high aspect-ratio, with or without surface coating, and filled with different types of electrolytes.

In relation to dissolution in nanoscale structures, it is interesting to investigate the response of the surface chemistry in small asymmetric geometries such as nanochannels. Such channels are now readily fabricated [144–147]. Surface chemistry models have primarily been applied in effective 1D models, either at parallel plates or cylindrical pores, without corner effects. Using our model, we set out to investigate the influence of corners on the surface chemistry and the ensuing effect on the electrokinetics in the channel cross-section.

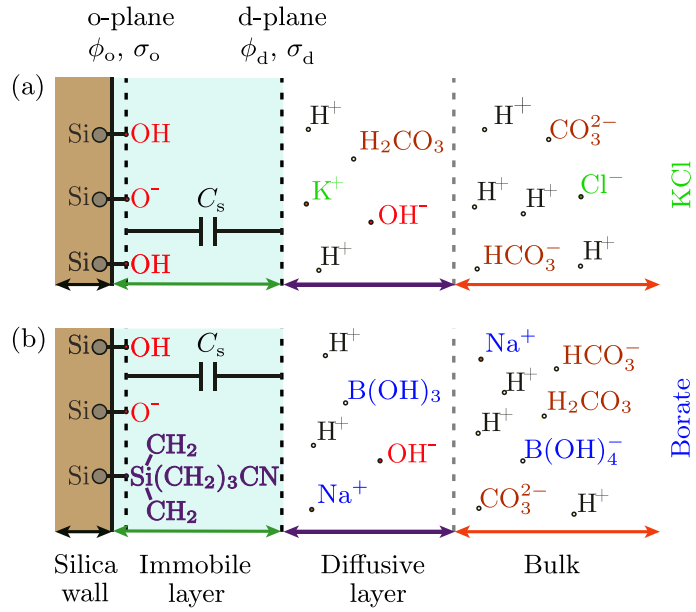

Figure 5.1: Sketch of the solid-liquid interface illustrating (a) a KCl solution in contact with a bare surface, and (b) a borate buffer in contact with a cyanosilane coated surface. Figure adapted from our paper [79].

5.2 Model

We consider long straight nanochannels connecting two large bulk reservoirs. We assume uniformity along the axial direction of the channel and the model geometry reduces to the channel cross section. Figure 5.1 shows the solid-liquid interface depicting in panel (a) a bare silica surface in contact with a KCl electrolyte and in panel (b) a cyanosilane coated surface in contact with a Borate electrolyte.

5.2.1 Surface chemistry

For the local surface chemistry we employ the two-layer model in Section 2.7.1 where we, due to the relatively high pH, only account for the neutral SiOH and negative SiO^- silanol surface groups through the reaction

$$\mathrm{SiOH} \rightleftharpoons \mathrm{SiO^-} + \mathrm{H_0^+}. \tag{5.1}$$

We do this by letting the dissociation constant for $SiOH_2^+$ in Eq. (2.68) tend to infinity $K_{\mathrm{SiOH_2}} \to \infty$ and obtain for the 0-plane surface charge density,

$$\sigma_0 = -e\Gamma_{\mathrm{tot}} \frac{K_{\mathrm{SiO}}}{c_{\mathrm{H},0}} \left(1 + \frac{K_{\mathrm{SiO}}}{c_{\mathrm{H},0}}\right)^{-1}. \tag{5.2}$$

We substitute from the Boltzmann distribution for the hydronium ion Eq. (2.60) and the Stern capacitor relation in Eq. (2.66) to obtain,

$$\sigma_0 = -e\Gamma_{\text{tot}} \left[1 + \frac{c_{\text{H,b}}}{K_{\text{SiO}}} \exp\left(\phi_{\text{d}} - \frac{\sigma_0}{C_{\text{s}}} \right) \right]^{-1}. \tag{5.3}$$

We use the standard boundary condition Eq. (2.21) relating the normal derivative of the potential to the surface charge density [14, 89, 90],

$$\sigma_0 = -\varepsilon \, \boldsymbol{n} \cdot \boldsymbol{\nabla} \phi. \tag{5.4}$$

Inserting this condition in Eq. (5.3) leads to a mixed non-linear boundary condition for the potential ϕ_{d} and its normal derivative $\boldsymbol{n} \cdot \boldsymbol{\nabla} \phi$ at the shear plane (d-plane) of the nanochannel. This effective boundary condition accounts for the surface chemistry of the two-layer model.

As in the previous study in Chapter 4 we account for the surface coating of cyanosilane by reducing the total number of available sites Γ_{tot} with 25 %.

We do not account for adsorption of metal cations onto the negative silanol groups which is reasonable since we use solutions of relatively low salt concentrations, 1 mM and 10 mM.

5.2.2 Bulk solution chemistry

Inside the 2D domain we solve the general Poisson–Boltzmann equation Eq. (2.19) using as input the bulk (reservoir) concentrations of the ionic species. The solution leads to the distribution of the electrical space charge density $\rho_{\text{el}} = \rho_{\text{el}}(y, z)$ in the channel cross-section.

The bulk concentrations are found through the solution of the electroneutrality condition in Eq. (2.54) using a modified version of the `Matlab` script ITPCalculator in Chapter A.3 [97, 105]. The electroneutrality condition is valid since we solve for the ion concentrations in the large reservoir and the ions are Boltzmann distributed.

In the bulk we consider the presence of borate,

$$\mathrm{B(OH)_3 + H_2O \rightleftharpoons B(OH)_4^- + H^+}, \tag{5.5}$$

of carbonic acid (from the dissolution of atmospheric carbon dioxide $\mathrm{CO_2}$, more details in Chapter 6),

$$\mathrm{H_2CO_3 \rightleftharpoons HCO_3^- + H^+}, \tag{5.6a}$$

$$\mathrm{HCO_3^- \rightleftharpoons CO_3^{2-} + H^+}, \tag{5.6b}$$

of potassium hydroxide and sodium hydroxide,

$$\mathrm{K^+ + \frac{1}{2} H_{2(g)} \rightleftharpoons K + H^+}, \tag{5.7a}$$

$$\mathrm{Na^+ + \frac{1}{2} H_{2(g)} \rightleftharpoons Na + H^+}, \tag{5.7b}$$

Table 5.1: List of the chemical family X, the valence Z, the reaction, and the dissociation constant $\mathrm{p}K_{\mathrm{X},Z}$. Table adapted from our paper [79].

X	Z	Reaction				$\mathrm{p}K_{\mathrm{X},Z}$[a]
$B(OH)_3$	1	$B(OH)_3 + H_2O$	$\rightleftharpoons$	$B(OH)_4^-$	$+H^+$	9.24
H_2CO_3	−1	H_2CO_3	$\rightleftharpoons$	HCO_3^-	$+H^+$	6.35
	−2	HCO_3^-	$\rightleftharpoons$	CO_3^{2-}	$+H^+$	10.33
KOH	1	$K^+ + \frac{1}{2}H_{2(g)}$	$\rightleftharpoons$	K	$+H^+$	14.00
NaOH	1	$Na^+ + \frac{1}{2}H_{2(g)}$	$\rightleftharpoons$	Na	$+H^+$	14.00
HCl	−1	HCl	$\rightleftharpoons$	Cl^-	$+H^+$	−7.00
H_2O	−1	H_2O	$\rightleftharpoons$	OH^-	$+H^+$	14.00
SiOH	−1	SiOH	$\rightleftharpoons$	SiO^-	$+H_0^+$	6.6 ± 0.6[b]

[a] From Ref. [105] at 25 °C unless mentioned otherwise.

[b] From Refs. [35, 74, 109, 112, 129, 148], uncertainty estimated.

of hydrochloric acid,

$$\mathrm{HCl} \rightleftharpoons \mathrm{Cl}^- + \mathrm{H}^+, \tag{5.8}$$

and of water ions,

$$\mathrm{H_2O} \rightleftharpoons \mathrm{OH}^- + \mathrm{H}^+. \tag{5.9}$$

The dissociation constant for all reactions are summarized in Table 5.1.

5.2.3 Hydrodynamics

Regarding the streaming current, we employ the Stokes equation for the axial pressure-driven velocity v_p where we assume that the applied pressure difference Δp leads to a constant (negative) pressure gradient along the length L of the channel. Neglecting electroviscous effects the Stokes equation Eq. (2.34) becomes

$$\nabla^2 v_\mathrm{p} = -\frac{\Delta p}{\eta L}, \tag{5.10}$$

to be solved in the 2D channel cross-section.

Regarding the EO flow, we again employ the Stokes equation to find the axial EO velocity v_eo where we assume that the applied potential difference ΔV leads to a constant axial electric field. Neglecting pressure gradients the Stokes equation Eq. (2.34) becomes

$$\nabla^2 v_\mathrm{eo} = -\rho_\mathrm{el}(y,z)\,\frac{\Delta V}{\eta L}, \tag{5.11}$$

in which ρ_el is the charge density found as described above in Section 5.2.2.

For both the pressure-driven and EO flow velocities we employ the no-slip condition at the surface of shear (d-surface),

$$v_\mathrm{p} = v_\mathrm{eo} = 0, \qquad \text{at the d-surface.} \tag{5.12}$$

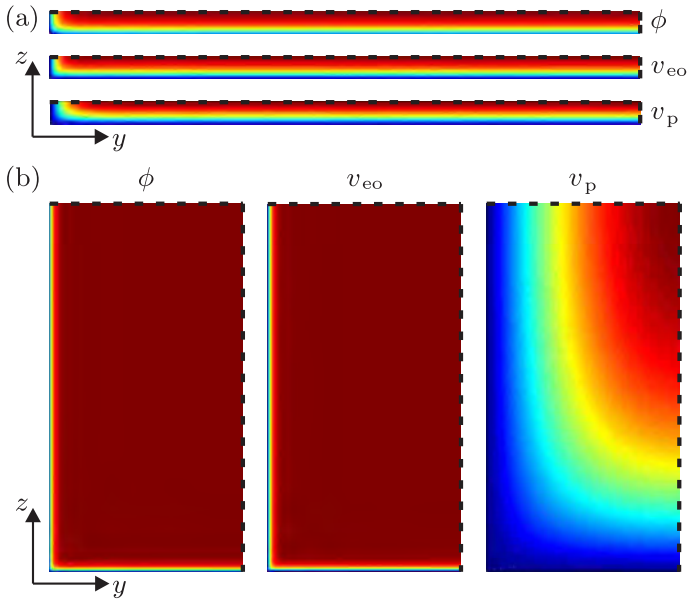

Figure 5.2: Color plots (blue=zero, red=maximum) in the channel cross-section of the calculated electrical potential ϕ, axial component of the EO flow velocity v_{eo}, and axial component of the pressure driven flow velocity v_p, in (a) the experimentally shallowest channel [$w/(2\,h) = 27$, $h/\lambda_D = 2$], and (b) the experimentally tallest channel [$w/(2\,h) = 0.5$, $h/\lambda_D = 106$]. Figure adapted from our paper [79].

5.2.4 EO flow velocity and streaming current

To facilitate comparison between theory and measurement we calculate the area-average of the EO flow velocity $\langle v_{eo}\rangle_\Omega$ and the pressure-driven streaming current I_p in the channel cross-section of width w and height $2\,h$,

$$\langle v_{eo}\rangle_\Omega = \frac{1}{hw}\int_0^h \int_0^w v_{eo}\,\mathrm{d}y\mathrm{d}z, \tag{5.13a}$$

$$I_p = 2\int_0^h \int_0^w \rho_{el} v_p\,\mathrm{d}y\mathrm{d}z. \tag{5.13b}$$

We non-dimensionalize the problem (details in our paper [79]) and identify two important dimensionless groups: the width-to-height aspect ratio $w/(2\,h)$ and the half-height-to-screening-length h/λ_D.

We use the symmetry that all field variables have even symmetry around the two lines bisecting the channel cross-section. This leads to the symmetry boundary conditions

$$\boldsymbol{n}\cdot\boldsymbol{\nabla}\phi = 0, \tag{5.14a}$$

$$\boldsymbol{n}\cdot\boldsymbol{\nabla}v_p = 0, \tag{5.14b}$$

$$\boldsymbol{n}\cdot\boldsymbol{\nabla}v_{eo} = 0, \tag{5.14c}$$

along the symmetry lines indicated in Fig. 5.2 (dashed lines). The figure also shows the calculated electrical potential, EO flow velocity, and the pressure-

Table 5.2: Basic physical parameters used in our model. Table adapted from our paper [79].

Quantity	Symbol	Value	Unit
Temperature	T	296	K
Viscosity, electrolyte solution	η	930	µPa s
Permittivity, electrolyte solution	ε	691	pF m^{-1}
Length of nanochannel	L	20	mm
Stern capacitance, bare silica[a]	C_s	0.3	F m^{-2}
Stern capacitance, coated silica[b]	C_s	0.2	F m^{-2}
Surface site density, bare silica[c]	Γ_tot	5.0	nm^{-2}
Surface site density, coated silica[d]	Γ_tot	3.8	nm^{-2}

[a] From Ref. [77]. [b] From Refs. [35, 76, 149]. [c] From Refs. [35, 111, 112, 129, 149]. [d] From Ref. [125].

driven flow velocity in a low [panel (a), $w/(2\,h) = 0.5$, $h/\lambda_\mathrm{D} = 106$] and a high [panel (b), $w/(2\,h) = 27$, $h/\lambda_\mathrm{D} = 2$] aspect-ratio channel.

To prevent numerical instabilities and to mimic the actual fabrication we round the corners of the channel by a 1-nm-radius quarter circle. We use the parameter values given in Table 5.2 similar to those determined in our previous work in Chapter 4.

5.2.5 The effect of corners

We investigate the effects of corners and side walls by comparing our full 2D model results with those from a similar 1D model. The 1D model is taken along the height-wise line bisecting the channel. Thus, the agreement between the 1D and 2D model is expected to be best far from the side walls, in the middle of the channel, and to become better with increasing aspect ratio $w/(2\,h)$.

Put another way, the 1D model applies constant surface potential and surface charge along the perimeter of the channel whereas the 2D model allows variations e.g. at the corners due to curvature effects. We introduce the relative difference δ between the 1D and 2D model,

$$\delta = \frac{f_\mathrm{1D} - f_\mathrm{2D}}{f_\mathrm{2D}}. \tag{5.15}$$

Regarding the chemical effects, Fig. 5.3 shows for the particular value of the aspect ratio $w/(2\,h) = 27$ and the dimensionless screening length $h/\lambda_\mathrm{D} = 2$ (motivated by our experimental channels) that the relative 1D-2D deviation along the channel perimeter is generally small except in the corners. There, the 1D potential is $\approx 25\,\%$ higher (thick red line) and the 1D surface charge density $\approx 30\,\%$ lower (thin blue line).

The inset shows that for $w/(2\,h) = 5$ and $h/\lambda_\mathrm{D} = 0.5$ the deviation is significant over a larger part of the perimeter, but with smaller fluctuations: $\approx 20\,\%$

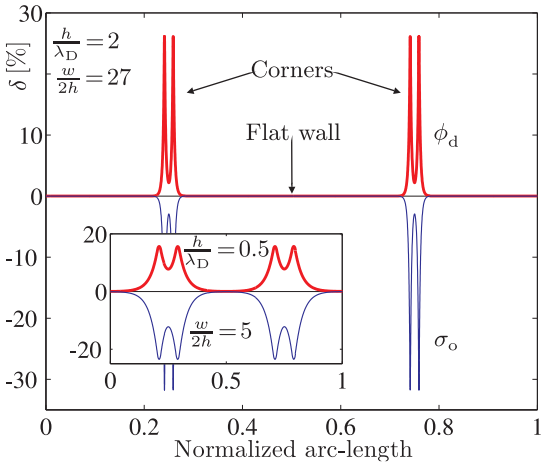

Figure 5.3: The deviation δ in ϕ_d (thick red curve) and σ_d (thin blue curve) along the perimeter of the channel cross-section for aspect ratio $w/(2\,h) = 27$ and screening length $h/\lambda_\mathrm{D} = 2$. Inset: $w/(2\,h) = 5$ and $h/\lambda_\mathrm{D} = 0.5$. Figure adapted from our paper [79].

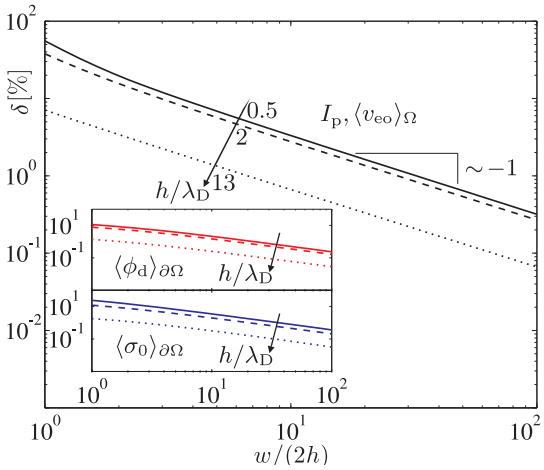

Figure 5.4: The dependence of the deviation δ in I_p and $\langle u_\mathrm{eo}\rangle$ (black curves), ϕ_d (red curves), and σ_0 (blue curves) on the aspect ratio $w/(2h)$ of the channel for three screening lengths $h/\lambda_\mathrm{D} = 0.5$, 2, and 13. Figure adapted from our paper [79].

higher in the potential and $\approx 20\,\%$ lower in the surface charge density. It is noteworthy that the magnitude of the deviation, when going around a corner, peaks on either side of the midpoint of the corner.

Regarding the effect of the side walls, Fig. 5.4 shows that the 1D-2D deviation in the streaming current and EO flow velocity is nearly identical and inversely proportional to the aspect ratio. We can understand this for thin screening layers $\lambda_\mathrm{D}/h \ll 1$ and along flat parts of the perimeter where the flow $v_\mathrm{p} = v_\mathrm{p}(n)$ and space charge density $\rho_\mathrm{el} = \rho_\mathrm{el}(n)$ only varies along the wall normal direction n. A Taylor expansion of the flow near the wall (equal to the flow in the thin EDL) yields $v_\mathrm{p}(n) = n\,\boldsymbol{n}\cdot\boldsymbol{\nabla} v_\mathrm{p}$. We introduce $I_n = \int_0^\infty \rho_\mathrm{el} n\,\mathrm{d}n$ and express the area integral in Eq. (5.13b) as an integral along the perimeter and an integral normal to the perimeter,

$$I_\mathrm{p} = \int_\Omega \rho_\mathrm{el} v_\mathrm{p}\,\mathrm{d}A \approx \int_{\partial\Omega}\int_0^\infty \rho_\mathrm{el} n\,\boldsymbol{n}\cdot\boldsymbol{\nabla} v_\mathrm{p}\,\mathrm{d}n\mathrm{d}s \tag{5.16a}$$

$$= I_n \int_{\partial\Omega} \boldsymbol{n}\cdot\boldsymbol{\nabla} v_\mathrm{p}\,\mathrm{d}s = I_n \int_\Omega -\nabla^2 v_\mathrm{p}\,\mathrm{d}A \tag{5.16b}$$

$$= 2\,hw\,I_n \frac{\Delta p}{\eta L}. \tag{5.16c}$$

This shows that in limit where the screening length goes to zero $\lambda_\mathrm{D}/h \to 0$ the 1D and 2D approaches are identical. Any deviation must thus come from a break with the assumption of thin screening layers or a flat surface.

Regarding the assumption of a flat surface (assuming thin screening layers), clearly, as the aspect ratio $w/(2h)$ increases so does the part of the perimeter

Table 5.3: List of the nanochannel number #, width w, height $2\,h$, and aspect ratio $w/(2\,h)$. Also, the dimensionless (inverse) screening length h/λ_{D}, along with the theoretical 1D-2D deviation δ (the last two parameters for both 1 mM KCl and 10 mM borate electrolyte). Table adapted from our paper [79].

#	$w \pm \Delta w$	$2\,h \pm \Delta h$	$w/(2\,h)$	1 mM KCl		10 mM borate	
	[nm]	[nm]	aspect	h/λ_{D}	δ [%]	h/λ_{D}	δ [%]
1	1043 ± 100	38.6 ± 0.6	27.0	2.0	1.0	10	0.3
2	1090 ± 100	68.8 ± 0.8	15.0	3.6	1.3	16	0.3
3	1113 ± 100	82.5 ± 0.5	13.5	4.3	1.3	19	0.3
4	1118 ± 100	103 ± 0.6	10.9	5.4	1.4	24	0.3
5	1021 ± 100	251 ± 0.8	4.1	13	1.6	59	0.4
6	1099 ± 100	561 ± 1.0	2.0	29	1.6	131	0.3
7	1181 ± 100	1047 ± 2.0	1.1	55	1.5	245	0.3
8	1067 ± 100	2032 ± 2.0	0.5	106	1.7	475	0.4

that can be considered flat and we thus recover that the deviation is inversely proportional to $w/(2h)$.

Regarding the assumption of thin screening layers, this is more complicated and we simply note that the deviation increases with λ_{D}/h as shown in Fig. 5.4. The insets in Fig. 5.4 show the deviation in the average along the perimeter of the potential $\langle\phi_{\mathrm{d}}\rangle_{\partial\Omega} = \int_{\partial\Omega} \phi_{\mathrm{d}}\,\mathrm{d}s$ and the surface charge density $\langle\sigma_0\rangle_{\partial\Omega} = \int_{\partial\Omega} \sigma_0\,\mathrm{d}s$.

5.3 Experiments

In short, we performed experiments on fused-silica nanochannels of eight different aspect ratios, with either bare or cyanosilane-coated walls, and filled with either a 1 mM KCl electrolyte or a 10 mM borate electrolyte. Below is a summary of the experimental process, more details may be found in our paper [79].

5.3.1 Fabrication and electrolyte

The nanochannels were made in fused-silica using conventional MEMS processing techniques. The exact steps and guidelines are reported elsewhere [66]. In short, reactive-ion etch was used to fabricate the channels of length $L = 20\,\mathrm{mm}$, width $w = 1.0\,\mu\mathrm{m} \pm 0.1\,\mu\mathrm{m}$, and with eight different heights varying from 40 nm to 2000 nm as shown in Table 5.3.

The channel heights were measured by profilometer, AFM, and/or SEM. The AFM measurements showed a roughness of less than 0.2 nm RMS. Each wafer had 6-12 channels (depending on yield) and the channels were connected to two 2-mm-diamter reservoirs, see Fig. 5.5(a).

The lid was made by drilling via holes in a second silica wafer and was sealed to the channel wafer using a thermal diffusion bonding process [66]. We coated one

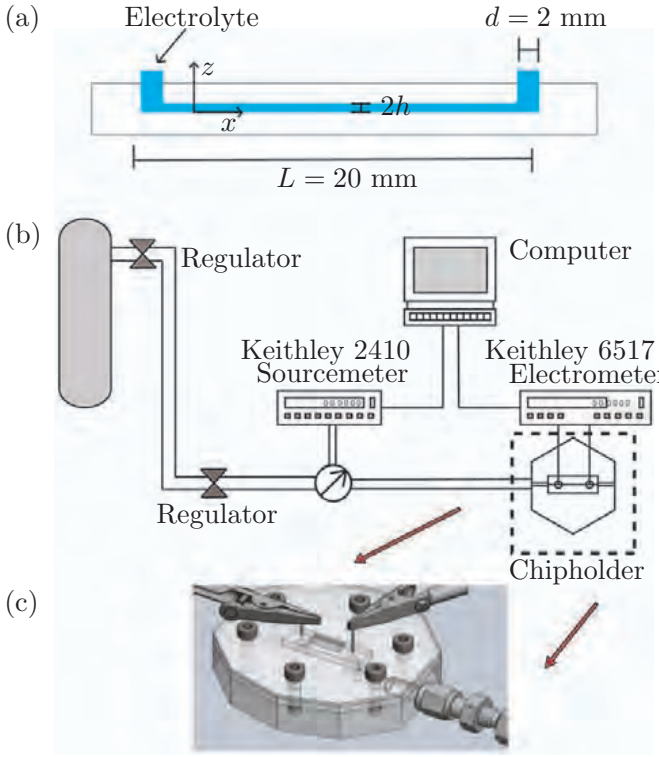

Figure 5.5: Sketch of (a) side view of the geometry, (b) the experimental setup, and (c) the chip-holder with electrical and hydraulic connections. Figure adapted from our paper [79].

channel from each wafer with cyanosilane (3-cyanopropyldimethylchlorosilane) as described in Section 4.3.4, but using a solution of 1 M cyanosilane.

The 1 mM KCl buffer was prepared by dissolving KCl pellets in deionized water and the 10 mM sodium borate buffer ($Na_2B_4O_7 \cdot 10\ H_2O$) was prepared by dissolving NaOH pellets into borax solution, titrating until pH 9.2, and finally diluting to 10 mM.

5.3.2 Setup

We made a custom-built, high-pressure chipholder with electrical and fluidic connections to the nanochannels, Fig. 5.5(b) and (c). Electrical connections were made using silver/silver-chloride (Ag/AgCl) electrodes inserted into the channel reservoirs. Stainless steel tubes were soldered directly into the chipholder and in combination with precision o-rings provided fluidic access to the reservoirs. A high-impedance electrometer, controlled by Labview, measured the streaming current.

Furthermore, a home-built Faraday cage was used to shield the entire setup. The applied pressure was controlled via two high-pressure single-stage regulators capable of regulating the pressure between 0 and 40 MPa ($\approx$ 6000 psi). The pressure was monitored with a high-precision pressure transducer. A source meter,

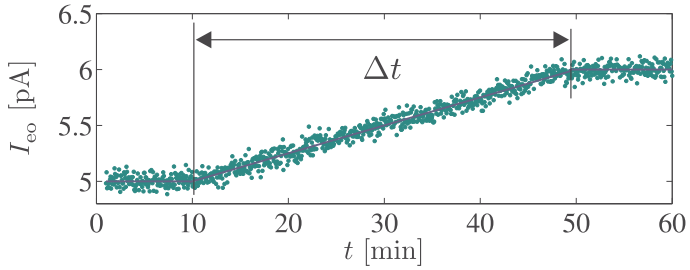

Figure 5.6: Determination of the mean EO flow velocity $\langle v_{eo}^{exp} \rangle$ by transiently monitoring the (ohmic) electrical current I_{el} during 60 minutes and extracting the displacement time Δt. Figure adapted from our paper [79].

controlled by Labview, both powered the transducer and recorded the output.

5.3.3 Procedure

The channels were initially filled with deionized water by capillary action and subjected to 3 kPa pressure difference to confirm a stable streaming current.

Next, we performed current monitoring according to the method of Sze *et al.* [132] and as described in Section 4.3.7. However, instead of the zeta potential we use the EO flow velocity

$$\langle v_{eo}^{exp} \rangle = \frac{L}{\Delta t} \tag{5.17}$$

as our measure. Figure 5.6 shows typical data from a current monitoring experiment.

Then, we applied a pressure drop $\Delta p = 8\,\mathrm{MPa}$ for a period of 48 h. The pressure was sampled once per second while the resulting streaming current was sampled ≈ 4.5 times per second (16000 times per hour). For each channel height, experiments were done on bare channels filled with 1 mM KCl, on bare channels filled with 10 mM borate, and on cyanosilane coated channels filled with 10 mM borate. Typical raw data of measured pressure $\Delta p(t)$ and measured streaming current $I_p(t)$ are shown in Fig. 5.7.

We verify that the increase in streaming current is statistically independent from the variation in pressure by fitting them to the expressions $I_p(t) = [\partial I_p/\partial t]_{meas}\, t + I_p(0)$ and $\Delta p(t) = (\partial \Delta p/\partial t)\; t + \Delta p(0)$. From the fit we obtain the four parameters $[\partial I_p/\partial t]_{meas}$, $I_p(0)$, $\partial \Delta p/\partial t$, $\Delta p(0)$ along with their 95 % confidence intervals. Based on this we find the relative change in pressure and streaming current over the 48 h for condition #1,

$$\frac{\partial \Delta p}{\partial t}\frac{\Delta t}{\Delta p(0)} = (0.2 \pm 0.2) \times 10^{-4}, \tag{5.18a}$$

$$\left[\frac{\partial I_p}{\partial t}\right]_{meas}\frac{\Delta t}{I_p(0)} = (153.4 \pm 1.0) \times 10^{-4}, \tag{5.18b}$$

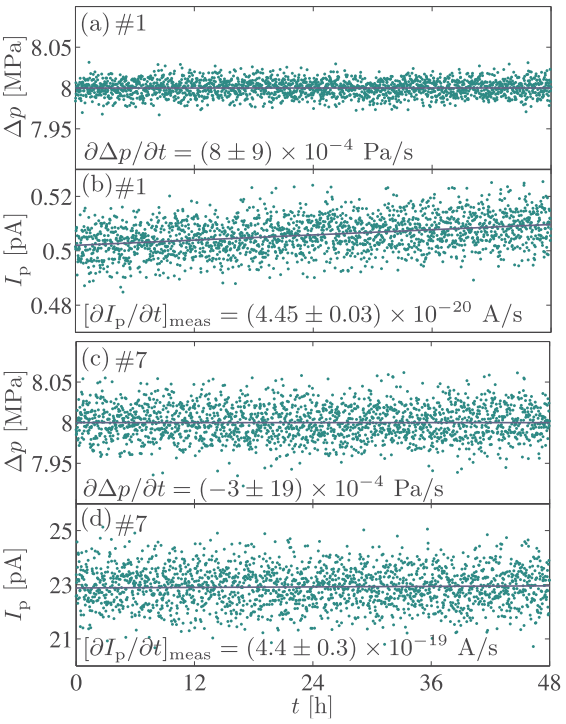

Figure 5.7: Raw data measured over 48 h for experimental condition #1 (see Table 5.3) of (a) the applied pressure difference Δp and (b) the resulting streaming current I_p. Panel (c) and (d) show the same as in panel (a) and (b) but for condition #7. Figure adapted from our paper [79].

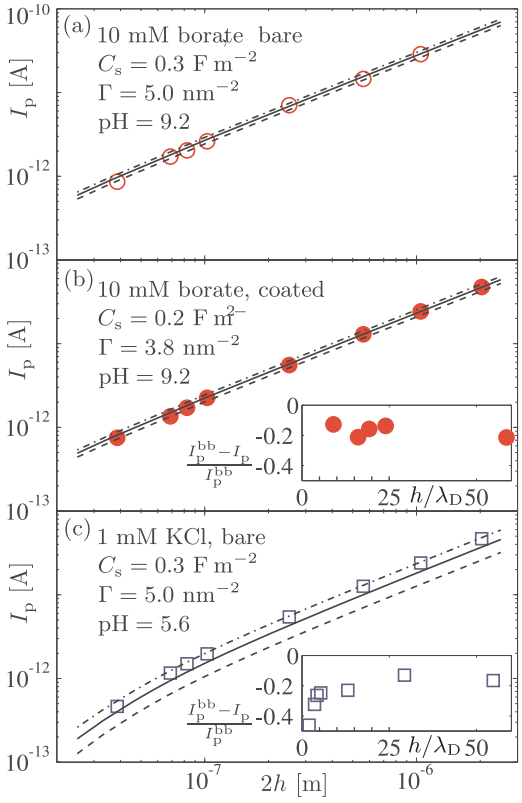

Figure 5.8: The dependence of the streaming current I_p on the channel height h for three different combinations of buffer and channel surface. Insets in (b) and (c) show the relative difference to that in (a). Figure adapted from our paper [79].

and for condition #7,

$$\frac{\partial \Delta p}{\partial t}\frac{\Delta t}{\Delta p(0)} = (-0.1 \pm 0.4) \times 10^{-4}, \tag{5.19a}$$

$$\left[\frac{\partial I_p}{\partial t}\right]_{meas}\frac{\Delta t}{I_p(0)} = (33.1 \pm 2.3) \times 10^{-4}. \tag{5.19b}$$

Thus, since the relative change in the streaming current is two to three orders of magnitude larger than the relative change in the pressure, we conclude that the increase in $I_p(t)$ is statistically independent from the variation in $\Delta p(t)$.

We represent the streaming current from each experiment by its value at time zero $I_p = I_p(0)$. We note that the relative uncertainty in the streaming current $\Delta I_p(0)/I_p(0)$ is $\approx 5 \times 10^{-5}$ for condition #1 and $\approx 1 \times 10^{-4}$ for condition #7. Figure 5.8 shows that these experimentally founded uncertainties are much smaller than the resulting uncertainty in the theoretical model when assuming a $\approx 10\,\%$

Table 5.4: Experimental $\langle v_{\mathrm{eo}}^{\mathrm{exp}} \rangle_\Omega$ and theoretical $\langle v_{\mathrm{eo}}^{\mathrm{theo}} \rangle_\Omega$ area-averaged EO flow velocity for the three combinations of surface condition and buffer.

	1 mM KCl, bare	10 mM Borate, bare	10 mM Borate, coated
$\langle v_{\mathrm{eo}}^{\mathrm{exp}} \rangle_\Omega$ ($\mu\mathrm{m\,s^{-1}}$)	7.0 ± 0.4	8.3 ± 0.4	7.0 ± 0.4
$\langle v_{\mathrm{eo}}^{\mathrm{theo}} \rangle_\Omega$ ($\mu\mathrm{m\,s^{-1}}$)	5.6 ± 1.8	8.4 ± 0.8	7.0 ± 0.7

variation in the surface dissociation constant $\mathrm{p}K_{\mathrm{SiO}} = 6.6 \pm 0.6$ (indicated by the non-solid curves).

5.4 Results

5.4.1 Streaming current

Figure 5.8 shows that the measured (symbols) and model predicted (full curves) streaming current increases with the channel height $2\,h$. Furthermore, for the three different combinations of surface condition and buffer type there is good agreement to within the estimated uncertainty (non-solid curves) between experiment and model using the literature values for the model parameters in Table 5.2.

The uncertainty (non-solid curves) is based on a $\approx 10\,\%$ variation in the surface dissociation constant $\mathrm{p}K_{\mathrm{SiO}} = 6.6 \pm 0.6$ estimated by comparing independent reports from the literature [35, 74, 109, 129, 148, 150].

The insets in Fig. 5.8(b) and (c) show the experimentally measured streaming current $\left(I_{\mathrm{p}}^{\mathrm{bb}} - I_{\mathrm{p}}\right)/I_{\mathrm{p}}^{\mathrm{bb}}$ relative to that in panel (a), the bare channel with borate buffer, denoted $I_{\mathrm{p}}^{\mathrm{bb}}$.

The inset in panel (b) shows that the streaming current is reduced by $\approx 20\,\%$ for all heights in agreement with the model assumption that the number of surface sites is reduced by $25\,\%$ by surface coating from $\Gamma_{\mathrm{tot}} = 5.0\,\mathrm{nm^{-2}}$ to $\Gamma_{\mathrm{tot}} = 3.8\,\mathrm{nm^{-2}}$.

The inset in panel (c) shows that the reduction in streaming current is again fairly constant at $\approx 20\,\%$ at high channel heights for non-overlapping screening layers $h/\lambda_{\mathrm{D}} \gtrsim 5$, but that the reduction increases with the screening layer overlap for $h/\lambda_{\mathrm{D}} \lesssim 5$ for low channel heights.

5.4.2 Electro-osmotic velocity

Independent of the streaming current measurements we determined the experimental $\langle v_{\mathrm{eo}}^{\mathrm{exp}} \rangle_\Omega$ [Eq. (5.17)] and theoretical $\langle v_{\mathrm{eo}}^{\mathrm{theo}} \rangle_\Omega$ [Eq. (5.13a)] area-averaged EO flow velocity in the tallest channel (channel #8 in Table 5.3) for the three different combinations of surface condition and electrolyte type, see Table 5.4.

The uncertainty in the theoretical prediction is again due to the estimated $\approx 10\,\%$ variation in the surface dissociation constant $\mathrm{p}K_{\mathrm{SiO}}$ while the experimental uncertainty is due to the $\approx 10\,\%$ variation in the channel width (see Table 5.3).

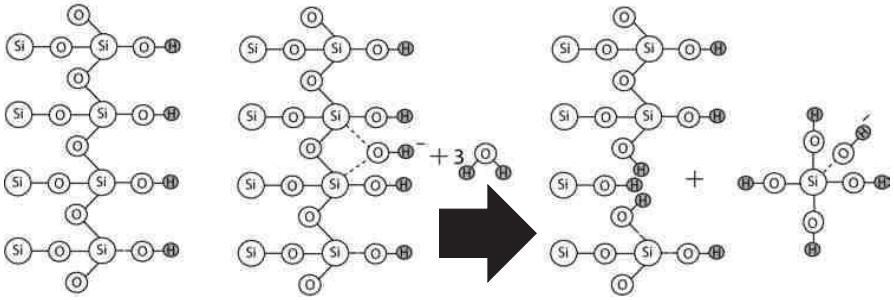

Figure 5.9: Proposed mechanism of silica dissolution in the presence of OH^-. Figure adapted from page 63 in Iler [151].

The agreement within the uncertainties between the model predictions and the experimental measurements further corroborates our analysis.

5.4.3 Dissolution rates

Having verified the model and the experiments for the forward problem, i.e. the determination streaming current and EO flow, we turn to the inverse problem of predicting dissolution rates based on the increase in streaming current over 48 h.

Silica dissolution in contact with an aqueous electrolyte is in Iler [151, page 64] reported to occur at a rate on the order of $0.01\,\mathrm{mg\,m^{-2}\,h^{-1}}$, and suggested to be due to the reaction shown in Fig. 5.9. The density of fused-silica is $2203\,\mathrm{kg\,m^{-3}}$ which we use to express the dissolution rate in different units,

$$1\,\mathrm{mg\,m^{-2}\,h^{-1}} \approx 0.4539\,\mathrm{nm\,h^{-1}} = 1.26 \times 10^{-13}\,\mathrm{m\,s^{-1}}, \tag{5.20}$$

and

$$1\,\mathrm{m\,s^{-1}} = 7.93 \times 10^{12}\,\mathrm{mg\,m^{-2}\,h^{-1}}. \tag{5.21}$$

We assume that the rise $[\partial I_\mathrm{p}/\partial t]_\mathrm{meas}$ in streaming current over time shown in Fig. 5.7 is due to dissolution of silica. The dissolution leads to increases in the cross-sectional area which in turn increases the streaming current. Moreover, we assume that products from the dissolution reaction makes a negligible contribution to the streaming current and that the dissolution occurs uniformly in the cross-section.

A thin dissolved layer of silica of thickness δl leads to a small change $\delta A = 2\,(w + 2\,h)\,\delta l$ in the cross-sectional area A which in turn results in a small change δI_p in the streaming current. We use Eq. (5.13b) to estimate this sensitivity $[\partial I_\mathrm{p}/\partial l]_\mathrm{calc}$ in our theoretical model,

$$\left[\frac{\partial I_\mathrm{p}}{\partial l}\right]_\mathrm{calc} = \frac{\partial I_\mathrm{p}}{\partial A}\frac{\partial A}{\partial l} \approx \frac{1}{\partial l}\left[I_\mathrm{p}\left(A + \delta A\right) - I_\mathrm{p}(A)\right], \tag{5.22}$$

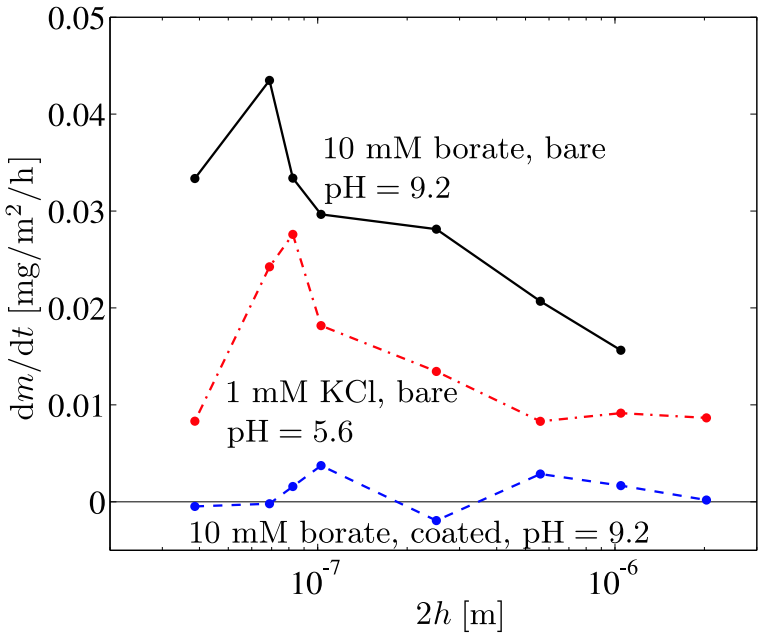

Figure 5.10: The dependence of the predicted silica dissolution rate $\mathrm{d}m/\mathrm{d}t$ on the channel height $2\,h$ for three different combinations of buffer and channel surface. Figure adapted from our paper [79].

where we use $\partial l = 0.01\,h$.

The dissolution rate is given in terms of the measured rate of change $[\partial I_\mathrm{p}/\partial t]_\mathrm{meas}$ divided by the calculated sensitivity $[\partial I_\mathrm{p}/\partial l]_\mathrm{calc}$,

$$\frac{\mathrm{d}m}{\mathrm{d}t} = 7.93 \times 10^{12} \frac{\mathrm{mg}}{\mathrm{m^2 h}} \frac{\mathrm{s}}{\mathrm{m}} \times \left[\frac{\partial I_\mathrm{p}}{\partial t}\right]_\mathrm{meas} \times \left[\frac{\partial I_\mathrm{p}}{\partial l}\right]^{-1}_\mathrm{calc}. \tag{5.23}$$

Figure 5.10 shows that order of magnitude of the predicted dissolution rates agrees with Iler [151]. Furthermore, also in agreement with previous studies, the dissolution rate increases with ionic strength and pH (going from the dot-dashed red curve to the full black curve). We also note that the dissolution rate in the coated channel fluctuates around zero in accordance with the expectation.

It is noteworthy that the dissolution rate increases with decreasing height until $2\,h \approx 100\,\mathrm{nm}$ below which it appears to drop. This may indicate that the dissolution rate is catalyzed by the screening layer interaction until the critical height $2\,h \approx 100\,\mathrm{nm}$ where the rate limiting step becomes the removal of chemical products from the dissolution reaction.

Finally, the maximum dissolution rate $\approx 0.045\,\mathrm{mg\,m^{-2}\,h^{-1}}$ corresponds to $\approx 0.02\,\mathrm{nm\,h^{-1}}$ whereby 1 nm of silica is dissolved in roughly 2 days or approximately 175 nm in one year. We have not performed direct measurements on the chips before and after dissolution and this would be an obvious next step.

In conclusion, we have proposed a theoretical model which shows that in the corners of nanochannels there exist curvature effects which leads to local perturbations in the surface potential and the surface charge density. In relation

to this, we have shown that the effect of sidewalls on the streaming current is inversely proportional to the aspect ratio and we have further shown this in combination with screening layer interaction.

We have also used our model to predict measured streaming currents and EO flow velocities in channels of varying height and of three different combinations of surface coating and electrolyte.

Finally, using the measured increase in streaming current over 48 h, verified to be statistically independent of the pressure variations, we predict silica dissolution rates and how they vary with surface coating, buffer composition, and screening layer interaction.

Future work in this direction could investigate geometries of different size and shape, the effect of varying the flow rate to affect the removal of products from the dissolution reaction, and additional different buffers of varying ionic strength and pH.

Chapter 6

Nanochannels: Conductance and CO_2 of dilute electrolytes

This study was carried out together with Professor Sumita Pennathur and her student Andrew Michael Crumrine, UC Santa Barbara. Moreover, it was done together with Kristian Lund Jensen and Jesper Toft Kristensen, DTU, whom I co-advised on their Bachelor thesis. The following is my personal presentation of our work in Chapter D where additional details may be found.

6.1 Introduction

Stein *et al.* [29] showed that at low salt concentrations the electrical conductance in nanochannels is approximately constant at a value set by the surface charge. Other studies have revealed the same phenomenon [30, 33, 34, 139, 152, 153].

In a flat nanochannel of height H the surface charge density σ leads to a screening charge of height-averaged concentration $\rho = 2\,\sigma/(ZeH)$ [154]. For a surface charge density of $10\,\mathrm{mC\,m^{-2}}$ and a height of 100 nm this leads to $\rho \approx 2 \times 10^{-3}\,\mathrm{M}$. Hence, we expect the conductance to scale with the salt concentration above ρ and to be set by ρ below.

In almost all studies the surface charge density is assumed to be constant, independent of the salt concentration and the pH. However, as we have shown in Chapters 4 and 5 the surface charge density is rarely constant but varies with the electrolyte properties and even with the position on curved parts of the surface.

In relation to this, the hydronium ion is important and even more so since atmospheric carbon dioxide CO_2 dissolves into aqueous electrolytes. This increases the H^+ concentration in deionized water from pH 7 ($c_H = 10^{-7}\,\mathrm{M}$) to approximately pH 5.7 ($c_H \approx 2 \times 10^{-6}\,\mathrm{M}$). As the mobility of aqueous H^+ is a factor of 5 times higher than some of the most mobile salt ions we expect that H^+ dominates the electrical conduction of electrolytes at salt concentrations below

Table 6.1: Independent literature studies showing experimental evidence of the conductance minimum and our calculation of δ [defined in Eq. (6.18)] of its relative size. Adapted from our paper [35].

Reference		Fig.	Year	δ	Model
[29]	Stein *et al.*	3	(2004)	1.06	Const
[152]	Karnik *et al.*	3	(2005)	1.38	Const
[139]	Schoch *et al.*	3	(2005)	1.19	Const
[155]	Cheng	2.9	(2008)	1.27	Const
[33]	Martins *et al.*	3	(2009)	1.68	Const
[34]	Duan *et al.*	3	(2010)	1.25	Dissoc
	This work	6(a)	(2010)	1.18	Dissoc

10^{-5} M. Furthermore, the H^+ ion in particular has a complex interaction with the surface charge.

As shown below, our main result is that the conductance does not monotonically converge to its low-salt limit, but has a minimum at salt concentrations around 10^{-5} M to 10^{-4} M. We quantify this minimum by the parameter δ defined in Eq. (6.18), and show in Table 6.1 that the minimum has appeared in several independent experimental studies.

We therefore set out to investigate the effect on the conductance in nanochannels when the surface charge is governed self-consistently by chemical reactions cf. our model framework in Chapter 2.

6.2 Model

We consider a long, straight and flat nanochannel connecting two large bulk reservoirs. We assume uniformity along the axial direction and the model geometry reduces to the 1D parallel plates. Figure 6.1 shows the solid-liquid interface.

6.2.1 Surface chemistry

We apply the two-layer model in Section 2.7.1 and thus accounting for the surface dissociation reactions

$$\mathrm{SiOH_2^+} \rightleftharpoons \mathrm{SiOH} + \mathrm{H_0^+}, \tag{6.1}$$

$$\mathrm{SiOH} \rightleftharpoons \mathrm{SiO^-} + \mathrm{H_0^+}. \tag{6.2}$$

However, we do not account for adsorption of metal cations onto the negative silanol groups which is reasonable since we are mainly concerned with the behavior at low salt concentrations.

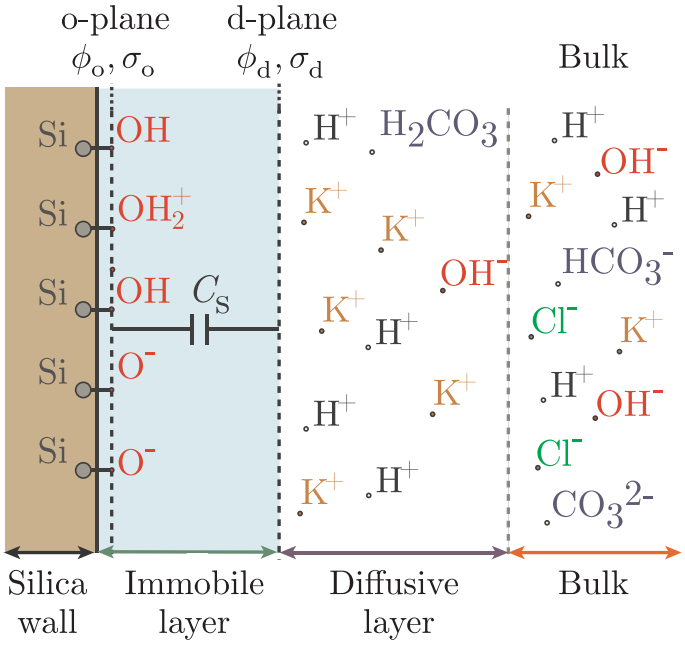

Figure 6.1: Sketch of the solid-liquid interface showing the surface groups SiOH, $SiOH_2^+$, and SiO^-, the Stern layer and Stern capacitance C_s, and the ions in the diffuse layer and in the bulk. Figure adapted from our paper [35].

6.2.2 Bulk solution chemistry

We have special focus in this study on the significance of carbonic acid H_2CO_3 from the dissolution of carbon dioxide CO_2 from the atmosphere. Hence, we start by giving details regarding the dissolution.

The CO_2/H_2CO_3 dissociation process is described using the equilibrium reactions

$$\begin{aligned} CO_{2(aq)} + H_2O_{(aq)} &\rightleftharpoons H_2CO_{3(aq)} \\ &\rightleftharpoons HCO^-_{3(aq)} + H^+_{(aq)}, \qquad pK_{H_2CO_3,-1}, \qquad (6.3a) \\ HCO^-_{3(aq)} &\rightleftharpoons CO^{2-}_{3(aq)} + H^+_{(aq)}, \qquad pK_{H_2CO_3,-2}, \qquad (6.3b) \end{aligned}$$

where the additional subindex (aq) indicates that the species is dissolved in the aqueous electrolyte. As shown by Harned and Davis [156], the difference in the free energy in the first reaction step in Eq. (6.3a) is zero which means that the dissociation of $H_2CO_{3(aq)}$ is directly related to $CO_{2(aq)}$. Thus, the dissociation constant $pK_{H_2CO_3,-1}$ relates to the entire two-step process in Eq. (6.3a) and not alone to the second single-step reaction.

The dissolved $CO_{2(aq)}$ and gaseous $CO_{2(g)}$ carbon dioxide are in equilibrium across the liquid-air surface,

$$CO_{2(g)} \rightleftharpoons CO_{2(aq)}. \qquad (6.4)$$

Henry's law relates the partial pressure $p_{CO_{2(g)}}$ of $CO_{2(g)}$ to the concentration

$c_{CO_{2(aq)}}$ of $CO_{2(aq)}$,

$$c_{CO_{2(aq)}} = H_{CO_2}\, p_{CO_{2(g)}}, \tag{6.5}$$

where the Henry coefficient $H_{CO_2} = 3.9 \times 10^{-2}\,\mathrm{M\,atm^{-1}}$ at 20 °C for carbon dioxide [156]. The partial pressure of carbon dioxide in the atmosphere is $p_{CO_{2(g)}} = 390\,\mathrm{ppmv} = 3 \times 10^{-4}\,\mathrm{atm}$ [157] which leads to a concentration of dissolved carbon dioxide, and thus carbonic acid, of $c_{H_2CO_{3(aq)}} = c_{CO_{2(aq)}} = 15 \times 10^{-6}\,\mathrm{M}$. This in turn leads to pH 5.7.

Since the dissolution occurs at the air-liquid surface it takes a certain equilibration time before the complete volume of deionized water reaches pH 5.7. We use such small volumes that this equilibration time is very short and we can assume that the electrolyte is fully saturated with CO_2.

Finally, as in the previous studies, the bulk concentrations are found through the solution of the electroneutrality condition in Eq. (2.54) using a modified version of the `Matlab` script ITPCalculator in Chapter A.3 [97, 105]. The electroneutrality condition is valid since we solve for the ion concentration in the large reservoirs and the ions are Boltzmann distributed.

In the bulk we consider the presence of carbonic acid

$$H_2CO_3 \rightleftharpoons HCO_3^- + H^+, \tag{6.6a}$$

$$HCO_3^- \rightleftharpoons CO_3^{2-} + H^+, \tag{6.6b}$$

of potassium hydroxide,

$$K^+ + \frac{1}{2}H_{2(g)} \rightleftharpoons K + H^+, \tag{6.7}$$

of hydrochloric acid,

$$HCl \rightleftharpoons Cl^- + H^+, \tag{6.8}$$

and of water ions,

$$H_2O \rightleftharpoons OH^- + H^+. \tag{6.9}$$

The dissociation constant for all reactions along with the mobility for all ionic species are summarized in Table 6.2.

6.2.3 Ion-ion effects

We correct for ion-ion interactions, which becomes significant at high ionic strength I, using Pitt's equation for a Z:Z electrolyte,

$$\mu_i^* = \mu_i - (\mu_0 Z_i + 0.23\, Z_i^2 \mu_i)\frac{\sqrt{I}}{1 + aB\sqrt{I}}, \tag{6.10}$$

where μ_i^* is the corrected mobility. Furthermore, $\mu_0 = 3.1 \times 10^{-8}\,\mathrm{m^2\,V^{-1}\,s^{-1}}$ is a constant mobility factor, $B = 0.33\,\mathrm{Å^{-1}\,M^{-\frac{1}{2}}}$ is an ion-ion interaction constant, and a is the effective radius of the ion in solution [105]. We use KCl solutions for which we take $a = 3\,\mathrm{Å}$ [158].

Table 6.2: List of the chemical family X, the valence Z, the reaction, the dissociation constant $\mathrm{p}K_{\mathrm{X},Z}$, and the electrophoretic mobility $\mu_{\mathrm{X},Z}$. Table adapted from our paper [35].

X	Z	Reaction				$\mathrm{p}K_{\mathrm{X},Z}$	$\mu_{\mathrm{X},Z}$ $[10^{-9}\,\frac{\mathrm{m}^2}{\mathrm{s\,V}}]$
H_2CO_3	-1	H_2CO_3	$\rightleftharpoons$	HCO_3^-	$+H^+$	6.35^a	-46.1^a
	-2	HCO_3^-	$\rightleftharpoons$	CO_3^{2-}	$+H^+$	10.33^a	-71.8^a
KOH	1	$K^+ + \frac{1}{2}H_{2(g)}$	$\rightleftharpoons$	K	$+H^+$	14.00^a	76.2^b
HCl	-1	HCl	$\rightleftharpoons$	Cl^-	$+H^+$	-7.00^a	-79.1^b
H_2O	1						362.4^c
	-1	H_2O	$\rightleftharpoons$	OH^-	$+H^+$	14.00^a	-205.2^d
SiOH	1	$SiOH_2^+$	$\rightleftharpoons$	SiOH	$+H_0^+$	-1.90^e	
	-1	SiOH	$\rightleftharpoons$	SiO^-	$+H_0^+$	6.56^f	

[a]From Ref. [105], infinite dilution at 25 °C. [b]From Ref. [127], infinite dilution at 25 °C. [c]Represents H^+. [d]Represents OH^-. [e]From Ref. [110]. [f]From this work.

6.2.4 Entrance effects and ion-selectivity

The ion-selectivity of a nanochannel increases as the ion concentration is lowered due to increasing overlap of the screening layers inside the channel and hence increasing electrostatic attraction of the counter-ions and repulsion of the co-ions. Due to the high ion-selectivity, the ions deplete and enrich on either side of the channel when they are forced to move, e.g. by an electric field. The resulting current will therefore approach asymptotically a limiting current I_{lim} as the ion concentrations in the depletion zone tend towards zero (more about this effect in Chapter 7).

Yossifon *et al.* [54] derived an expression for the limiting current for nano-slit channels which takes the field-focusing effect from the bulk reservoir into the flat channel entrance into account,

$$I_{\mathrm{lim}} = 2\,\pi\, eAD\frac{c_{\mathrm{ref}}}{L_{\mathrm{ref}}}\left[\ln\left(\frac{L_{\mathrm{ref}}}{H}\right)\right]^{-1}\left(\frac{\eta+1}{\eta-1}\right), \tag{6.11}$$

in which A is the cross-sectional area, c_{ref} is the reference concentration in the reservoir, L_{ref} is the reference length from the "bulk" to the entrance, $H = 2\,h$ is the channel height, and $\eta = I_+/I_-$ is a measure of the selectivity of the channel in terms of the current carried by the cation (counter-ion) I_+ and anion (co-ion) I_-.

A posteriori, we estimate the limiting current in our system and list it in Table 6.3 for the lowest concentrations used in our experimental study. Also shown in the table are the ionic strength I, the degree of screening layer overlap λ_{D}/h, the mid-channel potential ϕ_{m}, and the measure of ion selectivity η.

The current has been below 0.2 nA in all of our experiments which is seen to be at least five times below the lowest estimate of the limiting current in Table 6.3. We therefore believe the measured conductance corresponds to the

Table 6.3: The experimentally used KCl salt concentration c_{KCl}, and calculated ionic strength I, degree of screening layer overlap λ_{D}/h, mid-channel potential ϕ_{m}, and estimated limiting current I_{lim}. Adapted from our paper [35].

c_{KCl}	I [μM]	λ_{D}/h	$-\phi_{\mathrm{m}}/V_{\mathrm{T}}$	I_{lim} [nA]
0.0	2.1	1.27	3.32	1.1
0.1	2.2	1.24	3.28	1.1
0.3	2.4	1.19	3.22	1.2
1.0	3.1	1.05	3.01	1.6
3.0	5.1	0.82	2.61	2.6
10.0	12.1	0.53	1.90	6.3
25.0	27.1	0.35	1.23	16.0
50.0	52.1	0.26	0.73	41.8

intrinsic nanochannel conductance. Furthermore, by reversing the direction of the current we verified the absence of current rectification effects.

6.2.5 Nanochannel conductance

We find the intrinsic conductance of the nanochannel by considering the integrated ionic mobility in the nanochannel cross-section. In essence, we solve the 1D Poisson–Boltzmann equation Eq. (2.19) in the channel cross-section self-consistently coupled to the chemical boundary condition.

The electrical current I_{el} is found by integrating the current density in Eq. (2.13) over the cross-section $I_{\mathrm{el}} = w\int_0^H i\,\mathrm{d}z$. Concentration gradients are negligible and the current density is given by a migration term $i_{\mathrm{mig}} = \sigma_{\mathrm{el}}E$ (Ohm's law, $E = \Delta V/L$) and an advection term $i_{\mathrm{adv}} = \rho_{\mathrm{el}}v$. Thus, the conductance $G_{\mathrm{mig}} = I_{\mathrm{mig}}/\Delta V$ due to migration becomes

$$\begin{aligned} G_{\mathrm{mig}} &= \frac{w}{\Delta V}\int_0^H i_{\mathrm{mig}}\,\mathrm{d}z = \frac{w}{L}\int_0^H \sigma_{\mathrm{el}}\,\mathrm{d}z \\ &= e\frac{w}{L}\sum_i Z_i\mu_i^* n_{i,\mathrm{b}}\int_0^H e^{-Z_i\phi/V_{\mathrm{T}}}\,\mathrm{d}z, \end{aligned} \tag{6.12}$$

while we use the expression for the EO velocity in Eq. (2.35) to find the conductance G_{adv} due to advection,

$$\begin{aligned} G_{\mathrm{adv}} &= \frac{w}{\Delta V}\int_0^H i_{\mathrm{adv}}\,\mathrm{d}z = \frac{w}{\Delta V}\int_0^H \rho_{\mathrm{el}}\,v_x\,\mathrm{d}z \\ &= e\frac{w}{L}\frac{\varepsilon}{\eta}\int_0^H \left(\sum_i Z_i n_{i,\mathrm{b}} e^{-Z_i\phi/V_{\mathrm{T}}}\right)(\phi-\phi_{\mathrm{d}})\,\mathrm{d}z. \end{aligned} \tag{6.13}$$

Added together, the total conductance G becomes

$$G = G_{\mathrm{mig}} + G_{\mathrm{adv}}. \tag{6.14}$$

Table 6.4: Model parameters. Adapted from our paper [35].

Parameter	symbol	value
Height	$H = 2\,h$	165 nm
Width	w	8.3 µm
Length	L	12.0 mm
Surface site density	Γ_{tot}	5 nm^{-2}
Stern capacitance	C_{s}	0.2 $\mathrm{F\,m}^{2}$
Viscosity of water	η	1.0 mPa s
Permittivity of water	ε	690 $\mathrm{pF\,m}^{-1}$
Temperature	T	298 K

Due to symmetry we use the condition $\partial_z \phi = 0$ at the middle of the channel and only consider half of the 1D channel cross section in the actual calculations.

6.3 Results

6.3.1 Theoretical results

6.3.1.1 Solution of the coupled equations

We mention two ways to solve the model equations.

In the first method, as in Section 5.2, we express the chemical surface equations as a mixed non-linear boundary condition for the Poisson–Boltzmann equation. Thus, the surface charge is given by Eq. (2.68),

$$\sigma_0 = e\Gamma_{\mathrm{tot}} \left(\frac{c_{\mathrm{H},0}}{K_{\mathrm{MOH}_2}} - \frac{K_{\mathrm{MO}}}{c_{\mathrm{H},0}} \right) \left(1 + \frac{K_{\mathrm{MO}}}{c_{\mathrm{H},0}} + \frac{c_{\mathrm{H},0}}{K_{\mathrm{MOH}_2}} \right)^{-1}, \tag{6.15}$$

in which the hydronium-ion concentration at the 0-plane is related through its Boltzmann factor and the Stern capacitor relation Eq. (2.66) to its bulk value,

$$c_{\mathrm{H},0} = c_{\mathrm{H,b}} \exp\left[-\frac{1}{V_{\mathrm{T}}} \left(\frac{\sigma_0}{C_{\mathrm{s}}} + \phi_{\mathrm{d}} \right) \right]. \tag{6.16}$$

Again, using that the surface charge is related to the derivative of the potential in the surface normal n_z direction,

$$\sigma_0 = -\varepsilon\, n_z\, \partial_z \phi, \tag{6.17}$$

we obtain by substitution of Eqs. (6.16) and (6.17) into Eq. (6.15) a mixed non-linear boundary condition for the electrical potential.

However, since the problem at hand is 1D and the above boundary condition is extremely non-linear (it may or may not be implementable in the solution routine), another method is a segregated process where the surface equations and the Poisson–Boltzmann equation are solved separately and iteratively. In relation to this, one approach is:

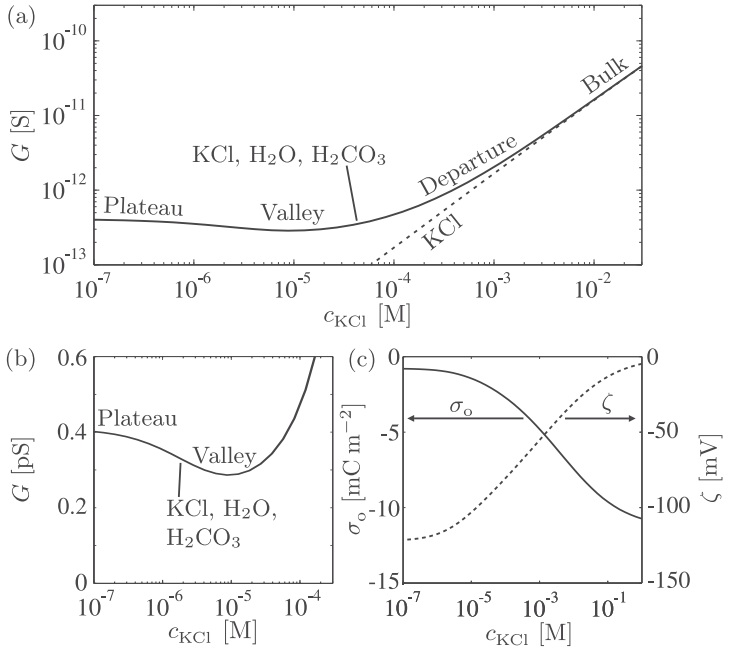

Figure 6.2: (a) Log-log plot of the dependence of the predicted nanochannel conductance G on the buffer KCl concentration c_{KCl} with indications of four regimes: plateau, valley, departure, and bulk. (b) The same as in panel (a) but in a semi-log plot to better illustrate the conductance minimum in the valley. (c) Semi-log plot of the dependence of σ_0 (left axis) and ζ (right axis) on c_{KCl}. Figure adapted from our paper [35].

- **Initialization**: Calculate ionic concentrations in the bulk and assume $\phi_{\mathrm{m}} = 0$ to calculate the channel pH.
- **Loop**: Solve the surface chemistry equations to obtain ϕ_{d}, then solve the Poisson–Boltzmann equation to obtain a new updated ϕ_{m}, then update the channel pH.
- **Test**: Repeat the loop until ϕ_{m} has converged.

Using either of the above two methods, after convergence we obtain the potential in the channel to be used in Eqs.(6.12)–(6.14) for the calculation of the conductance.

We use the parameters listed in Table 6.4 where the channel height, width, and length are chosen to correspond to the experimental work and the surface site density and Stern capacitance are chosen to correspond to the literature values used previously in Chapters 4 and 5.

6.3.1.2 Nanochannel conductance

We calculate the nanochannel conductance for salt concentrations ranging from the very dilute regime 10^{-7} M to the concentrated regime 10^{-1} M. Figure 6.2(a) shows the resulting nanochannel conductance. Based on this curve we identify

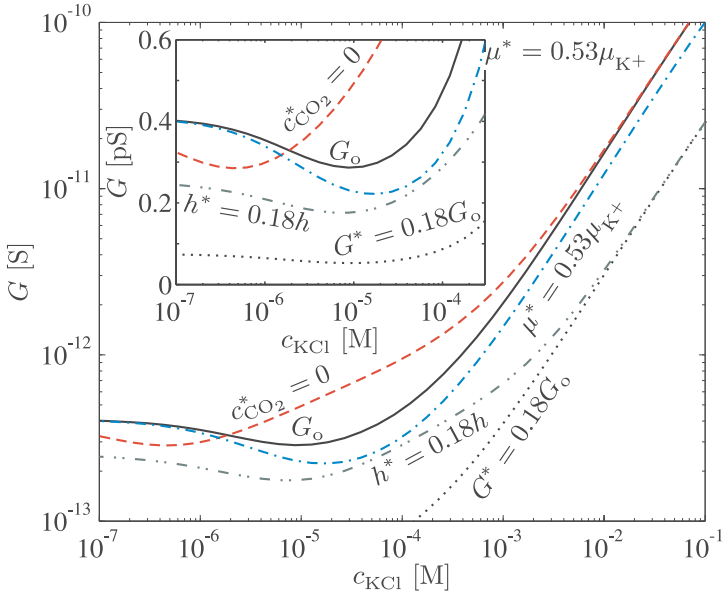

Figure 6.3: Log-log plot of the dependence of the nanochannel conductance G on the buffer KCl concentration c_{KCl} showing the base state G_0 (full black curve) subjected to: no CO_2 (dashed red curve), lower counter-ion (cation) mobility (dot-dashed blue curve), lower channel height (dot-dot-dashed green curve), scaling by a factor (dotted black curve). The inset is a semi-log plot to better illustrate the behavior around the conductance minimum. Figure adapted from our paper [35].

four concentration intervals, going from high concentration to low: (i) the bulk, (ii) the departure, (ii) the valley, and (iv) the plateau. We stress that the conductance minimum is one of the main theoretical predictions by our model.

To quantify the "depth" of the minimum we define the parameter δ as the ratio of the largest conductance G_{max} on the low-concentration side of the minimum to the conductance G_{min} at the minimum,

$$\delta = \frac{G_{\mathrm{max}}}{G_{\mathrm{min}}}. \tag{6.18}$$

As already mentioned, the conductance minimum appears in several independent experimental studies, which we have compiled in Table 6.1, in which δ ranges from 1.06 to 1.68. For the minimum in Fig. 6.2 we calculate $\delta = 1.42$.

The minimum can be difficult to appreciate in the log-log plot and we therefore plot in Fig. 6.2(b) the same conductance curve in a semi-log plot with the conductance on the linear axis whereby the minimum becomes visually much clearer.

Figure 6.2(c) shows the model predicted variation in the surface charge density and zeta potential (ϕ_{d}) with salt concentration. Contrary to the common assumption, the surface charge density is not constant, but has a sigmoid shape and saturates at a small value ($\approx -1\,\mathrm{mC\,m^{-2}}$) for low c_{KCl} and at a high value ($\approx 12\,\mathrm{mC\,m^{-2}}$) for high c_{KCl}.

In Fig. 6.3 we perform a parametric study of our model by varying the carbon dioxide concentration, the counter-ion mobility, and the channel height.

The significance of atmospheric carbon dioxide is illustrated when we remove it from the model (dashed red curve, $c_{CO_2} = 0$) whereby the conductance increases significantly for intermediate salt concentrations in the range 10^{-5} M to 10^{-3} M, by a factor of ≈ 2 to 3, and the conductance minimum shifts towards a lower concentration around $\approx 10^{-7}$ M. In this case, the shape of the conductance curve resembles poorly that seen in any of the experimental studies which would agree with them having been carried out at atmospheric conditions.

Regarding the change of counter-ion mobility we substitute KCl with LiCl (dot-dashed blue curve) as the mobility of Li^+ is 0.53 times that of K^+. We note three changes in the conductance: (i) For high salt concentration in the range 10^{-3} M to 10^{-1} M the conductance drops by a factor of ≈ 0.75 consistent with the lower LiCl salt conductivity. (ii) For very low salt concentration in the range 10^{-7} M to 10^{-6} M the conductance is at the same level as for KCl confirming that hydronium ion dominate in this regime. (iii) For intermediate salt concentration in the range 10^{-6} M to 10^{-3} M the position occurs at a higher concentration and its magnitude is increased from $\delta \approx 1.42$ to $\delta \approx 1.77$ which is consistent with the lower mobility of the counter-ion.

Regarding the change of the nanochannel height we reduce it by a factor of 0.18 to 30 nm (dot-dot-dashed green curve) and note two changes: (i) For high salt concentration in the range 10^{-3} M to 10^{-1} M the conductance is lower by a factor of 0.18 consistent with the reduced height. (ii) For low salt concentration in the range 10^{-7} M to 10^{-5} M the conductance is only lower by a factor 0.6 due to more strongly overlapping screening layers. That is, the higher degree of overlap has lead to a relatively higher average concentration of ions in the channel at the smaller height. To appreciate this effect more clearly, we have added a simple scaling by 0.18 (dotted black curve) of the base curve which is seen to be coincident with the dot-dot-dashed curve at high concentrations, but smaller by approximately a factor 0.3 for low concentrations.

Below we describe the experimental work carried out to confirm the predicted non-monotonic conductance behavior.

6.3.2 Experimental results

Figure 6.4(a) shows a sketch of the experimental setup. We used fused-silica nanochannels 165 nm high, 8.3 µm wide, and 12 mm long, connected at both ends to circular reservoirs 1.5 mm in diameter and 0.5 mm deep.

The nanochannels were filled with KCl solutions of concentration in the range 10^{-7} M to 10^{-1} M, and furthermore with solutions of the same KCl concentration and with 5×10^{-5} M HCl added.

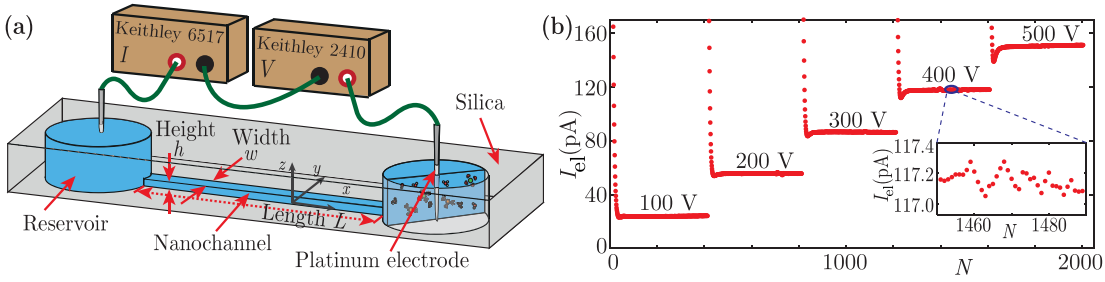

Figure 6.4: (a) Sketch of the experimental setup. (b) Experimental data showing the measured current I_{el} versus the sample number N at different applied voltages. Inset is a zoom. Figure adapted from our paper [35].

6.3.2.1 Bulk conductance

We measured the bulk conductivity of the salt solutions to validate the bulk agreement between measurements and model. Figure 6.5(a) shows the bulk conductivity for the KCl solution without HCl. The ion-ion correction at high concentration $\approx 1\,\mathrm{M}$ is just visible on the model curves (black). The dotted curve shows the predicted conductivity if only KCl ions are accounted for.

The full curve accounts for KCl, water H_2O, and carbon dioxide H_2CO_3 and starts to level off around $c_{KCl} \approx 10^{-5}\,\mathrm{M}$ as expected cf. the discussion in the introduction Section 6.1. The inset shows a relative deviation X between model and experiment within 10 %.

Figure 6.5(b) shows the conductivity after the addition of $5 \times 10^{-5}\,\mathrm{M}$ HCl which shifts the dilute-limit plateau upwards. In this case the relative deviation is within 20 %. Thus, we have good agreement in the bulk conductivity between our model and experiments which leads us to consider the nanochannel conductance.

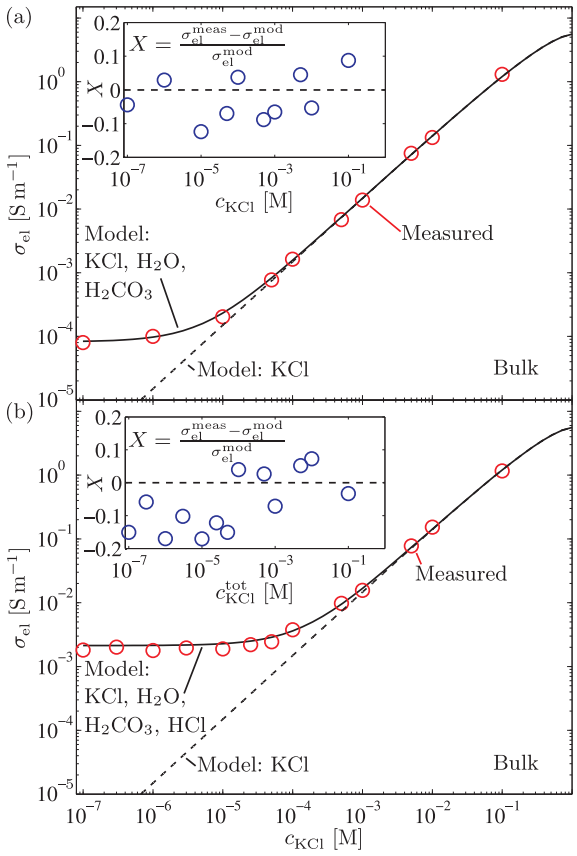

Figure 6.5: (a) Log-log plot of the dependence of the electrical conductivity σ_{el} in the bulk of the buffer on the buffer KCl concentration c_{KCl} showing the measured data (red circles) and the model prediction (black curves). The inset shows the relative deviation X between the experimental data the model. (b) As in panel (a) but with the addition of HCl. Figure adapted from our paper [35].

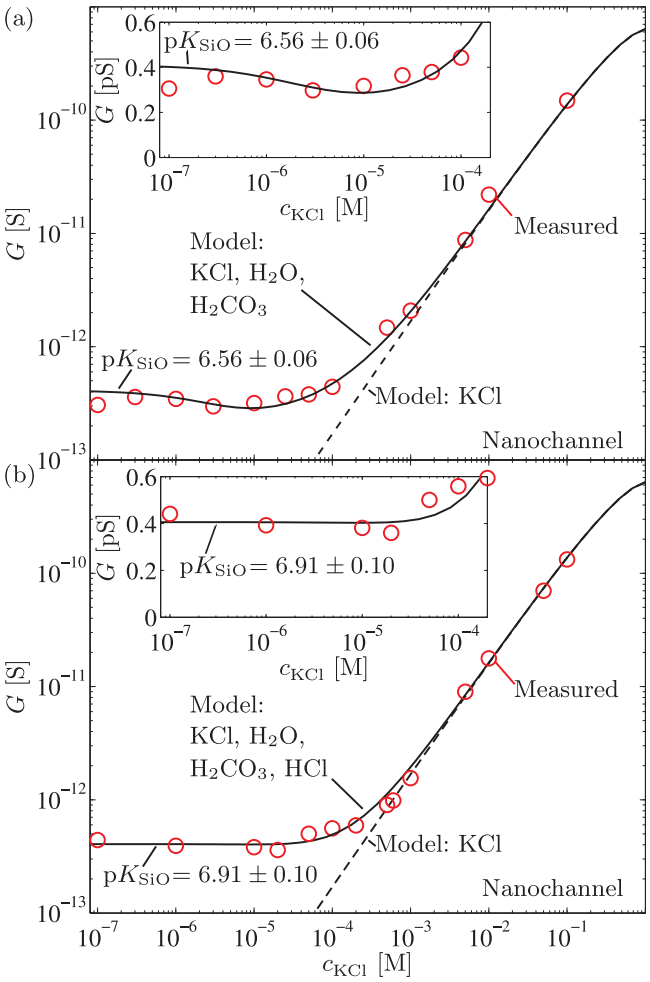

Figure 6.6: (a) Log-log plot of the dependence of the nanochannel conductance G on the buffer KCl concentration c_{KCl} showing the measured data (red circles) and the model prediction (black curves). The inset is a semi-log plot to better appreciate the conductance minimum. (b) As in panel (a) but with the addition of HCl. Figure adapted from our paper [35].

6.3.2.2 Nanochannel conductance

The nanochannel conductance was measured by rinsing the channels thoroughly with deionized water using EO flow. Five voltages were applied, each one for a duration of ≈ 40 s, leading to current data as shown in Fig. 6.4(b). Furthermore, for concentrations lower than 10^{-5} M, we covered the system with a Faraday cage to limit external interference.

Figure 6.6(a) shows the measured (circles) and calculated (curves) nanochannel conductance for various KCl concentrations. The surface dissociation constant was found to be $pK_{SiO} = 6.56 \pm 0.06$ after adjustment to optimize the agreement between theory and data. This value agrees well with our previous studies and the literature [129].

Notably, the model predicts a conductance minimum with $\delta = 1.42$. The experimental data is not conclusive but does indicate a minimum. The data point at the lowest concentration is furthest off the curve which agrees with the extreme sensitivity at this low concentration. We note that previous models that assume constant surface charge does not predict the non-monotonic behavior of the conductance curve [29, 33, 139, 152].

We then added HCl to the solution to further verify the model. As shown in Fig. 6.6(b) the conductance minimum disappears in the model (the surface dissociation constant adjusts to $pK_{SiO} = 6.91 \pm 0.10$ for the best fit). Again, the experimental data is not completely conclusive but conforms with the model prediction of the absence of a conductance minimum.

Finally, as a control experiment we measured the pH and conductance in CO_2-oversaturated KCl solutions by immersion in dry ice vapor (dry ice is frozen carbon dioxide). In this case, the pH dropped by ≈ 20 % and the conductance increased by ≈ 30 % (data not shown) in accordance with our expectations. Still, it remains to carry out more well-controlled experiments with accurate control of the CO_2 in the local atmosphere.

We note that electrolysis does not affect the measurement. First, we estimate the pH change in the reservoir to be $7.7 \times 10^{-4}\,s^{-1}$, using a similar approach as in Persat *et al.* [97]. Second, we estimate the volumetric flow rate during experiments to be $\approx 4 \times 10^{-15}\,m^3\,s^{-1}$ which is small compared to the volume of the reservoir of $\approx 10^{-9}\,m^3$. Third, the carbonic acid H_2CO_3 acts as a buffer. Finally, we renewed the reservoirs every 3 min.

In conclusion, our model takes into account the all chemical equilibria in the bulk electrolyte and at the surface and the full Poisson–Boltzmann equation. Notably, our model predicts the conductance of nanochannels across a wide range of concentrations.

For common conditions, here a KCl electrolyte solution containing carbonic acid from dissolved atmospheric carbon dioxide in silica nanochannels, the model predicts a non-monotonic conductance curve, contrary to previous models assuming constant surface charge, with a distinct conductance minimum for intermediate concentration in the range 10^{-5} M to 10^{-4} M. Here, specifically, the minimum is a factor 0.7 lower than the limiting value at low concentrations.

This minimum has appeared in other independent experimental studies in the literature but has gone unnoticed. The conductance minimum is important where sensitive measurements of the nanochannel conductance is required.

We also performed experimental measurements to verify the model predictions. Although not entirely conclusive, the experimental data conforms with the model predictions.

Future work in this direction could carry out more well-controlled experiments in terms of controlling the CO_2 content in the local atmosphere. As a natural extension to our previous work the effect of surface coatings could be studied, as well as the use of different types of electrolytes, in particular LiCl is interesting due to its more pronounced conductance minimum.

Chapter 7

Membranes: Over-limiting current

This study was carried out together with Professor Martin Z. Bazant, MIT, Professor Ali Mani, Stanford University, Doctor P. Maarten Biesheuvel, Wageningen University, and Doctor Michiel van Soestbergen, Eindhoven University of Technology. The following is my personal presentation of our work in Chapter E where additional details may be found.

7.1 Introduction

Ion transport through ion-selective media, such as membranes and nanochannels, plays a major role in ion-exchange and desalination [7, 85], electrophysiology [86], fuel cells [87, 88], and lab-on-a-chip devices [17, 18, 45, 46, 159]. A major challenge is the theoretical understanding of over-limiting current (OLC) exceeding the classical diffusion limit [160].

There exist many aspects of OLC including electro-osmotic instability (EOI) [46, 54, 54, 122, 161–167], surface morphology [168–170], surface conduction [48, 49, 51, 154, 171, 172], water splitting [173–179], the Kharkats effect [180], catalysis by surface groups [181–184], and direct conduction through the space-charge layer [185–190]. Nikonenko *et al.* [191] have given a review of mechanisms for OLC.

The archetypical picture involves an ideally ion-selective boundary that only allows one charge-type of ion, the counter-ion, to pass, and is impenetrable to the other charge-type of ion, the co-ion. This boundary is in contact with mobile ions in, say, a symmetric Z:Z electrolyte, which has a constant concentration c_0 some distance L away. Then, a forcing, for example an electrical field E, makes the counter-ions move into the boundary and the co-ions away from the boundary. Since the co-ions are not replenished at the boundary they deplete there, and the counter-ions also deplete "shadowing" the co-ion due to the constraint of electroneutrality. For not too high a forcing, after a transient equilibration, the steady-state co-ion electromigration flux $D\,Z\,c\,\mathrm{d}\tilde{\phi}/\mathrm{d}x$ away from the boundary

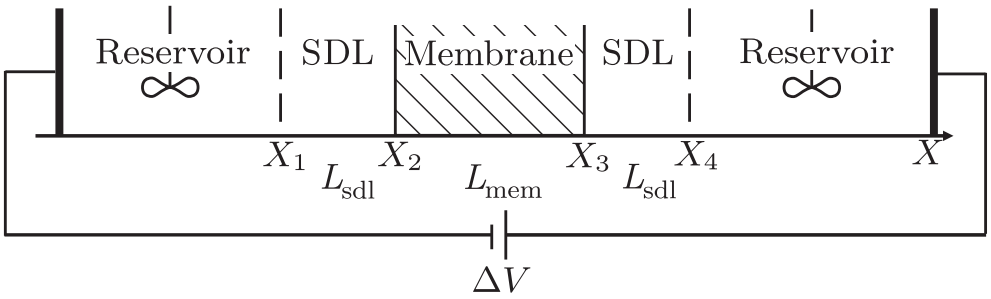

Figure 7.1: The 1D model system of an ion-selective membrane sandwiched between well-stirred electrolyte reservoirs and with a sub-milimeter thin stagnant diffusion layer (SDL) on the membrane surface.

is balanced by an opposite diffusional flux $D\,\mathrm{d}c/\mathrm{d}x$ towards the boundary. The resulting steady-state concentration of both ions drops linearly from the reservoir to the boundary. The flux j of the counter-ion determines the concentration $c_0 - j\,(2\,D/L)^{-1}$ right next to the boundary. Clearly, there is a critical flux, called the limiting flux $j_{\text{lim}} = 2\,D\,c_0/L$ [160], at which the concentration at the boundary becomes zero. The limiting flux is a singularity in the sense that the resistance of the systems grows towards infinity as the concentration drops towards zero. Thus, the classical theory predicts that the flux through the system approaches the limiting flux asymptotically and does not go above it.

Even though the "paradox" of currents above the limiting flux has existed for more than half a century a complete unified understanding is still lacking. It has appeared that EOI probably plays an important role and EOI vortices have been observed in experiments [54, 166, 167], but a clear one-to-one comparison between EOI theory and experimental observations is still lacking. It is therefore unclear to which degree EOI can explain OLC.

Here, we propose a new mechanism called current-induced membrane discharge (CIMD). It is a chemical mechanism coupling the ionization degree of the membrane, and hence its ion-selectivity, to the local properties of the electrolyte in terms of pH and concentration. We show that as the current approaches the limiting flux large pH changes appear that lowers the ionization degree of the membrane and thus "opens up the membrane" for OLC.

7.2 Model

We consider the prototypical electrodialysis system sketched in Fig. 7.1, where an ion-selective membrane of width L_{mem} is sandwiched between two electrolyte solutions. Some distance away from the membrane the electrolyte solution is well-stirred and assumed to have constant bulk properties. There is a zone of width L_{sdl} in the electrolyte close to the membrane surface where stirring is unable to maintain bulk properties called the stagnant diffusion layer (SDL).

The electrolyte consists of cations (+) and anions (−) as well as hydronium

ions (H^+) and hydroxyl ions (OH^-). In this study, we use upper-case notation for dimensional quantities and lower-case notation for non-dimensional quantities. Note that the upper-case version of the Greek letter ρ is P. If a given quantity does not appear in non-dimensional form we use its default letter-case notation. Additionally, we introduce the function $f = f(A, B)$ which equals A in the SDLs and B in the membrane,

$$f(A,B) = \begin{cases} A & \text{in the SDLs,} \\ B & \text{in the membrane.} \end{cases} \tag{7.1}$$

The membrane consists of a network of entangled polymers in between which there is a void volume V_{void} constituting the pores. The electrolyte is only able to access these open pores whereas the electric field penetrates all parts of the membrane i.e. it penetrates the entire volume V_{total} of the membrane. We define concentration and ionic flux with respect to the open pore space and we denote the porosity of the membrane ϵ_{p},

$$\epsilon_{\text{p}} = \frac{V_{\text{void}}}{V_{\text{total}}}. \tag{7.2}$$

We take into account the combined effect of porosity and tortuosity on ionic transport through the hindrance factor k_{p} which can be theoretically related to the porosity, $k_{\text{p}} = (d-1)\,\epsilon_{\text{p}}/(d-\epsilon_{\text{p}})$, in which d is the dimensionality. However, this expression for k_{p} underestimates the experimentally measured values and we therefore base k_{p} on the experimental data given by Elattar *et al.* [192].

The macroscopic electrical permittivity ε_{mem} in the membrane can be estimated as a weighted average of that ε_{sdl} of the electrolyte and that ε_{mat} of the solid matrix. We assume linear dielectrics $\varepsilon_j = \varepsilon_{\text{r},j}\varepsilon_0$, in which $\varepsilon_{\text{r},j}$ is the relative permittivity of media j.

The empirical Lichteneker–Rother relation relates the macroscopic permittivity of the membrane to that of the electrolyte and to the porosity $\varepsilon_{\text{mem}} = \epsilon_{\text{p}}^{1/\beta}\varepsilon_{\text{sdl}}$, where $\beta \approx 0.5$ [193], and thus does not take the microscopic permittivity of the solid matrix into account. In this regard, the theoretically founded Hashin–Shtrikman theory takes the microscopic permittivity of all three phases into account, and the macroscopic permittivity of the membrane becomes

$$\varepsilon_{\text{mem}} = \langle\varepsilon\rangle - \frac{(\varepsilon_{\text{sdl}} - \varepsilon_{\text{mat}})^2\,\epsilon_{\text{p}}(1-\epsilon_{\text{p}})}{\langle\tilde{\varepsilon}\rangle + \varepsilon_{\text{sdl}}(d-1)}. \tag{7.3}$$

The bracket expressions are defined in the following way, $\langle\varepsilon\rangle = \epsilon_{\text{p}}\varepsilon_{\text{sdl}} + (1-\epsilon_{\text{p}})\varepsilon_{\text{mat}}$ and $\langle\tilde{\varepsilon}\rangle = (1-\epsilon_{\text{p}})\varepsilon_{\text{sdl}} + \epsilon_{\text{p}}\varepsilon_{\text{mat}}$. If $d = 3$, $\epsilon_{\text{p}} = 0.4$, $\varepsilon_{\text{r,sdl}} = 78$ and $\varepsilon_{\text{r,mat}} = 4$ then $\varepsilon_{\text{r,mem}} \approx 27$.

7.2.1 Governing Equations

7.2.1.1 Chemical origin of charge formation in the membrane

We assume that the pores of the membrane are sufficiently small and average all variables across the cross-section. The electrical background charge density in the membrane depends on the local hydronium-ion concentration. This assumption is based on chemical equilibrium between the mobile hydronium ions in the electrolyte solution and the ionizable surface groups in the membrane, similar to the titration phenomenon during capillary filling of nanochannels in Chapter 4.

We consider a simplified version of the two-layer model in Section 2.7.1 where the surface is the polymer backbone. Furthermore, the surface groups on the polymer backbone is assume to interact with the solution through a single dissociation reaction.

Examples of such dissociation equilibria are in the case of cation-selective membranes containing negatively charged sulfonate or carboxylate surface groups,

$$\mathrm{P{-}SO_3H} \rightleftharpoons \mathrm{P{-}SO_3^-} + \mathrm{H^+}, \tag{7.4a}$$
$$\mathrm{P{-}COOH} \rightleftharpoons \mathrm{P{-}COO^-} + \mathrm{H^+}, \tag{7.4b}$$

and in the case of anion-selective membranes containing positively charged primary, secondary, or tertiary amine surface groups,

$$\mathrm{P{-}NH_3^+} \rightleftharpoons \mathrm{P{-}NH_2} + \mathrm{H^+}, \tag{7.5a}$$
$$\mathrm{P{=}NH_2^+} \rightleftharpoons \mathrm{P{=}NH} + \mathrm{H^+}, \tag{7.5b}$$
$$\mathrm{P{\equiv}NH^+} \rightleftharpoons \mathrm{P{\equiv}N} + \mathrm{H^+}. \tag{7.5c}$$

We use a general notation accounting for both positive charge sign $\theta = 1$ and negative charge sign $\theta = -1$ of the surface groups whereby the above dissociation equilibria can be compactly written as

$$\mathrm{RH}^{(\theta+1)/2} \rightleftharpoons \mathrm{R}^{(\theta-1)/2} + \mathrm{H^+}, \tag{7.6}$$

where $\mathrm{RH}^{(\theta+1)/2}$ and $\mathrm{R}^{(\theta-1)/2}$, $\theta = -1$ and 1, are surface groups in the membrane with charge denoted by the exponent, $(\theta+1)/2$ or $(\theta-1)/2$. For clarity, we write out explicitly the above equilibria,

$$\mathrm{RH} \rightleftharpoons \mathrm{R^-} + \mathrm{H^+}, \qquad \theta = -1 \quad \text{(cation-selective)}, \tag{7.7a}$$
$$\mathrm{RH^+} \rightleftharpoons \mathrm{R} + \mathrm{H^+}, \qquad \theta = 1 \quad \text{(anion-selective)}. \tag{7.7b}$$

As discussed in Section 2.6 the equilibrium reaction Eq. (7.6) is described by the equation,

$$K_{\mathrm{mem}} = \frac{C_{\mathrm{R}^{(\theta-1)/2}} C_{\mathrm{H}}}{C_{\mathrm{RH}^{(\theta+1)/2}}}, \tag{7.8}$$

where K_{mem} is the equilibrium constant and C_i is the smeared-out volume-average concentration of species i.

In relation to this, mass conservation of the surface groups are given by

$$C_{\mathrm{mem}} = C_{\mathrm{RH}^{(\theta+1)/2}} + C_{\mathrm{R}^{(\theta-1)/2}}, \tag{7.9}$$

where C_{men} is the total smeared-out volume-average concentration of surface groups in the membrane.

The ionization degree α of the membrane is defined as the fraction of the surface groups that are charged. Using Eqs. (7.8) and (7.9) the ionization degree can be expressed as the classical Langmuir-type adsorption isotherm in terms of the local proton concentration,

$$\alpha = \left[1 + \left(\frac{K_{\mathrm{mem}}}{C_{\mathrm{H}}}\right)^{\theta}\right]^{-1} = \left[1 + 10^{\theta(\mathrm{pH}-\mathrm{p}K_{\mathrm{mem}})}\right]^{-1}, \tag{7.10}$$

where the $\alpha = 1$ and 0 corresponds to complete or zero ionization of the membrane, respectively.

The electrical space charge density P_{mem} due to the immobile charged surface groups in the membrane relates to the charge sign θ of the surface groups and the ionization degree α,

$$P_{\mathrm{mem}} = \theta\, \alpha\, e\, C_{\mathrm{mem}}\, f\left(0, \epsilon_{\mathrm{p}}\right), \tag{7.11}$$

where the function $f(0, \epsilon_{\mathrm{p}})$ ensures that $P_{\mathrm{mem}} = 0$ outside the membrane and that C_{mem} is scaled by ϵ_{p} inside the membrane. The scaling is necessary because C_{mem} is defined with respect to the total volume.

7.2.1.2 Ion transport and electrostatics

We neglect advection and the transport of ionic species is due to diffusion and electromigration alone. Hence, we employ the 1D steady-state version of the ionic mass conservation Eq. (2.8) and the Poisson equation Eq. (2.2),

$$\frac{\mathrm{d}J_i}{\mathrm{d}X} = R_i, \qquad i = +, -, \mathrm{H}, \mathrm{OH}, \tag{7.12a}$$

$$-\frac{\mathrm{d}}{\mathrm{d}X}\left[f(\varepsilon_{\mathrm{sdl}}, \varepsilon_{\mathrm{mem}})\frac{\mathrm{d}\Phi}{\mathrm{d}X}\right] = P_{\mathrm{ion}} + P_{\mathrm{mem}}, \tag{7.12b}$$

where P_{ion} is the electrical space charge density due to the mobile ionic species and the function $f(\varepsilon_{\mathrm{sdl}}, \varepsilon_{\mathrm{mem}})$ accounts for the permittivity being $\varepsilon_{\mathrm{sdl}}$ outside the membrane and $\varepsilon_{\mathrm{mem}}$ inside the membrane.

The ionic flux, given by the Nernst–Planck equation Eq. (2.12), becomes

$$J_{\pm} = f(1, k_{\mathrm{p}}) D_{\pm}\left(-\frac{\mathrm{d}C_{\pm}}{\mathrm{d}X} \mp Z\frac{C_{\pm}}{V_{\mathrm{T}}}\frac{\mathrm{d}\Phi}{\mathrm{d}X}\right), \tag{7.13}$$

where $D_\pm$ is the diffusivity and Z the valence of the binary, but not necessarily symmetric, electrolyte. The function $f(1, k_\mathrm{p})$ accounts for the scaling of the flux by unity outside the membrane and by the ionic hindrance factor k_p inside the membrane.

Furthermore, we assume that the cation and anion are chemically inert,

$$R_\pm = 0, \tag{7.14}$$

and we stress that we account for the chemical water self-ionization reaction as shown below.

The ionic charge density is given in terms of the four ionic species,

$$P_\mathrm{ion} = f(1, \epsilon_\mathrm{p}) e \left(Z C_+ - Z C_- + C_\mathrm{H} - C_\mathrm{OH} \right), \tag{7.15}$$

where the function $f(1, \epsilon_\mathrm{p})$ accounts for the scaling of the concentration by unity outside the membrane and by ϵ_p inside the membrane.

7.2.1.3 Special considerations concerning transport of H^+ and OH^-

The transport of H^+- and OH^- ions (water ions) is complicated by the fact that these ions are chemically active in the water self-ionization reaction Eq. (2.42),

$$\mathrm{H_2O} + \mathrm{H_2O} \underset{b_\mathrm{w}}{\overset{f_\mathrm{w}}{\rightleftharpoons}} \mathrm{OH^-} + \mathrm{H_3O^+}, \tag{7.16}$$

where $f_\mathrm{w} = 2.7 \times 10^{-5}\ \mathrm{s^{-1}}$ is the water forward reaction rate constant and $b_\mathrm{w} = 1.5 \times 10^{11}\ \mathrm{M^{-1}\,s^{-1}} \approx 2.5 \times 10^{-16}\ \mathrm{m^3\,s^{-1}}$ is the water backward reaction rate constant. As mentioned in Section 2.6.1, a way to reduce the mathematical complexity of the governing equations is to utilize the chemical equilibrium. In that spirit, we follow van Soestbergen [194] and introduce the diffusivity weighted sum C_w and difference P_w of the concentrations of the water ions,

$$C_\mathrm{w} = \frac{D_\mathrm{H} C_\mathrm{H} + D_\mathrm{OH} C_\mathrm{OH}}{D_\mathrm{w}}, \tag{7.17a}$$

$$P_\mathrm{w} = \frac{D_\mathrm{H} C_\mathrm{H} - D_\mathrm{OH} C_\mathrm{OH}}{D_\mathrm{w}}, \tag{7.17b}$$

with corresponding reverse mapping,

$$C_\mathrm{H} = \frac{1}{2} \frac{D_\mathrm{w}}{D_\mathrm{H}} \Big(C_\mathrm{w} + P_\mathrm{w} \Big), \tag{7.18a}$$

$$C_\mathrm{OH} = \frac{1}{2} \frac{D_\mathrm{w}}{D_\mathrm{OH}} \Big(C_\mathrm{w} - P_\mathrm{w} \Big), \tag{7.18b}$$

where $D_\mathrm{w} = (D_\mathrm{H} D_\mathrm{OH})^{\frac{1}{2}}$ is the geometric mean of the H^+ and OH^- diffusivities.

The production terms for the water ions are the same and denoted R_w,

$$R_\mathrm{w} = R_\mathrm{H} = R_\mathrm{OH} = f_\mathrm{w} C_{\mathrm{H_2O}}^2 - b_\mathrm{w} C_\mathrm{H} C_\mathrm{OH}. \tag{7.19}$$

We introduce the sum $J_\mathrm{v} = J_\mathrm{H} + J_\mathrm{OH}$ and difference $J_\mathrm{w} = J_\mathrm{H} - J_\mathrm{OH}$ of the water ion fluxes,

$$J_\mathrm{v} = f(1,k_\mathrm{p})D_\mathrm{w}\Big(-\frac{\mathrm{d}C_\mathrm{w}}{\mathrm{d}X} - \frac{P_\mathrm{w}}{V_\mathrm{T}}\frac{\mathrm{d}\Phi}{\mathrm{d}X}\Big), \tag{7.20a}$$

$$J_\mathrm{w} = f(1,k_\mathrm{p})D_\mathrm{w}\Big(-\frac{\mathrm{d}P_\mathrm{w}}{\mathrm{d}X} - \frac{C_\mathrm{w}}{V_\mathrm{T}}\frac{\mathrm{d}\Phi}{\mathrm{d}X}\Big), \tag{7.20b}$$

which together with C_w, P_w, and R_w lead to the reformulated ionic conservation equations,

$$\frac{\mathrm{d}J_\mathrm{v}}{\mathrm{d}X} = 2\,b_\mathrm{w}\left[K_\mathrm{w} - \frac{C_\mathrm{w}^2 - P_\mathrm{w}^2}{4}\right], \tag{7.21a}$$

$$\frac{\mathrm{d}J_\mathrm{w}}{\mathrm{d}X} = 0. \tag{7.21b}$$

We scale the P_w and C_w concentrations by $\sqrt{K_\mathrm{w}}$, length by L, and thus the J_v and J_w flux by $\sqrt{K_\mathrm{w}}D_\mathrm{w}/L$ and obtain the dimensionless equations,

$$\frac{\mathrm{d}j_\mathrm{v}}{\mathrm{d}x} = Da\left[1 - \frac{c_\mathrm{w}^2 - \rho_\mathrm{w}^2}{4}\right], \tag{7.22a}$$

$$\frac{\mathrm{d}j_\mathrm{w}}{\mathrm{d}x} = 0, \tag{7.22b}$$

where $Da = \tau_\mathrm{diff}/\tau_\mathrm{reac} = 2\,b_\mathrm{w}\sqrt{K_\mathrm{w}}L^2/D_\mathrm{w}$ is the Damköhler number, see also Eq. (2.17), in which $\tau_\mathrm{reac} = 1/(\sqrt{K_\mathrm{w}}b_\mathrm{w})$ is the reaction time scale and $\tau_\mathrm{diff} = L^2/D_\mathrm{w}$ is the diffusion time scale. We note that $D_\mathrm{H} = 9.312 \times 10^{-9}\ \mathrm{m^2\,s^{-1}}$ and $D_\mathrm{OH} = 5.260 \times 10^{-9}\ \mathrm{m^2\,s^{-1}}$ and hence $D_\mathrm{w} = 7.000 \times 10^{-9}\ \mathrm{m^2\,s^{-1}}$ whereby $\tau_\mathrm{reac} \approx 70\,\mu\mathrm{s}$. This suggests that for ionic transport of $\mathrm{H^+}$ and $\mathrm{OH^-}$ ions driven by gradients with a length scale $L \gg \left[D_\mathrm{w}/(2\sqrt{K_\mathrm{w}}b_\mathrm{w})\right]^{1/2} \approx 176$ nm the diffusion time is much longer than the reaction time, or $Da \gg 1$, and the left-hand-side in Eq. (7.22a) is negligible leading to the relation set by the right-hand-side,

$$C_\mathrm{w}^2 - P_\mathrm{w}^2 = 4\,K_\mathrm{w}, \tag{7.23}$$

which is the classical water self-ionization equilibrium condition, also expressible in the more familiar form, $C_\mathrm{H}C_\mathrm{OH} = K_\mathrm{w}$ [see Eq. (2.43)].

Due to its definition the concentration sum $C_\mathrm{w} \geq 0$ is non-negative and can be expressed by Eq. (7.23) unambiguously in terms of the concentration difference P_w,

$$C_\mathrm{w} = \left[4\,K_\mathrm{w} + P_\mathrm{w}\right]^{\frac{1}{2}}, \tag{7.24}$$

whereby ionic mass conservation of the water ions is given by

$$J_\mathrm{w} = f(1,k_\mathrm{p})D_\mathrm{w}\left[-\frac{\mathrm{d}P_\mathrm{w}}{\mathrm{d}X} - \frac{1}{V_\mathrm{T}}\left(4\,K_\mathrm{w} + P_\mathrm{w}^2\right)^{\frac{1}{2}}\frac{\mathrm{d}\Phi}{\mathrm{d}X}\right], \tag{7.25a}$$

$$\frac{\mathrm{d}J_\mathrm{w}}{\mathrm{d}X} = 0. \tag{7.25b}$$

We note that it is not straight forward to change variable from $P_{\rm w}$ to $C_{\rm w}$ in Eq. (7.25) since $P_{\rm w}$ can be both negative and positive and it is difficult to unambiguously determine the sign of $P_{\rm w}$ in Eq. (7.23).

For simplicity, we assume that the water self-ionization reaction is in equilibrium in all parts of the domain even though the presence of the small screening length $\lambda_{\rm D} \sim O(\text{nm})$ hints that there could be local points where the reaction is brought out of equilibrium. The assumption of water self-ionization equilibrium is also compromised since in Eq. (7.22) the small parameter $(1/Da)$ multiplies onto the highest derivative which indicates the possibility of formation of boundary layers, which is even more likely to occur in the present system since it contains phase boundaries in contrast to systems just dealing with free unbounded solution. A proper treatment would involve singular perturbation theory but for simplicity we leave this for future work. In our computational results we check the validity of the water self-ionization equilibrium assumption in Eq. (7.23) *a posteriori* by comparing against Da locally the numerical value of the left-hand-side in Eq. (7.22a).

7.2.1.4 Boundary conditions

At the reservoir-SDL interfaces at X_1 and X_4, see Fig. 7.1, we assume fixed pH equal to $\text{pH}_{\rm res}$ corresponding to $C_{\rm H} = C_{\rm H}^{\rm res}$ and $C_{\rm OH} = K_{\rm w}/C_{\rm H}^{\rm res}$ in which

$$C_{\rm H}^{\rm res} = 10^{-\text{pH}_{\rm res}}. \tag{7.26}$$

In terms of the concentration difference $P_{\rm w}$ this becomes

$$P_{\rm w}(X_1) = P_{\rm w}(X_4) = \left(D_{\rm H} C_{\rm H}^{\rm res} - D_{\rm OH} \frac{K_{\rm w}}{C_{\rm H}^{\rm res}} \right) D_{\rm w}^{-1}. \tag{7.27}$$

Electroneutrality then dictates that any H^+/OH^- charge imbalance be compensated by the salt ions. Hence, we perturb the cation and anion concentrations around the reservoir concentration $C_{\rm res}$ to obtain electroneutrality in the reservoirs,

$$C_+(X_1) = C_+(X_4) = C_{\rm res} + \frac{1}{Z} \frac{K_{\rm w}}{C_{\rm H}^{\rm res}}, \tag{7.28}$$

$$C_-(X_1) = C_-(X_4) = C_{\rm res} + \frac{1}{Z} C_{\rm H}^{\rm res}. \tag{7.29}$$

The electrostatic potential is grounded in the left reservoir and biased to the potential ΔV in the right reservoir,

$$\Phi(X_1) = 0, \qquad \Phi(X_4) = \Delta V. \tag{7.30}$$

7.2.1.5 Non-dimensionalization

Governing equations We introduce the following non-dimensional quantities,

$$j_{\pm} = J_{\pm}\left(2D_{\pm}\frac{C_{\mathrm{res}}}{L_{\mathrm{sdl}}}\right)^{-1}, \qquad x = \frac{X}{L_{\mathrm{sdl}}}, \qquad c_{\pm} = \frac{C_{\pm}}{C_{\mathrm{res}}}, \tag{7.31a}$$

$$j_{\mathrm{w}} = J_{\mathrm{w}}\left(D_{\mathrm{w}}\frac{\sqrt{K_{\mathrm{w}}}}{L_{\mathrm{sdl}}}\right)^{-1}, \qquad \phi = \frac{\Phi}{V_{\mathrm{T}}}, \qquad \rho_{\mathrm{w}} = \frac{P_{\mathrm{w}}}{\sqrt{K_{\mathrm{w}}}}, \tag{7.31b}$$

whereby mass conservation of all ionic species in Eq. (7.12a) is compactly written as

$$\frac{\mathrm{d}j_i}{\mathrm{d}x} = 0, \qquad i = +, -, \mathrm{w}, \tag{7.32a}$$

$$j_{\pm} = \frac{f(1,k_{\mathrm{p}})}{2}\left(-\frac{\mathrm{d}c_{\pm}}{\mathrm{d}x} \mp Zc_{\pm}\frac{\mathrm{d}\phi}{\mathrm{d}x}\right), \tag{7.32b}$$

$$j_{\mathrm{w}} = f(1,k_{\mathrm{p}})\left\{-\frac{\mathrm{d}\rho_{\mathrm{w}}}{\mathrm{d}x} - \left[4+\rho_{\mathrm{w}}^2\right]^{\frac{1}{2}}\frac{\mathrm{d}\phi}{\mathrm{d}x}\right\}. \tag{7.32c}$$

The relations in Eqs. (7.17) and (7.18) become in terms of the dimensionless variables

$$c_{\mathrm{w}} = \left[4+\rho_{\mathrm{w}}^2\right]^{\frac{1}{2}}, \tag{7.33a}$$

$$\rho_{\mathrm{w}} = \frac{D_{\mathrm{H}}c_{\mathrm{H}} - D_{\mathrm{OH}}c_{\mathrm{OH}}}{D_{\mathrm{w}}}, \tag{7.33b}$$

$$c_{\mathrm{H}} = \frac{D_{\mathrm{w}}}{D_{\mathrm{H}}}\left\{\frac{\rho_{\mathrm{w}}}{2} + \left[1+\left(\frac{\rho_{\mathrm{w}}}{2}\right)^2\right]^{\frac{1}{2}}\right\}, \tag{7.33c}$$

$$c_{\mathrm{OH}} = \frac{D_{\mathrm{w}}}{D_{\mathrm{OH}}}\left\{-\frac{\rho_{\mathrm{w}}}{2} + \left[1+\left(\frac{\rho_{\mathrm{w}}}{2}\right)^2\right]^{\frac{1}{2}}\right\}. \tag{7.33d}$$

Furthermore, we introduce the non-dimensionalized charge densities ρ_{ion} and ρ_{mem},

$$\rho_{\mathrm{ion}} = \frac{P_{\mathrm{ion}}}{ZeC_{\mathrm{res}}} = f(1,\epsilon_{\mathrm{p}})\Big[c_+ - c_- + \delta_{\mathrm{w}}(c_{\mathrm{H}} - c_{\mathrm{OH}})\Big], \tag{7.34a}$$

$$\rho_{\mathrm{mem}} = \frac{P_{\mathrm{mem}}}{eC_{\mathrm{mem}}} = f(0,\epsilon_{\mathrm{p}})\,2\,\theta\frac{\alpha}{\beta}, \tag{7.34b}$$

where

$$\beta = 2\,Z\frac{C_{\mathrm{res}}}{C_{\mathrm{mem}}} \tag{7.35}$$

is the reservoir-salt-to-membrane concentration ratio and

$$\delta_{\mathrm{w}} = \frac{\sqrt{K_{\mathrm{w}}}}{ZC_{\mathrm{res}}} \tag{7.36}$$

is the water-ion-to-reservoir-salt concentration ratio.

Non-dimensionalization of the Poisson equation Eq. (7.12b) yields

$$-2\,Z\lambda\frac{\mathrm{d}}{\mathrm{d}x}\left[f\left(1,\frac{\varepsilon_{\mathrm{mem}}}{\varepsilon_{\mathrm{sdl}}}\right)\frac{\mathrm{d}\phi}{\mathrm{d}x}\right]=\rho_{\mathrm{ion}}+\rho_{\mathrm{mem}}, \tag{7.37}$$

where

$$\lambda=\frac{\lambda_{\mathrm{D}}}{L_{\mathrm{sdl}}} \tag{7.38}$$

is the dimensionless screening length. The Debye screening length is defined in Eq. (2.6) and here specifically given as

$$\lambda_{\mathrm{D}}=\sqrt{\frac{\varepsilon_{\mathrm{sdl}}k_{\mathrm{B}}T}{2(Ze)^2C_{\mathrm{res}}}}. \tag{7.39}$$

Typically, λ, β, and δ_{w} are all small quantities; $10^{-6}\lesssim\lambda\lesssim10^{-3}$, $10^{-6}\lesssim\beta\lesssim10^{-1}$, and $10^{-6}\lesssim\delta_{\mathrm{w}}\lesssim10^{-3}$.

Boundary conditions At the bulk-SDL interfaces at x_1 and x_4 we have $c_{\mathrm{H}}=c_{\mathrm{H}}^{\mathrm{res}}$ and $c_{\mathrm{OH}}=1/c_{\mathrm{H}}^{\mathrm{res}}$, in which

$$c_{\mathrm{H}}^{\mathrm{res}}=10^{-\mathrm{pH}_{\mathrm{res}}}\frac{1}{\sqrt{K_{\mathrm{w}}}}. \tag{7.40}$$

We introduce the reservoir concentration sum $\rho_{\mathrm{w}}^{\mathrm{res}}$,

$$\rho_{\mathrm{w}}^{\mathrm{res}}=\left(D_{\mathrm{H}}c_{\mathrm{H}}^{\mathrm{res}}-\frac{D_{\mathrm{OH}}}{c_{\mathrm{H}}^{\mathrm{res}}}\right)D_{\mathrm{w}}^{-1}. \tag{7.41}$$

The boundary conditions for the water ions and salt ions become

$$\rho_{\mathrm{w}}(x_1)=\rho_{\mathrm{w}}(x_4)=\rho_{\mathrm{w}}^{\mathrm{res}}, \tag{7.42a}$$

$$c_+(x_1)=c_+(x_4)=1+\frac{\delta_{\mathrm{w}}}{c_{\mathrm{H}}^{\mathrm{res}}}, \tag{7.42b}$$

$$c_-(x_1)=c_-(x_4)=1+\delta_{\mathrm{w}}c_{\mathrm{H}}^{\mathrm{res}}, \tag{7.42c}$$

while for the electrostatic potential,

$$\phi(x_1)=0,\qquad\phi(x_4)=\Delta v, \tag{7.43}$$

in which

$$\Delta v=\frac{\Delta V}{V_{\mathrm{T}}}. \tag{7.44}$$

7.3 Analytical results assuming electroneutrality $j_c < 1$

Below, in the analytical analysis, we assume electroneutrality to leading order in both the diffusion layers and in the membrane. Hence, the analysis is not valid for over-limiting conditions and we use it instead to illustrate the fundamental behavior of the water ions. The results obtained here is useful to understand and corroborate the numerical results.

The EDL at the SDL-membrane interface is assumed to be in quasi-equilibrium and is therefore modeled using the Donnan jump condition. Furthermore, we assume the charge from salt ions is everywhere much larger than the charge from water ions such that the problem decouples.

The leading problem then concerns the salt ions and the electric potential and is decoupled from the water ions. The perturbative problem concerns the water ions and is solved after the fact subject to the electric potential as determined by the salt ions.

We do not assume that the membrane is perfectly selective i.e. we allow for a non-zero co-ion current.

7.3.1 Solution to the leading problem; salt ions $c_\pm$ and electrical potential ϕ

7.3.1.1 Reformulation of the governing equations

We recall that the dimensionless Nernst–Planck flux expressions for the salt ions are

$$2\frac{j_+}{f(1,k_\mathrm{p})} = -\frac{\mathrm{d}c_+}{\mathrm{d}x} - Zc_+\frac{\mathrm{d}\phi}{\mathrm{d}x}, \tag{7.45a}$$

$$2\frac{j_-}{f(1,k_\mathrm{p})} = -\frac{\mathrm{d}c_-}{\mathrm{d}x} + Zc_-\frac{\mathrm{d}\phi}{\mathrm{d}x}. \tag{7.45b}$$

Electroneutrality between the salt ions and the membrane surface groups leads by Eqs. (7.34) and (7.37) to the relation

$$0 = c_+ - c_- + 2\,\theta\frac{\alpha}{\beta}\,f(0,1). \tag{7.46}$$

Next, we introduce the dimensionless salt concentration c and the dimensionless flux expressions j_c and j_q,

$$c = \frac{1}{2}\left(c_+ + c_-\right), \tag{7.47a}$$

$$j_c = j_+ + j_-, \tag{7.47b}$$

$$j_q = j_+ - j_-, \tag{7.47c}$$

and we reformulate the dimensionless Nernst–Planck equations Eq. (7.45) to

$$\frac{j_c}{f(1,k_\mathrm{p})} = -\frac{\mathrm{d}c}{\mathrm{d}x} + f(0,1)\,Z\theta\,\frac{\alpha}{\beta}\frac{\mathrm{d}\phi}{\mathrm{d}x}, \tag{7.48a}$$

$$\frac{j_q}{f(1,k_\mathrm{p})} = -Zc\frac{\mathrm{d}\phi}{\mathrm{d}x}. \tag{7.48b}$$

7.3.1.2 Salt and electrical potential in the SDLs

In the two SDLs there is no hindrance of the ions $f(1,k_\mathrm{p}) = 1$ and no membrane background charge $f(0,1) = 0$, and Eq. (7.48) reduces to

$$j_c = -\frac{\mathrm{d}c}{\mathrm{d}x}, \tag{7.49a}$$

$$j_q = -Zc\frac{\mathrm{d}\phi}{\mathrm{d}x}. \tag{7.49b}$$

These equations are readily integrated in the left and right SDLs subject to the boundary conditions in Section 7.2.1.5 which to leading order become

$$c(x_1) = c(x_4) = 1, \tag{7.50}$$

and

$$\phi(x_1) = 0, \qquad \phi(x_4) = \Delta v. \tag{7.51}$$

Thus, to leading order, in the SDLs the salt ions and the electrical potential are

$$c = 1 - j_c(x - x_i), \qquad i = 1,4, \tag{7.52a}$$

$$\phi = \frac{1}{Z}\frac{j_q}{j_c}\ln\Big[1 - j_c(x - x_i)\Big] + \phi(x_i), \qquad i = 1,4, \tag{7.52b}$$

where the solution for $i = 1$ pertains to the left SDL and that for $i = 4$ pertains to the right SDL.

This is the classical result of a linearly varying salt concentration profile and a potential that diverges at the left SDL-membrane interface $x = x_2$ when the flux approaches the limiting value $j_c \to 1$. If the membrane were assumed to be perfectly selective then from Eq. (7.47) $|j_c| = |j_q|$. However, we do not assume that the membrane is ideal.

7.3.1.3 Salt and electrical potential matching at the SDL-membrane interfaces

The thinness of the dimensionless screening length in Eq. (7.37) leads to quasi-equilibrium across the SDL-membrane interface. We find the potential difference, the Donnan potential $\Delta\phi_{\mathrm{D},i}$, across the interface by utilizing constant electrochemical potentials and electroneutrality in the membrane,

$$\Delta\phi_{\mathrm{D},i} = \frac{1}{Z}\sinh^{-1}\left[\frac{\alpha}{\beta}\frac{\theta}{c(x_i^{\mathrm{sdl}})}\right], \qquad i = 2,3, \tag{7.53}$$

where the point x_i^{sdl} is on the SDL side of the interface at $x = x_i$ immediately outside the electric double layer. Hence, the matching conditions at the SDL-membrane interfaces are

$$c(x_i^{\mathrm{mem}}) = c(x_i^{\mathrm{sdl}}) \cosh\left[Z\Delta\phi_{\mathrm{D},i}\right] = c(x_i^{\mathrm{sdl}}) \left\{1 + \left[\frac{\alpha}{\beta}\frac{1}{c(x_i^{\mathrm{sdl}})}\right]^2\right\}^{\frac{1}{2}}, \qquad i = 2, 3, \tag{7.54a}$$

$$\phi(x_i^{\mathrm{mem}}) = \phi(x_i^{\mathrm{sdl}}) + \Delta\phi_{\mathrm{D},i}, \qquad i = 2, 3, \tag{7.54b}$$

where x_i^{mem} is located inside the membrane and in the same way as x_i^{sdl} described above. The necessary specific values of the solution in the SDLs at $x = x_i^{\mathrm{sdl}}$ are by Eq. (7.52)

$$c(x_2^{\mathrm{sdl}}) = 1 - j_c, \qquad c(x_3^{\mathrm{sdl}}) = 1 + j_c, \tag{7.55a}$$

$$\phi(x_2^{\mathrm{sdl}}) = \frac{1}{Z}\frac{j_q}{j_c}\ln\left(1 - j_c\right), \qquad \phi(x_3^{\mathrm{sdl}}) = \frac{1}{Z}\frac{j_q}{j_c}\ln\left(1 + j_c\right) + \Delta v. \tag{7.55b}$$

7.3.1.4 Salt and electrical potential in the membrane interior

For notational reasons we rearrange Eq. (7.48),

$$A_2 = -\frac{\mathrm{d}c}{\mathrm{d}x} + \frac{A_2}{A_1}\frac{1}{c}, \tag{7.56a}$$

$$\frac{\mathrm{d}\phi}{\mathrm{d}x} = \frac{\theta}{Z}\frac{\beta}{\alpha}\frac{A_2}{A_1}\frac{1}{c}, \tag{7.56b}$$

in which the variables A_1 and A_2 are

$$A_1 = -\theta\frac{\beta}{\alpha}\frac{j_c}{j_q}, \tag{7.57a}$$

$$A_2 = \frac{j_c}{k_{\mathrm{p}}}. \tag{7.57b}$$

Integration of Eq. (7.56a) subject to the boundary condition that at $x = x_3^{\mathrm{mem}}$ the concentration is $c(x_3^{\mathrm{mem}})$ yields

$$c(x) = \frac{1}{A_1}\left(1 + W\left\{\left[A_1 c(x_3^{\mathrm{mem}}) - 1\right]e^{-A_1A_2(x - l_{\mathrm{mem}}) + \left[A_1 c(x_3^{\mathrm{mem}}) - 1\right]}\right\}\right), \tag{7.58a}$$

$$\phi(x) = \phi(x_3^{\mathrm{mem}}) + \frac{1}{Z}\frac{j_q}{j_c}\ln\left[\frac{A_1 c(x) - 1}{A_1 c(x_3^{\mathrm{mem}}) - 1}\right] \tag{7.58b}$$

$$= \phi(x_3^{\mathrm{mem}}) - \frac{\theta}{Z}\frac{\beta}{\alpha}\left[c(x_3^{\mathrm{mem}}) - c(x) - A_2\left(x - l_{\mathrm{mem}}\right)\right], \tag{7.58c}$$

where $W(x)$ is the Lambert W function defined by the equation $x = W(x)e^{W(x)}$ and $l_{\mathrm{mem}} = L_{\mathrm{mem}}/L_{\mathrm{sdl}}$ is the dimensionless membrane thickness.

To close the system in terms of the two remaining unknowns, j_c and j_q, we evaluate the solution in Eq. (7.58) at $x = x_2^{\text{mem}}$ and apply the matching conditions in Eq. (7.54) to obtain

$$c(x_2^{\text{mem}}) = \frac{1}{A_1}\left(1 + W\left(\left[A_1 c(x_3^{\text{mem}}) - 1\right] e^{A_1 A_2 l_{\text{mem}} + \left[A_1 c(x_3^{\text{mem}}) - 1\right]}\right)\right), \tag{7.59a}$$

$$\phi(x_2^{\text{mem}}) = \phi(x_3^{\text{mem}}) + \frac{1}{Z}\frac{j_q}{j_c} \ln\left[\frac{A_1 c(x_2^{\text{mem}}) - 1}{A_1 c(x_3^{\text{mem}}) - 1}\right]. \tag{7.59b}$$

These are two coupled algebraic equations for the determination of j_c and j_q.

For notational reasons we introduce the variable κ and the functions $K_- = K_-(j_c)$ and $K_+ = K_+(j_c)$,

$$\kappa = \theta \frac{j_q}{j_c}, \tag{7.60a}$$

$$K_- = \left\{1 + \left[\frac{\beta}{\alpha}(1 - j_c)\right]^2\right\}^{\frac{1}{2}}, \tag{7.60b}$$

$$K_+ = \left\{1 + \left[\frac{\beta}{\alpha}(1 + j_c)\right]^2\right\}^{\frac{1}{2}}, \tag{7.60c}$$

Furthermore, we introduce the functions $F_1 = F_1(j_c, \kappa)$ and $F_2 = F_2(j_c, \kappa)$ and reformulate Eqs. (7.59) to obtain

$$F_1(j_c, \kappa) = \kappa \ln\left(\frac{\kappa + K_-}{\kappa + K_+}\right) + \frac{1}{\gamma}\frac{\beta}{\alpha} j_c + K_+ - K_- = 0, \tag{7.61a}$$

$$F_2(j_c, \kappa) = \kappa \ln\left(\frac{\kappa + K_-}{\kappa + K_+}\right) + 2\,(\kappa - 1)\tanh^{-1}(j_c) + \theta Z \Delta v + \ln\left(\frac{1 + K_+}{1 + K_-}\right) = 0, \tag{7.61b}$$

in which $\gamma = k_{\text{p}}/l_{\text{mem}}$ is the "accumulated" ionic hindrance along the width of the membrane. We combine these equations to obtain an equation for κ in terms of j_c alone,

$$\kappa = \kappa(j_c) = 1 - \frac{1}{2\,\tanh^{-1}(j_c)}\left\{\theta Z \Delta v + \left[\ln\left(\frac{1 + K_+}{1 + K_-}\right) + K_- - K_+\right] - \frac{1}{\gamma}\frac{\beta}{\alpha} j_c\right\}. \tag{7.62a}$$

This relation can be used in either of the Eqs. (7.61) to obtain a single transcendental equation for the unknown j_c. We use the first equation,

$$F_1\left[j_c, \kappa(j_c)\right] = 0, \tag{7.63}$$

which we can solve numerically in `Matlab` as a parametric function of Δv.

The solution of Eq. (7.63) leads to the current response to an applied potential difference for arbitrary values of the membrane charge density ρ_{mem}. In the limit where the membrane charge density remains large the transcendental equation simplifies as shown below.

7.3.1.5 Simplified results for large membrane charge $\alpha/\beta \gg 1$

In the limit of a large membrane charge density $\alpha/\beta \gg 1$ three of the terms in Eq. (7.61) simplify,

$$\kappa \ln\left(\frac{\kappa + K_-}{\kappa + K_+}\right) = -\frac{2\,\kappa}{1+\kappa}\left(\frac{\beta}{\alpha}\right)^2 j_c, \tag{7.64a}$$

$$K_+ - K_- = 2\left(\frac{\beta}{\alpha}\right)^2 j_c, \tag{7.64b}$$

$$\ln\left(\frac{1+K_+}{1+K_-}\right) = \left(\frac{\beta}{\alpha}\right)^2 j_c, \tag{7.64c}$$

whereby Eq. (7.61a) leads to the relation

$$\kappa = -\left(1 + 2\,\gamma\frac{\beta}{\alpha}\right), \tag{7.65}$$

whereby Eq. (7.61b) yields to first order in $\gamma\beta/\alpha$ the simplified transcendental equation for j_c,

$$4\left(1+\gamma\frac{\beta}{\alpha}\right)\tanh^{-1}(j_c) + \frac{1}{\gamma}\frac{\beta}{\alpha}\,j_c - \theta Z\Delta v = 0. \tag{7.66}$$

The other variable j_q is then given by Eq. (7.65),

$$j_q = -\theta\, j_c\left(1 + 2\,\gamma\frac{\beta}{\alpha}\right). \tag{7.67}$$

We note that to zeroth order in $\gamma\alpha/\beta$ we recover the classical result for a perfectly selective membrane,

$$j_c = \tanh\left(\theta\frac{Z\Delta v}{4}\right). \tag{7.68}$$

The solution for j_c and j_q leads by Eqs. (7.52) and (7.58) to the determination of the concentration c and the electrical potential ϕ in the entire system. We next use this solution, in particular for the electrical potential, to solve for the distribution of the water ions throughout the system.

We expand Eq. (7.66) in the limit of small voltage and current and obtain the linear current-voltage relation

$$j_c = \frac{\Delta v}{\phi_0}, \tag{7.69}$$

where the scaling factor ϕ_0 is

$$\phi_0 = \theta\frac{4}{Z}\left[1 + \left(\gamma + \frac{1}{4\,\gamma}\right)\frac{\beta}{\alpha}\right]. \tag{7.70}$$

7.3.2 Solution to the perturbative problem; H^+- and OH^- ions

We assume that the charge density due to water ions is small relative to the charge density due to salt ions, $Z(C_+ - C_-) \gg C_H - C_{OH}$. Hence, we assume that the salt concentration and the electrical potential are undisturbed to leading order by the presence of the water ions. We reiterate that the combined problem thus decouples into that of the salt and the electric potential and that of the water ions, where the solution of the former serves as input to that of the latter.

We follow the same approach as for the salt-potential problem by integrating the transport equation for ρ_w in the SDLs and in the membrane and subsequently determine the integration constant and j_w by matching at the SDL-membrane interfaces. We assume that the water ions are in quasi-equilibrium across the SDL-membrane interface.

The high non-linearity of the flux expression for ρ_w in Eq. (7.32c) makes a full, closed form, analytic solution intractable and we therefore perform a linearization.

7.3.2.1 H^+- and OH^- ions in the SDLs for small currents $j_c \ll 1$

In the SDLs we assume that the deviation in the water charge from its equilibrium value is small $(\rho_w - \rho_w^{res})^2/4 \ll 1$ whereby we limit our analysis to small currents $j_c \ll 1$. We then approximate the original non-linear transport equation (7.32c) with the linearized version,

$$j_w = -\frac{d\rho_w}{dx} - \rho_0 \frac{d\phi}{dx}, \tag{7.71}$$

where

$$\rho_0 = \left[4 + (\rho_w^{res})^2\right]^{\frac{1}{2}} \tag{7.72}$$

is a constant. The gradient of the electrical potential is assumed to be independent of the water ions and determined solely by the salt ions by Eq. (7.52),

$$\frac{d\phi}{dx} = -\frac{j_q}{Z}\left[1 - j_c\,(x - x_i)\right]^{-1}. \tag{7.73}$$

We integrate Eq. (7.71) and use the boundary condition that $\rho_w = \rho_w^{res}$ at x_1 and x_4 and obtain

$$\rho_w = \rho_w^{res} - j_w(x - x_i) - \frac{\rho_0}{Z}\frac{j_q}{j_c}\ln\left[1 - j_c\,(x - x_i)\right], \qquad i = 1, 4, \tag{7.74}$$

where we reiterate that the solution for $i = 1$ pertains to the left SDL and that for $i = 4$ pertains to the right SDL. We note the values,

$$\rho_w(x_2^{sdl}) = \rho_w^{res} - j_w - \frac{\rho_0}{Z}\frac{j_q}{j_c}\ln\left[1 - j_c\right], \tag{7.75a}$$

$$\rho_w(x_3^{sdl}) = \rho_w^{res} + j_w - \frac{\rho_0}{Z}\frac{j_q}{j_c}\ln\left[1 + j_c\right], \tag{7.75b}$$

used below when we match at the SDL-membrane interface.

7.3.2.2 H^+- and OH^- ions in the membrane interior

Due to the relatively high membrane charge, we expect ρ_w to have a large absolute value $|\rho_w/2| \gg 1$ in the membrane. Furthermore, the sign of ρ_w must be positive in cation-selective ($\theta = -1$) membranes and negative in anion-selective ($\theta = 1$) membranes. Thus, the absolute value of ρ_w can be written as $|\rho_w| = -\theta\rho_w$. We use this in the linearization of the flux expression for ρ_w in Eq. (7.32c),

$$\frac{j_w}{k_p} = -\frac{d\rho_w}{dx} + \theta\rho_w\frac{d\phi}{dx}. \tag{7.76}$$

Again, the electrical potential gradient is assumed independent of ρ_w and determined solely by the salt ions. It turns out that the general form of the solution to Eq. (7.76) is

$$\rho_w = e^{\theta[\phi(x)-\phi(x_0)]}\left\{\rho_w(x_0) - \frac{j_w}{k_p}\int_{x_0}^{x} e^{-\theta[\phi(\xi)-\phi(x_0)]}\,d\xi\right\}. \tag{7.77}$$

7.3.2.3 H^+- and OH^- ion matching at the solution-membrane interfaces

As mentioned in Section 2.4, at equilibrium the flux is zero and the resulting balance between diffusion and electromigration, found by integration of Eq. (7.32c), yields the condition

$$\rho_w = 2\sinh(A - \phi), \tag{7.78}$$

where A is an integration constant. Using as reference points x_i^{sdl} right outside the EDL at the SDL-membrane interface we obtain the matching condition for the water charge,

$$A_i = \sinh^{-1}\left[\frac{\rho_w(x_i^{sdl})}{2}\right], \qquad i = 2, 3, \tag{7.79a}$$

$$\rho_w(x_i^{mem}) = 2\sinh(A_i - \Delta\phi_{D,i}), \qquad i = 2, 3. \tag{7.79b}$$

Matching at the left and right interface allow us to determine in Eq. (7.77) both the integration constant $\rho_w(x_0)$ and the flux j_w. We choose $x_0 = x_3^{mem}$ and get

$$\rho_w = e^{\theta\left[\phi(x)-\phi(x_3^{mem})\right]}\left\{\rho_w(x_3^{mem}) - \frac{j_w}{k_p}\int_{x_3^{mem}}^{x} e^{-\theta\left[\phi(\xi)-\phi(x_3^{mem})\right]}\,d\xi\right\}. \tag{7.80}$$

We close the system by matching at the left SDL-membrane interface $x = x_2^{mem}$,

$$-\rho_w(x_2^{mem}) + e^{\theta\left[\phi(x_2^{mem})-\phi(x_3^{mem})\right]}\left\{\rho_w(x_3^{mem}) - \frac{j_w}{k_p}\int_{x_3^{mem}}^{x_2^{mem}} e^{-\theta\left[\phi(\xi)-\phi(x_3^{mem})\right]}\,d\xi\right\} = 0. \tag{7.81}$$

Given the electrical potential from the salt-potential problem the solution of Eq. (7.81) determines together with j_c and j_q the flux j_w and by Eqs. (7.74) and (7.80) the distribution of ρ_w, and thus c_H, in the entire system.

7.3.2.4 Simplified results for large membrane charge $\alpha/\beta \gg 1$

In the case of a large membrane charge $\alpha/\beta \gg 1$ we expand Eq. (7.48a),

$$\mathrm{d}x = \theta \frac{Z}{k_\mathrm{p}} \frac{\alpha}{\beta} \frac{1}{j_c} \mathrm{d}\phi, \tag{7.82}$$

which leads to the potential difference across the inside of the membrane $\Delta\phi^\mathrm{mem} = \phi(x_3^\mathrm{mem}) - \phi(x_2^\mathrm{mem})$,

$$\Delta\phi^\mathrm{mem} = \frac{\theta}{Z} \frac{\beta}{\alpha} \frac{j_c}{\gamma}. \tag{7.83a}$$

This potential difference $\Delta\phi^\mathrm{mem}$ is small whereby we approximate the integral in Eq. (7.81),

$$\int_{x_3^\mathrm{mem}}^{x_2^\mathrm{mem}} e^{-\theta\left[\phi(\xi) - \phi(x_3^\mathrm{mem})\right]} \mathrm{d}\xi = l_\mathrm{mem}. \tag{7.84}$$

All together, Eq. (7.81) simplifies to

$$\rho_\mathrm{w}(x_3^\mathrm{mem}) - \rho_\mathrm{w}(x_2^\mathrm{mem}) \exp\left(\frac{\theta}{Z} \frac{\beta}{\alpha} \frac{j_c}{\gamma}\right) + \frac{j_\mathrm{w}}{\gamma} = 0. \tag{7.85}$$

In the limits of a large membrane charge density $\alpha/\beta \gg 1$ and for small currents $j_c \ll 1$ this equation determines j_w. $\rho_\mathrm{w}(x_i^\mathrm{mem})$ is given by Eqs. (7.79) and (7.75). This leads by Eqs. (7.74) and (7.80) to the distribution of ρ_w, and thus c_H, in the entire system.

7.3.3 The semi-analytical model: solving the coupled system with dynamic membrane charge

The salt-potential and water-ion systems are coupled through the membrane ionization degree α in Eq. (7.10). For simplicity, we consider the large membrane charge limit $\alpha/\beta \gg 1$ in which the ionization degree is approximately constant across the membrane. The same applies to the hydronium-ion concentration in the membrane which can be found by Eq. (7.33c) using a simple average $\rho_\mathrm{w} = \left[\rho_\mathrm{w}(x_3^\mathrm{mem}) + \rho_\mathrm{w}(x_2^\mathrm{mem})\right]/2$ for the water charge in the membrane. Thus, in our semi-analytical model, to take into account the dynamic membrane charge, we solve self-consistently the coupled system of equations consisting of Eqs. (7.10), (7.66), and (7.85).

7.3.4 I-V curve and conductance for large membrane charge $\alpha/\beta \gg 1$

Using Eq. (7.47) we express the cation j_+ and anion j_- flux in terms of j_c and j_q,

$$j_+ = \frac{1}{2}\left(j_c + j_q\right), \tag{7.86a}$$

$$j_- = \frac{1}{2}\left(j_c - j_q\right). \tag{7.86b}$$

In the limit of a large membrane charge this simplifies by Eq. (7.67) to

$$j_+ = \frac{1}{2}\left[1 - \theta\left(1 + 2\,\gamma\frac{\beta}{\alpha}\right)\right] j_c, \tag{7.87a}$$

$$j_- = \frac{1}{2}\left[1 + \theta\left(1 + 2\,\gamma\frac{\beta}{\alpha}\right)\right] j_c. \tag{7.87b}$$

The total current J_{tot} in the system is defined as

$$J_{\text{tot}} = Z\left(J_+ - J_-\right) + J_{\text{w}}. \tag{7.88}$$

We reformulate this expression using the scaling relations in Eq. (7.31),

$$\frac{J_{\text{tot}}}{J_{\text{lim}}} = j_c\left[1 + 2\,\gamma\frac{\beta}{\alpha}\left(1 - \theta\frac{D_+ - D_-}{D_+ + D_-}\right)^{-1}\right] + \frac{J_{\text{w}}^{\text{ref}}}{J_{\text{lim}}} j_{\text{w}}, \tag{7.89}$$

where the limiting current J_{lim}, the (signed) counter-ion diffusivity $D_{-\theta}$, and the reference water-ion flux are defined as

$$J_{\text{lim}} = 2\,ZD_{-\theta}\frac{C_{\text{res}}}{L_{\text{sdl}}}, \tag{7.90a}$$

$$D_{-\theta} = \frac{1}{2}\left[D_+\left(1 - \theta\right) - D_-\left(1 + \theta\right)\right], \tag{7.90b}$$

$$J_{\text{w}}^{\text{ref}} = D_{\text{w}}\frac{\sqrt{K_{\text{w}}}}{L_{\text{sdl}}}. \tag{7.90c}$$

Even though Eq. (7.89) is derived on the assumption of electroneutrality and a large membrane charge density it does hint to the existence of over-limiting current. Note that by Eq. (7.62a) [or Eq. (7.68)] $j_c \to 1$ as $\theta\Delta v \to \infty$. The first term in Eq. (7.89) is the classical term where the current approaches asymptotically its classical limiting value J_{lim}. The second term is due to the non-ideality of the membrane, i.e. that the membrane allows a finite concentration of co-ions inside it. Thus, the limiting current is higher than the classical value. But not only that, the second term is inversely proportional to the ionization degree α which means that the term grows when α drops. And α drops due to current-induced pH changes in the membrane. This constitutes a main part of the explanation for the current-induced membrane discharge mechanism. The third term in Eq. (7.89) is the current due to water ions which is more difficult to predict.

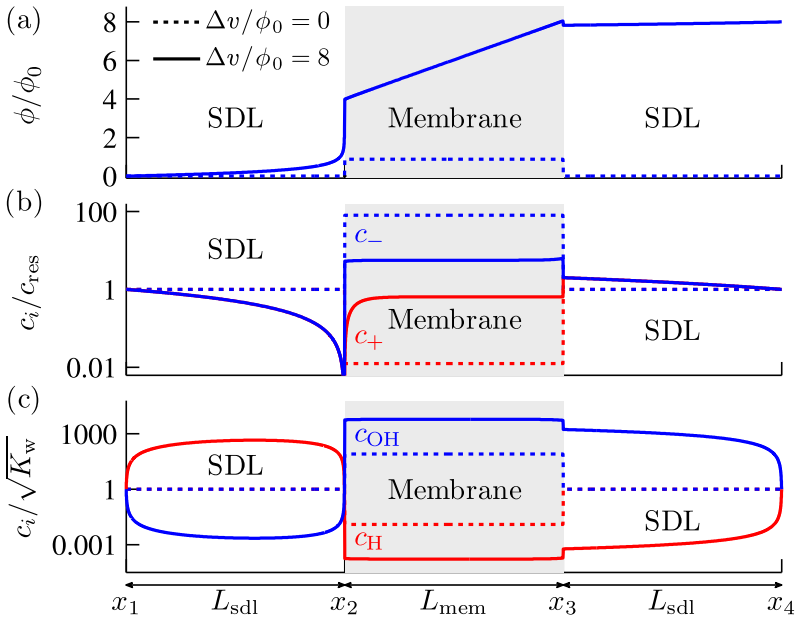

Figure 7.2: (a) The electrical potential ϕ in the membrane and the two SDLs for $\Delta v/\phi_0 = 0$ (dotted curve) and $\Delta v/\phi_0 = 8$ (full curve). (b) As in panel (a) but for the salt anion (counter-ion) concentration c_- and the salt cation (co-ion) concentration c_+. (c) As in panel (a) but for the hydroxyl-ion concentration $c_{\rm OH}$ and the hydronium-ion concentration $c_{\rm H}$. Figure adapted from our paper [195].

7.4 Numerical results for over-limiting current

We proceed with a full numerical solution of the governing equations for dynamic membrane charge Eq. (7.10), for ionic mass conservation of four ionic species (cation, anion, hydronium ion, hydroxyl ion) Eq. (7.32), and for electrostatics Eq. (7.37).

These equations are subject to the boundary conditions for the salt ions and the water ions Eq. (7.42) and for the electrostatic potential Eq. (7.43). Numerical results show that for symmetric transport properties of the salt- and water ions the CIMD effect is the same in both cation-selective and anion-selective membranes. Thus, we focus on one type of membrane, here an anion-selective membrane ($\theta = 1$).

In our simulations we choose the following typical values for our set of basis parameters: $C_{\rm mem} = 5\,{\rm M}$, $pK_{\rm mem} = 9.5$, $L_{\rm mem} = L_{\rm sdl} = 100\,\mu{\rm m}$, $\varepsilon_{\rm r,sdl} = 78$, $\varepsilon_{\rm r,mem} = 29$, $\epsilon_{\rm p} = 0.4$, $k_{\rm p} = 0.02$ [192], $Z = 1$, $D_+ = 1.3 \times 10^{-9}\,{\rm m^2\,s^{-1}}$ and $D_- = 2.0 \times 10^{-9}\,{\rm m^2\,s^{-1}}$ (corresponding to NaCl), $D_{\rm H} = 9.3 \times 10^{-9}\,{\rm m^2\,s^{-1}}$, and $D_{\rm OH} = 5.3 \times 10^{-9}\,{\rm m^2\,s^{-1}}$. We also use $pH_{\rm res} = 7$ and $\beta = 2\,C_{\rm res}/C_{\rm mem} = 0.02$, unless otherwise noted.

Figure 7.2 shows the distribution of the electrical potential, the cation and anion concentration, and the water ion concentrations, for an applied potential difference of $\Delta v/\phi_0 = 0$ and 8 [here ϕ_0 is defined using $\alpha = 1$ in Eq. (7.70)].

For $\Delta v/\phi_0 = 0$ we recognize the higher potential in the membrane due to

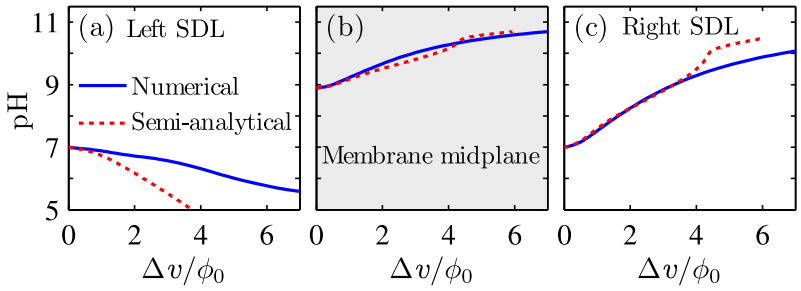

Figure 7.3: The dependence of the pH on the applied voltage difference $\Delta\phi$ at the left SDL-membrane interface (a), in the membrane (b), and at the right SDL-membrane interface (c), predicted by the full model (full blue curves) and the semi-analytical model (dashed red curves). Figure adapted from our paper [195].

the Donnan potential jump at the membrane-SDL interfaces. In relation to this, the concentration of the cation is lowered and that of the anion raised in the membrane, while the same is true for the hydronium and hydroxyl ions.

For $\Delta v/\phi_0 = 8$ (over-limiting regime) we note how a large part of the voltage is dropped at the left membrane-SDL interface. This is related to the concentration polarization across the membrane, with a strong ion depletion at the left membrane-SDL interface and a moderate enrichment at the right interface. Moreover, due to the membrane discharge, the "gap" between the cation and anion concentration levels in the membrane is diminished.

Finally, and perhaps most notably, the hydronium ion displays extreme behavior. In the left and right SDL c_{H} is raised and lowered by a factor of 10^3, respectively. Moreover, in the membrane c_{H} is lowered, contrary to the increase in c_+. The existence of these pH variations across the domain has been observed experimentally in similar systems [176, 196–198].

We verify the current-induced pH variations by comparing in Fig. 7.3 the predictions from the semi-analytical model in Section 7.3.3 and the full numerical model. We compare the pH at three positions: in both SDLs at the SDL-membrane interface right outside the equilibrium EDL [panels (a) and (c)] and in the middle of the membrane [panel (b)]. For the chosen parameters the pH variation across the membrane is small and therefore well-represented by the value at the middle.

We note good agreement between the models for $\Delta v/\phi_0 \lesssim 1$ which corresponds the electroneutral regime of validity of the semi-analytical model. Both models predict the pH to drop in the left SDL and to increase in the membrane and the right SDL.

For voltages $\Delta v/\phi_0 > 1$ the largest discrepancy between the two models occurs in the left SDL which agrees with the fact that the electroneutrality assumption is most strongly violated there in the ion depletion zone.

Thus, we have verified the agreement between the semi-analytical and full numerical models and move on to consider further predictions by the full numerical

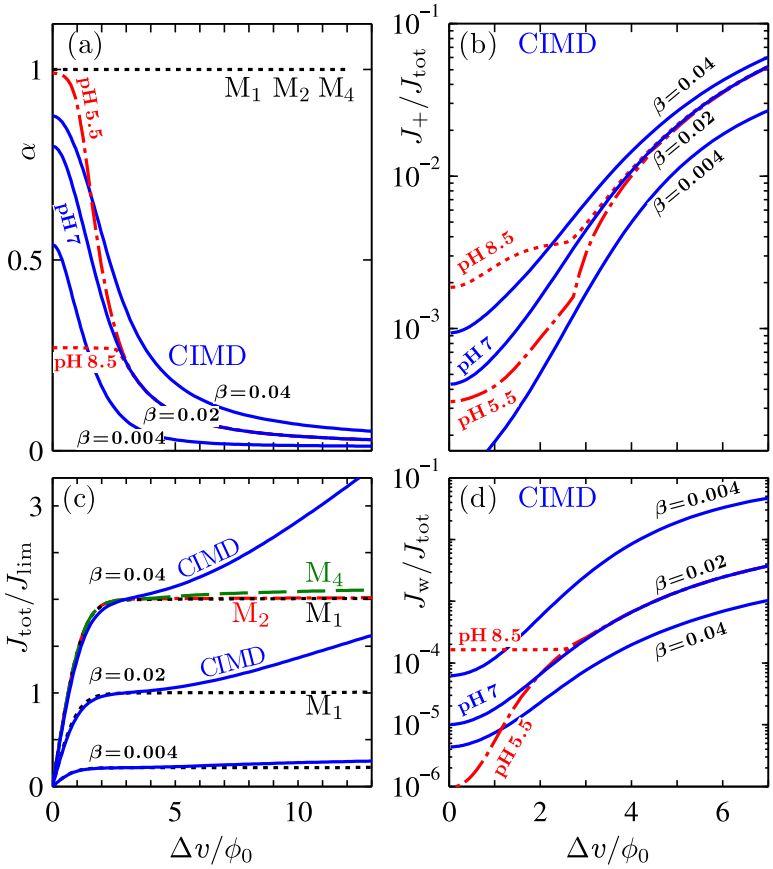

Figure 7.4: The dependence on the applied voltage difference $\Delta\phi$ of (a) the ionization degree α, (b) the cation (co-ion) current J_+, (c) the total current J_{tot}, and (d) the water ion current J_{w}, for three values of the concentration ratio $\beta = 2\,C_{\text{res}}/C_{\text{mem}} = 0.004$, 0.02, and 0.04, and for three values of the reservoir pH, $\text{pH}_{\text{res}} = 5.5$, 7, and 8.5. In panel (a) and (c) additionally show results from the M_1, M_2, and M_4 models. Figure adapted from our paper [195].

model.

In Fig. 7.4 is shown predictions by the full numerical CIMD model for two combinations of parameter values: (i) a reservoir pH_{res} of 7 and varying concentration ratio $\beta = 0.004$, 0.02, and 0.04, and (ii) the concentration ratio $\beta = 0.02$ and a varying pH_{res} of 5.5, 7, and 8.5. Furthermore, for comparison, we also show results from three other models. The classical model M_1, used in all prior work on EOI [163–167], makes three assumptions (i) the co-ion concentration $c_+ = 0$ is zero in the membrane, (ii) zero concentration $c_{\text{H}} = c_{\text{OH}} = 0$ of the water ions everywhere in the system, and (iii) the ionization degree of the membrane $\alpha = 1$ is unity for all conditions. The two remaining intermediate models include the co-ion in the membrane, still assume constant $\alpha = 1$ for all conditions, and either exclude (M_2) or include (M_4) water ions, i.e. take 2 or 4 ions into account in the membrane, respectively.

Figure 7.4(a) shows the strong decrease in the ionization degree of the membrane with increasing voltage. For a pH of 7 there is an initial sharp decrease

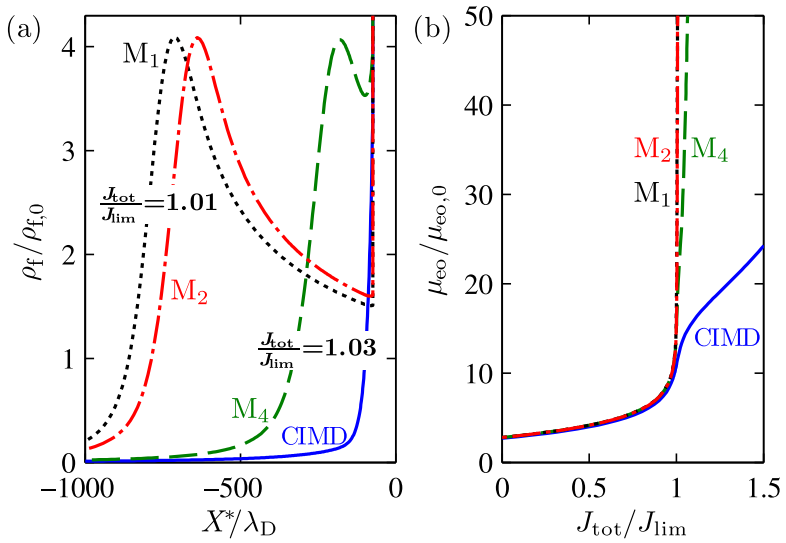

Figure 7.5: (a) The dependence of the electrical space charge density ρ_{ions} on the distance $X^* = X - X_2$ from the membrane in the ion-depleted zone. (b) The dependence of the transverse electro-osmotic mobility μ_{eo} on the total current J_{tot}. Figure adapted from our paper [195].

in α up to $\Delta v/\phi_0 \approx 5$ above which the slope levels off. Notably, for $\beta = 0.02$ the initial decrease becomes less strong with increasing pH_{res}. For any of the three values of pH_{res}, the ionization degree becomes equal to that of $pH_{res} = 7$ for voltages $\Delta v/\phi_0 \gtrsim 3$ suggesting that the reservoir pH_{res} has little influence in the over-limiting regime. The black dotted line shows the constant ionization $\alpha = 1$ of the M_1, M_2, and M_4 models.

Similar trends are seen in Fig. 7.4(b) where the co-ion (cation) flux becomes increasingly significant with voltage, here $\Delta v/\phi_0 = 7$ yields $J_+/J_{tot} \approx 0.05$. The insignificance of pH_{res} on the over-limiting regime is further verified.

Figure 7.4(c) shows most clearly the over-limiting current predicted by the CIMD model. The relative magnitude of the over-limiting current increases with increasing concentration ratio β. For all $\beta = 0.004$, 0.02, and 0.04 is shown the classical current saturation at the limiting current predicted by the M_1 model. Furthermore, for $\beta = 0.04$ is shown that no other model than the CIMD predicts significant over-limiting current.

Finally, Fig. 7.4(d) shows the relative contribution to the total current from the water ions. Perhaps most important is the fact that this contribution is insignificant in relation to the strong over-limiting currents for $\beta = 0.02$ and 0.04. However, for $\beta = 0.004$ the relative contribution becomes significant, but also in this case the over-limiting current is small.

Moreover, Fig. 7.5 illustrates how CIMD can further explain over-limiting current at the expense of the importance of EOI. Figure 7.5(a) shows the space charge density in the local region of ion depletion at the left SDL-membrane interface. For currents in the over-limiting regime all the models M_1, M_2, and M_4 predict a

space charge layer extending away from the membrane surface. The classical M_1 model even predicts the strongest space charge layer for the slightly over-limiting current $J_{tot}/J_{lim} = 1.01$. Contrary, even for the larger current $J_{tot}/J_{lim} = 1.03$ the CIMD model does not predict the extended space charge layer. Thus, this shows that the formation of the space charge layer that drives EOI is suppressed in the CIMD model.

The suppression of EOI is further illustrated in Fig. 7.5(b) where the transverse EO mobility $\mu_{eo}/\mu_{eo,0}$ (our measure of the propensity of EOI) is seen to diverge at the limiting current $J_{tot}/J_{lim} = 1$ for all the models M_1, M_2, and M_4, but remains finite in the CIMD model. The transverse electro-osmotic mobility is equal to the first moment of the charge density in the left SDL, or equivalently, to the potential drop across the left SDL,

$$\frac{\mu_{eo}}{\mu_{eo,0}} = \frac{1}{\varepsilon_{sdl} V_T} \int_{X_2}^{X_1} X \, P_{ion} \, dX = \phi(x_1) - \phi(x_2), \tag{7.91}$$

and is a measure of the propensity of EOI to develop.

In conclusion, we have theoretically demonstrated that CIMD can lead to over-limiting current through aqueous ion-selective membranes. This results from a loss of ion-selectivity due to (de-)protonation of the membrane surface groups coupled to ion transport and water self-ionization. The loss of ion-selectivity is unwanted in electrodialysis but could be exploited in current-assisted ion exchange or pH control. Further, CIMD suppresses the formation of the space charge layer and thereby the propensity of EOI to develop. Thus, models considering fluid flow and EOI should include CIMD.

Chapter 8

ICEO: finite Debye-length effects

This study was carried out together with Professor Carl Meinhart and his student Doctor Gaurav Soni, UC Santa Barbara. The following is my personal presentation of our work in Chapter F where additional details may be found.

8.1 Introduction

Induced-charge electro-osmosis (ICEO) experienced a "revival" in the year 2004 with the work of Bazant and Squires [94, 103] who pointed out the great potential of the phenomenon in microfluidic systems. Before then, electrokinetic phenomena were mainly known in the context of colloids [2]. In microfluidics, electrokinetic phenomena can be used as a means of pumping, mixing, and controlling, even locally, the fluid or suspended particles.

In this context ICEO is particularly interesting because the generated flow does not depend on the direction of the driving electric field; it scales with the square of the electric field strength E^2. Thus, it is possible to use alternating currents and avoid some of the drawbacks of using direct current such as electrodialysis. While there has been good qualitative agreement between theoretically predicted and experimentally observed ICEO flows, the quantitative agreement has been poor [123, 199–201].

ICEO resembles ordinary EO flow in the sense that an electric field acts on the diffuse charge in the electrolyte at an interface. Only, in ICEO, the charge is induced by the electric field itself. The induced charge arises around polarizable objects, such as metal structures, which remain equipotentials and ends up with induced screening layers that are positively and negatively charged on either side of the object in the direction of the external field. The electric field that induces the charge also acts upon it and forces the ions to move by electromigration. This in turn drags the liquid along by viscous friction and the ICEO flow arises.

The dipole-like structure of the induced electric screening layers means that

the flow typically consists of counter-rotating flow rolls. Furthermore, contrary to a wall with fixed chemical charges and surface potentials equal to typically a few times the thermal voltages, the induced charge in ICEO can be driven to even higher zeta potentials. Thus, ICEO easily leads to strongly non-linear electrokinetic phenomena.

The extent λ_D of the induced screening layer is often much smaller than the scale a of the polarized object and the Helmholtz–Smoluchowski slip velocity Eq. (2.36) can be applied, but is strictly only valid in the limit where the screening layer is infinitely thin $\lambda_D/a \to 0$. For typical electrolyte concentrations the screening length is on the order of 10 nm while the extent of typical microfluidic objects are on the order of 10 µm which leads to a ratio of $\lambda_D/a \approx 10^{-3}$.

Through our numerical work we noticed for small screening layers $\lambda_D/a \ll 1$ a surprisingly large deviation between predicted ICEO flows from a full resolution of the boundary layer and from the slip velocity approximation. We therefore set out to investigate this discrepancy in more detail. We define a linear slip (LS) model that ignores dynamics in the EDL. Moreover, we define a non-linear slip (NLS) model that takes into account surface conduction in the EDL. The LS and NLS models are compared against a full resolution of the EDL boundary layer, the so-called full non-linear (FN) model.

8.2 Model

Figure 8.1 shows our model system which consists of an electrolyte-filled chamber, translationally invariant in the y-direction, and square of side length $2\,L$ in the xz-plane. A flat ideally polarizable object (or "metal strip") of width $2\,a$ and height h sits at the bottom-mid of the chamber. The left and right domain boundaries are ideal electrodes with an applied potential difference of $2\,V_0$ between them. The remaining walls are electrically insulating. We consider steady-state and the ICEO flow consists of two counter-rotating flow rolls above the metal strip, see Fig. 8.1.

The electrolyte consists of two monovalent and chemically inert salt ions of concentrations c_+ (cations) and c_- (anions). The ions have the same diffusion coefficient D. The electrolyte has relative electric permittivity ε_r, viscosity η, and mass density ρ_m.

8.2.1 Governing equations

8.2.1.1 Full non-linear (FN) model

For the two ionic species we employ the steady-state ionic conservation equation Eq. (2.8) without production term in which the flux is given by the Nernst–Planck equation Eq. (2.12). For the electrical potential we use the Poisson equation Eq. (2.2) where the electrical space charge density is given as $\rho_{el} = e(n_+ -$

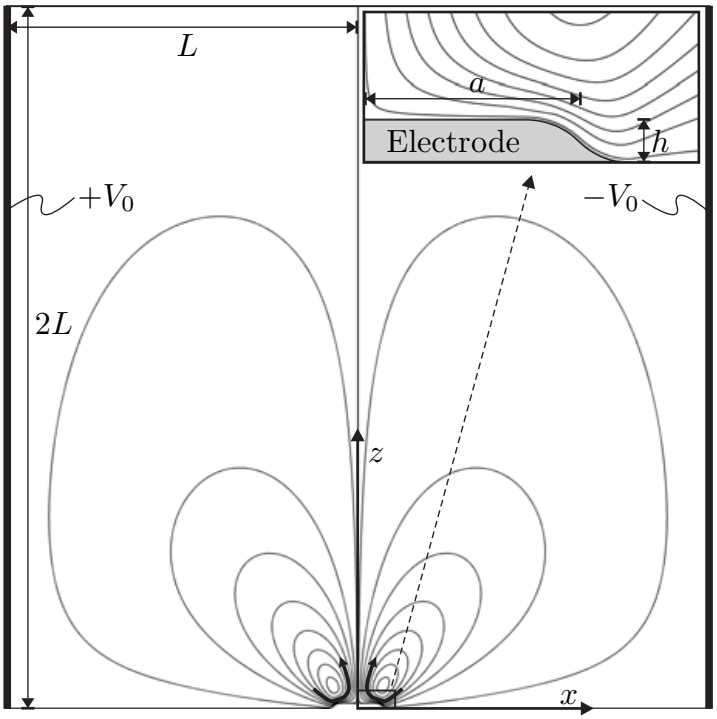

Figure 8.1: The 2D rectangular model domain of side length $2\,L$ and with external electrodes (thick lines) applying a potential difference of $2\,V_0$ across the un-biased electrode (bottom mid) of width $2\,a$ and height h. Figure adapted from our paper [202].

n_-). Finally, mass conservation of the fluid is given by the continuity equation Eq. (2.27) and momentum conservation in the fluid is described by the steady-state Navier–Stokes equation Eq. (2.32) in which we stress that we retain the electrical (Coulomb) body force density. Figure 8.2(a) shows the dimensionless equations and boundary conditions and indicates that we take advantage of the symmetry by only considering the right half of the domain.

Dimensionless form The induced zeta potential on the metal strip has extrema on either side and we estimate their magnitude as $\zeta_0 = V_0\,a/L$. From this, we define a dimensionless zeta potential

$$\alpha = \frac{\zeta_0}{V_\mathrm{T}} = \frac{a}{L}\frac{V_0}{V_\mathrm{T}} \tag{8.1}$$

which is a measure of the non-linearity in the induced screening layer. Small $\alpha \ll 1$ corresponds to the Debye–Hückel limit and larger $\alpha \gtrsim 1$ corresponds to the non-linear regime.

We define a characteristic velocity v_0 based on the Helmholtz–Smoluchowski expression using ζ_0 as the characteristic zeta potential,

$$v_0 = \frac{\varepsilon\zeta_0}{\eta}\frac{V_0}{L}. \tag{8.2}$$

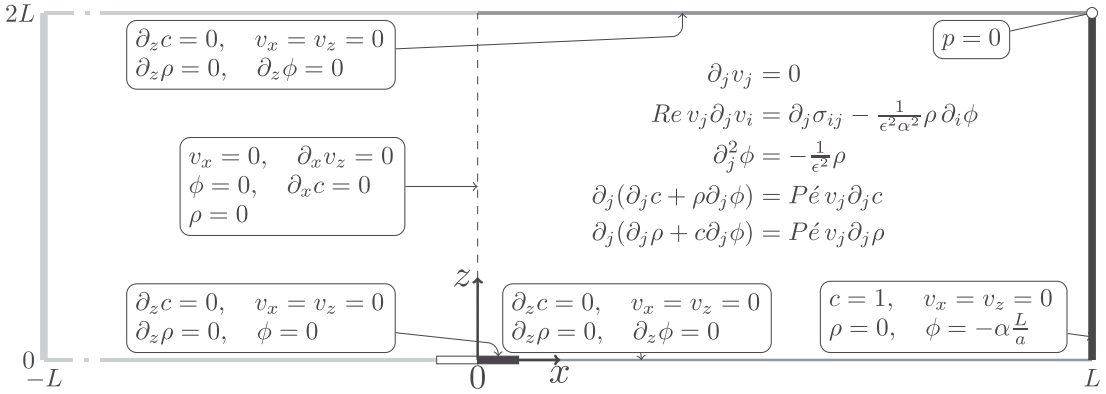

Figure 8.2: The dimensionfull governing equations and boundary conditions. Figure adapted from our paper [202].

Furthermore, we use the following as characteristic scales: the geometric half-length a of the metal strip, the bulk ion concentration c_0, the thermal voltage $V_\mathrm{T} = k_\mathrm{B}T/e$, and the pressure scale $p_0 = \eta v_0/a$. Using these scales the dimensionless variables (denoted by a tilde) become

$$\tilde{\boldsymbol{r}} = \frac{\boldsymbol{r}}{a}, \quad \tilde{c}_\pm = \frac{c_\pm}{c_0}, \quad \tilde{\phi} = \frac{\phi}{V_\mathrm{T}}, \quad \tilde{\boldsymbol{v}} = \frac{\boldsymbol{v}}{v_0}, \quad \tilde{p} = \frac{p}{p_0}. \tag{8.3}$$

We exploit the left-right symmetry in the problem by defining the salt concentration $c = (c_+ + c_-)/2$ and the charge concentration $\rho = (c_+ - c_-)/2$ with corresponding flux densities $\boldsymbol{J}_c = (\boldsymbol{J}_+ + \boldsymbol{J}_-)/2$ and $\boldsymbol{J}_\rho = (\boldsymbol{J}_+ - \boldsymbol{J}_-)/2$. The dimensionless form of the governing equations become for the ionic species,

$$\tilde{\boldsymbol{\nabla}} \cdot \tilde{\boldsymbol{J}}_c = \tilde{\boldsymbol{\nabla}} \cdot \tilde{\boldsymbol{J}}_\rho = 0, \tag{8.4a}$$

$$\tilde{\boldsymbol{J}}_c = -\tilde{\rho}\tilde{\boldsymbol{\nabla}}\tilde{\phi} - \tilde{\boldsymbol{\nabla}}\tilde{c} + Pe\, \tilde{c}\, \tilde{\boldsymbol{v}}, \tag{8.4b}$$

$$\tilde{\boldsymbol{J}}_\rho = -\tilde{c}\tilde{\boldsymbol{\nabla}}\tilde{\phi} - \tilde{\boldsymbol{\nabla}}\tilde{\rho} + Pe\, \tilde{\rho}\, \tilde{\boldsymbol{v}}, \tag{8.4c}$$

$$Pe = \frac{v_0 a}{D}, \tag{8.4d}$$

for the electrical potential,

$$\tilde{\nabla}^2 \tilde{\phi} = -\frac{\tilde{\rho}}{\epsilon^2}, \tag{8.5}$$

and for the velocity field,

$$\tilde{\boldsymbol{\nabla}} \cdot \tilde{\boldsymbol{v}} = 0, \tag{8.6a}$$

$$Re\, \left(\tilde{\boldsymbol{v}} \cdot \tilde{\boldsymbol{\nabla}}\right) \tilde{\boldsymbol{v}} = -\tilde{\boldsymbol{\nabla}}\tilde{p} + \tilde{\nabla}^2 \tilde{\boldsymbol{v}} - \frac{\tilde{\rho}}{\epsilon^2\, \alpha^2} \tilde{\boldsymbol{\nabla}}\tilde{\phi}, \tag{8.6b}$$

$$Re = \frac{\rho_\mathrm{m} v_0 a}{\eta}. \tag{8.6c}$$

The small dimensionless parameter $\epsilon = \lambda_\mathrm{D}/a$ expresses the relative thickness of the screening layer to the extent of the metal strip.

Boundary conditions We use the symmetry around the line $x = 0$ and consider only the right half ($0 < x < L$) of the domain. On the metal strip the boundary is impenetrable to ions, the potential is constant (zero due to symmetry), and the fluid velocity is zero,

$$\boldsymbol{n} \cdot \tilde{\boldsymbol{J}}_c = 0, \quad \boldsymbol{n} \cdot \tilde{\boldsymbol{J}}_\rho = 0, \quad \tilde{\phi} = 0, \quad \tilde{\boldsymbol{v}} = \boldsymbol{0}. \tag{8.7}$$

On the solid walls the boundary is impenetrable to ions and electrically insulating, and the fluid velocity is zero,

$$\boldsymbol{n} \cdot \tilde{\boldsymbol{J}}_c = 0, \quad \boldsymbol{n} \cdot \tilde{\boldsymbol{J}}_\rho = 0, \quad \boldsymbol{n} \cdot \tilde{\boldsymbol{\nabla}}\tilde{\phi} = 0, \quad \tilde{\boldsymbol{v}} = \boldsymbol{0}. \tag{8.8}$$

On the driving electrodes the ion concentrations are fixed to that in the bulk, the potential is set externally, and the fluid velocity is zero,

$$\tilde{c} = 1, \quad \tilde{\rho} = 0, \quad \tilde{\phi} = \frac{V_0}{V_\mathrm{T}} = \alpha\frac{L}{a}, \quad \tilde{\boldsymbol{v}} = \boldsymbol{0}. \tag{8.9}$$

Finally, the symmetries on the $x = 0$ boundary are even in the salt concentration, odd in the charge concentration, odd in the potential, and even in the fluid velocity field (no normal flow and no tangential stress),

$$\boldsymbol{n} \cdot \tilde{\boldsymbol{J}}_c = 0, \quad \rho = 0, \quad \tilde{\phi} = 0, \quad \boldsymbol{n} \cdot \tilde{\boldsymbol{v}} = 0, \quad \boldsymbol{t} \cdot \boldsymbol{\sigma} \cdot \boldsymbol{n} = 0, \tag{8.10}$$

where $\boldsymbol{t}$ is the tangential vector and sigma is the viscous stress tensor Eq. (2.31).

To numerically handle the strong non-linearity at high applied voltages we implement a reformulated version of the equations as shown in Section A.2.1.

8.2.1.2 Slip velocity models

Above we formulated the equations and boundary conditions for the full-nonlinear (FN) model in which the screening layer is fully resolved. The slip-models below have the advantage that the thin screening layer is modeled through effective boundary conditions. The slip-models employed here have in common the use of the standard Helmholtz–Smoluchowski velocity Eq. (2.36) and the assumption of a charge neutral bulk with uniform concentration. This simplifies the governing equations in that ionic transport is trivial, the Poisson equation reduces to the Laplace equation, and the electrical body force in the Navier–Stokes equations vanishes. The simplified equations for the electrical potential and the fluid velocity field become

$$\tilde{\nabla}^2\phi = 0, \tag{8.11a}$$

$$Re\left(\tilde{\boldsymbol{v}} \cdot \tilde{\boldsymbol{\nabla}}\right)\tilde{\boldsymbol{v}} = -\tilde{\nabla}\tilde{p} + \tilde{\nabla}^2\tilde{\boldsymbol{v}}, \tag{8.11b}$$

together with the continuity equation Eq. (8.6a).

We know from the symmetry of the problem that the "real" potential of the metal strip, below the boundary layer, is zero, whereby the induced zeta potential

is the negative of the electrical potential on the boundary $\zeta = -\phi$. This is used in the Helmholtz–Smoluchowski expression.

The problem has decoupled to a one-way coupling through the slip-condition from the electrostatic problem to the hydrodynamic problem. This has the advantage that the electrostatic problem can be solved independently and subsequently used to evaluate the hydrodynamic problem. The dimensionless Helmholtz–Smoluchowski slip condition on the metal strip is

$$\tilde{v}_{\mathrm{hs}} = \frac{1}{\alpha^2}\tilde{\phi}\,\partial_{\tilde{x}}\tilde{\phi}. \tag{8.12}$$

Linear slip (LS) model The linear slip (LS) model assumes that the charge in the screening layer on the metal strip is in static equilibrium and thus without flux of charge normal to the boundary layer. This leads to the insulation condition,

$$\boldsymbol{n}\cdot\tilde{\boldsymbol{\nabla}}\tilde{\phi} = 0. \tag{8.13}$$

Non-linear slip (NLS) model The non-linear slip (NLS) model takes into account dynamics of the induced charge on the metal strip. The dynamics in the screening layer also sets up gradients in the salt concentration [203, 204], but we neglect this chemi-osmotic effect here and leave it for future work.

In steady-state the surface divergence in the tangential surface current $\sigma_{\mathrm{el,s}}\partial_x\phi$ inside the screening layer is balanced by a normal current $\sigma_{\mathrm{el}}\partial_z\phi$ from the bulk,

$$0 = \boldsymbol{n}\cdot(\sigma_{\mathrm{el}}\boldsymbol{\nabla}\phi) + \boldsymbol{\nabla}_s\cdot(\sigma_{\mathrm{el,s}}\boldsymbol{\nabla}_s\phi)\,, \tag{8.14}$$

where $\sigma_{\mathrm{el,s}}$ is the surface conductivity and $\boldsymbol{\nabla}_s$ is the surface derivative (here equal to ∂_x).

The surface conductivity for a binary symmetric $Z{:}Z$ electrolyte relates to the screening length, the bulk conductivity, and the zeta potential [3],

$$\sigma_{\mathrm{el,s}} = 4\,\lambda_{\mathrm{D}}\sigma_{\mathrm{el}}(1+m)\sinh^2\left(\frac{Ze\zeta}{4\,k_{\mathrm{B}}T}\right), \tag{8.15}$$

in which the relative contribution of electro-osmotic-to-ohmic conduction is given by the dimensionless group

$$m = 2\frac{\varepsilon}{\eta D}\left(\frac{k_{\mathrm{B}}T}{Ze}\right)^2, \tag{8.16}$$

where in this case $m \approx 0.46$.

The dimensionless form of the current balance in Eq. (8.14) becomes

$$0 = \boldsymbol{n}\cdot\left(\tilde{\boldsymbol{\nabla}}\tilde{\phi}\right) + \tilde{\boldsymbol{\nabla}}_s\cdot\left(Du\,\tilde{\boldsymbol{\nabla}}_s\tilde{\phi}\right), \tag{8.17}$$

where

$$Du = \frac{\sigma_{\mathrm{el,s}}}{\sigma\,a} = 4\,\epsilon\,(1+m)\sinh^2\left(\frac{Ze\zeta}{4\,k_{\mathrm{B}}T}\right) \tag{8.18}$$

is the Dukhin (or Bikerman) number that indicates the relative importance of surface conduction.

Furthermore, since Eq. (8.17) is a differential equation to be solved on the metal-strip boundary it needs to be accompanied by boundary conditions. To this end, we assume that the surface current at the edges of the metal strip at $x = \pm a$ is zero,

$$Du\,\partial_{\tilde{x}}\tilde{\phi} = 0, \tag{8.19}$$

which is a reasonable as explained by Khair *et al.* [204].

For details regarding the numerical implementation using the weak form, see Section A.2.2.

8.3 Results

Our analysis is based on the three dimensionless parameters

$$\epsilon = \frac{\lambda_\mathrm{D}}{a}, \qquad \alpha = \frac{a}{L}\frac{V_0}{V_\mathrm{T}}, \qquad \beta = \frac{h}{a}, \tag{8.20}$$

which relate to the screening length λ_D, the applied voltage difference V_0, and the metal-strip height h, respectively. To quantify the strength of the ICEO flow we use the kinetic energy

$$E_\mathrm{kin} = \frac{1}{2}\rho_\mathrm{m}\int_\Omega \boldsymbol{v}^2\,\mathrm{d}x\mathrm{d}z, \tag{8.21}$$

as this measure is numerically well suited.

8.3.1 Zero height of the metal strip $\beta = 0$

We consider the electrode with zero height $\beta = 0$ in which case the kinetic energy $E_\mathrm{kin}^\mathrm{LS}$ in the linear-slip (LS) model is independent of the screening length.

The kinetic energy in the three models is shown relative to $E_\mathrm{kin}^\mathrm{LS}$ in Fig. 8.3 and to $E_\mathrm{kin}^\mathrm{FN}$ in Fig. 8.4 as a function of the (inverse) screening length $1/\epsilon$ for applied voltages in the linear $\alpha = 0.05$, weakly non-linear $\alpha = 0.5$, and strongly non-linear $\alpha = 5$ regime.

In the linear voltage regime $\alpha = 0.05$ the LS and NLS models overestimate the FN model by approximately the same factor for all screening lengths. Notably, even in this regime and for a relatively thin screening layer $1/\epsilon = 10^2$ the LS and NLS models still overestimate the kinetic energy by approximately a factor 1.2 (or 20 %). It takes a screening layer thinner than $\epsilon = 10^{-3}$ to have the LS and NLS models agree within a factor 1.01 (or 1 %) of the FN model.

In the weakly non-linear voltage regime $\alpha = 0.5$ the NLS model starts to improve toward the FN model for thick screening layers $\epsilon > 10^{-2}$. Still, for thin

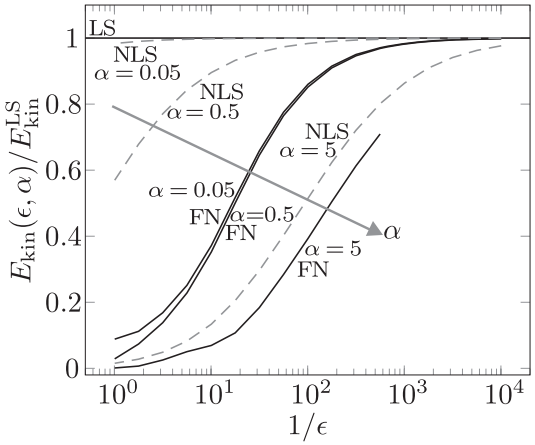

Figure 8.3: The dependence of the ICEO flow kinetic energy $E_{\rm kin}$ on the inverse screening length $1/\epsilon = a/\lambda_{\rm D}$ for three different applied voltages $\alpha = aV_0/(LV_{\rm T}) = 0.05$, 0.5, and 5. Figure adapted from our paper [202].

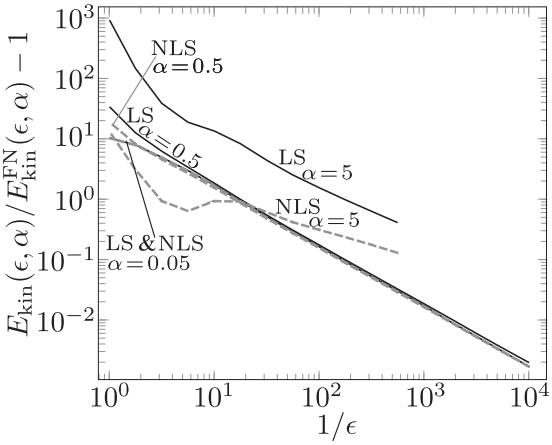

Figure 8.4: As in Fig. 8.3 but for the relative deviation in $E_{\rm kin}$ to that in the full nonlinear (FN) model. Figure adapted from our paper [202].

screening layers $\epsilon < 10^{-2}$ the conclusions are more or less the same as for the linear voltage regime.

In the strongly non-linear voltage regime $\alpha = 5$ the FN model did not converge for the thinnest screening layers $\epsilon < 10^{-3}$. In this case, the LS model overestimates considerably more than the NLS model compared to the FN model, especially for thick screening layers $10^{-1} < \epsilon < 10^{0}$. Quite remarkably, for thick screening layers, the LS model overestimates by a factor 10 to 10^3, whereas the NLS model has improved to only overestimate by approximately a factor 2. For the relatively thin screening layer $\epsilon = 10^{-2}$ the LS model overestimates by approximately a factor 3 (or 300 %) and the NLS model by a factor 1.4 (or 40 %).

Figure 8.5 shows the same data as above, the kinetic energy predicted by the LS and NLS models relative to that predicted by the FN model, as a function of the applied dimensionless voltage α.

For voltages in the linear regime $\alpha < 0.5$ the overestimate by the LS and NLS models is approximately the same for all screening lengths. Again, notably, for the relatively thin screening layer $\epsilon = 0.01$ the overestimate is by a factor of approximately 1.2 (or 20 %).

For voltages in the weakly non-linear and non-linear regimes $\alpha > 0.5$ the overestimate by the LS model increases rapidly with the voltage, and, remarkably, apparently even faster so for thinner screening layers. The NLS overestimate shows the same behavior for thin screening layers, and, notably, actually starts to improve with voltage for thick screening layers.

The overestimates by the LS and NLS models are surprisingly large. For a typical dimensionfull screening length of $\lambda_{\rm D} = 10\,{\rm nm}$ the dimensionless screening length of $\epsilon = 10^2$ corresponds to a metal-strip width of $2\,\mu{\rm m}$ comparable to Refs. [199, 205, 206].

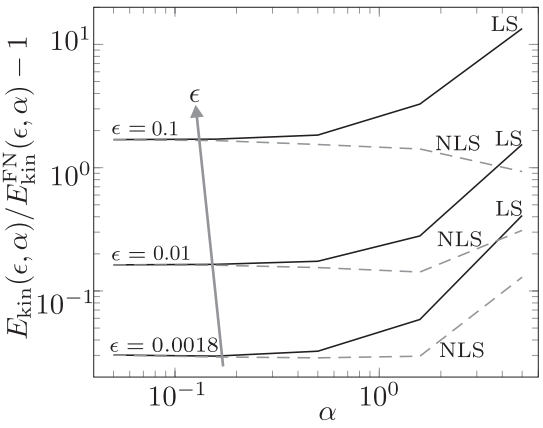

Figure 8.5: As in Fig. 8.3 but for the dependence on the voltage α for the screening lengths $\epsilon = 0.0018$, 0.01, and 0.1. Figure adapted from our paper [202].

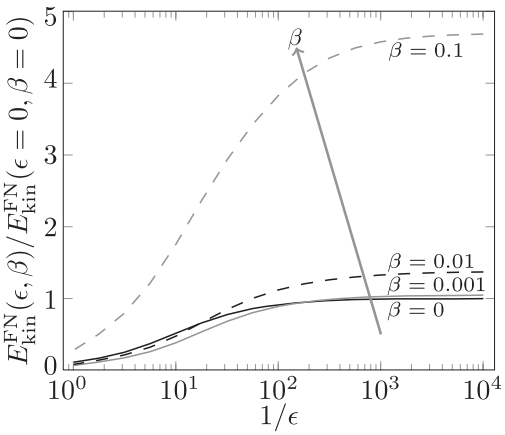

Figure 8.6: The dependence of $E_{\mathrm{kin}}^{\mathrm{FN}}(\epsilon,\beta)/E_{\mathrm{kin}}^{\mathrm{FN}}(\epsilon=0,\beta=0)$ on the inverse Debye length $1/\epsilon$ for four different electrode heights $\beta = h/a = 0$, 0.001, 0.01, and 0.1 for applied voltage $\alpha = 0.1$. $E_{\mathrm{kin}}^{\mathrm{FN}}(\epsilon=0,\beta=0)$ is taken as $E_{\mathrm{kin}}^{\mathrm{LS}}(\beta=0)$. Figure adapted from our paper [202].

8.3.2 Finite height of the metal strip $\beta > 0$

Above we studied how the finite thickness of the screening layer leads to a surprisingly large overestimate by common ICEO slip-velocity models. It is also of interest to investigate how the finite thickness of the metal strip affects the predicted ICEO flow. Experimentally, a metal strip can be fabricated by evaporation techniques and it typically has a thickness on the order of 20 nm to 200 nm. Relative to a metal-strip width of $a \approx 2\,\mu\mathrm{m}$ this leads to a dimensionless height in the range of $10^{-2} < \beta < 10^{-1}$.

Figure 8.6 shows the relative kinetic energy $E_{\mathrm{kin}}^{\mathrm{FN}}(\epsilon,\beta)/E_{\mathrm{kin}}^{\mathrm{FN}}(\epsilon=0,\beta=0)$ as a function of the screening layer thickness for four metal-strip heights and for linear voltage $\alpha = 0.1$. Note that the kinetic energy for zero metal-strip height and an infinitely thin screening layer corresponds to the LS model $E_{\mathrm{kin}}^{\mathrm{FN}}(\epsilon=0,\beta=0) = E_{\mathrm{kin}}^{\mathrm{LS}}(\beta=0)$. For zero height $\beta = 0$ the curve corresponds to those in Fig. 8.3.

For relatively small heights of the metal strip $10^{-3} < \beta < 10^{-2}$ the flow becomes slightly weaker for thick screening layers $\epsilon > 10^{-2}$ and slightly stronger for thin screening layers $\epsilon < 10^{-2}$.

For a relatively high metal strip $\beta = 0.1$ the flow is enhanced by approximately a factor 5 for all screening lengths. We speculate that this enhancement may be due to an increased electric field strength around the curved corner of the raised metal strip as compared to the flat metal strip.

In conclusion, we have investigated the accuracy of two common electroosmotic slip velocity models in the context of ICEO. The slip models assume an infinitely thin screening layer and we compare them in terms of the kinetic energy in the flow to a numerical simulation fully resolving the boundary layer.

As a function of the screening layer thickness and the applied voltage, we show to which degree the slip models agrees with the full model.

The overestimation of the energy is surprisingly large in the linear voltage regime for both models. For the linear voltage $\alpha = 0.05$ the overestimation is 20 % for the relatively thin screening layer thickness $\lambda_D/a = 10^{-2}$. The advanced slip model takes surface conduction into account and performs better for higher voltages where it even improves in the limit of thick screening layers. Still, for thick screening layers and high voltages the linear slip model overestimates the full model by a factor of 10 to 10^3.

Finally, we show that the effect of including a finite height of the metal strip is a general amplification of the flow compared to a metal strip of zero height.

Chapter 9

Conclusion and outlook

Conclusion

We have successfully applied our model framework to different phenomena in nanofluidics and ion-selective membranes. Our model framework consists of the coupling of electrostatics, ionic transport, hydrodynamics, bulk solution equilibrium chemistry, and surface equilibrium chemistry.

First, we applied our model in bare and cyanosilane coated nanochannels, and compared against two independent types of experiments. We adjusted the low-value surface dissociation constant and the Stern layer capacitance, and we obtained good agreement with the experimentally measured zeta potential and capillary dark-to-bright length-ratio (interpretable as the surface charge density).

Second, we applied the model to 2D nanochannels and modeled the surface chemistry by an effective boundary condition along the perimeter of the channel cross-section. We used the previously found values for the adjustable parameters, and obtained good agreement between the model and the experimentally measured zeta potential and streaming current. In addition, we used the model together with transient measurements of increasing streaming current to predict dissolution rates in silica nanochannels.

Third, we used our model to predict a conductance minimum in nanochannels filled with dilute electrolytes. Our model shows that hydronium is responsible for the minimum, and it also shows that dissolved carbonic acid from atmospheric CO_2 plays an essential role in this regard. We performed experiments that conformed with the model predictions. Furthermore, we showed that the conductance minimum has been experimentally measured in several independent studies in the literature.

Fourth, we applied our model framework to ion-selective membranes, and predicted a new mechanism for over-limiting current called current-induced membrane discharge (CIMD). Our model shows that over-limiting currents can be due

to a chemically induced loss of ion-selectivity even in the absence of fluid flow. Our model even predicts that the extended space charge layer responsible for the electro-osmotic instability is suppressed. CIMD is a novel and strong alternative to the interpretation of over-limiting currents.

Finally, we digressed a bit from dynamic surface charge, and looked at the effect of a finite Debye length in induced-charge electro-osmosis. We did this by comparing two common slip-velocity models to a full boundary-layer resolving model. The slip models are strictly only correct in the limit of a vanishing Debye length, and we showed surprisingly large deviations to the full model even at relatively thin screening layers.

All together, we have tested our model framework against diverse nanofluidic phenomena. Our unified model framework has thus proved itself valuable and should be developed and tested further. Specifically, our model has shown the importance of considering the coupling of electrostatics, ionic transport, hydrodynamics, bulk solution equilibrium chemistry, and surface equilibrium chemistry.

The combination of unified models with well-controlled experiments makes a huge potential for discovering and explaining fundamental phenomena in nanofluidics and its related scientific disciplines.

Outlook

In relation to over-limiting current through ion-selective membranes, we are currently pursuing a 1D model in which we account for the presence of microchannel walls outside the membrane. This corresponds to have a porous media with large pores, such as a porous frit, in connection with the fine porous membrane. With dynamic surface charge, the model will be able to test the recent prediction of over-limiting current due to microchannel surface charge conduction in this type of system [154].

Moreover, we are planning to expand the 1D model to 2D to allow for non-laminar fluid flow in the channel. We expect that as the microchannel height increases, advection will start to become significant in the local region of ion-depletion next to the membrane. For this to be numerically feasible, we have developed a 1D-2D scheme where only the ion-depleted low-concentration thick-screening-layer part of the microchannel is modeled in 2D. Thus, the scheme dynamically and self-consistently determines the 1D-2D domain boundary.

It is also interesting to look at the transient response of dynamic charge systems. We have implicitly touched upon this in Chapter 4 in the transient setting of capillary filling. However, in that work, the small transverse direction in the cross-section of the channel leads to instant equilibrium. Instead, it would be interesting to investigate the time scale for steady-state to occur and the transient effect of (de-)protonation in the membrane. If the time scale for steady-state is very long, this could lead to interesting transient effects such as the desalination shocks observed in similar systems [48, 49, 51, 172].

Moreover, another possibility is to make a combined study of the over-limiting

current in Chapter 7, the surface transport in nanochannels in Chapter 6, and the multispecies transport at chemical equilibrium described in Section 2.6.1. This would allow for a detailed investigation of the effect of absorbed CO_2 in complex electrodialysis systems with ion-depletion and strong pH variations.

Appendix A

Main text appendices

A.1 Nanochannels: Surface-dependent thermodynamic constants

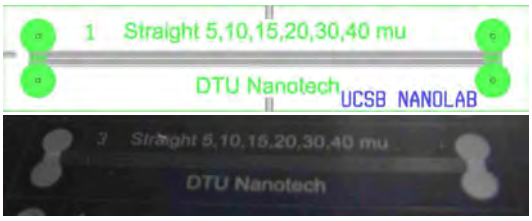

(a) Nanochannel chip; mask design (top) and photo (bottom).

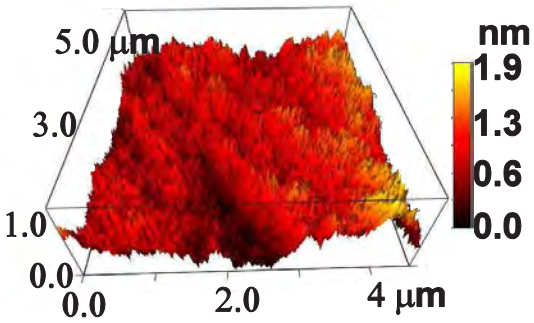

(b) Example of AFM measured surface roughness in the reservoir on a cyanosilane coated chip.

(c) Example of DI water on bare silica slide.

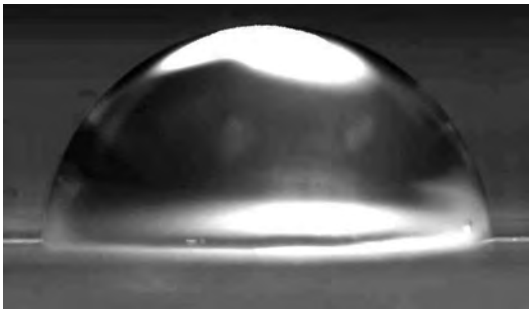

(d) Example of DI water on cyanosilane coated silica slide.

Figure A.1: Figures adapted from our paper [76].

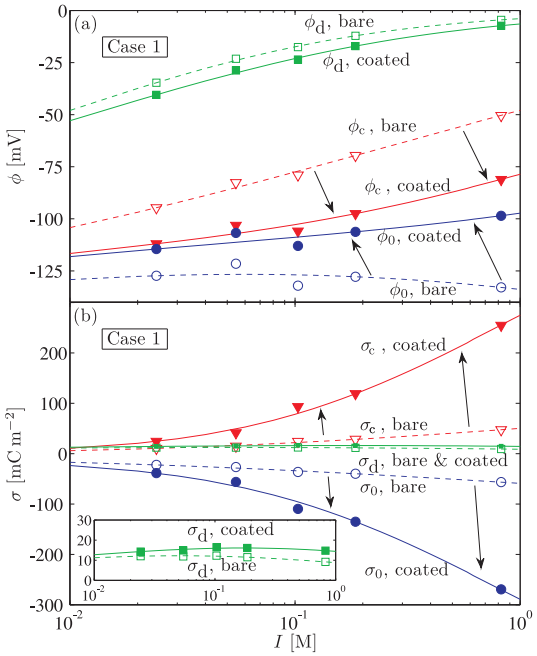

Figure A.2: As in Fig. 4.12 but using the parameters for the case "Case 1". Figure adapted from our paper [76].

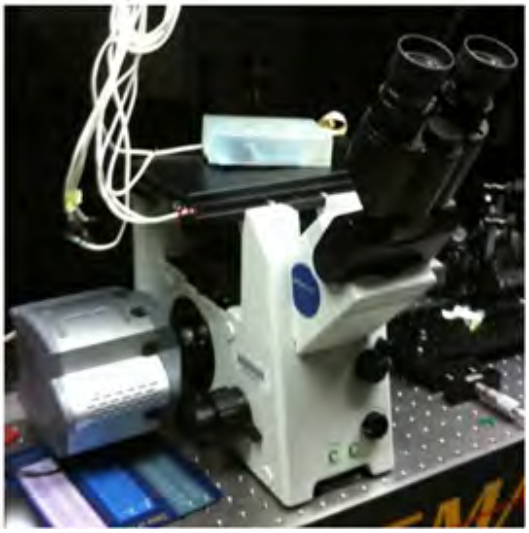

Figure A.3: Photo of the experimental setup described in Chapter 4 showing the microscope with CCD camera attached into its left side and the electrical connections for the chip going into a white, protective box placed on the top stage with optical access from below (inverted microscopy). Figure adapted from our paper [76].

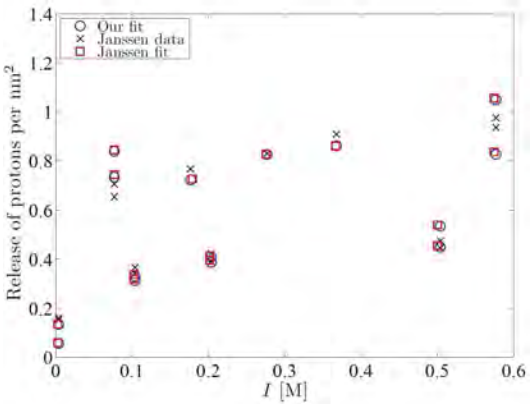

Figure A.4: Benchmark of the model described in Chapter 4 against that of Janssen *et al.* [74] showing that our model (blue circles) reproduces the result of the Janssen model (red squares) when simplified to the Janssen-model and fitted to the same experimental data (black crosses). Figure adapted from our paper [76].

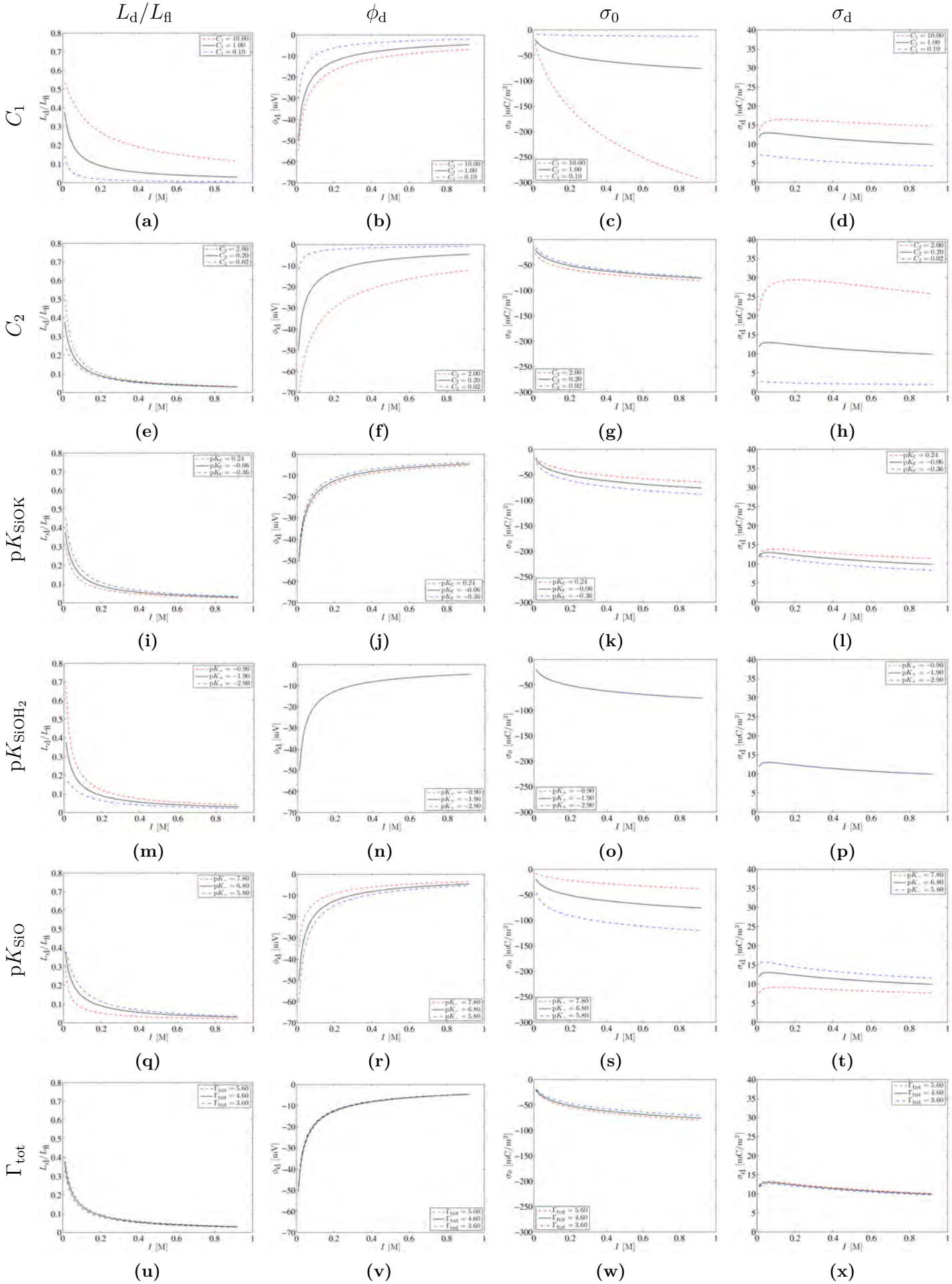

Figure A.5: Parametric study of the dependence of L_d/L_{fl}, ϕ_d, σ_0, and σ_d (top "row") on the ionic strength I and variations in C_1, C_2, pK_{SiOK}, pK_{SiOH_2}, pK_{SiO}, and Γ_{tot} (leftmost "column") around the base state $\{1\,\mathrm{F\,m^{-2}}$, $0.2\,\mathrm{F\,m^{-2}}$,-0.06, -1.9, 6.8, $4.6\,\mathrm{m^{-2}}\}$ in the model described in Chapter 4. Figures adapted from our paper [76].

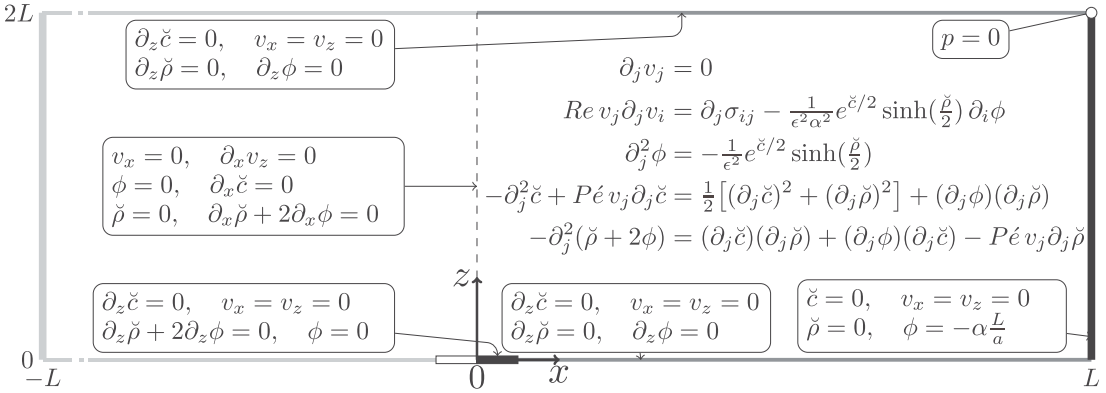

Figure A.6: The dimensionless governing equations and boundary conditions. Figure adapted from our paper [202].

A.2 ICEO: finite Debye-length effects

A.2.1 Strongly non-linear regime

At large driving voltages there is strong depletion of the ions on the metal strip with the concentration being very small which is a problem numerically due to round-off errors. We overcome this issue by transforming logarithmically the concentrations to new (computational) fields $\bar{c}_\pm$ using the relations

$$\bar{c}_\pm = \log\left(\frac{c_\pm}{c_0}\right), \tag{A.1a}$$

$$c_\pm = c_0 \exp\left(\bar{c}_\pm\right). \tag{A.1b}$$

Again, to exploit the symmetry we define the fields $\bar{c} = \bar{c}_+ + \bar{c}_-$ and $\bar{\rho} = \bar{c}_+ - \bar{c}_-$ and the transformed equations become

$$\tilde{\nabla}^2 \bar{c} = Pe\, \tilde{\boldsymbol{v}} \cdot \tilde{\boldsymbol{\nabla}} \bar{c} - \frac{1}{2}\left[\left(\tilde{\boldsymbol{\nabla}} \bar{c}\right)^2 + \left(\tilde{\boldsymbol{\nabla}} \bar{\rho}\right)^2\right] - \tilde{\boldsymbol{\nabla}} \tilde{\phi} \cdot \tilde{\boldsymbol{\nabla}} \bar{\rho}, \tag{A.2a}$$

$$\tilde{\nabla}^2 \left(\bar{\rho} + 2\,\tilde{\phi}\right) = Pe\, \tilde{\boldsymbol{v}} \cdot \tilde{\boldsymbol{\nabla}} \bar{\rho} - \tilde{\boldsymbol{\nabla}} \bar{c} \cdot \tilde{\boldsymbol{\nabla}} \bar{\rho} - \tilde{\boldsymbol{\nabla}} \tilde{\phi} \cdot \tilde{\boldsymbol{\nabla}} \bar{c}, \tag{A.2b}$$

$$\tilde{\nabla}^2 \tilde{\phi} = -\frac{1}{\epsilon^2} \exp\left(\frac{\bar{c}}{2}\right) \sinh\left(\frac{\bar{\rho}}{2}\right), \tag{A.2c}$$

$$Re\, \left(\tilde{\boldsymbol{v}} \cdot \tilde{\boldsymbol{\nabla}}\right) \tilde{\boldsymbol{v}} = -\tilde{\nabla} \tilde{p} + \tilde{\nabla}^2 \tilde{\boldsymbol{v}} - \frac{1}{\epsilon^2 \alpha^2} \exp\left(\frac{\bar{c}}{2}\right) \sinh\left(\frac{\bar{\rho}}{2}\right) \tilde{\boldsymbol{\nabla}} \tilde{\phi}, \tag{A.2d}$$

while the continuity equation (8.6a) remains the same. The transformed equations and boundary conditions are summarized in A.6.

A.2.2 Weak-form implementation

We implement the reformulated equations (A.2) using second order Lagrange elements for all field variables, except the pressure for which we use first order Lagrange elements.

The Helmholtz–Smoluchowski slip condition is a one-way coupling from the electrical potential to the fluid velocity. Numerically, we account for the one-way coupling by making an asymmetric implementation where the reaction force is applied entirely to the fluid field test function. One way to do this is to explicitly introduce the reaction force, here the tangential viscous stress, on the metal strip as Lagrange multipliers f_i,

$$f_i = \sigma_{ij} n_j. \tag{A.3}$$

We follow the strong-to-weak reformulation procedure in Section 3.2 and obtain for the Navier–Stokes equation after moving the divergence of the viscous stress tensor to the boundary (here tilde refers to test functions)

$$\int_{\partial\Omega} \tilde{v}_i \sigma_{ij} n_j \,\mathrm{d}s. \tag{A.4}$$

We then introduce the Lagrange multiplier in Eq. (A.3) on the part of the boundary $\partial\Omega_{\mathrm{ms}}$ that constitute the metal strip and obtain

$$\int_{\partial\Omega_{\mathrm{ms}}} \tilde{v}_i \sigma_{ij} n_j \,\mathrm{d}s = \int_{\partial\Omega_{\mathrm{ms}}} \left[\tilde{v}_i f_i + \tilde{f}_i \left(v_i - v_{\mathrm{hs},i} \right) \right] \mathrm{d}s, \tag{A.5}$$

which illustrates the weak form implementation of the Helmholtz–Smoluchowski slip boundary condition.

The implementation of the current-balance condition in Eq. (8.17) $n_i \partial_i \phi = -\partial_s \left(Du \, \partial_s \phi \right)$ is done by considering the metal-strip boundary after the divergence of the electric field has been moved from the bulk to the boundary

$$\begin{aligned} \int_{\partial\Omega_{\mathrm{ms}}} \tilde{\phi} n_i \partial_i \phi \,\mathrm{d}s &= -\int_{\partial\Omega_{\mathrm{ms}}} \tilde{\phi} \, \partial_s \left(Du \, \partial_s \phi \right) \mathrm{d}s \\ &= -[\tilde{\phi} \, Du \, \partial_s \phi]_{x=-a}^{x=+a} + \int_{\partial\Omega_{\mathrm{ms}}} \left(\partial_s \tilde{\phi} \right) \left(Du \, \partial_s \phi \right) \mathrm{d}s, \end{aligned} \tag{A.6}$$

where it is straight forward to employ the condition of zero tangential current at the edge in Eq. (8.19).

We made sure the numerical simulation were sufficiently converged using a mesh adaptation routing. This routine calculates the problem several times for the same parameters, each time refining the mesh based on an error estimate such that regions with the highest error are refined the most.

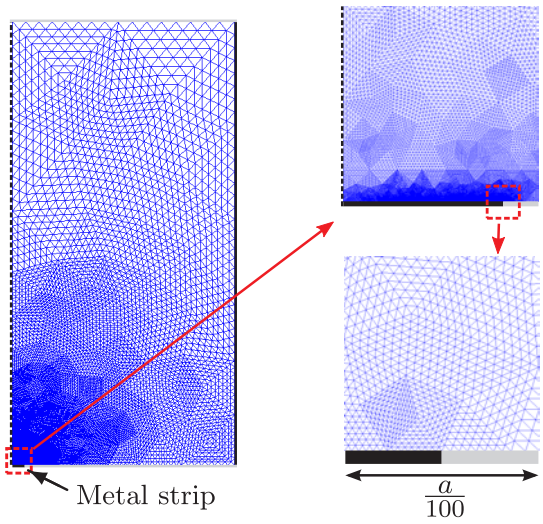

Figure A.7: The finite element mesh in the right half of the chamber used for numerical simulation.

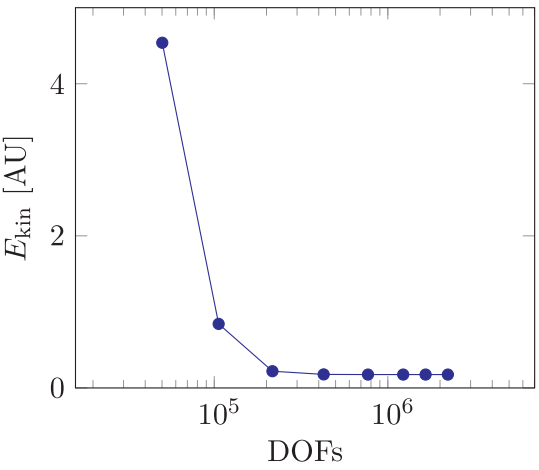

Figure A.8: The convergence of the kinetic energy in the chamber with increasing degrees of freedom (DOFs).

Figure A.7 shows the mesh after some iterations of the mesh adaptation routine. Note the very fine mesh on the metal strip and especially around its corner. Figure A.8 shows the convergence of the kinetic energy with increasing degrees of freedom (DOFs). We quantify relative differences down to 10^{-3} and we therefore made sure that all solutions were converged to within 10^{-5}. All simulations ended with more than 10^6 DOFs.

A.3 Matlab scripts

Matlab script; Surface-dependent thermodynamic constants

```
% Self consistent surface charge model MBA 2012-02-18
clear all, close all, format short g % initialize workspace

% parameters
c_KPh_b = 5e-3; % Potassium phosphate salt [M]
c_NaFl_b = 1e-5; % Sodium fluorescein salt [M]
pH_b = 7.2; % buffers were titrated to this pH
eps_r = 78; % relative permitivity
T = 295; % room temp [K]
eps_0 = 8.854e-12; % vacuum permittivity [F/m]
NA = 6.022e23; % avagodros constant [1/mol]
e = 1.602e-19; % elementary charge [C]
kB = 1.381e-23; % boltzman constant [J/K]
c_ref = 1; % reference concentration [M]
h = 135e-9; % height of channel [m]
w = 20e-6; % width of channel [m]
INP={
[-1  37.7e-9  2.15  -2 59.7e-9 7.21  -3 97.3e-9 12.33 ]; % phosphoric acid
[ 1  22.0e-9  2.22  -1 25.0e-9 4.34  -2 49.5e-9  6.68 ]; % fluorescein
[ 1  51.9e-9 14.0                                     ]; % sodium hydroxide
[ 1  76.2e-9 14.0                                     ]; % potassium hydroxide
[-1 -79.1e-9 -7.0                                     ]; % hydrochloric acid
};
c_Ph_b = c_KPh_b; % Phosphoric acid concentration in bulk [M]
c_Fl_b = c_NaFl_b; % Fluorescein concentration in bulk [M]
c_K_b = c_KPh_b; % K concentration in bulk [M]
c_Na_b = 2*c_NaFl_b; % Na concentration in bulk [M]
c_HCl_b =  0; % HCl concentration in bulk [M]
c_tot = [c_Ph_b,c_Fl_b,c_Na_b,c_K_b,c_HCl_b]; % bulk concentrations [M]
G_tot = 4.6e18; % surface site density [1/m^2]
C_1 = 0.77; % surface capacitance [F/m^2]
C_2 = 0.2; % surface capacitance [F/m^2]
pK_K = -0.06; % K surface adsorption constant
K_K = 10.^(-pK_K); % K surface adsorption constant
pK_1 = -1.61; % H surface adsorption constant
pK_2 = 6.8; % H surface adsorption constant
K_1 = 10^(-pK_1); % H surface adsorption constant
K_2 = 10^(-pK_2); % H surface adsorption constant
pH_pzc = (pK_1+pK_2)/2; % point of zero charge

% solve added KOH to titrated to pH_b
obj_fun1 = @(x)ITPcalculator_mod(INP,c_tot+[0 0 0 x 0])-pH_b; % define function
c_KOH_phb = fzero(obj_fun1,7); % use fzero to obtain KOH-titration quantity
[pH, Is, zMat, cizMat] = ITPcalculator_mod(INP,c_tot...
    +[0 0 0 c_KOH_phb 0]); % obtain composition at phb

% expressions and equations
% x = [ phi3 , cH1 , sigma3 ]
phi2 = @(x) x(1)-x(3)/C_2; % expression
cK2 = @(x) (c_K_b+c_KOH_phb)*exp(-e*phi2(x)/(kB*T)); % expression
Gsioh = @(x) G_tot*(1+K_2/x(2)+x(2)/K_1+K_K*K_2*cK2(x)/x(2))^(-1); % expression
Gsioh2 = @(x) x(2)*Gsioh(x)/K_1; % expression
Gsio = @(x) K_2*Gsioh(x)/x(2); % expression
Gsiok = @(x) K_K*Gsio(x)*cK2(x); % expression
sigma1 = @(x) e*(Gsioh2(x)-Gsio(x)-Gsiok(x)); % expression
phi1 = @(x) phi2(x)+sigma1(x)/C_1; % expression
sigma2 = @(x) e*Gsiok(x); % expression
sub_sum = @(x) 10^(-pH)*(exp(-e*x(1)/(kB*T))-1)+10^(pH-14)*(exp(+e*x(1)/(kB*T))-1); % contribu-...
    % tion to Grahame from H and OH
eq_grahame = @(x) x(3)^2-2*eps_r*eps_0*kB*T*1000*NA*(sum(sum(cizMat.*(exp(-e*zMat*x(1)/(kB*T))...
    -1)))+sub_sum(x)); % Grahame
eq_1 = @(x) sigma1(x)+sigma2(x)+x(3); % equation
eq_2 = @(x) x(2)-10^(-pH)*exp(-e*phi1(x)/(kB*T)); % equation

% solve equations
obj_fun2 = @(x)[eq_grahame(x);eq_1(x);eq_2(x)]; % define objective function
sol = fsolve(obj_fun2,[-1e-3,1e-7,1e-5]); % use fsolve
phi3 = sol(1); % extract solution
cH1 = sol(2); % extract solution
sigma3 = sol(3); % extract solution

% check if fundamental equations are satisfied
chk(1) = C_1*(phi2(sol)-phi1(sol)) - (-sigma1(sol));
chk(2) = C_2*(phi3-phi2(sol))-sigma3;
chk(3) = eq_grahame(sol);
chk(4) = K_K - Gsiok(sol)/(Gsio(sol)*cK2(sol));
chk(5) = K_1 - Gsioh(sol)*cH1/Gsioh2(sol);
chk(6) = K_2 - Gsio(sol)*cH1/Gsioh(sol);
chk(7) = cH1 - 10^(-pH)*exp(-phi1(sol)/(kB*T/e));
chk(8) = cK2(sol) - c_K_b*exp(-phi2(sol)/(kB*T/e));
chk(9) = (G_tot - (Gsioh(sol)+Gsioh2(sol)+Gsio(sol)+Gsiok(sol)))/G_tot;
chk(10) = sigma1(sol)+sigma2(sol)+sigma3;
chk(11) = sigma1(sol) - e*(Gsioh2(sol)-Gsio(sol)-Gsiok(sol));
chk(12) = sigma2(sol) - e*Gsiok(sol);

% solve for Bs and length ratio
obj_fun3 = @(x)ITPcalculator_mod(INP,c_tot+[0 0 0 c_KOH_phb x])-pH_pzc; % define func
c_HCl_pzc = fzero(obj_fun3,1e-3); % use fzero to obtain HCl-titration quantity (also =Bs)
[pH_pzc_num, Is_pzc, zMat, cizMat_pzc] = ITPcalculator_mod(INP,c_tot+...
    [0 0 0 c_KOH_phb c_HCl_pzc]); % obtain composition at pzc
Bs = sum(sum(zMat(1:end-1,:).*(cizMat_pzc(1:end-1,:)-cizMat(1:end-1,:))))+10^(-pH_pzc)...
    -10^(-pH); % obtain Bs (remember to exclude "virtual" HCl and add H/pH)
Ld_Lfl = -2*(1+h/w)*sigma1(sol)/(e*1000*NA*Bs*h); % obtain length ratio
fprintf('Is=%3.2g, LdLfl=%3.2g\n',Is,Ld_Lfl)
```

Matlab script; Ionic equilibria ITPcalculator

```
% Calculate Equilibrium Reactions
% Moran Bercovici, v1.0 May 2008: First version
% Moran Bercovici, v1.1 Feb 2009: Comments added
% MBA, Feb 2012: slight modification

function [pH, Is, zMat, cizMat] = ITPcalculator_mod(INP,cTot)
% close all;
% clc;
format short g

global F Rmu Temp Kw muH muOH
global met2lit

% INPUT DATA
%-------------------------------------------------------------------------
%-------------------------------------------------------------------------
% Input sructure consists of [valence, mobility, pKa] triplets
% the order or triplets doesn't matter (ok to go from z=-1 to z=2 or vice versa).
%         z    mu [m^2/Vs]        pKa
% INP={
% [-1 3.77e-8 2.15  -2 5.97e-8 7.21  -3 9.73e-8 12.33]; % phosphoric acid
% };
% Total concentration for each species
% cTot=[10e-3]; % Total concentration [M]
%-------------------------------------------------------------------------
%-------------------------------------------------------------------------

% Define constants
F=9.65E4; % Faraday's const.[C/mol]
Rmu=8.31; % Universal gas const. [J/mol*K]
Temp=295; % Temperature [K]
Kw=1E-14; % Water equilibrium constant
muH=362E-9/F; % Mobility of Hydronium   % [m^2/s*V]/F --> [mol*s/Kg]
muOH=205E-9/F; % Mobility of Hydroxide   % [m^2/s*V]/F --> [mol*s/Kg]
met2lit=1000;

% Call Equilibrium Solution routine
```

```
[cH,zMat,muMat,muMat2,muEffVec,cizMat]=SolveEquilibrium(INP,cTot);
pH = -log10(cH); % output pH

% loop on all species
for ij=1:size(cizMat,1)
    % Create vector to be displayed
    DispVec(1:2:2*size(cizMat,2)-1)=zMat(ij,:); % Every odd entry will show the valence
    DispVec(2:2:2*size(cizMat,2))=cizMat(ij,:); % Every even entry will show the concentration ...
        corresponding to the valence
end %for ij

Is = sum(diag(zMat.^2*cizMat')); % ionic strength
Is = (Is+cH+Kw/cH)/2; % add contribution from protons and hydroxide ions

% calculate conductivity based on ionic mobilities
sigma = 0;
for ii=1:size(cizMat,1)
    sigma = sigma + sum(abs(zMat(ii, :)).*muMat2(ii, :).*cizMat(ii, :)*met2lit)*F;
end %for ii

%-------------------------------------------------------------------------
function [cH,zMat,muMat,muMat2,muEffVec,cizMat]=SolveEquilibrium(INP,cTot)
global F Rmu Nspecies Temp Kw

% INPUT: INP  - Structure, Containing the valence, mobility and pKa of each species
%        cTot - Vecotr, containing the concentration [mol/lit] of each species
% OUTPUT: cH   - Scalar, concentration of hydronium ions  ( pH = -log10(cH) )
%         zMat  - Matrix, every row corresponds to a difrernt species and contains valence ...
    values for that species
%         muMat - Matrix, every row corresponds to a difrernt species and contains mobility ...
    values for that species
%         muEff - Vector, effective mobility values for all species
%         cizCube - Matrix, concentration values. Every row correponds to a different species.
%         every columns corresponds to a differnt valence within that species.

Nspecies=size(INP,1);

% PREPARE L Matrix
%-----------------
% Calculate the number of columns required for the matrix.
% this is determined by the maximum value of (p_i - n_i) for all species
% p_i - n_i = difference between most positive and most negative valence.
MaxCol=-Inf;
for j=1:size(INP,1)
    MaxCol=max([MaxCol,max(INP{j}(1:3:end))-min(INP{j}(1:3:end))+1]);
end
% Initialize matrices to zero
LMat=zeros(size(INP,1),MaxCol);
zMat=LMat; muMat=LMat; muMat2=LMat; KaMat=LMat; DMat=LMat;

% Loop on species
for j=1:Nspecies
    zList=INP{j}(1:3:end); % Get list of valences
    muList=INP{j}(2:3:end)./(F*abs(zList)); % Get list of normalized mobilities
    muList2=INP{j}(2:3:end); % Get normal mobilities
    pKaList=INP{j}(3:3:end); % Get list of pKa
    KaList=10.^(-pKaList); % Create list of Ka
    DList=Rmu*Temp*muList; % Creale list of diffusivities using Nernst-Einstein relation

    [zList,Index]=sort(zList); % Sort the valence in increasing order, and get indices
    KaList=KaList(Index); % Use indices to sort the other list in a consistent order
    muList=muList(Index);
    muList2=muList2(Index);
    DList=DList(Index);

    Ip1=find(zList==1);     Im1=find(zList==-1); % Find indices where the valence value is +1 ...
        and -1 (at least one of these valences must always for any species used).
    zList  = [zList(1:Im1),0,zList(Ip1:end)]; % Add the neutral state to the list of valence, ...
        between negative and positive values
    muList = [muList(1:Im1),0,muList(Ip1:end)]; % Add the value of mobility corresponding to ...
        the neutral state (zero)
    muList2 = [muList2(1:Im1),0,muList2(Ip1:end)]; % Add the value of mobility corresponding to ...
        the neutral state (zero)
    DList  = [DList(1:Im1),mean(DList),DList(Ip1:end)]; % Assign the neutral state a ...
        diffusivity which is the average of all other diffusivities
    KaList = [KaList(1:Im1),1,KaList(Ip1:end)]; % 1 added to the list of Ka values for math ...
        reasons (see formulation for 'L' matrix)

    zMat(j,1:length(zList))=zList; % Put all lists into corresponding matrices.
    muMat(j,1:length(muList))=muList; % Each row in the matrix corresponds to a different species
    muMat2(j,1:length(muList2))=muList2; % Each row in the matrix corresponds to a different ...
        species
    KaMat(j,1:length(KaList))=KaList;
    DMat(j,1:length(DList))=DList;

    zListArranged{j}=zList;
    % Get minimum and maximum valences for this species
    % and construct the matrix L
    nj=min(zList);    pj=max(zList);
    for z=zList
        if z<0
            LMat(j,z-nj+1)=prod(KaList(z-nj+1:-nj));
        elseif z>0
            LMat(j,z-nj+1)=1/prod(KaList(-nj+2:z-nj+1));
        elseif z==0
            LMat(j,z-nj+1)=1;
        end %if
    end % for z

end %for ij

% CONSTRUCT POLYNOMIALS
%----------------------
% Construct the polynomial Q by multiplying all the polynomials in the
% matrix L (all rows). Multiplying polynomials is equivalent to convolving
% their vectors of coefficients
Q1=1;
for j=1:size(LMat,1)
    Q1=conv(Q1,LMat(j,:));
end %for j
Q2=[-Kw 0 1];
Q=conv(Q1,Q2);

% Construct the polynomials Pi
% Loop on all species
for i=1:Nspecies
    LMatMod=LMat; % Defined Modified L Matrix, initially identical to L Matrix
    LMatMod(i,:)=LMat(i,:).*zMat(i,:); % Modify just the row i

    % convolve all rows in the LMatMod to construct the polynomial
    Pi=1;
    for kl=1:size(LMatMod,1)
        Pi=conv(Pi,LMatMod(kl,:));
    end %for j
    Pi=conv([0 1],Pi);
    PMat(i,:)=Pi; % Insert all polynomials Pi as rows in the matrix PMat
end %for i

cTotMat=repmat(cTot',1,size(PMat,2)); % All the enries in each row are identical and equal to ...
    the total concentration of that specie
P=sum(cTotMat.*PMat,1); % The polynomial P is the sum of c_i * P_i

Poly=PolSum(P,Q); % Construct the final polynomial as the sum of P and Q
roo=roots(fliplr(Poly)); % Find all roots of the polynomial
roo=roo(imag(roo)==0); % Eliminate complex solutions
cH=roo(roo>0); % Choose the positive solution. Note that cH is in mol/lit

PolDeg=size(LMat,2); % Polynomial degree
cHPolVec=[1;cumprod(ones(PolDeg-1,1)*cH,1)]; % Create vector of cH Powers (cH^0, cH^1, ... , ...
    cH^(PolDeg-1))
cHMatPower=repmat(cHPolVec',[Nspecies,1]); % Replicate powers vector to create matrix
M1Mat=repmat(cTot'./(LMat*cHPolVec),[1,PolDeg]); % Temporarty matrix (see formulation for c_i_z)
cizMat=LMat.*cHMatPower.*M1Mat; % Calculate concentration of each ionic state (valence) of each ...
    species
muEffVec=F*sum(cizMat.*muMat.*zMat,2)./cTot'; % Calculate effective mobility

% Sum arbitrary length polynomials
%---------------------------------------------------
function out=PolSum(P1,P2)
% This essentially pads the shorter vecotr with zeros, and then sums the
```

```
% two vectors
Psize=max(length(P1),length(P2)); % get the length of the largest polynomial
P1out=zeros(1,Psize); P2out=P1out; % Set temporary vectors of size Psize to zero.
```

```
P1out(1:length(P1))=P1; % Inject P1 values into temporar vector
P2out(1:length(P2))=P2; % Inject P2 values into temporar vector
out=P1out+P2out; % sum both vectors
```

Appendix B

Paper published in J Colloid Interface Sci

M. B. Andersen, J. Frey, S. Pennathur, and H. Bruus, Surface-dependent chemical equilibrium constants and capacitances in bare and 3-cyanopropyldimethylchlorosilane coated silica nanochannels, J Colloid Interface Sci 353, 301 (2011).

Journal of Colloid and Interface Science 353 (2011) 301–310

Contents lists available at ScienceDirect

Journal of Colloid and Interface Science

www.elsevier.com/locate/jcis

Surface-dependent chemical equilibrium constants and capacitances for bare and 3-cyanopropyldimethylchlorosilane coated silica nanochannels

Mathias Bækbo Andersen [a,*], Jared Frey [b], Sumita Pennathur [b], Henrik Bruus [a]

[a] Department of Micro- and Nanotechnology, Technical University of Denmark, DTU Nanotech Building 345 East, DK-2800 Kongens Lyngby, Denmark
[b] Department of Mechanical Engineering, University of California, Santa Barbara, CA 93106, USA

ARTICLE INFO

Article history:
Received 2 July 2010
Accepted 9 September 2010
Available online 17 September 2010

Keywords:
Nanofluidics
Gouy–Chapman–Stern triple-layer model
Silica nanochannels
Cyanosilane surface coating
Capillary filling

ABSTRACT

We present a combined theoretical and experimental analysis of the solid–liquid interface of fused-silica nanofabricated channels with and without a hydrophilic 3-cyanopropyldimethylchlorosilane (cyanosilane) coating. We develop a model that relaxes the assumption that the surface parameters C_1, C_2, and pK_+ are constant and independent of surface composition. Our theoretical model consists of three parts: (i) a chemical equilibrium model of the bare or coated wall, (ii) a chemical equilibrium model of the buffered bulk electrolyte, and (iii) a self-consistent Gouy–Chapman–Stern triple-layer model of the electrochemical double layer coupling these two equilibrium models. To validate our model, we used both pH-sensitive dye-based capillary filling experiments as well as electro-osmotic current-monitoring measurements. Using our model we predict the dependence of ζ potential, surface charge density, and capillary filling length ratio on ionic strength for different surface compositions, which can be difficult to achieve otherwise.

1. Introduction

Understanding silica surfaces is important especially in the field of micro- and nanofluidics due to the emerging applications in pharmaceuticals, environmental health and safety, and bioanalytical systems [1–3]. Additionally, silica surfaces are scientifically of great interest, displaying rich phenomena because of the coupling of surface chemistry, electrokinetics, and fluid dynamics bridging molecular and continuum macroscopic length scales. As a result, new properties are observed which are not present in the bulk, e.g. vastly increased viscosity near solid surfaces, changes in thermodynamic properties, and changes in chemical reactivity at the liquid–solid interface [4,5]. The solid–liquid interface is therefore a subject of general interest; it is here where most of the unique inherent physics of nanofluidic systems is found.

Recently, due to the advances in nanofabrication technology, there has been an increasing number of experimental studies of the solid–liquid interface using nanochannels [6–11]. Though much work has been dedicated towards understanding how the electric double layer influences the flow of electrolytes at the nanoscale [12–14], there are still large quantitative discrepancies between theoretical modeling and experimental observations [5,15]. One of the complicating factors with studying nanofluidic transport processes is the influence from external forces typically used to drive transport at the nanoscale [2,4,5]. Therefore, capillary filling is an ideal platform to study intrinsic electrochemical reactions between the channel surface and the advancing electrolyte [9,16–18].

Janssen and co-workers [9] investigated the deprotonation in silica nanochannels during capillary filling. The authors used the pH-sensitive fluorescent dye fluorescein as an indicator of the local pH of the electrolyte in the channel during the transient capillary filling. Two regions were observed: (i) one region closest to the nanochannel entrance of full fluorescence signal and hence with the original pH (above the point of fluorescent quenching), and (ii) a dark region closest to the meniscus of no fluorescence signal and therefore with a pH equal to that of the point of zero charge pH_{pzc} of the surface (below the point of fluorescent quenching). The ratio of the extent of these two regions combined with knowledge of the composition of the buffer indicated the amount of protons that were released from the wall, which was found to be in the range 0.1–1 protons per nm^2. These values were then fitted to a theoretical model as a function of ionic strength and bulk pH, using electrolytes with different amounts of KCl and Tris–HCl buffer. Good agreement between theory and experiment was found by fitting a Stern-layer capacitance of 2.3 F m^{-2}.

Although this capillary filling study has provided valuable insight regarding the solid–liquid interface of bare silica, different surface coatings have yet to be investigated, and a general theoretical model of the interface is still missing. Therefore the aim of this

* Corresponding author. Fax: +45 45887762.
E-mail address: mathias.andersen@nanotech.dtu.dk (M.B. Andersen).
URL: http://www.nanotech.dtu.dk/microfluidics (M.B. Andersen).

0021-9797/$ - see front matter © 2010 Elsevier Inc. All rights reserved.
doi:10.1016/j.jcis.2010.09.025

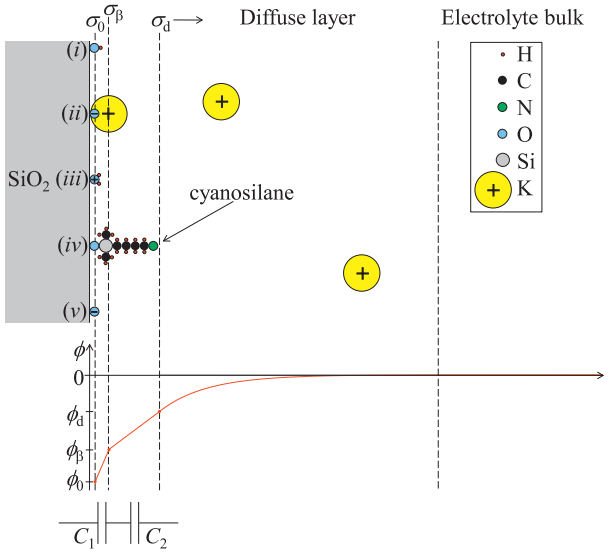

Fig. 1. Sketch of the solid-electrolyte interface showing the atoms/ions as hard spheres of sizes proportional to their hydrated or covalent radii (see Supporting information Sec. S2). To the left are the five possible surface site complexes: (i) SiOH, (ii) SiOK, (iii) $SiOH_2^+$, (iv) $SiC_6H_{12}NSi$ (cyanosilane), and (v) SiO^-. In between the solid SiO_2-wall and the charge neutral bulk there are three interfacial layers with the following surface charges: σ_0, the layer containing the reactive surface groups; σ_β, the layer containing adsorbed K^+ and cyanosilanes; and σ_d, the diffuse screening layer. Also indicated on the figure is a graph of the electric potential ϕ (red full curve) and the three interfacial potentials ϕ_0, ϕ_β, and ϕ_d. (For interpretation of the references to colour in this figure legend, the reader is referred to the web version of this article.)

work is to extend the current model to allow surface-related parameters, such as Stern-layer capacitance C_s and the surface equilibrium pK_a constants to vary with the composition of the solid–liquid interface as sketched in Fig. 1. We quantify these dependencies combining an extended version of current theoretical modeling and capillary filling experiments in bare and coated silica nanochannels.

The paper is organized as follows: in Section 2 we present a description of our solid–liquid interface model. Next, we introduce the equations that define the model. In Section 3 we list the chemicals used in our study and present the design, fabrication, and characterization of the silica nanochannels. In Section 4 we describe the experimental setup and the experiments performed to validate our model, as well as the determination of the parameters used as input in our model. In Section 5 we show the results of our combined experimental and theoretical investigation. Finally, in Sections 6 and 7 we discuss our findings and summarize our conclusions.

2. Theoretical modeling

The basis of our theoretical model is the Gouy–Chapman–Stern theory [19,9] combined with the more elaborate triple-layer model [20–23] of the solid–liquid interface. This complexity of modeling is necessary to simultaneously describe the observations for bare and cyanosilane-coated silica nanochannels. Our theoretical model involves three elements: (i) chemical equilibrium of the bulk electrolyte in terms of ionic concentrations and equilibrium pK_a constants [24]; (ii) electrochemical equilibrium of the proton and metal adsorption at the surface in terms of electrostatics, concentration of adsorption sites and ions, and equilibrium pK_a constants [20,21,23]; and (iii) electrochemical coupling between bulk and surface in terms of the Poisson–Boltzmann equation. An important point in our work is that we let the surface capacitances and the surface pK_a constants vary self-consistently with the chemical composition of the wall.

2.1. Schematic description of the model

We model the solid-electrolyte interface as consisting of three different interfacial layers, as sketched in Fig. 1. All quantities have been averaged on planes parallel to the silica wall, which is assumed flat on the microscopic length scale. The parameters of our model are listed in Table 1.

The first interfacial layer (subscript 0) closest to the wall consists of surface silanol sites being either neutral SiOH, deprotonated SiO^-, or protonated $SiOH_2^+$, which together give rise to a surface charge density σ_0. The electric potential here is denoted ϕ_0.

The second interfacial layer (subscript β) is comprised of adsorbed metallic cations, K^+ in this particular study. These cations produce a surface charge density σ_β at the plane defined by their mean position when adsorbed onto SiO^-. The electric potential here is denoted ϕ_β. Adsorption of anions is neglected because the bulk pH values studied in this work are always higher than pH_{pzc}.

The third interfacial layer (subscript d) is the diffuse layer of mobile ions screening the surface charge densities σ_0 and σ_β over a distance given by the Debye–Hückel screening length λ_D, which in this work ranges from approximately 0.3–2 nm. When integrating the charge density of the diffuse layer along the direction perpendicular to the interface, a resulting surface charge density σ_d

Table 1
Input and output parameters used in our model.

Quantity	Symbol	Unit
Input parameters, literature		
Viscosity	η	Pa s
Surface tension	γ	N m^{-1}
Relative permittivity, electrolyte	$\varepsilon_r = 78$	
Ionic valences	z	
Chemical family	X	
Chemical family member (ion)	X^z	
Valence minimum/maximum	n_X/p_X	
Equilibrium constants for bulk	$pK_{X,z}$	
Diffusion constants	D	m^2 s^{-1}
Electrophoretic mobilities	μ	m^2 $s^{-1}V^{-1}$
Total surface site density	Γ_{tot}	nm^{-2}
pK_-: $SiOH \leftrightharpoons SiO^- + H_0^+$	pK_-	
pK_K: $SiO^- + K_\beta^+ \leftrightharpoons SiOK$	pK_K	
Input parameters, measured		
Channel dimensions	h,w,L	m
Contact angle	θ	
Temperature	T	K
Fluorescent, dark zone-length	L_{fl}, L_d	m
Meniscus position	$L_{fl} + L_d$	m
Applied potential difference	ΔV	V
Conductivity	σ_{el}	S m^{-1}
pH of bulk	pH_b	
Input parameters, fitting		
Inner-layer Stern capacitance	C_1	F m^{-2}
Outer-layer Stern capacitance	C_2	F m^{-2}
pK_+: $SiOH_2^+ \leftrightharpoons SiOH + H_0^+$	pK_+	
Output variables, bulk		
Bulk concentrations		
Molarity	$c_{X,z}$	M
Number density	$n_{X,z}$	m^{-3}
Ionic strength	I	M
Debye–Hückel screening length	λ_D	m
Titration concentration of H^+	B_s	M
Output variables, surface		
pH of point of zero charge	pH_{pzc}	
Electric potentials	ϕ_0, ϕ_β, ϕ_d	V
Surface charge densities	σ_0, σ_β, σ_d	C m^{-2}
Surface site densities	Γ_{SiO^-}, Γ_{SiOH}	m^{-2}
	$\Gamma_{SiOH_2^+}$, Γ_K	m^{-2}

and corresponding potential drop ϕ_d are obtained. The electrical potential is defined to be zero outside the diffuse part of the double layer.

2.2. Bulk electrolyte chemistry

The equilibrium composition of the electrolyte is calculated using the scheme presented by Persat and co-workers [24]. This scheme builds on mass conservation, electroneutrality, and chemical equilibrium theory, and it unifies the entire system of equations for a given buffer in a systematic way that facilitates efficient numerical implementation. In our implementation of the scheme, X denotes a family of chemical species, with X^z being a particular member having valence charge z. Denoting the minimum and maximum valences within a family by n_X and p_X, respectively, the chemical equilibrium reactions for the family X are

$$X^{p_X} \rightleftharpoons X^{p_X-1} + H^+, \quad pK_{X,p_X-1}, \tag{1a}$$

$$X^{p_X-1} \rightleftharpoons X^{p_X-2} + H^+, \quad pK_{X,p_X-2}, \tag{1b}$$

$$\cdots$$

$$X^{n_X+1} \rightleftharpoons X^{n_X} + H^+, \quad pK_{X,n_X}, \tag{1c}$$

where each $pK_{X,z}$ is an equilibrium constant. For instance, for phosphoric acid the family is $X^0 = H_3PO_4$, $X^{-1} = H_2PO_4^{1-}$, $X^{-2} = HPO_4^{2-}$, and $X^{-3} = PO_4^{3-}$ with $p_X = 0$ and $n_X = -3$. In terms of ionic concentrations in the bulk, each $pK_{X,z}$ can be expressed as

$$pK_{X,z} = -\log_{10}\left(\frac{c_{X,z}c_H}{c_{X,z+1}c_{ref}}\right), \tag{2}$$

where $c_{X,z}$ is the concentration of species X in valence state z, c_H is the concentration of protons, and $c_{ref} = 1$ M is a reference concentration.

Mass conservation within each family implies that

$$c_X = \sum_{z=n_X}^{p_X} c_{X,z}, \tag{3}$$

where c_X equals the total analytical concentration, and electroneutrality requires

$$\sum_X \sum_{z=n_X}^{p_X} z c_{X,z} = 0. \tag{4}$$

Note that this expression is only valid outside the diffuse layer. Finally, the important auto-dissociation reaction of water is

$$H_2O \leftrightharpoons OH^- + H^+, \quad pK_w = 14, \tag{5}$$

and bases are formally modeled as deprotonation reactions, e.g. the base XOH is assigned the reaction [24]

$$X^+ + \frac{1}{2}H_{2,g} \leftrightharpoons X + H^+, \tag{6}$$

with the pK_a assigned to be 14 to ensure that the equilibrium state is complete dissociation. The addition of a salt is modeled as the addition of the equivalent amounts of corresponding acid and base. For example, the salt KH_2PO_4 is modeled as the addition of the base KOH and the acid H_3PO_4. The actual chemicals used in our experiments (see Section 3) are modeled as: (i) phosphoric acid, (ii) dihydrogen fluorescein, (iii) potassium hydroxide, and (iv) sodium hydroxide, as listed in Table 2.

From Eqs. (2)–(4) an equation for the concentration of protons c_H can be derived and solved through numerical iteration using the Matlab script developed in the group of Santiago [24]. Consequently, knowing the pH value a priori, the ionic concentrations $c_{X,z}$ can be calculated directly. This enables us to find the bulk concentration of protons B_s required for the titration from the initial pH in the bulk pH_b to pH_{pzc} as

$$B_s = \sum_X \sum_{z=n_X}^{p_X} z\left(c_{X,z}^{pzc} - c_{X,z}^{b}\right). \tag{7}$$

This quantity is necessary for relating the experimentally observed capillary filling length ratios to the model.

Finally, the bulk electrolyte is characterized by the ionic strength I and the electrical conductivity σ_{el},

$$I = \frac{1}{2}\sum_X \sum_{z=n_X}^{p_X} z^2 c_{X,z}, \tag{8a}$$

$$\sigma_{el} = e\sum_X \sum_{z=n_X}^{p_X} z\mu_{X,z}n_{X,z}, \tag{8b}$$

where $n_{X,z} = 10^3$ L m^{-3} N_A $c_{X,z}$ is the bulk ion number concentration (m^{-3}), N_A being the Avogadro constant. Parameter values used in our model are listed in Table 2.

Table 2
List of chemical families X used in this work, including formulae, valences z, equilibrium constants $pK_{X,z}$, diffusion constants $D_{X,z}$, and electrophoretic mobilities $\mu_{X,z}$. For $z > 0$ and $z < 0$ the $pK_{X,z}$ value pertains to the reaction $z \leftrightharpoons z-1$ and $z \leftrightharpoons z+1$, respectively.

X	Formula	z	$pK_{X,z}$[a]	$D_{X,z}$[b] (10^{-9} m^2/s)	$\mu_{X,z}$[b] (10^{-9} T^{-1})
Phosphoric acid	H_3PO_4	0			
		−1	2.15	0.959	−37.3
		−2	7.21	0.759	−59.1
		−3	12.33	0.824	−96.2
Fluoresein	$C_{20}H_{12}O_5$	1	2.22[c]	0.57[d]	22.0[d]
		0			
		−1	4.34[c]	0.64[e]	−25.0[e]
		−2	6.68[c]	0.502[e]	−39.5[e]
Potassium hydroxide	KOH	1	14.0	1.96	76.2
		0			
Sodium hydroxide	NaOH	1	14.0	1.33	51.9
		0			
Water	H_2O	0		9.311[f]	362.4[f]
		−1	14.0	5.273[f]	−205.2[f]
Silanol	SiOH	1	−1.9[g]		
		0			
		−1	6.8[g]		
Ion pair	SiOK	0			
		−1	−0.06[g]		

[a] For acids pK_a values are at infinite dilution and at 25 °C from Ref. [24] unless otherwise stated.
[b] $D_{X,z}$ values and $\mu_{X,z}$ values at infinite dilution at 25°C from Ref. [25] unless otherwise stated.
[c] pK_a values at infinite dilution and at 25 °C from Ref. [26].
[d] Estimate.
[e] $\mu_{X,z}$ values from Ref. [24] with $D_{X,z}$ values calculated from these using $D_{X,z} = \mu_{X,z}k_BT/(ze)$.
[f] Here $z = 0$ represents H^+ and $z = -1$ represents OH^-.
[g] For bare silica: SiOH [27,28] and SiOK [23].

2.3. Surface chemistry

The equations for the surface chemistry involve surface reactions, surface sites, site densities, and surface equilibrium constants. Here we summarize the well established surface chemical equilibrium model involving singly coordinated surface silanol sites [29,30,20,21]

$$SiOH_2^+ \rightleftharpoons SiOH + H_0^+, \quad pK_+, \tag{9a}$$

$$SiOH \rightleftharpoons SiO^- + H_0^+, \quad pK_-, \tag{9b}$$

where $SiOH_2^+$, SiOH, and SiO^- are the protonated, neutral, and deprotonated surface hydroxyl groups, H_0^+ is a proton in solution

at the 0-plane, and $pK_{\pm}$ the equilibrium constants, which for bare silica are $pK_{+} = -1.9$ [27] and $pK_{-} = 6.8 \pm 0.2$ [28]. The adsorption of cations onto negative surface hydroxyl groups can be described by a similar equilibrium reaction [30,20,21]

$$SiO^{-} + K^{+}_{\beta} \rightleftharpoons SiOK, \quad pK_K, \tag{10}$$

where K^{+}_{β} is the cation in solution at the β-plane and where $pK_K = -0.06 \pm 0.30$ [23]. Note that SiOK is an ion pair, giving rise to one negative charge (SiO^{-}) in the 0-plane and one positive charge (K^{+}) in the β-plane. The point of zero charge pH_{pzc} used for the evaluation of B_s in Eq. (7) is then given as

$$pH_{pzc} = \frac{1}{2}(pK_{+} + pK_{-}). \tag{11}$$

The appearance of pK_{+} in this relation implies, together with Eq. (7), that we must keep Eq. (9a), a reaction which under normal conditions can be neglected [31]. The equilibrium equations for Eqs. (9a), (9b) and (10) are

$$pK_{+} = -\log_{10}\left(\frac{\Gamma_{SiOH} c_{H,0}}{\Gamma_{SiOH_2^+} c_{ref}}\right), \tag{12}$$

$$pK_{-} = -\log_{10}\left(\frac{\Gamma_{SiO^-} c_{H,0}}{\Gamma_{SiOH} c_{ref}}\right), \tag{13}$$

$$pK_K = -\log_{10}\left(\frac{\Gamma_K c_{ref}}{\Gamma_{SiO^-} c_{K,\beta}}\right), \tag{14}$$

where Γ_{SiOH}, $\Gamma_{SiOH_2^+}$, and Γ_{SiO^-} are the site densities of the neutral, positive, and negative surface silanol groups, respectively. Γ_K is the site density of ion pairs of a negative surface site and a cation, and $c_{H,0}$ and $c_{K,\beta}$ are the concentrations of protons and cations at the 0- and β-plane, respectively. The total available density of sites is constant, and for silica surfaces reported to be $\Gamma_{tot} = 4.6 \times 10^{18}$ m^{-2} [32]. In our model Γ_{tot} is

$$\Gamma_{tot} = \Gamma_{SiOH} + \Gamma_{SiO^-} + \Gamma_{SiOH_2^+} + \Gamma_K. \tag{13}$$

Silane coating is modeled by decreasing Γ_{tot}, see Section 5.

2.4. Electrical equations and bulk/surface coupling

The bulk and surface are coupled through equations involving electrical potentials, ionic concentrations, surface charge densities, and surface capacitances. For the two inner layers the equations relating surface charge densities to site densities are

$$\sigma_0 = e(\Gamma_{SiOH_2^+} - \Gamma_{SiO^-} - \Gamma_K), \tag{14a}$$

$$\sigma_\beta = e\Gamma_K, \tag{14b}$$

whereas the surface charge density σ_d of the diffuse layer is linked to ϕ_d through Grahame's equation [33]

$$\sigma_d = -\mathrm{sgn}(\phi_d)\left[2\varepsilon_r\varepsilon_0 k_B T \sum_X \sum_{z=n_X}^{p_X} n_{X,z}\left(e^{-\frac{ze\phi_d}{k_B T}} - 1\right)\right]^{\frac{1}{2}}. \tag{15}$$

Due to electroneutrality the surface charge densities are related by the constraint

$$\sigma_0 + \sigma_\beta + \sigma_d = 0. \tag{16}$$

Assuming charge-independent dielectric permittivities and no free charges in between the surface layers, the electric displacement field between the surface planes can be found using Gauss's law. Integrating this from the 0- to the β-plane and from the β- to the d-plane yields,

$$\phi_\beta - \phi_0 = -\frac{\sigma_0}{C_1}, \tag{17a}$$

$$\phi_d - \phi_\beta = \frac{\sigma_d}{C_2}, \tag{17b}$$

where C_1 is the inner and C_2 the outer layer capacitance (F m^{-2}), which are important surface dependent parameters in our model. These capacitances are coupled in series and relate to the Stern-layer capacitance C_s as $1/C_s = 1/C_1 + 1/C_2$.

Using the dilute assumption to neglect higher order effects, the electrochemical potential consists of a purely entropic and a purely electric term, leading to Boltzmann distributed concentrations. The proton (cation) concentration $c_{H,0}$ ($c_{K,\beta}$) at the 0-plane (β-plane) and in the bulk c_H (c_K) are thus related by

$$c_{H,0} = c_H \exp\left(-\frac{e\phi_0}{k_B T}\right), \tag{18a}$$

$$c_{K,\beta} = c_K \exp\left(-\frac{e\phi_\beta}{k_B T}\right). \tag{18b}$$

For use in the subsequent numerical fitting we combine Eqs. (12)–(18) to obtain

$$\Gamma_K = \frac{\Gamma_{tot} + \frac{\sigma_d}{e}}{1 + \frac{c_{H,0}}{c_{K,\beta}}\left(10^{pK_-} + 2\frac{c_{ref}}{c_{H,0}}\right)10^{pK_K}}, \tag{19a}$$

$$\Gamma_{SiOH} = \frac{\Gamma_{tot} + \frac{\sigma_d}{e} - \Gamma_K}{1 + 2\frac{c_{ref}}{c_{H,0}}10^{-pK_-}}, \tag{19b}$$

$$\Gamma_{SiOH_2^+} = \Gamma_{SiO^-} - \frac{\sigma_d}{e}. \tag{19c}$$

Eqs. (1)–(19) define our model, which can be characterized as a triple layer version of the Gouy–Chapman–Stern model. A list summarizing the input and output parameters of the model is given in Table 1.

3. Materials and methods

3.1. Chemicals

The ionic solutions used in our experiments were potassium phosphate (KH_2PO_4) based solutions with $pK_a = 7.21$ (Fisher Scientific P285-500). Buffer concentrations of 10, 30, 50, 100, and 383 mM were prepared by mixing KH_2PO_4 powder with deionized (DI) water and titrated to the desired pH value using 1 M KOH. The fluorescent analytes used in our experiments were 0.01 mM pH-sensitive sodium fluorescein (Riedel-de Haen) and 0.01 mM pH-insensitive Alexa Fluor 488 (Invitrogen). Prior to use, bulk pH and conductivities were measured (Oakto, Inc) and all solutions were filtered using 0.2 μm PTFE syringe filters (Nalgene). Solutions were stored at 4 °C covered by aluminum foil to prevent contamination and photo bleaching. Directly prior to experiments, buffers were heated to ambient room temperature and re-mixed with a vortexer (Dencille Scientific Inc.). These precautions ensured that both the fluorescent dye maintained constant emission properties and the solutions were well preserved.

3.2. Design and fabrication of silica nanochannels

The design of the nanochannels followed that of Tas et al. [17] and Persson et al. [34]. Nanochannels were fabricated using fused-silica wafers at the UCSB nanofabrication facility with conventional MEMS processing techniques [14] based on mask design sets from DTU Nanotech [34]. The design of the channels consisted of pairwise parallel inlet/outlet microwells, each 2 mm × 5 mm rounded with 5-mm-diameter caps and etched to a depth of 1.6 μm. The pairs of reservoir wells were connected by 12 parallel nanochannels of length $L = 5$ cm, with etched ruler markings in increments of 100 μm. Widths w varied from 5 to 40 μm, with depths h on different chips of either 115, 145, or 195 nm (within ± 3 nm). Fig. 2b shows the inlet of a nanochannel during capillary filling (see Supporting information Sec. S1).

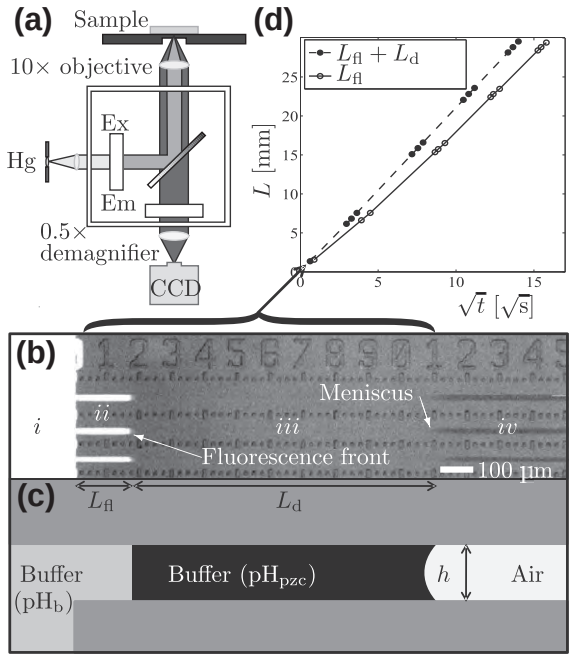

Fig. 2. (a) Block diagram showing the experimental setup (detailed in Section 4.1) comprising of sample, optics, mercury lamp, and EMCCD camera. (b) Image at the beginning of the capillary filling of the 30 mM KH_2PO_4 buffer seeded with 0.01 mM fluorescein into three of the twelve parallel nanochannels. Four regions can be seen: (i) inlet well with fluorescent buffer, (ii) fluorescent buffer in nanochannel region of length L_{fl}, (iii) dark buffer in nanochannel region of length L_d, (iv) black air-filled part of the nanochannel. (c) A schematic side view of one of the nanochannels of height h from panel (b) defining the lengths L_{fl} and L_d as well as the corresponding pH conditions; pH_b in the fluorescent regions (i) and (ii), and pH_{pzc} in the dark point of zero charge region (iii). (d) Experimental capillary filling data for a bare nanochannel showing the meniscus position $L_{fl} + L_d$ (points and dashed line) and L_{fl} (points and full line) versus the square root of time t (see Section 4.3). The first data point (black square) corresponds to the image in panel (b).

3.3. Surface coating and cleaning

To change the surface properties and characteristics of the silica nanochannels, we chose to coat the channel after fabrication with a liquid-phase silane. 3-Cyanopropyldimethylchlorosilane (cyanosilane, Gelest Inc.) was chosen because it has been shown to form a fully wettable, slightly hydrophilic, stable lipid monolayer on glass [35], and was straightforward to coat after bonding without changing any of the channel dimensions or introducing any variability in the channel fabrication process. The coating process is known to replace ~25% of negative charge sites with a neutral cyanosilane group [36] (see Fig. 1).

Immediately after fabrication and dicing, all devices were precleaned using 0.2 μm-filtered DI water driven through the nanochannels by electro-osmosis (EO). Platinum wires, inserted into the inlet/outlet microwells and fixed by scotch tape, served as EO-electrodes. The EO-flushing was powered by an electric field of 5000 V/m delivered by a source meter (Keithley 2410, sampling frequency of 100/min), and the associated electric current was monitored using a high impedance electrometer (Keithley 6517, sampling frequency of 400/min) controlled using custom LabVIEW software and analyzed with Matlab.

The initial DI-water EO-flushing ran for 60 min, while monitoring that the current remained stable at the range of ~1 pA, after a short transient period of ~1–2 min. The EO-flushing was continued using 0.1 M KOH for 15 min, and finally proceeded by a second 60 min EO-flushing with DI water. At this point, the devices were either stored in DI water or treated with the cyanosilane coating.

The devices to be coated were dried on a hotplate at 150 °C for 30 min, after which they were filled using capillary forces with a solution of 0.1 M cyanosilane in 0.2 μm filtered acetonitrile (Fisher Scientific). The filled nanochannels were then EO-flushed with the cyanosilane solution for approximately 30 min. The whole device was then incubated in cyanosilane solution overnight (~12 h) to allow the silane groups to attached themselves to the channel walls (see Supporting information Sec. S4). After this surface modification was completed, the devices were rinsed with copious amounts of filtered ethanol, EO-flushed with pure acetonitrile for 1 h, and EO-flushed with DI water for approximately 30 min until the electrical current stabilized. The coated channels were stored wet in filtered ethanol to preserve the coating and prevent degradation [37].

3.4. Surface characterization

The roughness of both uncoated and coated channel walls were characterized using standard AFM techniques and found to be approximately 0.3 nm and 0.7 nm, respectively (see Supporting information Sec. S1). Contact angle measurements were experimentally found by depositing 10 μL of DI water onto each surface, and imaging the water droplets at the contact interface (see Supporting information Sec. S1). The contact angle of the uncoated and coated surfaces was found to be 32° and 75°, respectively, in good agreement with previously reported values [38,39]. An interferometer (Wyko NT1100) was used to image the microwell and entrance to the nanochannels (see Supporting information Sec. S1). Further characterization of the surfaces was performed using the current monitoring method, described in more detail in Section 4.2.

4. Experimental setup and procedure

4.1. Optical and electrical setup

Recordings of the propagating buffer in our filling experiments were performed using an inverted epifluorescent microscope (Olympus IX70) and automated stage (Prior Proscan II) controlled via custom LabVIEW software (LabVIEW V8.6). Images were captured using a back illuminated EMCCD camera (Andor iXon +) with a 200 ms exposure time using a 10× objective (Olympus UPlanFL 10 × 2, NA = 0.3) with a 0.5× demagnifying lens (U-TV0.5xC-3) as seen in Fig. 2a. A stationary halogen lamp was used to illuminate the fluid front, whereas an aligned and focused mercury arc lamp (Olympus U-RFL-T) filtered with a 488 nm excitation and 532 nm emission FITC filter cube (Chroma Technology 31001FITC/RSGFP/Fluo 3/DiO Acradine Orange(+DNA)) was used to illuminate the fluorescent front. Electric fields for channel cleaning and buffer characterization were generated across the nanofluidic channels by a Keithley multimeter (Model 2410), and currents were recorded in series with a Keithley electrometer (Model 6517) connected to platinum wire electrodes placed within each fluid reservoir of the device. A schematic of this electrical setup is shown in the inset of Fig. 3a (see Supporting information Sec. S1).

4.2. Current monitoring

Both the conductivity and the ζ potential were measured by current monitoring techniques following Ref. [40]. One reservoir was initially filled with an electrolyte of concentration 0.9 c^*, where c^* was a predefined target concentration. A voltage drop was applied between the inlet and outlet well to drive an EO flow. After about 15 min the current was stabilized, indicating complete filling in the nanochannel by the 0.9 c^* electrolyte. Then all

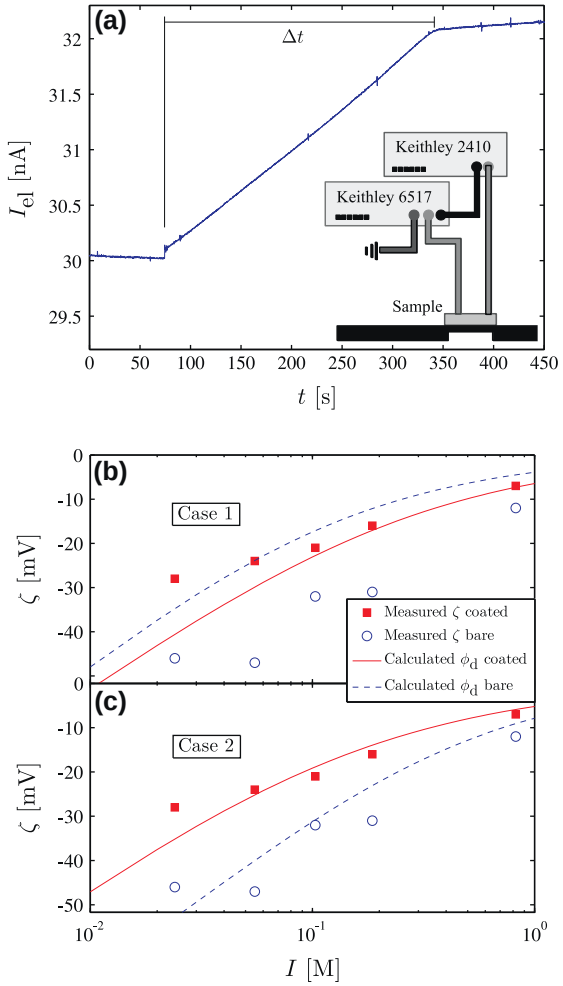

Fig. 3. (a) Raw data showing electrical current I_{el} versus time t in an EO-flow measurement. Initial buffer concentration is 9 mM. At t = 80 s the buffer in the inlet well is replaced by a 10 mM buffer. At t = 340 s the 10 mM solution has filled the channel completely. The ζ potential is determined by Eq. (20) with Δt = 340 − 80 s. Inset shows schematic of the experimental setup including the sourcemeter (Keithley 2410) and the electrometer (Keithley 6517), see Section 4.2. (b) Lin-log plot of measured ζ potential for bare (blue empty circles) and coated (red filled squares) as function of ionic strength I. Curves are theoretical predictions of the diffuse layer potential ϕ_d for bare (blue dashed) and coated (red full) channels for case 1, Table 5, where C_2 = 0.2 F m^{-2}. (c) As panel (b) except that the theoretical predictions are for case 2, Table 5, where the values of C_2 are 0.8 F m^{-2} and 0.15 F m^{-2} for bare and coated channels, respectively. Note the improved agreement between theory and experiment going from case 1 to case 2. (For interpretation of the references to colour in this figure legend, the reader is referred to the web version of this article.)

electrolyte was removed from the inlet well and replaced with electrolyte of concentration c^*. The current was monitored over time, with typical results shown in Fig. 3a. Measurements were performed for every concentration c^* used in the capillary filling experiments (10, 30, 50, 100, and 383 mM) at two different electric field strengths (6 kV/m and 12 kV/m). Voltage and current were supplied and monitored using the equipment described in Section 3.3. For determination of the ζ potential, the filling speed $L/\Delta t$ is set equal to the Helmholtz–Smoluchowski velocity $(\varepsilon\zeta/\eta)\Delta V/L$ [41],

$$\zeta = \frac{\eta L^2}{\varepsilon \Delta V \Delta t}. \tag{20}$$

Table 3, Fig. 3b and c shows measured ζ potential for both bare and coated channels of length L at all concentrations used in this study. Also shown are theoretically fitted curves for ϕ_d described in Section 5.

Table 3
Calculated ionic strength I from Eq. (8a), measured ζ potential for bare and coated channels, and measured electrical conductivity σ_{el}^{meas} divided by I. From the fit in Fig. 4 we find $\sigma_{el}^{meas}/I = 9.1$ S m^{-1} M^{-1} in the limit $I \to 0$, while using Eq. (8b) in the same limit gives $\sigma_{el}^{calc}/I = 9.36$ S m^{-1} M^{-1}, deviating less than 3%.

I (M)	0.024	0.055	0.103	0.186	0.823
ζ^{bare} (mV)	−47	−48	−32	−31	− 12
ζ^{coat} (mV)	−29	−24	−21	−16	− 7
σ_{el}^{meas}/I ((S/m)/M)	7.083	7.909	5.728	5.000	5.033

We also characterized the electrical properties of the system by measuring the conductivity σ_{el} versus ionic strength I, see Table 3. This was done using both a conductivity meter and simultaneous current and voltage measurements. The Kohlrausch plot in Fig. 4 of σ_{el}/I versus I shows good agreement (3%) between the measured conductivity extrapolated to zero ionic strength and the theoretical dilute limit.

4.3. Capillary filling experiments

In our experiments, we filled both bare and cyanosilane-coated silica nanochannels with KH_2PO_4 buffers of concentrations in the range 10–383 mM mixed with a 0.01 mM tracer dye, either pH-sensitive fluorescein or pH-insensitive Alexa Fluor 488 (see Section 3.1). During filling, the advancing electrolyte meniscus ($L_{fl} + L_d$) and the fluorescence front (L_{fl}) were recorded optically as shown in Fig. 2 using the equipment described in Section 4.1. A list of the performed experiments is given in Table 4, and the exact procedure is detailed below.

A given nanochannel was removed from its wet storage and optically examined for defects and clogs. Next we flushed the channel using EO-flow for 30 min until the current stabilized to around 1 pA, which is a typical indication that the channel is not contaminated. All the liquid was evaporated from the channel by placing the chip on a hotplate at 300 °C for 30 min before it was placed on the automated microscope stage where it was aligned and focused relative to the EMCCD camera. We then pipetted the buffer solution into the inlet microwell and recorded videos of the propagation of the meniscus using the experimental setup described in Section 4.1. To capture the entire filling process, which lasts less than 5 min, the automated stage was centered to five different positions and the filling fronts were recorded as they passed the field of view. An experimental video is provided in the Supporting information. Fig. 2d shows a typical experimental data set

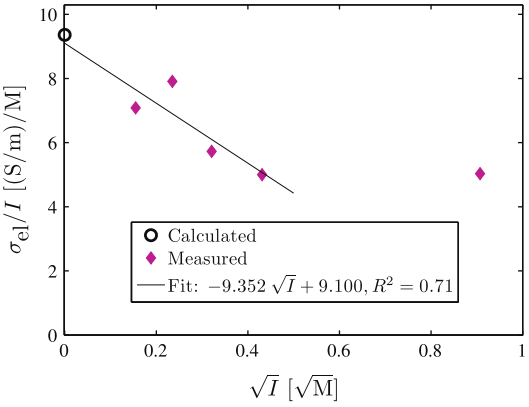

Fig. 4. Kohlrausch plot: the measured electrical conductivity σ_{el} divided by ionic strength I versus $\sqrt{I}$. The highest ionic strength data point clearly deviates from the Kohlrausch law and has thus been excluded from the fit. Extrapolation of the fit to I = 0 deviates only 3% from the theoretically predicted value at infinite dilution (black circle), see Eq. (8b).

Table 4
List of the 43 capillary filling experiments, specifying the phosphate buffer concentration c_{buf} in mM, the pH of the buffer, type of the 0.01 mM dye (F: fluorescein of charge −2, A: Alexa Fluor of charge 0), type of surface (B: bare, C: cyanosilane coated), and channel height h.

#	c_{buf}	pH	Dye	Surf	h (nm)
1–3	10	7.2	F	B	145, 145, 145
4–6	30	7.1	F	B	124, 124, 115
7–12	50	7.3	F	B	142, 142, 145, 145, 142, 142
13–19	100	7.2	F	B	145, 145, 145, 145, 142, 142, 142
20–23	383	7.2	F	B	115, 115, 115, 115
24–26	10	7.2	F	C	142, 142, 145
27–32	30	7.1	F	C	124, 124, 115, 124, 124, 115
33–35	50	7.3	F	C	142, 142, 142
36–38	100	7.2	F	C	195, 115, 115
39	383	7.2	F	C	115
40	10	7.2	A	B	142
41	100	7.2	A	B	142
42	10	7.2	A	C	115
43	100	7.2	A	C	115

demonstrating that both the fluoresent signal and the meniscus follows the Washburn relation Eq. (21). Once the channel was completely filled, we EO-flushed the channel with DI water until the current decreased to a stable level of about 1 pA. The channel was then stored wet.

4.4. Extraction of parameters by capillary filling

The filling dynamics of cylindrical capillaries was first described by Washburn [42] and later applied to rectangular nanochannels of low height-to-width aspect ratio by others [17,34]. For the latter systems, relevant to this study, the time-dependent position $L(t) = L_{fl} + L_d$ of the electrolyte meniscus is

$$L(t) = L_{fl} + L_d = \sqrt{\frac{\gamma h \cos\theta}{3\eta}\, t}, \tag{21}$$

where γ is the electrolyte/air surface tension, θ the contact angle, h the height of the nanochannel, and η the viscosity of the electrolyte.

As the electrolyte containing the tracer dye fluorescein fills the nanochannel there is a region in the front of the liquid column without fluorescent signal, as shown in Fig. 2. Fluorescein is a pH-sensitive dye and therefore one might speculate that the quenching is due to a change in pH in this zone stemming from deprotonation of the silica surface silanol sites as described in Ref. [9]. This assumption is further corroborated by the fact that none of our control experiments containing pH-insensitive Alexa Fluor dye showed a region without fluorescent signal (data not shown). To evaluate the surface properties using the observed dark zone we assume that: (i) the pH is constant within each of the two regions in the liquid column, (ii) the pH in the dark region equals the value pH_{pzc} of the point of zero charge, and (iii) the pH in the fluorescent region is that of the bulk pH_b. With these assumptions one can estimate the amount of protons $N_{H^+}^{ads}$ necessary to bring the volume of buffer in the dark region from pH_b to pH_{pzc}. This amount must equal the volume whL_d of the dark region multiplied by the concentration of protons B_s necessary to titrate from pH_b to pH_{pzc}

$$N_{H^+}^{ads} = whL_d B_s, \tag{22}$$

where B_s is calculated using the theory described in Section 2.2. Note that ionic concentrations may not be constant across the nanochannel due to the influence of the electrical double layer, but for our high concentration systems the change in ionic concentration over the entire volume of the channel does not change by more than 5% from the bulk.

The release of protons from the channel walls can be estimated using the assumption that all the wall deprotonation occurs at the interface between the dark and fluorescent regions. It then follows that by multiplying the amount per area (Γ_{H^+}) of protons released by the channel wall, by the surface area in the fluorescent region of the channel, the amount of protons released into the dark region is

$$N_{H^+}^{rel} = 2(w+h)L_{fl}\Gamma_{H^+}. \tag{23}$$

Equating $N_{H^+}^{ads}$ and $N_{H^+}^{rel}$ yields Γ_{H^+} in terms of the experimentally measured lengths of the fluorescent and dark zones

$$\Gamma_{H^+} = B_s \frac{h}{2(1+h/w)} \frac{L_d}{L_{fl}}. \tag{24}$$

Assuming that all the sites on the channel wall prior to contact with the electrolyte are SiOH, the amount of deprotonation per area is given by the surface charge density of the innermost layer as $\Gamma_{H^+} = -\sigma_0/e$, e being the elementary charge. Combining this with Eq. (24) we obtain the following relation between the experimentally observed length ratio and the theoretically calculated surface charge density,

$$\frac{L_d}{L_{fl}} = -\frac{2(1+h/w)}{eB_s h}\sigma_0. \tag{25}$$

4.5. Numerical fitting procedure

We use the experimentally observed length ratios L_d/L_{fl} to fit C_1 and pK_+. Below we outline the fitting procedure implemented in Matlab (see Supporting information Sec. S3) [43]. The number of independent variables is reduced to two and in the actual computation the equations are non-dimensionalized to obtain higher numerical accuracy.

1. Calculate the electrolyte ionic concentrations $c_{X,z}$ and the ionic strength I for the observed L_d/L_{fl}-ratio for each of the five experimental conditions $\{c_{buf}\}_{i=1,\ldots,5}$ of Table 4 using the bulk theory in Section 2.2.
2. Use the output from the bulk theory as input for the surface chemistry and bulk/surface coupling equations from Sections 2.3 and 2.4 as outlined below. Repeat until convergence.
   (a) Estimate and update the fitting parameters C_1 and pK_+.
   (b) Update pH_{pzc} using Eq. (11).
   (c) Update $\{B_s\}_{i=1,\ldots,5}$ from Eq. (7).
   (d) For each L_d/L_{fl}-ratio give initial guess for ϕ_0 and ϕ_d and solve the surface equation system:
      i. σ_d from Eq. (15).
      ii. ϕ_β from Eq. (17b).
      iii. $c_{H,0}$ and $c_{K,\beta}$ from Eqs. (18).
      iv. Γ_K from Eq. (19a).
      v. σ_β and Γ_{SiOH} from Eqs. (14b) and (19b).
      vi. σ_0 and Γ_{SiO^-} from Eqs. (16) and (13).
      vii. $\Gamma_{SiOH_2^+}$ from Eq. (19c).
      viii. Check if Eqs. (12) and (17a) are converged and update ϕ_0 and ϕ_d accordingly.
   (e) Output obtained upon convergence.
   (f) Use Eq. (25) to update the calculated length ratios $\{L_d/L_{fl}\}_{i=1,\ldots,5}$. Compare these calculated length ratios against those measured. If not converged go back to 2.
3. Analyze parameters and produce goodness-of-fit values R^2, plots *etc.*

5. Results

Fig. 5 shows length ratio L_d/L_{fl} as function of ionic strength I measured (symbols) and fitted theoretically (curves) for bare surfaces (blue, open symbols and dashed curve) and for coated

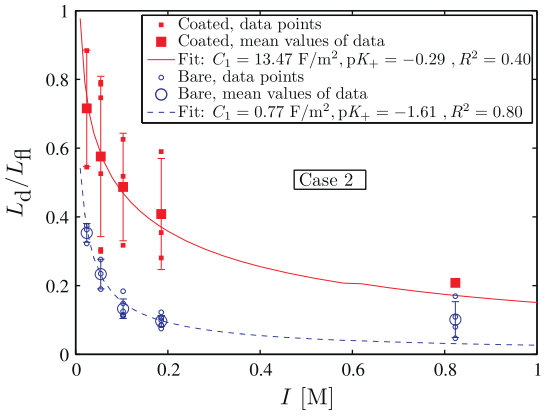

Fig. 5. Plot of the experimentally measured (symbols) and theoretically fitted (curves) length ratio L_d/L_{fl} as function of ionic strength I for the bare surfaces (blue, open symbols and dashed curve) and coated surfaces (red, filled symbols and full curve) with parameters corresponding to case 2 as given in Table 5. (For interpretation of the references to colour in this figure legend, the reader is referred to the web version of this article.)

surfaces (red, filled symbols and full curve). Here, the parameters kept constant are pK_- = 6.8 [28] and pK_K = −0.06 [23]. For the coated channels we assume that 25% of the surface sites have a cyanosilane molecule attached [36], which reduces the surface site density Γ_{tot} from the bare value of 4.6 nm^{-2} to 3.45 nm^{-2}. In the literature the value of C_2 is often taken to be C_2 = 0.2 F m^{-2} [23] (denoted case 1). This value of C_2 did not explain the observed trends for different surfaces, and in fact, no other single fixed value could do so. We therefore allow C_2 to be surface dependent. Optimization led to the values $C_2^{bare} = 0.8$ F m^{-2} and $C_2^{coated} = 0.15$ F m^{-2} which we denote case 2 in the following discussion. Parameters that are fitted are C_1 and pK_+, and a list of parameter values for cases 1 and 2 are summarized in Table 5.

In both cases pK_-, pK_K, and Γ_{tot} are parameters taken from literature [28,23,32]. In case 1, we fix the outer capacitance C_2 for both the bare and coated surfaces to the value 0.2 F m^{-2} often quoted in literature [20,22,44,23]. Choosing this value of constant C_2 led to fitted and calculated parameters with a decent R^2 value (see Table 5) but showed poor agreement with ζ potential experimental data. In fact, Fig. 3b shows theoretical trends which are exactly opposite of measured data, where the coated channels are estimated theoretically to have higher ζ potential values than the bare, a trend that is not observed experimentally. In case 2 we remedy this discrepancy by optimizing C_2 to not only match the L_d/L_{fl} experimental values in Fig. 5, but also the ζ potential values in Fig. 3c. Here, we note the improved match between the calculated ϕ_d and measured ζ potential for both bare and coated data. Figs. 6 and 7 show potentials and surface charge densities for both cases. However, given the better fit of case 2 the remainder of our discussion is focused on this case.

Table 5
Two cases of setting the outer Stern capacitance C_2. Case 1: using the literature value 0.20 F m^{-2} for both bare (B) and coated (C) surfaces. Case 2: changing C_2 to obtain match between calculated ϕ_d and measured ζ, see panel (b) and (c) in Fig. 3. Also shown are fitted and calculated parameters from Fig. 5, while other set parameters are pK_- = 6.8, pK_K = −0.06, and Γ_{tot} = 4.6 nm^{-2} (bare) and Γ_{tot} = 3.45 nm^{-2} (coated).

Case	Set C_2 (F/m^2)	Fitted		Calculated		
		C_1 (F/m^2)	pK_+	R^2	C_s (F/m^2)	pH$_{pzc}$
1 B	0.20	0.69	−1.03	0.81	0.16	2.9
1 C	0.20	15.47	−0.54	0.40	0.20	3.1
2 B	0.80	0.77	−1.61	0.80	0.39	2.6
2 C	0.15	13.47	−0.29	0.40	0.15	3.3

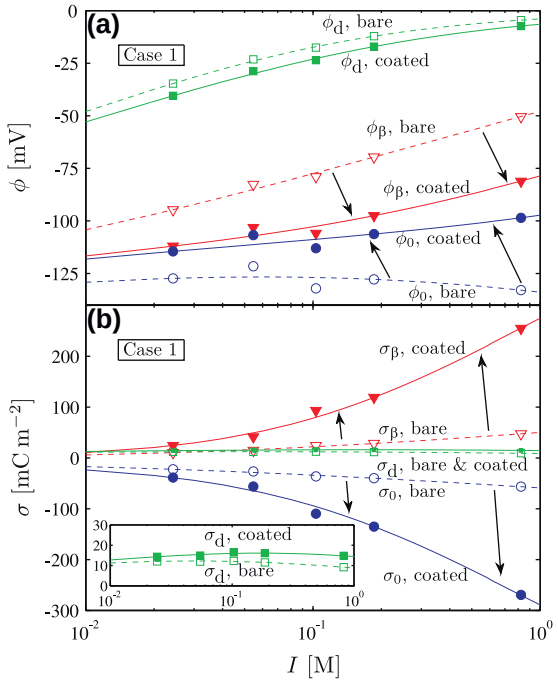

Fig. 6. Case 1: calculated potentials ϕ and surface charge densities σ plotted versus ionic strength I for bare channels (open symbols and dashed curves) and coated channels (filled symbols and full curves). Each point represents the average over channel heights (see Table 4) while curves are for fixed h = 135 nm. In this case 1 C_2 = 0.2 F m^{-2}, while other parameters are given in Table 5. (a) Calculated ϕ_0 (blue circles), ϕ_β (red triangles), and ϕ_d (green squares). The arrows indicate shifting of curves going from bare to coated channels. (b) Calculated σ_0 (blue circles), σ_β (red triangles), and σ_d (green squares). The inset is a zoom on the diffuse layer surface charge density σ_d. (For interpretation of the references to colour in this figure legend, the reader is referred to the web version of this article.)

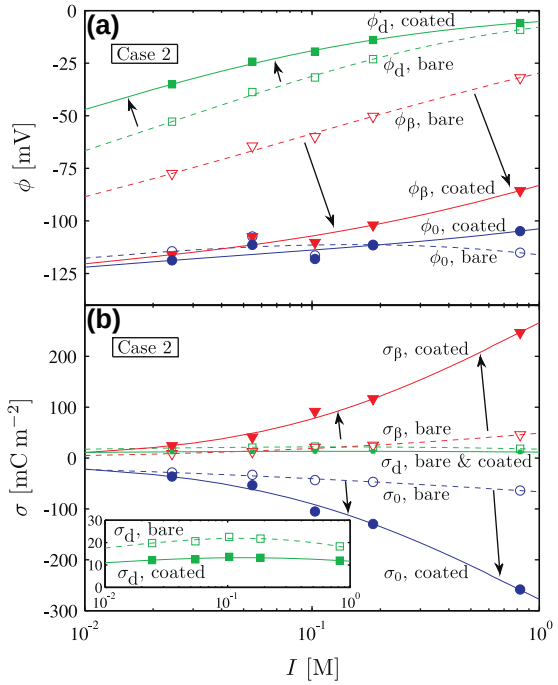

Fig. 7. Case 2: same as in Fig. 6 except that the parameters are: C_2 = 0.80 F m^{-2} (bare) and C_2 = 0.15 F m^{-2} (coated) as listed in Table 5.

Fig. 7a shows the surface potential ϕ_0, the metal layer potential ϕ_β, and the diffuse layer potential ϕ_d for the bare and coated channels versus ionic strength as sketched in Fig. 1. As expected, the

values of the potentials increase from the surface layer to the metal layer to the diffuse layer. Next, we note that the metal potential ϕ_β is much lower for coated channels than for bare channels, while the surface potential ϕ_0 and the diffuse potential ϕ_d remain almost the same. In all cases, we note that the metal and diffuse potentials increase with ionic strength whereas the surface potential for the bare channel decreases slightly.

For cases 1 and 2, respectively, Figs. 6 and 7b show the surface charge densities at the surface, metal and diffuse layer. Here, we note that the charge density at the surface decreases with ionic strength, whereas the charge density at the metal layer increases with ionic strength, both more pronounced for the coated surface than for the bare.

By comparing Figs. 6 and 7 we note that changes in C_2 primarily affect the diffuse layer potential ϕ_d and charge density σ_d. Different values of C_2 for the bare and coated surfaces will therefore not affect much the final outcome of the fitting procedure in terms of the other variables such as the surface charge density σ_0. This is the reason that the R^2 is essentially the same for both cases as seen in Table 5. These observations speak in favor of using the values of C_2 in case 2 in Table 5.

6. Discussion

There is a clear trend of the capillary filling length ratio L_d/L_{fl} decreasing with increasing ionic strength. We can explain this through Eq. (25), where we describe the length ratio as a function of the surface charge density σ_0 and the proton concentration B_s needed to lower the pH of the buffer front to pH_{pzc}. Since the length ratio decreases we conclude that B_s increases faster than σ_0 decreases. B_s is mainly influenced by the $pH_{pzc} = (pK_+ + pK_-)/2$ and thus by pK_+.

To achieve the most reliable fit with the data, we investigated the influence of C_1, C_2, pK_K, pK_+, pK_-, and Γ_{tot} by varying each parameter individually around some chosen reference value (see Supporting information Sec. S5). Here we summarize the observed sensitivity of each parameter. First, changing C_1 raises and lowers the values of L_d/L_{fl} without significantly affecting the shape of the curve. Given the fact that the bare and coated experimental data curves follow the same shape, this strongly suggests that C_1 changes with surface type. Next we notice that C_2, pK_K, pK_-, and Γ_{tot} have a negligible effect on the L_d/L_{fl} curve, which indicates that these parameters are most likely constant and can be determined from literature values. However, as mentioned in the previous section, we notice that varying C_2 has a strong influence on the ζ potential, which is consistent with the assumption that it only affects ϕ_d and σ_d. Finally, we note that varying pK_+ has a strong influence on the value of L_d/L_{fl} at low concentrations but very little effect at high concentrations. Indeed, this is what we observe in our experimental data and therefore this suggests that pK_+ must be varied with surface composition. Furthermore, because pK_+ couples into B_s through pH_{pzc} it should have an influence on L_d/L_{fl}. In conclusion, C_1 and pK_+ are our obvious choices for parameters to be fit.

The literature value of $pK_+ = -1.9$ [27] for the bare silica surface is close to the value of -1.61 theoretically determined for the bare channel when using the case 2 capacitance value of $C_2 = 0.80$ F m^{-2}. For case 1 ($C_2 = 0.20$ F m^{-2}) the model calculates a higher value ($pK_+ = -1.03$) which lends further support for case 2. For the coated channels $pK_+ = -0.54$ (case 1) and $pK_+ = -0.29$ (case 2). Given the strong evidence for case 2 parameters we believe that $pK_+ = -0.29$ should be the value used in the future for cyanosilane-coated silica surfaces. However, we emphasize that this value is contingent upon the experimental conditions used in our study. For example, when comparing values of C_1 with Wang et al. [23] we find slightly different values which most likely can be attributed to the fact that we used different electrolytes.

Examining the trends seen in Fig. 7 we note that the surface potential ϕ_0 varies less than 10% over the range of ionic strength used in this study, which validates a constant surface potential model in both bare and coated channels given our experimental conditions. Next, we note that the metal potential ϕ_β and diffuse layer potential ϕ_d significantly increase with increasing ionic strength, which is consistent with trends reported in literature [23]. Consistent with case 2, we hypothesize that the amount of metal ions that can adsorb onto the surface is highly dependent on the composition of the surface. Moreover, because $C_1^{bare} \sim 0.7$ F m^{-2} is much lower than $C_1^{coated} \sim 14$ F m^{-2} this hypothesis is further justified since ϕ_β^{bare} is much higher than ϕ_β^{coated}.

Finally, the surface charge density σ_0 of the coated channels decreases more rapidly than that of the bare channels also due to the fact that C_1 is much higher for the coated channels. This again indicates that more metal ions can adsorb to the surface without changing the potential. Because $\sigma_\beta = -(\sigma_0 + \sigma_d)$, σ_β increases with increasing ionic strength faster in the coated channels than in the bare channels. We note that σ_d is relatively constant with ionic strength and surface coating providing justification to use the Grahame Eq. (15) to solve for diffuse layer potentials [30]. Using our optimized values of C_2, Fig. 3c shows that σ_d for the bare channel is higher than the coated channel, matching experimental trends (data not shown). We note that σ_d is lower than the 60 mC m^{-2} quoted in literature for fused silica nanochannels [45] but similar to the 25 mC m^{-2} quoted for amorphous silica nanochannels [46]. Stein et al. [45] used the neutral CH_3 head group doctodecyltrichlorosilane as surface coating and found a decrease in the surface charge density, consistent with our curves in the inset in Fig. 7b. However, in both Refs. [45,46] aqueous KCl was used as the electrolyte in contrast to our KH_2PO_4, and as discussed in Refs. [47,48] the different co-ions may lead to different actual values of σ_d.

We can also use our model to examine the surface site densities Γ_i. Fig. 8 shows Γ_i for bare (open symbols and dashed curves) and coated (filled symbols and full curves) channels using case 2 parameters. The amount of adsorbed cations (K^+) is significant for the coated channels especially at high ionic strengths when compared to the bare channels. This is consistent with the result of C_1 being much higher for the coated channels than for the bare channel. Furthermore, a sensitivity analysis of the effect of Γ_{tot} shows that changing the amount of sites available at the wall does not change the results shown in Fig. 7 (see Supporting information Sec. S5). Therefore, our results will be relatively accurate despite

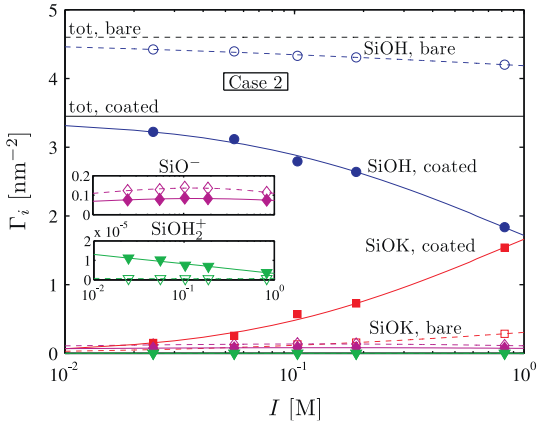

Fig. 8. The surface site densities Γ_i for bare channels (open symbols and dashed curves) and coated channels (filled symbols and full curves) for case 2. The four surface site densities are Γ_{SiOH} (blue circles), Γ_{SiO^-} (purple diamonds), $\Gamma_{SiOH_2^+}$ (green triangles), and Γ_{SiOK} (red squares). The insets are magnifications of the low-density sites Γ_{SiO^-} and $\Gamma_{SiOH_2^+}$. (For interpretation of the references to colour in this figure legend, the reader is referred to the web version of this article.)

the experimental uncertainty of Γ_{tot} after coating with cyanosilane.

Throughout our experiments, we have assumed that the flourescein quenches exactly at pH_{pzc}. This is a reasonable assumption as flourescein is known to quench at pH values below 5 [49,50], and our model predicts $pH_{pzc} < 5$ in all cases (see Table 5 and Supporting information Sec. S6).

To date, it has been difficult or almost impossible to use a model to predict experimental data mainly due to difficulties in modeling the Stern layer [15]. Here, we show that by just changing C_1, C_2, and pK_+ while using literature values for all other surface parameters, we can find ζ potential values that almost exactly match experimentally determined values for both bare and cyanosilane-coated silica nanochannels. We believe our model will be important to predict experimentally observed phenomena, for example, geological studies have shown that silica is known to dissolve in the presence of an electrolyte [51]. This dissolution process, although negligible in microfluidic systems, may become important at the nanoscale. Therefore, having a model which can predict the change of channel size with the measured experimental values may prove to be of utility to the field. We are currently pursuing such uses of the model.

7. Conclusion

In this work, we presented a combined theoretical and experimental analysis of the solid–liquid interface of fused-silica nanofabricated channels with and without hydrophilic 3-Cyanopropyldimethlychlorosilane coating. Our theoretical model couples chemical equilibrium theory of both the surface and the bulk buffer with a self-consistent extended Gouy–Chapman–Stern model of the electrochemical triple layer. We use the model to optimize the surface parameters given both experimental capillary filling data and electro-osmotic current-monitoring data, which allows for analysis of surface parameters both with and without the influence of applied external fields. Our model shows that the important fitting parameters are the capacitance C_1 between the silica layer and the metal ion layer, as well as the pK_+ constant. Furthermore, we find that changing the capacitance C_2 between the metal ion layer and the diffuse layer with surface composition results in more accurate fits of experimentally determined ζ potential values. This model is of value to predict experimentally observed phenomena in nanofluidic systems.

Acknowledgments

K.G.H. Janssen is grateful acknowledged for helpful and clarifying discussions and for sharing data from Ref.[9]. We thank M.B.L. Mikkelsen and T. Wynne for help with mask design and fabrication.

Appendix A. Supplementary material

Supplementary data associated with this article can be found, in the online version, at doi:10.1016/j.jcis.2010.09.025.

References

[1] T.M. Squires, S.R. Quake, Rev. Mod. Phys. 77 (2005) 977.
[2] R. Schoch, J. Han, P. Renaud, Rev. Mod. Phys. 80 (2008) 839.
[3] W. Sparreboom, A. van den Berg, J.C.T. Eijkel, Nat. Nanotechnol. 4 (2009) 713.
[4] L. Bocquet, E. Charlaix, Chem. Soc. Rev. 39 (2010) 1073.
[5] M. Napoli, J.C.T. Eijkel, S. Pennathur, Lab Chip 10 (2010) 957.
[6] P.M. Biesheuvel, W.B.S. de Lint, J. Colloid Interface Sci. 241 (2001) 422.
[7] W.B.S. de Lint, P.M. Biesheuvel, H. Verweij, J. Colloid Interface Sci. 251 (2002) 131.
[8] N.R. Tas, J.W. Berenschot, P. Mela, H.V. Jansen, M. Elwenspoek, A. van den Berg, Nano Lett. 2 (2002) 1031.
[9] K.G.H. Janssen, H.T. Hoang, J. Floris, J. de Vries, N.R. Tas, J.C.T. Eijkel, T. Hankemeier, Anal. Chem. 80 (2008) 8095.
[10] H.T. Hoang, I.M. Segers-Nolten, J.W. Berenschot, M.J. de Boer, N.R. Tas, J. Haneveld, M.C. Elwenspoek, J. Micromech. Microeng. 19 (2009) 065017.
[11] R.B.H. Veenhuis, E.J. van der Wouden, J.W. van Nieuwkasteele, A. van den Berg, J.C.T. Eijkel, Lab Chip (2009).
[12] C.L. Rice, R. Whitehead, J. Phys. Chem. 69 (1965) 4017.
[13] S. Pennathur, J.G. Santiago, Anal. Chem. 77 (2005) 6772.
[14] S. Pennathur, J.G. Santiago, Anal. Chem. 77 (2005) 6782.
[15] M.Z. Bazant, M.S. Kilic, B.D. Storey, A. Ajdari, Adv. Colloid Interface Sci. 152 (2009) 48.
[16] N.R. Tas, P. Mela, T. Kramer, J.W. Berenschot, A. van den Berg, Nano Lett. 3 (2003) 1537.
[17] N.R. Tas, J. Haneveld, H.V. Jansen, M. Elwenspoek, A. van den Berg, Appl. Phys. Lett. 85 (2004) 3274.
[18] L.H. Thamdrup, F. Persson, H. Bruus, A. Kristensen, H. Flyvbjerg, Appl. Phys. Lett. 91 (2007) 163505.
[19] S.H. Behrens, D.G. Grier, J. Chem. Phys. 115 (2001) 6716.
[20] J.A. Davis, R.O. James, J.O. Leckie, J. Colloid Interface Sci. 63 (1978) 480.
[21] J.A. Davis, J.O. Leckie, J. Colloid Interface Sci. 67 (1978) 90.
[22] R. Charmas, W. Piasecki, W. Rudzinski, Langmuir 11 (1995) 3199.
[23] M. Wang, A. Revil, J. Colloid Interface Sci. 343 (2010) 381.
[24] A. Persat, M.E. Suss, J.G. Santiago, Lab Chip 9 (2009) 2454.
[25] D.R. Lide, CRC Handbook of Chemistry and Physics, 90th ed., CRC Press/Taylor and Francis, Boca Raton, FL, 2010, (Internet Version 2010).
[26] S.A. Smith, W.A. Pretorius, Water SA 28 (2002) 395.
[27] T. Hiemstra, W.V. Riemsdijk, G. Bolt, J. Colloid Interface Sci. 133 (1989) 91.
[28] P. Schindler, H.R. Kamber, Helv. Chim. Acta 51 (1968) 1781.
[29] S. Levine, A.L. Smith, Discuss. Faraday Soc. 52 (1971) 290.
[30] D.E. Yates, S. Levine, T.W. Healy, J. Chem. Soc., Faraday Trans. 1 (70) (1974) 1807.
[31] P.M. Biesheuvel, J. Colloid Interface Sci. 275 (2004) 514.
[32] C.G. Armistead, A.J. Tyler, F.H. Hambleton, S.A. Mitchell, J.A. Hockey, J. Phys. Chem. 73 (1969) 3947.
[33] D.C. Grahame, Chem. Rev. 41 (1947) 441.
[34] F. Persson, L.H. Thamdrup, M.B. Mikkelsen, S.E. Jaarlgard, P. Skafte-Pedersen, H. Bruus, A. Kristensen, Nanotechnology 18 (2007) 245301.
[35] R.J. White, E.N. Ervin, T. Yang, X. Chen, S. Daniel, P.S. Cremer, H.S. White, J. Am. Chem. Soc. 129 (2007) 11766.
[36] S.J. Oh, S.J. Cho, C.O. Kim, J.W. Park, Langmuir 18 (2002) 1764.
[37] T. Driehorst, P. O'Neill, D.K. Fygenson, S. Pennathur, in: Proceedings of the Thirteenth International Conference on Miniaturized Systems on Miniaturized Chemical and BioChemical Analysis Systems (uTAS2009), Jeju, Korea, 1st–5th November, 2009.
[38] S. Falipou, J.M. Chovelon, C. Martelet, J. Margonari, D. Cathignol, Sens. Actuators, A 74 (1999) 81.
[39] S. Falipou, J. Chovelon, C. Martelet, J. Margonari, D. Cathignol, Bioconjugate Chem. 10 (1999) 346.
[40] A. Sze, D. Erickson, L. Ren, D. Li, J. Colloid Interface Sci. 261 (2003) 402.
[41] R.F. Probstein, Physicochemical Hydrodynamics: an Introduction, Wiley-Interscience, 1994.
[42] E.W. Washburn, Phys. Rev. 17 (1921) 273.
[43] The full code can be downloaded at <http://www.nanotech.dtu.dk/microfluidics>, 2010.
[44] J. Lützenkirchen, Environ. Sci. Technol. 32 (1998) 3149.
[45] D. Stein, M. Kruithof, C. Dekker, Phys. Rev. Lett. 93 (2004).
[46] R.B. Schoch, P. Renaud, Appl. Phys. Lett. 86 (2005) 253111.
[47] Y. Gushikem, J. Moreira, J. Colloid Interface Sci. 107 (1985) 70.
[48] L.T. Kubota, J.C. Moreira, Y. Gushikem, Analyst 114 (1989) 1385.
[49] M.M. Martin, L. Lindqvist, J. Lumin. 10 (1975) 381.
[50] H. Diehl, R. Markuszewski, Talanta 32 (1985) 159.
[51] G.W. Greene, K. Kristiansen, E.E. Meyer, J.R. Boles, J.N. Israelachvili, Geochim. Cosmochim. Acta 73 (2009) 2862.

Appendix C

Paper published in J Colloid Interface Sci

M. B. Andersen, H. Bruus, J. P. Bardhan, and S. Pennathur, Streaming current and wall dissolution over 48 h in silica nanochannels, J Colloid Interface Sci 360, 262 (2011).

Journal of Colloid and Interface Science 360 (2011) 262–271

Contents lists available at ScienceDirect

Journal of Colloid and Interface Science

www.elsevier.com/locate/jcis

Streaming current and wall dissolution over 48 h in silica nanochannels

Mathias Bækbo Andersen [a,*], Henrik Bruus [a], Jaydeep P. Bardhan [b], Sumita Pennathur [c]

[a] Department of Micro- and Nanotechnology, Technical University of Denmark, DTU Nanotech Building 345 East, DK-2800 Kongens Lyngby, Denmark
[b] Department of Molecular Biophysics and Physiology, Rush University Medical Center, Chicago, IL 60612, USA
[c] Department of Mechanical Engineering, University of California, Santa Barbara, CA 93106, USA

ARTICLE INFO

Article history:
Received 30 November 2010
Accepted 7 April 2011
Available online 16 April 2011

Keywords:
Nanofluidics
Silica dissolution
Gouy–Chapman–Stern model
Streaming current
Cyanosilane surface coating

ABSTRACT

We present theoretical and experimental studies of the streaming current induced by a pressure-driven flow in long, straight, electrolyte-filled nanochannels. The theoretical work builds on our recent one-dimensional model of electro-osmotic and capillary flow, which self-consistently treats both the ion concentration profiles, via the nonlinear Poisson–Boltzmann equation, and the chemical reactions in the bulk electrolyte and at the solid–liquid interface. We extend this model to two dimensions and validate it against experimental data for electro-osmosis and pressure-driven flows, using eight 1-μm-wide nanochannels of heights varying from 40 nm to 2000 nm. We furthermore vary the electrolyte composition using KCl and borate salts, and the wall coating using 3-cyanopropyldimethylchlorosilane. We find good agreement between prediction and experiment using literature values for all parameters of the model, i.e., chemical reaction constants and Stern-layer capacitances. Finally, by combining model predictions with measurements over 48 h of the streaming currents, we develop a method to estimate the dissolution rate of the silica walls, typically around 0.01 mg/m^2/h, equal to 45 pm/h or 40 nm/yr, under controlled experimental conditions.

1. Introduction

Advances in nanofabrication technology promise to allow the emergence of nanofluidic devices as enabling technologies in a diverse set of emerging applications, including pharmaceuticals, environmental health and safety, and bioanalytical systems. Nanoscale coupling of surface chemistry, electrokinetics, and fluid dynamics provides a rich set of phenomena not available in larger devices, which in turn allow nanofluidic systems to offer novel functional capabilities. To fully exploit the potential of nanofluidics, a detailed understanding of electrokinetic phenomena is thus required including the distributions of ions in electrical double layers, surface charge effects, and electric potential effects on the fluid [1–5].

Because fused silica is one of the most prevalent materials used to fabricate nanochannels, its behavior in electrolyte solutions is particularly important and has received much specialized attention. Two important aspects pertaining to the use of silica for nanosystems are deterioration due to dissolution [6–9] and the effects induced by corners in channels where a full 2D modeling of the channel cross section is necessary rather than the usual planar 1D approximation [10–13].

Regarding the dissolution rate, it is important to determine whether dissolution of silica is significant when it is used to confine electrolytes in nanometer-sized channels. For example, Greene et al. [9] studied the dissolution rates in systems of electrolytes in nanometer-sized confinement under pressure between quartz (SiO_2) and mica. They found that the dissolution rate of quartz initially is 1–4 nm/min and that this drops over several hours to a constant rate around 0.01 nm/min or 5 μm/yr. Such rates might influence the long-term stability and operability of silica nanofluidic devices, and devising ways to inhibit such dissolution phenomena, by surface coatings [14], is therefore important.

Regarding 2D corner effects in pressure-driven flows in nanometer-sized geometries, some studies involved complex or poorly defined networks of nanochannels, such as those found in porous glass [15], columns packed with latex beads [16], and sandstone cores [17], while other studies on desalination [18–20] and energy conversion [15,21–24] involved geometries where simpler 1D models sufficed. In the latter studies, streaming currents were measured in individual rectangular silica nanochannels as functions of varying pressure, channel height, as well as salt concentration. Good agreement was obtained between measurements and predictions from different 1D models for the electrostatic properties of the surface, including chemical-equilibrium models. The 1D planar-wall chemical-equilibrium model has proved successful in several other studies [25–28]. Recently, we extended the chemical-equilibrium model to allow surface-related parameters, such

* Corresponding author.
E-mail address: mathias.andersen@nanotech.dtu.dk (M.B. Andersen).

0021-9797/$ - see front matter © 2011 Elsevier Inc. All rights reserved.
doi:10.1016/j.jcis.2011.04.011

as Stern-layer capacitance C_s and the surface equilibrium pK_a constants, to vary with the composition of the solid-liquid interface and validated it experimentally by both capillary filling methods and electrokinetic current monitoring [14,29]. However, as rectangular nanochannels with low aspect ratios are now readily fabricated and operated with significant overlap of the electric double layer, as in this work and by others [10–13], it is relevant to study how the presence of side walls and corners affects the electrokinetics of chemical-equilibrium models.

The structure of the paper is as follows. We present our theoretical 2D model in Section 2 and describe its numerical implementation along with a theoretical 1D–2D modeling comparison in Section 3. In contrast to our previous work [14,29], this model contains no adjustable parameters. We validate our model by comparing predicted values of electro-osmotic flow velocity and of streaming currents to those measured in eight different bare and cyanosilane-coated nanochannels with depths ranging nominally between 40 nm and 2000 nm. The experimental setup and procedure are described in Section 4, while the theoretical and experimental results are presented and discussed in Section 5. At the end of Section 5, we combine model prediction with 48 h of streaming current measurements to estimate the dissolution rate of the silica walls under controlled experimental conditions. We end with concluding remarks in Section 6.

2. Theory

Theoretical modeling of ionic transport in nanochannels is traditionally based on three components: the Gouy–Chapman–Stern model of electrostatic screening, a position-independent boundary condition at the wall (either given potential, given surface charge, or equilibrium deprotonation reactions [25–28,30,31,14,29]), and continuum fluid dynamics equations [32,33,21–24,34,5,29]. In the present work, we extend the prior chemical-equilibrium modeling by allowing the surface charge, potential and pH (the concentration of the hydronium ion H^+) to vary with position along the surface through a full 2D modeling of the channel cross section. The bulk pH is a function of the composition of the electrolyte, and the entire bulk chemistry is modeled using chemical-equilibrium acid–base reactions described in Section 2.1; the physical parameters used in our model are listed in Table 1. After solving the nonlinear electrostatic Poisson–Boltzmann equation in the full 2D cross-sectional geometry, we determine the electro-osmotic flow or the streaming current arising in the system by applying an external electrical potential drop or a pressure drop along the channel, respectively.

Our extended 2D electrokinetic chemical-equilibrium model thus consists of four parts: (*i*) chemical reactions in the bulk, which determine the concentrations of the ions in our electrolyte $[H^+, OH^-, HCO_3^-, CO_3^{2-}, K^+, Cl^-, Na^+, B(OH)_4^-]$, (*ii*) chemical reactions at the surface, which determine the electric potential and charge of the bare or coated silica surface, (*iii*) the 2D Poisson–Boltzmann equation for the electrical potential combining the first two parts, and (*iv*) the 2D Stokes equation including external force densities from the externally applied drop along the channel in pressure or electrical potential. We solve parts (*i*)–(*iii*) self-consistently and then insert the resulting distributions of charged species in part (*iv*) to calculate the flow velocity and the current density. The silica wall is sketched in Fig. 1.

Table 1
Basic physical parameters used in our model.

Quantity	Symbol	Value	Unit
Temperature	T	296	K
Viscosity, electrolyte solution	η	930	μPa s
Permittivity, electrolyte solution	ε	691	pF m^{-1}
Length of nanochannel	L	20	mm
Stern capacitance, bare silica[a]	C_s	0.3	F m^{-2}
Stern capacitance, coated silica[b]	C_s	0.2	F m^{-2}
Surface site density, bare silica [c]	Γ	5.0	nm^{-2}
Surface site density, coated silica [d]	Γ	3.8	nm^{-2}

[a] From Ref. [21].
[b] From Refs. [35,14,29].
[c] From Refs. [35–37,27,29].
[d] From Ref. [38].

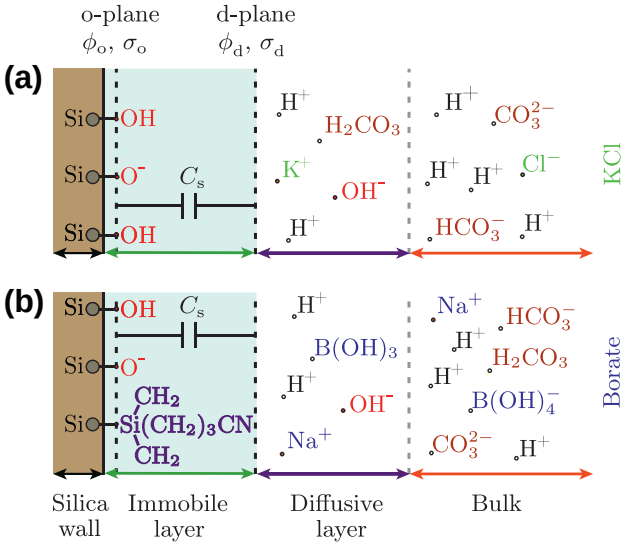

Fig. 1. (a) Sketch of a silica wall (brown) and its Stern layer (blue), with surface capacitance C_s, in contact with an aqueous KCl solution. The four regions of main interest are identified as: the silica wall, the immobile Stern layer, the diffusive layer, and the bulk. The dashed vertical line denoted "o-plane" is where the bound surface charge σ_o resides, while the dashed black line denoted "d-plane" marks the beginning of the diffuse, mobile layer, a layer stretching from the d-plane to the bulk, and in which a mobile screening charge per area $\sigma_d = -\sigma_o$ resides. The electrical potential at the o- and d-plane is denoted ϕ_o and ϕ_d, respectively. (b) Same as panel (a) except now for an electrolyte containing sodium borate ions. Also indicated is a surface coating of cyanosilane $Si(CH_2)_5CN$ molecules. C_s is constant along the surface, while σ_o and ϕ_o vary. (For interpretation of the references to color in this figure legend, the reader is referred to the web version of this article.)

2.1. Bulk chemistry

As in our previous work [14,29], we calculate all bulk ionic concentrations of the reservoirs using the method of "chemical families" [39,40]. Briefly, this approach provides a simple, yet powerful means to manage the book-keeping associated with modeling multiple protonatable species. For example, the chemical family for H_2CO_3 has three members: the fully protonated H_2CO_3 (valence 0), the singly deprotonated HCO_3^- (valence −1), and the doubly deprotonated HCO_3^{-2} (valence −2). We define the limits for the valence z_X of a chemical family X as $n_X \leqslant z_X \leqslant p_X$, so here $n_X = -2$ and $p_X = 0$. The chemical families relevant for this work, the associated dissociation reactions, and the reaction constants pK_{X,z_X} are listed in Table 2. We next employ two assumptions about the bulk solutions in the reservoirs: the total concentration c_X^{tot} of every chemical family is known, and the bulk solution is homogeneous and electrically neutral. This allows us to calculate the bulk concentrations c^b_{X,z_X} from the equations

$$K_{X,z_X} c^b_{X,z_X+1} = c^b_{X,z_X} c^b_H, \quad \text{dissociation reactions}, \tag{1a}$$

$$\sum_{z_X=n_X}^{p_X} c^b_{X,z_X} = c_X^{tot}, \quad \text{conservation of mass}, \tag{1b}$$

$$\sum_{X,z_X} z_X c^b_{X,z_X} = 0, \quad \text{charge neutrality}, \tag{1c}$$

Table 2
List of the chemical families X used in this work together with charge states z_X, the associated reaction schemes, and reaction constants $pK_{X,z_X} = -\log_{10}(K_X, z_X/1\ M)$. Note that the pK_{X,z_X} values are for dissociation processes. The silanol family involves surface reactions, while all other families involve bulk reactions.

Chemical family X	z_X	Reaction scheme (dissociation)		pK_{X,z_X}
Potassium	0	KOH		–
hydroxide	+1	KOH	$\rightleftharpoons K^+ + OH^-$	14.00 [a]
Sodium	0	NaOH		–
hydroxide	+1	NaOH	$\rightleftharpoons Na^+ + OH^-$	14.00 [a]
Hydrochloric	0	HCl		–
acid	−1	HCl	$\rightleftharpoons Cl^- + H^+$	−7.00 [a]
Boric	0	$HB(OH)_4$		–
acid	+1	$HB(OH)_4$	$\rightleftharpoons B(OH)_4^- + H^+$	9.24 [a]
Carbonic	0	H_2CO_3		–
acid	−1	H_2CO_3	$\rightleftharpoons HCO_3^- + H^+$	6.35[a]
	−2	HCO_3^-	$\rightleftharpoons CO_3^{2-} + H^+$	10.33[a]
Water	0	H_2O		
	±1[b]	H_2O	$\rightleftharpoons OH^- + H^+$	14.00
Silanol	0	SiOH		–
	−1	SiOH	$\rightleftharpoons SiO^- + H^+$	6.6 ±0.6 [c]

[a] From Ref. [41] at 25 °C.
[b] For sum over OH^- and H^+ ions see the remark after Eq. (1c).
[c] From Refs. [42,25,31,43,27,29].

where c_H^b is the bulk concentration of hydronium ions. Note that the index z_X includes neither H^+ nor OH^- for any family X, except for water where z_X includes both H^+ and OH^-. A more detailed account of the reactions is given in the Supplementary information.

Once the bulk concentrations c^b_{X,z_X} are known, two parameters characterizing the electrolyte can be determined: the ionic strength c_I and the Debye screening length λ_D,

$$c_I = \frac{1}{2}\sum_{X,z_X}(z_X)^2 c^b_{X,z_X}, \tag{2a}$$

$$\lambda_D = \left[\frac{\epsilon k_B T}{2e^2 c_I}\right]^{\frac{1}{2}}. \tag{2b}$$

The two ionic strengths used in this work are c_I = 1 mM and 20 mM, for which $\lambda_D \approx 10$ nm and 2 nm, respectively.

2.2. Surface chemistry

In Fig. 1 is shown a sketch of the interface between the silica wall and the electrolyte. We model the solid/liquid interface in three parts [14]: the silanol surface (the "o-surface" with surface charge σ_o and potential ϕ_o), the electrically charged, diffusive screening layer (extending a few times the Debye length λ_D from the "d-surface" and having space charge per area σ_d and zeta potential ϕ_d), and the immobile Stern layer in between having capacitance per unit area C_s. For bare silica surfaces, we use C_s = 0.3 F m^{-2} [21], and for cyanosilane-coated silica, we use C_s = 0.2 F m^{-2} consistent with Ref. [14].

For the pH range relevant in this work, deprotonation of silica is the only important surface reaction, making SiOH and SiO^- the only significant surface groups, and the corresponding equilibrium equation is,

$$SiOH \rightleftharpoons SiO^- + H_o^+, \tag{3a}$$

$$10^{-pK}\Gamma_{SiOH} = \Gamma_{SiO^-} c_H^o, \tag{3b}$$

where H_o^+ is a hydronium ion at the o-surface, Γ_i is the surface site density of surface group i, c_H^o is the concentration of hydronium ions at the o-surface, and pK = 6.6 ± 0.6 [42,25,31,43,27,29], see Table 2. The sum of the site densities equals the known total site density Γ [36,37,35,27,29,38],

$$\Gamma_{SiOH} + \Gamma_{SiO^-} = \Gamma = \begin{cases} 5.0\ nm^{-2}, & \text{bare silica}, \\ 3.8\ nm^{-2}, & \text{coated silica}, \end{cases} \tag{4}$$

and the surface charge is given by the site density of negative surface groups as

$$\sigma_o = -e\Gamma_{SiO^-}. \tag{5}$$

Assuming a Boltzmann distribution of ions, we obtain

$$c_H^o = c_H^b \exp\left(-\frac{e}{k_B T}\phi_o\right), \tag{6}$$

and the usual linear capacitor model of the immobile Stern layer becomes

$$C_s(\phi_o - \phi_d) = \sigma_o. \tag{7}$$

Finally, the diffuse-layer potential ϕ_d can be expressed in terms of the surface charge σ_o [25] by combining Eqs. (3b)–(7)

$$\phi_d(\sigma_o) = \frac{k_B T}{e}\left[\ln\left(\frac{-\sigma_o}{e\Gamma + \sigma_o}\right) - \frac{pH_b - pK}{\log_{10}(e)}\right] - \frac{\sigma_o}{C_s}, \tag{8}$$

where $pH_b = -\log_{10}(c_H^b/1\ M)$. This equation constitutes a nonlinear mixed boundary condition for the 2D Poisson–Boltzmann equation described in the following section.

2.3. Electrohydrodynamics in the 2D channel cross section

Much work in nanochannels has involved very large width-to-height ratios making a 1D approximation valid. However, for smaller aspect ratios, this approximation breaks down and a full 2D treatment of the channel cross section should at least be checked. Here, we set out to investigate the model predictions from such a 2D treatment using the chemical-equilibrium surface charge model of the previous section. For the experimental systems of interest in this work, the aspect ratio of the rectangular nanochannels ranges from 27 to 0.5, and in some cases involve overlapping or nearly overlapping electrical double layers, see Section 4. We verify our theoretical model by comparing the predictions with two independent sets of measurements: electro-osmotically driven flow and pressure-generated streaming currents.

For a straight nanochannel of length L along the x-axis, width w along the y-axis, and height $2h$ along the z-axis, the domain of interest is the 2D cross-sectional geometry of the nanochannel parallel to the yz-plane. The electrohydrodynamics of the electrolyte is governed by the Poisson–Boltzmann equation of the electric potential $\phi(y,z)$ coupled to the Stokes equation of the axial velocity field $u(y,z)$. The electric potential obeys the Poisson equation

$$-\epsilon\nabla^2\phi(y,z) = \rho_{el}(y,z), \tag{9}$$

where ρ_{el} is the electric charge density, which for Boltzmann-distributed ions is given by

$$\rho_{el}(y,z) = e\sum_X \sum_{z_X=n_X}^{p_X} z_X c^b_{X,z_X}(y,z)\exp\left[-\frac{z_X e\phi(y,z)}{k_B T}\right]. \tag{10}$$

Together, Eqs. (9) and (10) form the Poisson–Boltzmann equation. The nonlinear, mixed boundary condition for ϕ is

$$\boldsymbol{n}\cdot\nabla\phi = -\frac{1}{\epsilon}\sigma_o(\phi_d), \quad \text{at the d-surface}, \tag{11}$$

where $\boldsymbol{n}$ is the surface normal vector pointing into the electrolyte. Together with Eq. (8) this constitutes a mixed nonlinear boundary condition which can be neatly implemented using the weak form, finite element modeling formalism in COMSOL as described in the Supplementary information.

The Reynolds number for the flow of the electrolyte in the long, straight nanochannel is much smaller than unity, so the velocity

field is governed by the Stokes equation with a body-force density. From symmetry considerations, it follows that only the axial velocity component is non-zero and depends only on the transverse coordinates. In this work, the flow is either purely electro-osmotically driven or purely pressure driven, and the resulting velocity field is denoted u_{eo} and u_p, respectively. The Stokes equation for the two cases becomes

$$\nabla^2 u_{eo}(y,z) = -\rho_{el}(y,z)\frac{\Delta V}{\eta L}, \tag{12a}$$

$$\nabla^2 u_p(y,z) = -\frac{\Delta p}{\eta L}, \tag{12b}$$

where we have assumed that the gradients along x in the electric potential and in the pressure, due to the applied potential difference ΔV and applied pressure difference Δp, respectively, are constant. For both velocity fields, the usual no-slip boundary condition applies at the wall (the d-surface)

$$u_{eo} = u_p = 0, \quad \text{at the d-surface.} \tag{13}$$

Note that in our model the electric and hydrodynamic fields ϕ and u are only coupled in the electro-osmotic case, Eq. (12a).

Once the electric charge density $\rho_{el}(y,z)$, the electro-osmotically driven velocity field $u_{eo}(y,z)$, and the pressure-driven flow velocity $u_p(y,z)$ have been determined, the area-averaged electro-osmotic flow velocity $\langle u_{eo} \rangle$ and the streaming current I_p can be found as

$$\langle u_{eo}\rangle = \frac{1}{hw}\int_0^w \mathrm{d}y \int_0^h \mathrm{d}z\, u_{eo}(y,z), \tag{14a}$$

$$I_p = 2\int_0^w \mathrm{d}y \int_0^h \mathrm{d}z\, \rho_{el}(y,z) u_p(y,z). \tag{14b}$$

2.4. Non-dimensionalization

To facilitate our numerical implementation, we non-dimensionalize our equations. We introduce the thermal voltage ϕ_T, the velocity scale u_o, the capacitance scale C_o, and the streaming current scale I_p^o

$$\phi_T = \frac{k_B T}{e}, \quad u_o = \frac{\lambda_D^2 \Delta p}{\eta L}, \tag{15a}$$

$$C_o = \frac{e^2 \Gamma}{k_B T}, \quad I_p^o = e c_I \frac{\lambda_D^4 \Delta p}{\eta L}. \tag{15b}$$

Grouping quantities with dimension of length $\boldsymbol{r} = \{y,z,h,w\}$, we define our dimensionless quantities, denoted by a tilde, as

$$\tilde{\boldsymbol{r}} = \frac{\boldsymbol{r}}{\lambda_D}, \quad \tilde{u} = \frac{u}{u_o}, \quad \widetilde{C}_s = \frac{C_s}{C_o}, \quad \widetilde{C}_{dl} = \frac{C_{dl}}{C_o}, \tag{16a}$$

$$\tilde{\phi}_d = \frac{\phi_d}{\phi_T}, \quad \tilde{\sigma}_o = \frac{\sigma_o}{e\Gamma}, \quad \tilde{\rho}_{el} = \frac{\rho_{el}}{e c_I}, \quad \widetilde{I}_p = \frac{I_p}{I_p^o}, \tag{16b}$$

where $C_{dl} = \epsilon/\lambda_D$ is the low-voltage diffuse-layer capacitance. As we are especially interested in the effects occurring when the electric double-layers overlap, λ_D is chosen as normalization for the length scales. The non-dimensionalized governing equations become

$$\tilde{\nabla}^2 \tilde{\phi}(\tilde{y},\tilde{z}) = -\frac{1}{2}\tilde{\rho}_{el}(\tilde{y},\tilde{z}), \tag{17a}$$

$$\tilde{\nabla}^2 \tilde{u}_{eo}(\tilde{y},\tilde{z}) = -\chi\tilde{\rho}_{el}(\tilde{y},\tilde{z}), \tag{17b}$$

$$\tilde{\nabla}^2 \tilde{u}_p(\tilde{y},\tilde{z}) = -1, \tag{17c}$$

where $\chi = c_I e\Delta V/\Delta p$ is the dimensionless electrohydrodynamic coupling constant. The corresponding dimensionless boundary conditions at the d-surface are

$$\tilde{\phi}_d = \ln\left(\frac{-\tilde{\sigma}_o}{1+\tilde{\sigma}_o}\right) - \frac{\mathrm{pH}_b - \mathrm{p}K}{\log_{10}(\mathrm{e})} - \frac{\tilde{\sigma}_o}{\widetilde{C}_s}, \tag{18a}$$

$$\boldsymbol{n}\cdot\tilde{\nabla}\tilde{\phi} = -\frac{\tilde{\sigma}_o}{\widetilde{C}_{dl}}, \tag{18b}$$

$$\tilde{u}_{eo} = \tilde{u}_p = 0. \tag{18c}$$

The non-dimensionalized area-averaged electro-osmotic velocity and streaming current $\widetilde{I}_p$ become

$$\langle \tilde{u}_{eo}\rangle = \frac{1}{\tilde{h}\tilde{w}}\int_0^{\tilde{w}} \mathrm{d}\tilde{y} \int_0^{\tilde{h}} \mathrm{d}\tilde{z}\, \tilde{u}_{eo}(\tilde{y},\tilde{z}), \tag{19a}$$

$$\widetilde{I}_p = 2\int_0^{\tilde{w}} \mathrm{d}\tilde{y} \int_0^{\tilde{h}} \mathrm{d}\tilde{z}\, \tilde{\rho}_{el}(\tilde{y},\tilde{z})\tilde{u}_p(\tilde{y},\tilde{z}). \tag{19b}$$

3. Numerical simulation

Numerical simulations are performed using the finite-element-method software COMSOL combined with Matlab by implementing in 2D the dimensionless coupled equations of Section 2.4. The nonlinear, mixed boundary condition Eqs. (18a) and (18b) for the electrostatic problem is conveniently implemented using the method of Lagrange multipliers as described in the Supplementary information.

Due to the two symmetry lines of the rectangular cross section, we only consider the lower left quarter of the channel cross section. At the symmetry lines, we apply standard symmetry boundary conditions

$$\boldsymbol{n}\cdot\tilde{\nabla}\tilde{\phi} = 0, \tag{20a}$$

$$\boldsymbol{n}\cdot\tilde{\nabla}\tilde{u}_{eo} = 0, \tag{20b}$$

$$\boldsymbol{n}\cdot\tilde{\nabla}\tilde{u}_p = 0. \tag{20c}$$

To avoid numerical convergence problems near the corners of the cross section and to mimic fabrication resolution, we represent the corners by 1-nm-radius quarter circles.

The simulation accuracy has been checked in several ways. For very large aspect ratios, the 2D results agree well with those ob-

Table 3
The cross-sectional geometry of the eight different 20-mm-long channels used in experiments: average width w (±standard deviation Δw), average height $2h$ (±standard deviation Δh), aspect ratio $w/(2h)$, dimensionless channel half-height $\tilde{h} = h/\lambda_D$, and relative deviation in the streaming current between 1D and 2D modeling $\delta_{1D,2D}$. $\tilde{h}$ and $\delta_{1D,2D}$ are listed for the 1 mM KCl solution (pH 5.6 and λ_D = 10 nm) and for the 10 mM borate buffer (pH 9.24 and λ_D = 2 nm).

#	$w \pm \Delta w$ (nm) width	$2h \pm \Delta h$ (nm) height	$w/(2h)$ aspect ratio	$\tilde{h}$ KCl 1 mM	$\delta_{1D,2D}$ KCl (%)	$\tilde{h}$ borate 10 mM	$\delta_{1D,2D}$ borate (%)
1	1043 ± 100	38.6 ± 0.6	27.0	2.0	1.0	10	0.3
2	1090 ± 100	68.8 ± 0.8	15.0	3.6	1.3	16	0.3
3	1113 ± 100	82.5 ± 0.5	13.5	4.3	1.3	19	0.3
4	1118 ± 100	103 ± 0.6	10.9	5.4	1.4	24	0.3
5	1021 ± 100	251 ± 0.8	4.1	13	1.6	59	0.4
6	1099 ± 100	561 ± 1.0	2.0	29	1.6	131	0.3
7	1181 ± 100	1047 ± 2.0	1.1	55	1.5	245	0.3
8	1067 ± 100	2032 ± 2.0	0.5	106	1.7	475	0.4

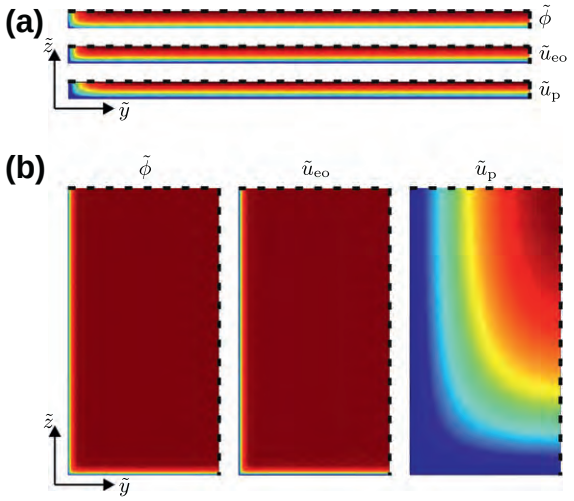

Fig. 2. Color plots (blue = zero, red = maximum) of calculated electric potential $\tilde{\phi}(\tilde{y},\tilde{z})$, electro-osmotic flow velocity $\tilde{u}_{eo}(\tilde{y},\tilde{z})$, and pressure-driven flow velocity $\tilde{u}_p(\tilde{y},\tilde{z})$ in the lower left corner of the rectangular nanochannel cross section. Full lines are the silica walls, while dashed lines are symmetry lines. Parameters correspond to the case of an aqueous 1 mM KCl solution (pH 5.6 and $\lambda_D \simeq 10$ nm) in bare silica channels (C_s = 0.3 F m^{-2}, Γ = 5.0 nm^{-2}, and pK = 6.6). (a) The shallowest channel used in our study; channel #1 in Table 3 with $w/(2h)$ = 27 and $\tilde{h} = 2$. (b) The tallest channel used in our study; channel #8 in Table 3 with $w/(2h)$ = 0.5 and $\tilde{h} = 106$. (For interpretation of the references to color in this figure legend, the reader is referred to the web version of this article.)

tained by a standard 1D method from the literature (data not shown). In addition, mesh convergence tests have been performed and show good convergence properties; an example is given in the Supplementary information of a plot of the calculated streaming current I_p as a function of the number of finite elements. Adequate convergence is achieved when employing more than a few thousand elements. Finally, by direct substitution of the computed solution, we have verified that the nonlinear, mixed boundary condition Eqs. (18a) and (18b) is obeyed. All tests we have performed support the claim that our predicted currents should be accurate to a relative error of 10^{-4} or better.

Qualitative color plots of calculated $\tilde{\phi}(\tilde{y},\tilde{z})$, $\tilde{u}_{eo}(\tilde{y},\tilde{z})$, and $\tilde{u}_p(\tilde{y},\tilde{z})$ are shown in Fig. 2 for the nanochannel cross sections having the largest and smallest aspect ratio, $w/(2h)$ = 27 in panel (a) and 0.5 in panel (b), respectively. Parameters correspond to the case of an aqueous 1 mM KCl solution (pH 5.6 and $\lambda_D \simeq 10$ nm) in bare silica channels (C_s = 0.3 F m^{-2}, Γ = 5.0 nm^{-2}, and pK = 6.6). In the shallow channel, panel (a), corresponding to channel #1 in Table 3 with $w/(2h)$ = 27 and $\tilde{h} = 2$, all three fields $\tilde{\phi}, \tilde{u}_{eo}$, and $\tilde{u}_p$, depend only on the z-coordinate except for the small edge region; thus, a 1D approximation is valid. In contrast, for smaller aspect ratio, see panel (b), corresponding to channel #8 in Table 3 with $w/(2h)$ = 0.5 and $\tilde{h} = 106$, only $\tilde{\phi}$ and $\tilde{u}_{eo}$ can locally be approximated by a 1D model, whereas this is clearly not the case for the pressure-driven velocity field $\tilde{u}_p$.

Furthermore, using our 2D model, we find that employing either constant-potential or constant-surface-charge boundary conditions is not accurate for small aspect-ratio channels. For the smallest channel height, $\tilde{h} = 2.0$, we plot in Fig. 3a the relative deviation for quantity f

$$\delta_{1D,2D} = \frac{f_{1D} - f_{2D}}{f_{2D}}, \tag{21}$$

of the locally varying value from the 2D model to that from a corresponding 1D model for the zeta potential ϕ_d (thick red curve) and

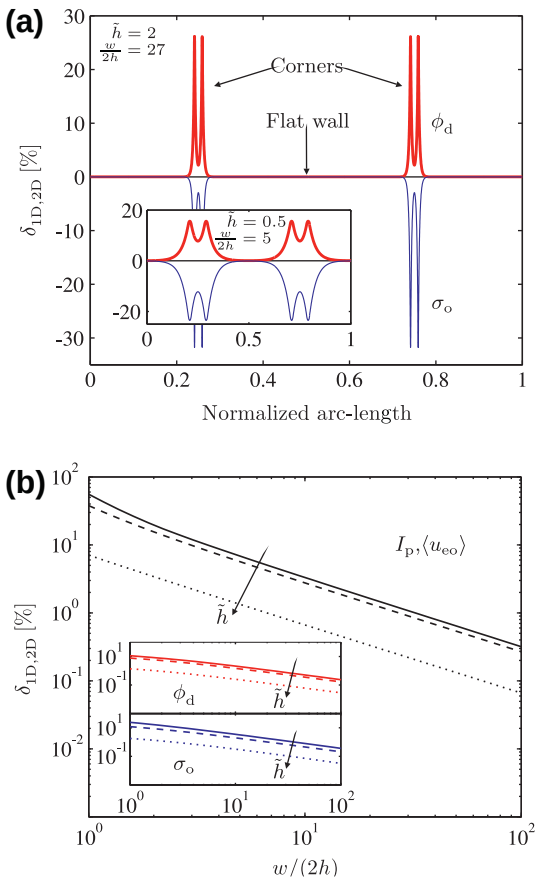

Fig. 3. The effect of corners calculated in 2D. (a) Relative deviation between the locally varying value from the 2D model and the constant value from a 1D model of the zeta potential ϕ_d (thick red curve) and surface charge σ_o (thin blue curve) versus the normalized arc-length along the d- and o-surface for channel #1 in Table 3 with 1 mM KCl, $\tilde{h} = 2$ and $w/(2h)$ = 27. The inset shows the case of $\tilde{h} = 0.5$ and $w/(2h)$ = 5. (b) Relative deviation of the value from the 2D model of the area-averaged electro-osmotic velocity $\langle u_{eo} \rangle$ (black), the streaming current I_p (black), the surface-average of ϕ_d (inset, blue), and the surface-average of σ_o (inset, red) to the corresponding values from a 1D model versus the aspect ratio $w/(2h)$ for $\tilde{h} = 0.5$ (full curves), $\tilde{h} = 2$ (dashed curves) and $\tilde{h} = 13$ (dotted curves). (For interpretation of the references to color in this figure legend, the reader is referred to the web version of this article.)

the surface charge σ_o (thin blue curve) along the normalized arc-length s of the d- and o-surfaces. This clearly shows the dependence of these variables on the position along the boundary of the 2D cross section: near the corners, the value of the potential increases about 25% and the surface charge drops about 30%. The inset in Fig. 3a shows the case with a higher degree of double-layer overlap, $\tilde{h} = 0.5$, and with smaller aspect ratio $w/(2h)$ = 5. Comparing the inset with the figure, it is clear that as the double-layer overlap becomes larger and the aspect ratio smaller 2D corner effects becomes increasingly significant as compared to a 1D model. We can therefore conclude that significant changes can be induced at corners in 2D domains in the chemical-equilibrium model. We now turn to look at how the combined effects from the equilibrium model and the presence of side-walls due to finite aspect-ratio geometries influence the difference between 1D and 2D modeling.

In Fig. 3b is shown a log-log plot of the relative deviation $\delta_{1D,2D}$ of the value from the 2D model of the area-averaged electro-osmotic velocity $\langle u_{eo} \rangle = \int_\Omega u_{eo}(y,z) dA$ (black), the streaming current I_p (black), the surface-averaged zeta-potential $\int_{\partial\Omega} \phi_d ds$ (inset, red), and the surface-averaged surface-charge $\int_{\partial\Omega} \sigma_o ds$ (inset, blue) to the corresponding values from a 1D model as a function of the aspect ratio $w/(2h)$. Three different cases are shown: strong double-

layer overlap, $\tilde{h} = 0.5$ (full curves), moderate overlap, $\tilde{h} = 2.0$ (dashed curves, corresponding to channel #1 in Table 3), and no overlap, $\tilde{h} = 13$ (dotted curves, corresponding to channel #5 in Table 3). Large deviations are observed for the streaming current in channels with aspect ratio close to unity: $\delta_{1D,2D} = 56\%$ for $\tilde{h} = 0.5$, 38% for $\tilde{h} = 2$ and 7% for $\tilde{h} = 13$. We also note that as the aspect ratio increases, the relative deviation becomes smaller with a slope close to -1 in the log-log plot indicating that the relative deviation is inversely proportional to the aspect ratio. It is remarkable that the relative deviations for the area-averaged electro-osmotic flow velocity and the streaming current are nearly identical and that they therefore cannot be distinguished in Fig. 3b.

To obtain a significant deviation $\delta_{1D,2D}$ between the 1D and 2D models, the corner regions must be significant, and thus the aspect ratio must be low ($2h \approx w$) and the double layers must overlap ($\tilde{h} \approx 1$). Theoretically, this follows from the observations that the electrokinetic effects are governed by the smallest length scale λ_D and the 2D dependence of the velocity field is unimportant: for a smooth, cusp-less surface we denote the local normal and tangential coordinates relative to the surface by ν and τ, respectively. Away from the corners, we have $\rho_{el}(\nu,\tau) \approx \rho_{el}(\nu)$, which decays on the small scale λ_D. Hence, by a Taylor expansion of the velocity around the no-slip value at the boundary, we obtain $\rho_{el}(\nu)u_p(\nu,\tau) \approx \rho_{el}(\nu)\nu\boldsymbol{n}\cdot\nabla u_p$. Neglecting corner effects (an error of the order $1/\tilde{h}$) and introducing $J_{\rho_{el}} = \int_0^\infty \nu\rho_{el}(\nu)d\nu$, the streaming current can therefore be written as

$$I_p = \int_\Omega \rho_{el}u_p d\nu d\tau \approx J_{\rho_{el}}\int_{\partial\Omega}\boldsymbol{n}\cdot\nabla u_p d\tau = J_{\rho_{el}}\int_\Omega -\nabla^2 u_p da$$
$$= J_{\rho_{el}}\frac{\Delta p}{\eta L}hw, \qquad (22)$$

which gives the same result in 1D and in 2D. If the 1D approximation involves neglecting the entire edge region, we expect $\delta_{1D,2D} \approx 2h/w$ as seen in Fig. 3. If only the corner regions (of size λ_D) are neglected, we expect $\delta_{1D,2D} \approx 1/\tilde{h}$. From Table 3 for the 1-mM KCl solution, we expect channels #1–4 to have $\delta_{1D,2D} \lesssim 1\%$ due to $2h/w \lesssim 1\%$, channels #6–8 to have $\delta_{1D,2D} \lesssim 3\%$ due to $1/\tilde{h} \lesssim 3\%$, and channel #4 to have $\delta_{1D,2D} \approx 7\%$ due to $1/\tilde{h} \approx 7\%$. The actual values are $\delta_{1D,2D} < 2\%$. The deviations for the 10-mM borate are expected to be even lower as $\tilde{h}$ is lower, and we see that $\delta_{1D,2D} < 0.4\%$. Although for the parameters set by our experimental channels there is not a significant difference between 1D and 2D modeling, Fig. 3 shows for which parameters this in fact is the case.

4. Experimental

The theoretical model presented above is tested against streaming current and electro-osmosis experiments performed on eight different in-house fabricated silica nanochannels, with either bare or cyanosilane-coated walls, and with two different electrolytes, a 1 mM KCl solution and a 10 mM borate solution.

4.1. Device fabrication and electrolytes

We fabricated nanochannel devices in fused-silica wafers (Hoya, model 4W55-325-15C) using conventional MEMS processing techniques. The fabrication protocol was originally developed at the Stanford Nanofabrication Facility (SNF), and detailed fabrication steps and guidelines for fabricating nanochannel devices are reported elsewhere [44]. Briefly, standard photolithography was used with very short etching processes to yield channels with micrometer lateral features and nanometer depths. In this particular study, we used a reactive ion etcher to fabricate straight anisotropic channels of length $L = 20$ mm with rectangular cross

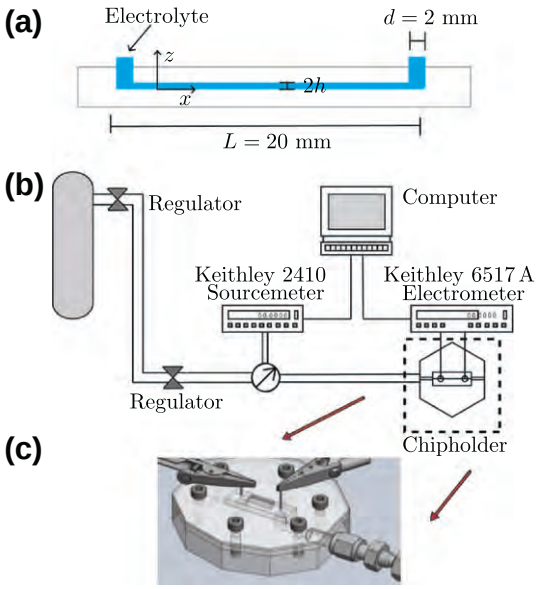

Fig. 4. (a) Side-view sketch of a nanofluidic channel used in our study. Channel lengths are typically (20 ± 1) mm, with inlet and exit diameters of 2 mm. Channel heights $2h$ vary from (38.6 ± 0.6) nm to (2032 ± 2) nm. KCl or borate buffers were the working electrolytes; channels were fabricated from fused silica, with one set coated with cyanosilane. (b) Experimental setup schematic depicting flow path of electrolyte during streaming current measurements. A high-pressure tank (rated to 6000 psi) is regulated down to the desired pressure of 8 MPa through two regulators. A sourcemeter is used in combination with a pressure transducer to electronically record pressure. A 1-fA-sensitivity electrometer is used to measure streaming currents through a custom-built chipholder. (c) Close-up sketch of the chipholder.

sections of width $w = (1.0 \pm 0.1)$ μm and with eight different heights $2h$ varying nominally from 40 nm to 2000 nm, as outlined in Table 3. Prior to bonding the channel heights $2h$ were measured using a profilometer, AFM, and/or SEM at three different locations (2 mm, 4 mm, and 6 mm) along the channel, and as verified by AFM the channels showed a roughness of less than 0.2 nm rms. Each wafer resulted in 6–12 channels at the desired height, depending on yield (50–100%). The channels were connected to two 2-mm-diameter reservoirs designed to serve as filters and support structures, as well as to minimize dead volume in the channel, Fig. 4a.

To fabricate the wafer lid, we drilled via holes in a second, fused silica wafer. To create the enclosed nanochannel device, we permanently sealed the channel wafer and lid wafer using a thermal diffusion bonding process [44]. Additionally, as also described in Ref. [14], we coated one channel from each wafer with cyano-silane (3-cyanopropyldimethylchlorosilane, Gelest, Inc.) to minimize adsorption of analyte and inhibit silica dissolution at the channel surface. The coatings were applied by filling the channels with a 1 M solution of cyano-silane in acetonitrile and leaving the solution in the channels for 12 h, which is expected to saturate the available negatively charged sites (≃25% of all silanol groups) with a neutral head group [38]. The channels were then rinsed and immersed in ethanol to prevent polymer formation during storage.

In this study, we used 1 mM KCl solutions prepared by dissolving KCl pellets (EMD chemicals) in deionized water, as well as 10 mM sodium borate buffer ($Na_2B_4O_7{\cdot}10H_2O$) prepared by dissolving NaOH pellets (Sigma, Inc.) into Borax solution (Sigma, inc), titrating until the desired pH (9.2) was achieved, and finally diluting to 10 mM. The bulk conductivity and pH of the prepared solutions were periodically measured to make sure that variations (due to temperature and humidity) did not exceed 5% of the original value. All solutions were filtered with 0.2-μm syringe filters

prior to use, (Nalgene, Inc.). Buffer exchanges were performed in a systematic fashion to avoid introducing bubbles or particulate matter into the channels.

4.2. Experimental setup

Electrical and fluidic connections to the nanochannels were made via a custom-built, high-pressure chipholder, Fig. 4b and c. Electrical connections were established by inserting silver-silver chloride (Ag/AgCl) electrodes through the top piece of the chipholder into the channel reservoirs. We soldered stainless steel tubing directly into the chipholder and established fluidic connections between the chipholder and channel reservoirs with precision O-rings (Applerubber, Inc.). A high-impedance electrometer (Keithley 6517) controlled by Labview was used to measure the streaming current (sampling frequency of 400/min) across the nanochannel. We also fabricated a home-built Faraday cage to shield the entire setup from electromagnetic radiation. We controlled the applied pressure using two high-pressure single-stage regulators that could regulate pressure between 0 and 40 MPa (≈6000 psi), and monitored the pressure with a high-precision pressure transducer (Kobold Instruments, KPK050002121). A source meter (Keithley 2410) controlled by Labview was used to both power the transducer and record the output (sampling frequency of 95/min).

4.3. Experimental procedure

Upon first use, the channel is filled with filtered deionized water via capillary action. After initial filling, the channel is examined under an epifluorescent microscope (Olympus IX70) fitted with a 40 X water immersion objective (N.A. 0.95) to ensure there are no bubbles within the channel. Then, we apply a pressure drop of 3 kPa along the channel to remove any unseen air bubbles and to achieve a stable streaming current. Once a stable current is established, the device is removed from the experimental setup, fluid from the wells is removed and the well is flushed five times with a pipettor, and the appropriate solution is placed in both wells.

Next, we perform current monitoring, following techniques of Sze [45], to determine the average experimental electro-osmotic velocity $\langle u_{eo}^{exp} \rangle$ of the system. Briefly, as in Ref. [14], one reservoir is filled with a background electrolyte with a concentration $0.9c^*$ of the target concentration c^*. Then, we raise the voltage of that well from zero to ΔV (relative to the other well that remains grounded) to allow for constant electro-osmotic flow to fill the channel with the electrolyte of concentration $0.9c^*$. After applying the voltage, the system is allowed to equilibrate for about 15 min. Finally, all liquid is removed from the well that still contains deionized water and replaced with electrolyte of concentration c^*. Voltage is applied with the opposite polarity and the current was monitored over time, as shown in Fig. 5a as the c^* concentration gradually replaces the $0.9c^*$ concentration in the nanochannel. Voltages are applied and current is monitored using a digital multimeter (Model 2410, Keithley) controlled with LabView. Platinum wires served as electrodes. Finally, $\langle u_{eo}^{exp} \rangle$ is determined as

$$\langle u_{eo}^{exp} \rangle = \frac{L}{\Delta t}, \tag{23}$$

where Δt is the time it took the c^* concentration to traverse the channel length L. Because the current monitoring procedure does not require an applied pressure gradient, and occurs in less than 1 h, we assumed negligible dissolution of the walls during this time period.

Once the channels are filled with their respective solutions and initial current measurements are taken, a pressure drop $\Delta p = 8$ MPa is applied for a period of 48 h and sampled every second, while the resulting streaming current I_p is sampled at a rate of 16,000 measurements per hour. For each channel height, we performed experiments on bare silica channels with 1 mM KCl, bare silica channels with 10 mM borate, and cyanosilane-coated channels with 10 mM borate buffer. The number of channels used per experiment varied from 1 to 4 depending on the fabrication yield. Typical raw data of $\Delta p(t)$ and $I_p(t)$ are shown in Fig. 5 for measurements on 1 mM KCl in channel #1 [panel (b–c)] and #7 [panel (d–e)], respectively. To verify that the pressure remains constant while the current increases over time, we fit the pressure and streaming current data using the expression $\Delta p(t) = (\partial \Delta p/\partial t)\ t + \Delta p(0)$ and $I_p(t) = [\partial I_p/\partial t]_{meas} t + I_p(0)$, respectively, via the build-in Matlab function *nlinfit*. Besides the fitting parameters $\partial \Delta p/\partial t$, $\Delta p(0)$, $[\partial I_p/\partial t]_{meas}$ and $I_p(0)$ the function also gives their associated uncertainties based on 95% confidence intervals. Using this information we note that for the representative cases in Fig. 5 the relative change of pressure and current over the measurement period $\Delta t = 48$ h is for channel #1

$$\frac{\partial \Delta p}{\partial t}\frac{\Delta t}{\Delta p(0)} = (0.2 \pm 0.2) \times 10^{-4}, \tag{24a}$$

$$\left[\frac{\partial I_p}{\partial t}\right]_{meas}\frac{\Delta t}{I_p(0)} = (153.4 \pm 1.0) \times 10^{-4}, \tag{24b}$$

and for channel #7

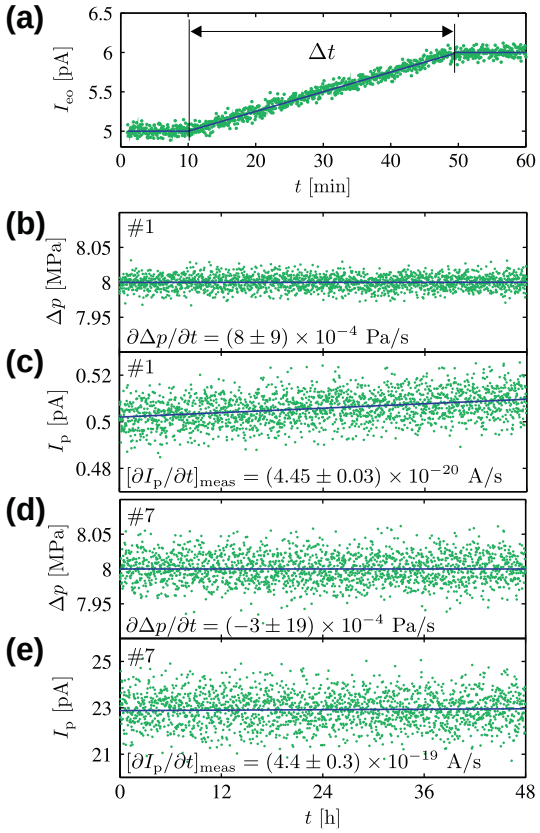

Fig. 5. (a) Typical raw data (green points) from an electro-osmotic flow filling experiment showing the current I_{eo} versus time t, as well as fitting lines (blue). (b) Measured applied pressure drop Δp (green points) versus time over a 48-h time period for 1 mM KCl solution (pH 5.6 and $\lambda_D = 10$ nm) in channel #1 (for clarity only ~2000 out of 172,800 data points are shown). Also shown is the fitting line (blue) from which the slope $\partial \Delta p/\partial t$ with associated uncertainty is determined. (c) The measured streaming current I_p (green points) resulting from the applied pressure drop in panel (b) versus time (for clarity only ~2000 out of 768,000 data points are shown). From the fitting line (blue), the slope $[\partial I_p/\partial t]_{meas}$ and initial current $I_p(0)$ with associated uncertainties are determined. (d–e) The same as panels (b) and (c) but for channel #7. (For interpretation of the references to color in this figure legend, the reader is referred to the web version of this article.)

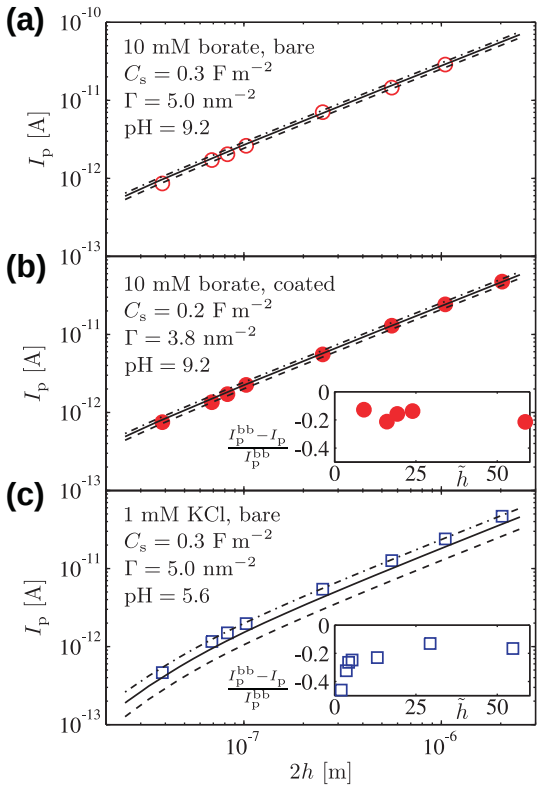

Fig. 6. Log–log plots of measured (symbols) and predicted (full lines, 2D model with pK = 6.6) streaming current I_p versus channel height $2h$ for: (a) 10 mM borate in bare channels (open red circles), (b) 10 mM borate in cyanosilane coated channels (filled red circles), and (c) 1 mM KCl in bare channels (open blue squares). Estimated theoretical error bounds are found using pK = 6.0 (dash-dotted lines) and pK = 7.2 (dashed lines). The relative experimental error is negligible, of order 10^{-4} as discussed in Section 4.3, and therefore undiscernable in the plot. The insets of panel (b) and (c) show the relative deviation of the same experimental data I_p from those of the 10 mM borate bare silica channel, I_p^{bb}. (For interpretation of the references to color in this figure legend, the reader is referred to the web version of this article.)

$$\frac{\partial \Delta p}{\partial t}\frac{\Delta t}{\Delta p(0)} = (-0.1 \pm 0.4) \times 10^{-4}, \tag{25a}$$

$$\left[\frac{\partial I_p}{\partial t}\right]_{meas}\frac{\Delta t}{I_p(0)} = (33.1 \pm 2.3) \times 10^{-4}, \tag{25b}$$

Hence, since the relative change in the current is two to three orders of magnitude larger than that of the pressure, we rule out that any systematic change in $\Delta p(t)$ could be responsible for the rise in $I_p(t)$.

Finally, we take the streaming current for a given experimental condition to be $I_p = I_p(0)$ in the aforementioned fit as the channels have their nominal height at $t = 0$. The experimental uncertainty, from e.g. pressure fluctuations and noise from the electrometer, can then be estimated from the 95% confidence interval half-width $\Delta I_p(0)$. For the experimental conditions in Fig. 5, the relative uncertainty $\Delta I_p(0)/I_p(0)$ of the streaming current is $\sim 5 \times 10^{-5}$ for channel #1 and $\sim 1 \times 10^{-4}$ for channel #7. In Fig. 6 we plot I_p versus height h for three different cases. The experimental uncertainty $\Delta I_p(0)/I_p(0)$ of order $\sim 10^{-4}$ is negligible in comparison to the uncertainty from the 10% variation in the surface pK-value, which is indicated by the non-solid curves.

5. Results and discussion

5.1. The electro-osmotic velocity

Using the procedure described in Section 4.3, the average electro-osmotic flow velocity $\langle u_{eo}^{exp} \rangle$, Eq. (23), was determined for the tallest nanochannel, #8 in Table 3, for bare silica walls with 1 mM KCl and with 10 mM borate, and for coated silica walls with 10 mM borate. The theoretically predicted electro-osmotic flow velocity $\langle u_{eo}^{thr} \rangle$ was determined using Eq. (19a), and the results including uncertainties are

1 mM KCl, bare

$$\langle u_{eo}^{exp} \rangle = (7.0 \pm 0.4)\ \frac{\mu m}{s}, \quad \langle u_{eo}^{thr} \rangle = (5.6 \pm 1.8)\ \frac{\mu m}{s}, \tag{26a}$$

10 mM borate, bare

$$\langle u_{eo}^{exp} \rangle = (8.3 \pm 0.4)\ \frac{\mu m}{s}, \quad \langle u_{eo}^{thr} \rangle = (8.4 \pm 0.8)\ \frac{\mu m}{s}, \tag{26b}$$

10 mM borate, coated

$$\langle u_{eo}^{exp} \rangle = (7.0 \pm 0.4)\ \frac{\mu m}{s}, \quad \langle u_{eo}^{thr} \rangle = (7.0 \pm 0.7)\ \frac{\mu m}{s}. \tag{26c}$$

In all three cases, the agreement between theory and experiment is good and within the given experimental and theoretical uncertainties. The relative deviations are of the order of 10%. The theoretical uncertainties are dominated by the assignment of pK as shown in Table 2, while the experimental ones are mainly due to the width measurements, see Table 2. The theoretical values are based on the full 2D model and account for relative deviations of u_{eo} from the flat-wall value, as shown in Fig. 3b

5.2. The streaming current

Results for the streaming current are shown in Fig. 6 as log-log plots of measurements (symbols) and theoretical predictions (full black curve, 2D model) of streaming current I_p versus channel height $2h$ for the three different conditions tested: 1 mM KCl in bare channels (open red circles), 10 mM borate in bare channels (filled red circles), and 10 mM borate buffer in cyanosilane-coated channels (open blue squares). There are no adjustable parameters, and the agreement between theory and experiment is good, within 10%.

We find that the two parameters that have the largest influence on the uncertainty in the 2D modeling are the channel width and the surface pK-value. In Table 3 is given an estimate of the error in the width of the channel of 10%. An equivalent 10% uncertainty in the pK-value is estimated based on literature values [42,25,31,43,27,29]. We find that of the two parameters the pK-value (pK = 6.6 ± 0.6, Table 2) dominates the resulting uncertainty in the 2D model. We therefore find the error bounds by calculating I_p using pK = 6.0 (dash-dotted lines) and 7.2 (dashed lines), respectively. For the experimental uncertainty, and as discussed in Section 4.3, the 95% confidence interval half-width $\Delta I_p(0)$ for the fitted streaming current $I_p = I_p(0)$ typically yield a relative uncertainty $\Delta I_p(0)/I_p(0) \sim 10^{-4}$, which is negligible in comparison with that from the pK-variation discussed earlier and not discernable in Fig. 6. Finally, based on the above uncertainties, we see from Fig. 6 that the measured data points lie within the error curves.

The insets of Fig. 6b and c show the experimental data plotted relative to the data from borate in bare channels. These plots highlight the behavior of our systems with coated channels as well as with a lower concentration buffer. First, it can be seen that the streaming current decreases by about 20% when the number of available surface sites is reduced by surface coating, going from 10 mM bare borate ($\Gamma = 5.0$ nm^{-2}) to the 10 mM coated borate ($\Gamma = 3.8$ nm^{-2}). This reduction in streaming current is fairly constant across channel heights, which is consistent with the assumption that only the surface charge density is different. However, when comparing the streaming current from the 10 mM bare borate channel to the 1 mM bare KCl channel, we note that the streaming current reduction is larger at lower channel heights. This is due to the fact that the double layers are strongly overlapping in

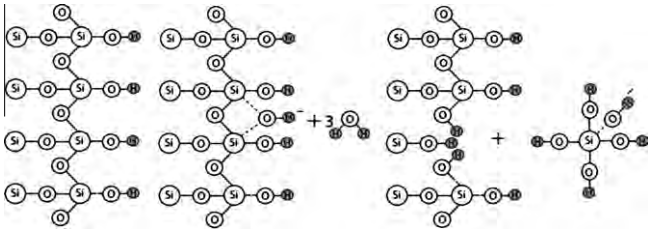

Fig. 7. One proposed mechanism for silica dissolution presented in, and image adapted from, Ref. [46].

this regime (whereas with 10 mM borate the double layers are still non-overlapping), which clearly reduces the streaming current.

Having verified the accuracy of the model for the forward problem, i.e., predicting streaming currents in the nanochannels of interest, we next turn to the inverse problem of estimating dissolution rates given extended time-sensitive streaming current measurements.

5.3. Method for determining dissolution rates

In geological systems, it has been found that saline solutions flowing through porous silicates dissolve the solid matrix at a rate of approximately 0.01 mg/m^2/h [46]. Given that the density of fused silica is 2203 kg/m^3, we obtain

$$1\ \frac{\mathrm{mg}}{\mathrm{m^2 h}} \sim 0.4539\ \frac{\mathrm{nm}}{\mathrm{h}} = 1.26\times 10^{-13}\ \frac{\mathrm{m}}{\mathrm{s}}, \tag{27a}$$

or conversely

$$1\ \frac{\mathrm{m}}{\mathrm{s}} = 7.93\times 10^{12}\ \frac{\mathrm{mg}}{\mathrm{m^2 h}}. \tag{27b}$$

The mechanism of silica dissolution is complex and not yet well understood, but one mechanism for the dissolution discussed in the literature [46] is shown in Fig. 7.

Here, we propose a method for determining dissolution rates under controlled experimental conditions using our model and experimental data. Referring back to Fig. 5b and c, we note that although the applied pressure drop remains constant over a period of 48 h, the streaming current steadily rises. This fact, together with the following three assumptions, forms the basis of the method: (*i*) all changes in current are due solely to dissolution of the wall, aided by the continuous renewal of fresh buffer by the axial flow; (*ii*) ionized silanol radicals are few and highly unstable and thus do not contribute to the current; (*iii*) spatial variations in the dissolution rate are averaged out over the entire surface of the channel.

To calculate dissolution rates, we use Eq. (14b) to obtain a numerical estimate for the change δI_p in the streaming current as a function of the change $\delta A = 2(w+h)\,\delta\ell$ in the cross-sectional area A, in terms of the (small) thickness $\delta\ell$ of the dissolved layer,

$$\left[\frac{\partial I_\mathrm{p}}{\partial \ell}\right]_\mathrm{calc} = \frac{\partial I_\mathrm{p}}{\partial A}\frac{\partial A}{\partial \ell} \approx \frac{1}{\delta\ell}\left[I_\mathrm{p}(A+\delta A) - I_\mathrm{p}(A)\right], \tag{28}$$

where we choose $\delta\ell = 0.01h$. Combining this with the experimentally measured rate of change $[\partial I_\mathrm{p}/\partial t]_\mathrm{meas}$ of the streaming current, Fig. 5c, yields the dissolution rate dm/dt per unit area (in units of mg/m^2/h) as,

$$\frac{\mathrm{d}m}{\mathrm{d}t} = 7.93\times 10^{12}\ \frac{\mathrm{mg}}{\mathrm{m^2 h}}\ \frac{\mathrm{s}}{\mathrm{m}} \times \left[\frac{\partial I_\mathrm{p}}{\partial t}\right]_\mathrm{meas} \times \left[\frac{\partial I_\mathrm{p}}{\partial \ell}\right]^{-1}_\mathrm{calc}. \tag{29}$$

In the Supplementary information, we list the numerical values of $[\partial I_\mathrm{p}/\partial t]_\mathrm{meas}$, $[\partial I_\mathrm{p}/\partial l]_\mathrm{calc}$, and d$m$/d$t$ for each experimental condition.

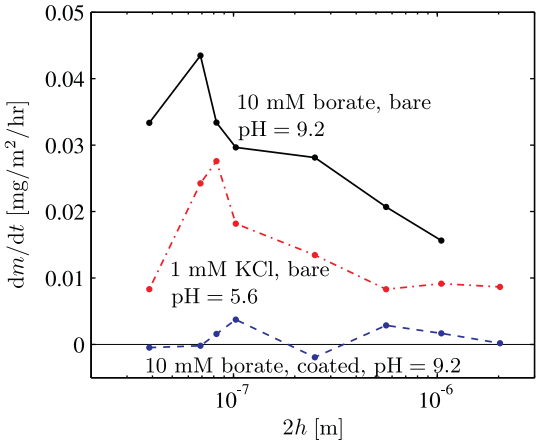

Fig. 8. Predicted silica dissolution rate dm/dt vs. channel height 2h based, via Eq. (29), on measured $[\partial I_\mathrm{p}/\partial t]_\mathrm{meas}$ and calculated $[\partial I_\mathrm{p}/\partial l]_\mathrm{calc}$ (numerical values are given in the Supplementary information). The three curves are for: 1 mM KCl in bare channel (dash-dotted red curve), 10 mM borate in bare channel (full black curve), and 10 mM borate in cyanosilane-coated channel (dashed blue curve). (For interpretation of the references to color in this figure legend, the reader is referred to the web version of this article.)

The theoretically predicted dissolution rates based on measured $[\partial I_\mathrm{p}/\partial t]_\mathrm{meas}$ for our experimental nanochannel system are shown in Fig. 8. We note that the estimated rates are on the same order of magnitude as previous results in the field of geological systems [46], which allows us to believe that our method is viable for silica dissolution studies. Furthermore, also in agreement with earlier findings [9], the dissolution rate increases as pH and ionic strength increase going from 1 mM KCl (pH 5.6) to 10 mM borate (pH 9.2) in bare silica channels. Other studies have pointed out that electric double-layer interaction in un-confined geometries increases the dissolution rates [9]. This we also see in our calculations, as the dissolution rate increases when the double layers start to overlap as the channel half-height h is decreased. A final point that corroborates our model is the prediction of a negligible dissolution rate (fluctuates around zero) for the cyanosilane-coated channel, a well-known feature from other studies [38,47,48].

On top of this, we can use our model for novel studies of silica dissolution, for example the influence of extreme confinement. From Fig. 8 we note that the increase in dissolution rate starts earlier for 1 mM KCl than 10 mM borate as channel height decreases, indicating that this may be due to electric double layer effects. However, because the peak is roughly at the same height for both cases, diffusion-limited dissolution may be the dominating physics at small channel heights. This is in line with a common viewpoint about dissolution, which holds that charges such as OH^- near the wall catalyze de-polymerization and that the newly dissolved silanol radicals diffuse away from the surface.

In general, using our method of hours-long streaming current measurements will enable systematic studies of the mechanism underlying dissolution of silica in a number of controlled experiments: The channel geometry can be varied from the case of thin non-overlapping double layers in very tall microchannels to that of strongly overlapping double layers at extreme confinement in very shallow nanochannels. Diffusion limited dissolution rates and the effect of continuous renewal of buffer can be studied through varying the imposed pressure-driven electrolyte flow. The chemical conditions can be varied through the detailed composition and ionic strength of the buffer as well as the coating conditions of the surface. The small size of micro- and nanofluidic systems facilitates accurate temperature control. These advantages suggest that our method may be useful for future studies of silica dissolution.

6. Conclusion

We have advanced the capabilities of our chemical-equilibrium electrokinetic model to account for pressure-driven flows and full 2D cross-sectional geometries without adjustable parameters. These advances have been validated against experimental results on eight bare and cyanosilane-coated silica nanochannels of heights between 40 nm and 2000 nm for 1 mM KCl solutions and 10 mM borate buffers. Numerical predictions, based on a finite-element-method implementation of our model, of the electro-osmotic velocities and streaming currents exhibit good agreement with measured data, and we have determined when the 2D model is necessary to employ. Finally, by combining model predictions with measurements over 48 h of the streaming currents, we have developed a method to estimate the dissolution rate of the silica walls, typically around 0.01 mg/m^2/h, under controlled experimental conditions.

Appendix A. Supplementary material

Supplementary data associated with this article can be found, in the online version, at doi:10.1016/j.jcis.2011.04.011.

References

[1] R. Schoch, J. Han, P. Renaud, Rev. Mod. Phys. 80 (3) (2008) 839–883.
[2] W. Sparreboom, A. van den Berg, J.C.T. Eijkel, Nat. Nanotechnol. 4 (11) (2009) 713–720.
[3] L. Bocquet, E. Charlaix, Chem. Soc. Rev. 39 (3) (2010) 1073–1095.
[4] M. Napoli, J.C.T. Eijkel, S. Pennathur, Lab. Chip. 10 (8) (2010) 957–985.
[5] W. Sparreboom, A. van den Berg, J.C.T. Eijkel, New J. Phys. 12 (1) (2010) 015004.
[6] P.M. Dove, Geochim. Cosmochim. Acta 63 (22) (1999) 3715–3727.
[7] P.M. Dove, N. Han, J.J.D. Yoreo, Proc. Natl. Acad. Sci. 102 (43) (2005) 15357–15362.
[8] P.M. Dove, N. Han, A.F. Wallace, J.J.D. Yoreo, Proc. Natl. Acad. Sci. 105 (29) (2008) 9903–9908.
[9] G.W. Greene, K. Kristiansen, E.E. Meyer, J.R. Boles, J.N. Israelachvili, Geochim. Cosmochim. Acta 73 (10) (2009) 2862–2874.
[10] N.R. Tas, J.W. Berenschot, P. Mela, H.V. Jansen, M. Elwenspoek, A. van den Berg, Nano Letters 2 (9) (2002) 1031–1032.
[11] Q. Xia, K.J. Morton, R.H. Austin, S.Y. Chou, Nano Letters 8 (11) (2008) 3830–3833.
[12] Y. Zhao, E. Berenschot, H. Jansen, N. Tas, J. Huskens, M. Elwenspoek, Microelectron. Eng. 86 (4–6) (2009) 832–835.
[13] S. Nam, M. Lee, S. Lee, D. Lee, S.M. Rossnagel, K. Kim, Nano Letters 10 (9) (2010) 3324–3329.
[14] M.B. Andersen, J. Frey, S. Pennathur, H. Bruus, J. Colloid Interface Sci. 353 (2011) 301–310.
[15] J. Yang, F. Lu, L.W. Kostiuk, D.Y. Kwok, J. Micromech. Microeng. 13 (6) (2003) 963–970.
[16] O. El-Gholabzouri, M.A. Cabrerizo, R. Hidalgo-Álvarez, J. Colloid Interface Sci. 214 (2) (1999) 243–250.
[17] S. Alkafeef, R.J. Gochin, A.L. Smith, Colloid Surface A 195 (1–3) (2001) 77–80.
[18] C. Fritzmann, J. Löwenberg, T. Wintgens, T. Melin, Desalination 216 (1–3) (2007) 1–76.
[19] M.A. Shannon, P.W. Bohn, M. Elimelech, J.G. Georgiadis, B.J. Marinas, A.M. Mayes, Nature 452 (7185) (2008) 301–310.
[20] P.M. Biesheuvel, M.Z. Bazant, Phys. Rev. E 81 (3) (2010) 031502.
[21] F. van der Heyden, D. Stein, C. Dekker, Phys. Rev. Lett. 95 (11) (2005) 116104.
[22] F.H.J. van der Heyden, D.J. Bonthuis, D. Stein, C. Meyer, C. Dekker, Nano Letters 6 (10) (2006) 2232–2237.
[23] F.H.J. van der Heyden, D. Stein, K. Besteman, S.G. Lemay, C. Dekker, Phys. Rev. Lett. 96 (22) (2006) 224502.
[24] F.H.J. van der Heyden, D.J. Bonthuis, D. Stein, C. Meyer, C. Dekker, Nano Letters 7 (4) (2007) 1022–1025.
[25] S.H. Behrens, D.G. Grier, J. Chem. Phys. 115 (14) (2001) 6716–6721.
[26] P.M. Biesheuvel, J. Colloid Interface Sci. 275 (2) (2004) 514–522.
[27] M. Wang, A. Revil, J. Colloid Interface Sci. 343 (1) (2010) 81–386.
[28] C. Duan, A. Majumdar, Nat. Nanotechnol. 5 (12) (2010) 848–852.
[29] K.L. Jensen, J.T. Kristensen, A.M. Crumrine, M.B. Andersen, H. Bruus, S. Pennathur, Phys. Rev. E 83, 056307 (2011).
[30] D.Y. Chan, T.W. Healy, T. Supasiti, S. Usui, J. Colloid Interface Sci. 296 (1) (2006) 50–158.
[31] K.G.H. Janssen, H.T. Hoang, J. Floris, J. de Vries, N.R. Tas, J.C.T. Eijkel, T. Hankemeier, Anal. Chem. 80 (21) (2008) 8095–8101.
[32] R.F. Probstein, Physicochemical Hydrodynamics: An Introduction, Wiley-Interscience, 1994.
[33] N.L. Burns, J. Colloid Interface Sci. 183 (1) (1996) 249–259.
[34] M.Z. Bazant, M.S. Kilic, B.D. Storey, A. Ajdari, Adv. Colloid Interface Sci. 152 (1–2) (2009) 48–88.
[35] R.E.G. van Hal, J.C.T. Eijkel, P. Bergveld, Adv. Colloid Interface Sci. 69 (1–3) (1996) 31–62.
[36] D.E. Yates, S. Levine, T.W. Healy, J. Chem. Soc., Faraday Trans. 1 (70) (1974) 807–1818.
[37] J.A. Davis, R.O. James, J.O. Leckie, J. Colloid Interface Sci. 63 (3) (1978) 480–499.
[38] R.J. White, E.N. Ervin, T. Yang, X. Chen, S. Daniel, P.S. Cremer, H.S. White, J. Am. Chem. Soc. 129 (38) (2007) 1766–11775.
[39] A. Persat, R.D. Chambers, J.G. Santiago, Lab. Chip. 9 (17) (2009) 2437.
[40] A. Persat, R.D. Chambers, J.G. Santiago, Buffer calculator, 2010. <http://microfluidics.stanford.edu/download>.
[41] A. Persat, M.E. Suss, J.G. Santiago, Lab. Chip. 9 (17) (2009) 2454.
[42] P. Schindler, H.R. Kamber, Helv. Chim. Acta 51 (7) (1968) 781–1786.
[43] R.B.H. Veenhuis, E.J. van der Wouden, J.W. van Nieuwkasteele, A. van den Berg, J.C.T. Eijkel, Lab. Chip. 9 (24) (2009) 3472–3480.
[44] S. Pennathur, J.G. Santiago, Anal. Chem. 77 (21) (2005) 6782–6789.
[45] A. Sze, D. Erickson, L. Ren, D. Li, Zeta-potential measurement using the smoluchowski equation and the slope of the current-time relationship in electroosmotic flow, J. Colloid Interface Sci. 261 (2) (2003) 402–410.
[46] R.K. Iler, The Chemistry of Silica: Solubility, Polymerization, Colloid and Surface Properties, and Biochemistry, Wiley, New York, 1979.
[47] S. Prakash, T.M. Long, J.C. Selby, J.S. Moore, M.A. Shannon, Anal. Chem. 79 (4) (2007) 1661–1667.
[48] S. Prakash, M. Karacor, S. Banerjee, Surf. Sci. Rep. 64 (7) (2009) 233–254.

Appendix D

Paper published in Phys Rev E

K. L. Jensen, J. T. Kristensen, A. M. Crumrine, M. B. Andersen, H. Bruus, and S. Pennathur, Hydronium-dominated ion transport in carbon-dioxide-saturated electrolytes at low salt concentrations in nanochannels, Phys Rev E 83, 056307 (2011).

Hydronium-dominated ion transport in carbon-dioxide-saturated electrolytes at low salt concentrations in nanochannels

Kristian Lund Jensen,[1] Jesper Toft Kristensen,[1] Andrew Michael Crumrine,[2] Mathias Bækbo Andersen,[1] Henrik Bruus,[1] and Sumita Pennathur[2]

[1]*Department of Micro- and Nanotechnology, Technical University of Denmark, DTU Nanotech Building 345 East, DK-2800 Kongens Lyngby, Denmark*

[2]*Department of Mechanical Engineering, University of California, Santa Barbara, California 93106, USA*

(Received 19 August 2010; revised manuscript received 19 January 2011; published 9 May 2011)

Nanochannel ion transport is known to be governed by surface charge at low ionic concentrations. In this paper, we show that this surface charge is typically dominated by hydronium ions arising from dissolution of ambient atmospheric carbon dioxide. Taking the hydronium ions into account, we model the nanochannel conductance at low salt concentrations and identify a conductance minimum before saturation at a value independent of salt concentration in the dilute limit. Via the Poisson–Boltzmann equation, our model self-consistently couples chemical-equilibrium dissociation models of the silica wall and of the electrolyte bulk, parametrized by the dissociation reaction constants. Experimental data with aqueous KCl solutions in 165-nm-high silica nanochannels are described well by our model, both with and without extra hydronium from added HCl.

DOI: 10.1103/PhysRevE.83.056307 PACS number(s): 47.57.jd, 47.61.−k, 66.10.−x, 82.65.+r

I. INTRODUCTION

Nanofluidics and specifically, ion transport through artificial nanochannels, are important for both fundamental scientific studies and for practical biomolecular and energy-based applications [1–3]. Of particular interest is the intricate interplay among surface chemistry, electrokinetics, and fluid dynamics spanning over molecular and continuum macroscopic length scales [4,5]. It has been demonstrated that the electrokinetic properties at this scale have enabled a range of innovations including those for chemical sensing and bioanalytics [6–12], energy harvesting systems, [13–18], and nanofluidic ion transport [19–26], including enrichment, depletion, and rectification effects [27–32].

For many of these applications, characterizing and understanding the conduction properties of electrolyte-filled nanochannels at low salt concentrations ($<10^{-3}$ M) is important, and this raises the question of the role of hydronium ions. It is well known that, under standard conditions, the dissolution of ambient atmospheric carbon dioxide in de-ionized (DI) water leads to the formation of carbonic acid, which, upon reaching chemical equilibrium with the water, gives rise to an inherent concentration of hydronium ions of $\sim 10^{-6}$ M corresponding to pH 5.7. Because hydronium has a uniquely high mobility, a factor of ~ 5 higher than common salt ions, in bulk solutions, it is found that hydronium ions begin to dominate the electrical conductivity when the salt concentration is lower than $\sim 5 \times 10^{-6}$ M. Furthermore, hydronium is also known to interact with the confining walls of the electrolyte. For oxide walls, most prominently silica, numerous studies have shown how hydronium affects the electrical properties of the wall-electrolyte interface and leads to a wall surface charge that depends on salt concentration [33–44] including our own recent study [26]. Finally, at sufficiently low salt concentration, this surface charge is found to dominate the conductance of electrolyte-filled nanochannels [8,11,19,24,27,28,32,45]. Given these facts, it is remarkable that the role of hydronium ions is largely unexplored in the literature on nanochannel conductance at low salt concentrations in unbuffered solutions.

TABLE I. Experimental observations of a nanochannel conductance minimum at low salt concentration: List of reference, figure number, year, magnitude δ of the minimum Eq. (21), and the applied surface-charge model (Const and Dissoc refer to constant surface-charge and chemical-equilibrium dissociation models, respectively). All studies involve silica nanochannels and aqueous KCl solutions, except Stein *et al.*, who used a 50%/50% mixture of isopropanol and an appropriately diluted KCl : TRIS (100 : 1) solution.

References		Figure	Year	δ	Model
[19]	Stein *et al.*	3	(2004)	1.06	Const
[28]	Karnik *et al.*	3	(2005)	1.38	Const
[45]	Schoch and Renaud	3	(2005)	1.19	Const
[46]	Cheng	2.9	(2008)	1.27	Const
[24]	Martins *et al.*	3	(2009)	1.68	Const
[32]	Duan *et al.*	3	(2010)	1.25	Dissoc
	This paper	-	(2010)	1.18	Dissoc

The main goal of this paper is to provide such an analysis mainly in terms of theoretical modeling, but also supported by our own experimental validation. Among the dozens of papers published on nanochannel conductance, we have only found a single very recent paper dealing directly with similar modeling [32].

Another motivation for our paper is to explain the appearance of a minimum in the nanochannel conductance as a function of salt concentration, which several groups have observed, but not noticed, see Table I. The minimum, which cannot be explained by depletion effects near the entrances, as this would lead to a decreased conductance at the lowest salt concentration, is found to occur for salt concentrations $\sim 5 \times 10^{-6}$ M, the above-mentioned crossover from salt to hydronium-dominated conductance. The main result of our analysis is that our model predicts such a minimum due to the presence of inherent hydronium ions.

II. MODEL

We consider a long straight nanochannel connecting two large bulk reservoirs. Traditionally, theoretical modeling of ionic transport in such systems is based on the Gouy–Chapman–Stern theory of electrostatic screening by the mobile co- and counterions in an aqueous salt solution of a wall with constant surface charge, coupled to the continuum fluid dynamics equations and, thus, forming the Poisson–Nernst–Planck transport equations [47]. This results in a monotonic decreasing nanochannel conductance as a function of decreasing salt concentration that levels off at a plateau in the dilute limit, as shown in Refs. [19,24,28,45,46] of Table I as well as in Refs. [8,11,27] and summarized by Fig. 8 in a recent review paper [2]. However, this is in contrast to the observed nonmonotonic conductance graphs with a minimum, and therefore, we choose to base our analysis on the other well-known class of modeling, where the surface charge is governed dynamically by chemical reaction constants of the proton dissociation processes in the bulk electrolyte and at the wall [26,32–44].

Building on our own recently published work [26], we extend these previous buffer/wall dissociation models to low concentration unbuffered electrolyte systems by the addition of two crucial features: First, we account for hydronium ions (here denoted as H^+ for brevity) from autoprotolysis of water and from dissociated carbonic acid induced by dissolution of ambient atmospheric carbon dioxide; and second, we calculate the surface charge from a self-consistent electrostatic coupling between hydronium dissociation models of the silanol groups at the wall and of all the bulk constituents, parametrized by the associated dissociation constants. Our model consists of three parts: (i) bulk dissociation reactions determining the concentrations of the involved H^+, OH^-, HCO_3^-, CO_3^{2-}, K^+, and Cl^- ions in the reservoirs, (ii) surface reactions determining the potential and charge of the nanochannel surface, and (iii) the Poisson–Boltzmann equation for the electrical potential coupling the first two parts.

Specifically, following Refs. [26,33–44], we model the solid/liquid interface as the layered structure shown in Fig. 1. The innermost plane is the silanol surface at the o plane with surface charge σ_o and potential ϕ_o. Next is the immobile Stern layer situated between the o plane and the d plane and having the capacitance C_s [F/m^2]. Following the Stern layer is the electrically charged diffusive screening layer extending from the d plane a few times the Debye screening length λ_D to the bulk and having surface charge σ_d and ζ potential ϕ_d. The last layer is the charge-neutral bulk of the reservoirs.

A. Bulk chemistry of the reservoirs

All bulk ionic concentrations in the reservoirs are calculated using the method of chemical families presented in Ref. [48] and supplemented by an open-source MATLAB-code buffer calculator [49]. For this paper, the carbonic acid family H_2CO_3 with charge states $z = 0, -1$, and -2 is of particular interest,

$$H_2CO_3 \rightleftharpoons HCO_3^- + H^+, \quad pK_{HCO_3^-} = 6.35, \tag{1a}$$

$$HCO_3^- \rightleftharpoons CO_3^{2-} + H^+, \quad pK_{CO_3^{2-}} = 10.33. \tag{1b}$$

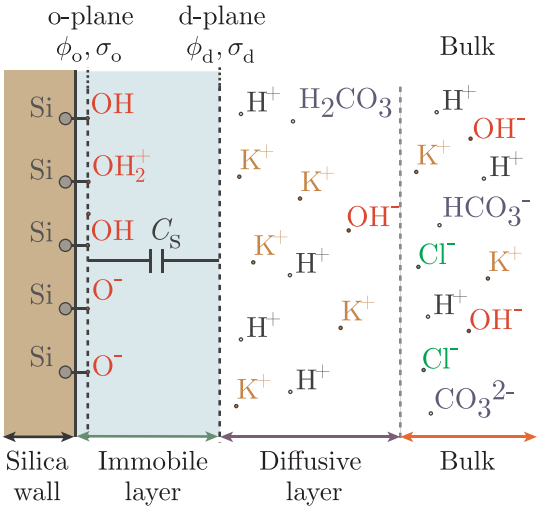

FIG. 1. (Color online) Model of a silica surface (dark brown) contacting an aqueous solution of KCl (white). At the bottom, the four regions of our model have been identified: the silica wall, the immobile Stern layer (light blue), the diffusive layer, and the bulk. The dashed line denoted as the o plane is where the bound surface charge σ_o resides, while the dashed line denoted as the d plane marks the beginning of the diffuse mobile layer, a layer stretching from the d plane to the bulk, and in which a mobile screening charge $\sigma_d = -\sigma_o$ resides. C_s is the (Stern) capacitance of the immobile layer. The potentials at the o and d planes are denoted as ϕ_o and ϕ_d, respectively.

For DI water with a saturated concentration of carbonic acid of 11.8 μM at 25 °C [50], pH = 5.68, in agreement with our own experimental measurements. Likewise, the salt KCl is represented by the potassium hydroxide family KOH, with charge states $z = 0$ and $+1$, together with the hydrochloric acid family HCl with charge states $z = 0$ and -1. A list of all involved chemical families taken into account in our model is shown in Table II.

When the total concentration c_X^{tot} of each chemical family in a given aqueous solution is known, the equilibrium reactions listed in Table II can be solved with respect to the bulk concentration c^b_{X,z_X} of each family member using the buffer calculator code [49]. This calculational scheme takes dissociation equilibrium, conservation of mass, and charge neutrality into account,

$$K_{X,z_X} c^b_{X,z_X+1} = c^b_{X,z_X} c^b_H, \text{ dissociation reactions}, \tag{2a}$$

$$\sum_{z_X} c^b_{X,z_X} = c^{tot}_X, \text{ conservation of mass}, \tag{2b}$$

$$\sum_{X,z_X} z_X c^b_{X,z_X} = 0, \text{ charge neutrality}. \tag{2c}$$

As Eqs. (2) describe the bulk ionic composition in the reservoirs, charge neutrality is a good approximation.

Once the bulk concentrations c^b_{X,z_X} are known, three parameters characterizing the bulk electrolyte can be determined: the

TABLE II. List of the chemical families X used in this paper together with the associated reaction schemes, charge states z_X, reaction constants $pK_{X,z_X} = -\log_{10}(K_{X,z_X}/1\,\mathrm{M})$, and electrophoretic mobilities μ^b_{X,z_X}. Note that the pK_{X,z_X} values are always associated with dissociation processes.

Chemical family X	z_X	Reaction scheme (dissociation)	pK_{X,z_X}	μ^b_{X,z_X} [10^{-9}/T]
Carbonic	0	H_2CO_3		0.0
acid	-1	$H_2CO_3 \rightleftharpoons HCO_3^- + H^+$	6.35[a]	-46.1[a]
	-2	$HCO_3^- \rightleftharpoons CO_3^{2-} + H^+$	10.33[a]	-71.8[a]
Potassium	0	KOH		0.0
hydroxide	$+1$	$KOH \rightleftharpoons K^+ + OH^-$	14.00[a]	76.2[b]
Hydrochloric	0	HCl		0.0
acid	-1	$HCl \rightleftharpoons Cl^- + H^+$	-7.00[a]	-79.1[b]
Water	0	H_2O		362.4[c]
	-1	$H_2O \rightleftharpoons OH^- + H^+$	14.00[a]	-205.2[c]
Silanol	0	SiOH		
	-1	$SiOH \rightleftharpoons SiO^- + H^+$	6.56[d]	
	$+1$	$SiOH_2^+ \rightleftharpoons SiOH + H^+$	-1.90[e]	

[a]From Ref. [52], infinite dilution at 25 °C.
[b]From Ref. [53], infinite dilution at 25 °C.
[c]Here, $z = 0$ represents H^+, and $z = -1$ represents OH^-.
[d]From this paper.
[e]From Ref. [38].

ionic strength c_I, the dilute-limit electric conductivity σ^o_{el}, and the Debye screening length λ_D,

$$c_I = \frac{1}{2}\sum_{X,z_X} z_X^2 c^b_{X,z_X}, \tag{3a}$$

$$\sigma^o_{el} = e\sum_{X,z_X} z_X \mu^b_{X,z_X} c^b_{X,z_X}, \tag{3b}$$

$$\lambda_D = \left[\frac{\epsilon k_B T}{2e^2 c_I}\right]^{1/2}. \tag{3c}$$

At ionic strengths above 1 mM, the dilute-limit electrophoretic mobility μ^b_{X,z_X} in Eq. (3b) is inaccurate, and we correct it using the Pitts equation, which, for a 1 : 1 electrolyte in water at 25 °C, takes the form [52]

$$\mu^{*b}_{X,z_X} = \mu^b_{X,z_X} - \left(Az_X + 0.23|z_X z_{X,ci}|\mu^b_{X,z_X}\right)\frac{\sqrt{c_I}}{1 + aB\sqrt{c_I}}, \tag{4}$$

where μ^{*b}_{X,z_X} is the mobility corrected for nonzero ionic strength, $A = 3.1 \times 10^{-8}$ m^2 V^{-1} s^{-1} is a constant, $z_{X,ci}$ is the valence of the counterion, $B = 0.33$ Å^{-1} M$^{-1/2}$ is a constant, and a is an effective atomic radius [52]. In this paper, the conductivity in the high ionic strength regime is dominated by K^+ and Cl^- ions, for which $a = 3$ Å [54], and therefore, we approximate the electrolyte as binary. We can then use these two corrected mobilities for K^+ and Cl^- in Eq. (3b) to improve the accuracy of our calculated electrical conductivity in the high ionic strength regime.

B. Nanochannel electrostatics

Near the walls in any given electrolyte system, charge transfer processes occur between the electrolyte and the wall, leading to a nonzero electric potential $\phi(\boldsymbol{r})$. Defining ϕ to be zero in the bulk reservoirs, and assuming that the ionic concentrations are small enough to neglect interionic correlations, the concentration c_{X,z_X} of the ions as a function of position $\boldsymbol{r}$ in charge state z_X of family X can be written in terms of the bulk concentration c^b_{X,z_X} multiplied by a Boltzmann distribution factor as

$$c_{X,z_X}(\boldsymbol{r}) = c^b_{X,z_X}\,\exp\left[-\frac{z_X e\phi(\boldsymbol{r})}{k_B T}\right], \tag{5}$$

where we take the electric potential to be zero in the reservoirs. It simplifies the analysis if we nondimensionalize electric potentials and concentrations by introducing $k_B T/e$ as the scale for the electric potentials and c_I as the scale for the concentrations. The dimensionless fields, denoted by a tilde, become

$$\tilde{\phi} = \frac{e}{k_B T}\phi, \qquad \tilde{c}_{X,z_X} = \frac{1}{c_I}c_{X,z_X}. \tag{6}$$

Henceforth, the electric charge density can be written as $\rho_{el} = ec_I\sum_{X,z_X} z_X\tilde{c}_{X,z_X}$, which together with Eq. (5) leads to the Poisson–Boltzmann equation for the dimensionless potential $\tilde{\phi}$,

$$\nabla^2\tilde{\phi} = -\frac{e\rho_{el}}{\epsilon k_B T} = -\frac{1}{2\lambda_D^2}\sum_{X,z_X} z_X\tilde{c}^b_{X,z_X}e^{-z_X\tilde{\phi}}. \tag{7}$$

For a symmetric binary electrolyte, this reduces to the well-known simple form $\nabla^2\tilde{\phi} = \sinh(\tilde{\phi})/\lambda_D^2$.

C. Nanochannel surface chemistry

The total surface density of charge-active silanol sites at the wall is denoted as Γ_{tot} [m^{-2}]. In our model, we take the three charge states $z = 0$, -1, and $+1$ into account, for SiOH, SiO^-, and $SiOH_2^+$, respectively, as well as the two associated hydronium dissociation processes listed under silanol in Table II. These surface charge states have the densities Γ_o, Γ_-, and Γ_+, respectively, and it is natural to nondimensionalize them relative to Γ_{tot} to obtain

$$\tilde{\Gamma}_o = \frac{1}{\Gamma_{tot}}\Gamma_o, \qquad \tilde{\Gamma}_- = \frac{1}{\Gamma_{tot}}\Gamma_-, \qquad \tilde{\Gamma}_+ = \frac{1}{\Gamma_{tot}}\Gamma_+, \tag{8}$$

with the obvious normalization condition

$$\tilde{\Gamma}_o + \tilde{\Gamma}_- + \tilde{\Gamma}_+ = 1. \tag{9}$$

The hydronium dissociation processes at the wall involve the concentration c^o_H of the hydronium ions at the o plane, which, through the Boltzmann distribution, is related to the bulk concentration c^b_H. Consequently, the dimensional dissociation constants $K_\pm$ for the two surface processes as well as their nondimensionalized counterparts $\tilde{K}_\pm = K_\pm/c^b_H$ become

$$K_- = \frac{\Gamma_-}{\Gamma_o}c^b_H e^{-(e/k_B T)\phi_o}, \qquad \tilde{K}_- = \frac{\tilde{\Gamma}_-}{\tilde{\Gamma}_o}e^{-\tilde{\phi}_o}, \tag{10a}$$

$$K_+ = \frac{\Gamma_o}{\Gamma_+}c^b_H e^{-(e/k_B T)\phi_o}, \qquad \tilde{K}_+ = \frac{\tilde{\Gamma}_o}{\tilde{\Gamma}_+}e^{-\tilde{\phi}_o}. \tag{10b}$$

The physical pK values $\mathrm{p}K_\pm = -\log_{10}(K_\pm/1\,\mathrm{M})$ are listed in Table II. The surface charge σ_o and its nondimensionalized counterpart $\tilde{\sigma}_\mathrm{o}$ normalized by $e\Gamma_\mathrm{tot}$ are

$$\sigma_\mathrm{o} = e(\Gamma_+ - \Gamma_-), \qquad \tilde{\sigma}_\mathrm{o} = \tilde{\Gamma}_+ - \tilde{\Gamma}_-. \tag{11}$$

Finally, by straightforward algebra combining Eqs. (9)–(11), we eliminate $\tilde{\Gamma}_\mathrm{o}$, $\tilde{\Gamma}_\pm$, and $\tilde{\Gamma}_-$ and obtain an expression of $\tilde{\sigma}_\mathrm{o}$ in terms of $\tilde{\phi}_\mathrm{o}$ and $\tilde{K}_\pm$,

$$\tilde{\sigma}_\mathrm{o}(\tilde{\phi}_\mathrm{o}) = \frac{e^{-2\tilde{\phi}_\mathrm{o}} - \tilde{K}_+\tilde{K}_-}{e^{-2\tilde{\phi}_\mathrm{o}} + \tilde{K}_+ e^{-\tilde{\phi}_\mathrm{o}} + \tilde{K}_+\tilde{K}_-}. \tag{12}$$

D. Relating the surface to the bulk

The above surface and bulk ionic concentrations can be coupled by the Poisson–Boltzmann equation. Whereas, hydronium ions can diffuse to the o plane, other ions may not penetrate past the d plane, forming the immobile Stern layer depicted in Fig. 1.

Following the Gouy–Chapman–Stern model, we introduce the Stern capacitance C_s [F/m^2] (nondimensionalized as $\tilde{C}_\mathrm{s}$). It enters in an assumed linear relation between the voltage drop $\phi_\mathrm{o} - \phi_\mathrm{d}$ across the immobile layer and the surface charge σ_o,

$$\phi_\mathrm{o} - \phi_\mathrm{d} = \frac{\sigma_\mathrm{o}}{C_\mathrm{s}}, \qquad \tilde{\phi}_\mathrm{o} - \tilde{\phi}_\mathrm{d} = \frac{\tilde{\sigma}_\mathrm{o}}{\tilde{C}_\mathrm{s}}, \qquad \tilde{C}_\mathrm{s} = \frac{k_\mathrm{B}T}{e^2\Gamma_\mathrm{tot}}C_\mathrm{s}. \tag{13}$$

The boundary conditions at the surface for the Poisson–Boltzmann equation (7) involve the surface charge $\tilde{\sigma}_\mathrm{o}$ through Eqs. (12) and (13), and they become both nonlinear and mixed,

$$\boldsymbol{n}\cdot\nabla\tilde{\phi} = \frac{1}{\lambda_\mathrm{D}\tilde{q}_I}\tilde{\sigma}_\mathrm{o}(\tilde{\phi}), \text{ at the d plane,} \tag{14a}$$

$$\tilde{q}_I = \frac{\sqrt{2\epsilon k_\mathrm{B}T c_I}}{e\Gamma_\mathrm{tot}}. \tag{14b}$$

Here, we have introduced the surface normal $\boldsymbol{n}$ and the nondimensionalized bulk charge area density $\tilde{q}_I$.

In the special case where the curvature effects of the boundary can be neglected, e.g., the tangential derivatives $\nabla_t^2\tilde{\phi}$ in $\nabla^2\tilde{\phi}$ are much smaller than the normal-direction derivatives $\partial_n^2\tilde{\phi}$, the Poisson–Boltzmann equation (7) can be integrated once. The standard trick is to multiply the equation by $\partial_n\tilde{\phi}$, and then to use that $(\partial_n\tilde{\phi})\,\partial_n^2\tilde{\phi} = \partial_n[(\partial_n\tilde{\phi})^2]/2$ and $-z_\mathrm{X}(\partial_n\tilde{\phi})\exp(-z_\mathrm{X}\tilde{\phi}) = \partial_n[\exp(-z_\mathrm{X}\tilde{\phi})]$. The result, known as Grahame's equation [55], is

$$(\tilde{\sigma}_\mathrm{o})^2 = \tilde{q}_I^2\sum_{\mathrm{X},z_\mathrm{X}}\tilde{c}^\mathrm{b}_{\mathrm{X},z_\mathrm{X}}[e^{-z_\mathrm{X}\tilde{\phi}_\mathrm{d}} - e^{-z_\mathrm{X}\tilde{\phi}_\mathrm{m}}], \tag{15}$$

where $\tilde{\phi}_\mathrm{m}$ is the potential at the midpoint between opposite walls in the normal direction. In this simplified case, Eqs. (12), (13), and (15) form a self-consistent set of algebraic equations for the determination of $\tilde{\sigma}_\mathrm{o}$, $\tilde{\phi}_\mathrm{o}$, and $\tilde{\phi}_\mathrm{d}$. This algebraic approach, in particular, can be employed for flat plane-parallel channels of a very large width-to-height aspect ratio, since in this case, the curvature effects only play a role for the vanishingly small region at the edges of the channel cross section.

E. Entrance effects and permselectivity

For low salt concentration, the electric double layers of opposite walls of the nanochannel begin to overlap. Counterions are attracted to the nanochannel, while coions are expelled, and the nanochannel becomes permselective to the counterions. At each entrance of the nanochannel, the ionic densities have to attain their respective bulk values. This is achieved by displacing ions across the entrance, resulting in an ionic screening layer of width λ_D outside the entrance and uncompensated wall charges in the nanochannel, thus, creating oppositely pointing electric dipoles at each entrance and spawning the Donnan potential [2]. For low currents (the linear regime), no additional dissipation is created by this process: The potential drop experienced when passing into the nanochannel through one dipole region is canceled by the potential gain when leaving the nanochannel through the other dipole region.

The linear regime breaks down when a certain critical current I_c, the so-called limiting current, is reached. In the limit of low flow velocities, I_c can be estimated by the classic Levich theory [2,56,57] corrected by the logarithmic flux-focusing factor [31],

$$I_\mathrm{c} = \frac{\pi}{\ln\left(\frac{L_\mathrm{o}}{2h}\right)}\left(\frac{\eta+1}{\eta-1}\right)2e\mathcal{A}_\mathrm{res}D\frac{c_I}{L_\mathrm{o}}, \tag{16}$$

where L_o is the distance from the nanochannel entrance to the electrode in the reservoir, $2h$ is the height of the nanochannel, $\eta = I_+/I_-$ is the ratio of counterion and coion currents, e is the elementary charge, $\mathcal{A}_\mathrm{res}$ is the reservoir cross-sectional area, D is the ionic diffusivity, and c_I is the ionic strength of the solution in the reservoir.

For currents above I_c, a finite-sized polarization concentration region with nearly zero ion concentration develops in front of the anode-side entrance of the nanochannel, and there will be a significant voltage drop across this region. When this happens, the measured conductance G of the system drops, and this more strongly for lower reservoir concentration, in stark contrast to the increased G observed on the low concentration side of the conductance minimum given by δ in Table I and Eq. (21).

In Table III, we list the estimates for the limiting current I_c for the low concentration ($c^\mathrm{tot}_\mathrm{KCl} < 0.1$ mM) data points in Sec. IV B. In our experiments described in Sec. IV, we have

TABLE III. Estimates based on Eq. (16) of the limiting current I_c for data points in Sec. IV B with $c^\mathrm{tot}_\mathrm{KCl} < 0.1$ mM. $\mathcal{A}_\mathrm{res} = 1.5$ mm $\times$ 0.5 mm, $L_\mathrm{o} = 0.75$ mm, and $D = 6\times10^{-9}$ m^2/s.

$c^\mathrm{tot}_\mathrm{KCl}$ [μM]	c_I [μM]	λ_D/h	$-\tilde{\phi}_\mathrm{m}$	η	I_c [nA]
0.0	2.1	1.27	3.32	759	1.1
0.1	2.2	1.24	3.28	707	1.1
0.3	2.4	1.19	3.22	619	1.2
1.0	3.1	1.05	3.01	413	1.6
3.0	5.1	0.82	2.61	186	2.6
10.0	12.1	0.53	1.90	44	6.3
25.0	27.1	0.35	1.23	12	16.0
50.0	52.1	0.26	0.73	4	41.8

made sure that all our measurements were performed in the linear regime by using currents below 0.2 nA, i.e., at least a factor of 5 below the estimated limiting current I_c. Therefore, the measured conductance is the intrinsic nanochannel conductance. Furthermore, by reversing the polarity, we have checked that no current rectification did take place (data not shown).

F. Nanochannel conductance

Operating under conditions where the entrance effects are negligible, the electrical conductance G of an aqueous-filled nanochannel is found as $G = I/\Delta V$ by applying a known voltage drop ΔV and measuring the resulting current I. The electromigrative contribution $G_{mig} = I_{mig}/\Delta V$ to G is found by integrating over the sum of the conductivities for the chemical families X. The external applied voltage also gives rise to an axial electric field $\Delta V/L$ driving an axial electro-osmotic flow $v(y,z)$ and resulting in an advective current I_{adv} with the corresponding contribution, $G_{adv} = I_{adv}/\Delta V$, to the conductance. The flow is found by solving the steady-state Navier-Stokes equation with an electrical body force in a rectangular channel [58]. For high-aspect-ratio rectangular channels (height $2h$ much smaller than width w), only the vertical z direction matters, and the explicit expression for the total conductance, $G = G_{mig} + G_{adv}$, is well approximated by

$$G = \frac{2ew}{L}\sum_{X,z_X} z_X \mu^{*b}_{X,z_X} c^b_{X,z_X} \int_{-h}^{0} e^{-z_X\tilde{\phi}(z)}\,dz + \frac{2\epsilon k_B T w}{\eta L}\sum_{X,z_X} z_X c^b_{X,z_X} \int_{-h}^{0} [\tilde{\phi}(z) - \tilde{\phi}_d] e^{-z_X\tilde{\phi}(z)}\,dz. \quad (17)$$

For zero internal potential ($\tilde{\phi} = 0$), the effects of the wall disappear, and we obtain the bulk conductivity σ^b_{el} as

$$\sigma^b_{el} = e\sum_{X,z_X} z_X \mu^{*b}_{X,z_X} c^b_{X,z_X}. \quad (18)$$

III. NUMERICAL ONE-DIMENSIONAL ANALYSIS

In the following numerical analysis, we consider the case of a channel aligned with the x axis and with a rectangular cross section in the yz plane of height $2h$ and width w such that $-h < z < h$ and $0 < y < w$, mimicking our experimental system described in Sec. IV. The width-to-height aspect ratio in this case is large, $w \gg 2h$ so that we can apply a one-dimensional (1D) approximation, where the side walls at $y = 0$ and $y = w$ can be neglected, and only the top and bottom walls at $z = \pm h$ play a role.

A. The numerical algorithm

The first part of our numerical scheme is using the buffer calculator [49] based on Eq. (2) to determine the bulk concentrations c^b_{X,z_X} for a given solution of the ions H^+, OH^-, HCO_3^-, CO_3^{2-}, K^+, and Cl^-. We then consider the self-consistent solution of Eqs. (12), (13), and (15), which, in this case, takes the form

$$\tilde{\sigma}_o = \tilde{C}_s(\tilde{\phi}_o - \tilde{\phi}_d), \quad (19a)$$

$$\tilde{\sigma}_o = \frac{e^{-2\tilde{\phi}_o} - \tilde{K}_-\tilde{K}_+}{\tilde{K}_-\tilde{K}_+ + \tilde{K}_+ e^{-\tilde{\phi}_o} + e^{-2\tilde{\phi}_o}}, \quad (19b)$$

$$(\tilde{\sigma}_o)^2 = \tilde{q}_I^2 \sum_{X,z_X} \tilde{c}^b_{X,z_X}[e^{-z_X\tilde{\phi}_d} - e^{-z_X\tilde{\phi}_m}], \quad (19c)$$

together with the 1D Poisson–Boltzmann equation for planar walls including boundary conditions at the wall, $z = -h$, and at the center of the channel, $z = 0$,

$$\partial_z^2\tilde{\phi} = -\frac{1}{2\lambda_D^2}\sum_{X,z_X} z_X \tilde{c}^b_{X,z_X} e^{-z_X\tilde{\phi}}, \quad (20a)$$

$$\tilde{\phi}(-h) = \tilde{\phi}_d, \qquad \partial_z\tilde{\phi}(0) = 0. \quad (20b)$$

We implement and solve the problem using MATLAB (Mathworks, Inc.) using the following self-consistent iteration algorithm:

Initialization: Calculate $pH = -\log_{10}(c^b_H)$ and ionic concentrations $\tilde{c}^b_{X,z_X}$ in the bulk using the buffer calculator [49] Eq. (2), and assume $\tilde{\phi}_m = 0$.
Loop: Solve Eq. (19) for $\tilde{\sigma}_o$, $\tilde{\phi}_o$, and $\tilde{\phi}_d$, then solve Eq. (20) for $\tilde{\phi}$, and finally obtain $\tilde{\phi}_m = \tilde{\phi}(0)$.
Test: Repeat the loop until $\tilde{\phi}_m$ has converged.

Once converged, the algorithm provides the potential $\tilde{\phi}(z)$ to be used in Eq. (17) for calculating the conductance G. This algorithm, which self-consistently couples the CO_2-induced hydronium, surface, and bulk reactions, as well as nonlinear electrokinetics of the double layer, is the first main theoretical result of this paper.

B. Prediction of the conductance minimum

The second theoretical result is the model prediction that the conductance G of a nanochannel depends nonmonotonically on the KCl concentration $c^{tot}_{KCl} = c^b_{K^+} = c^b_{Cl^-}$ in the reservoirs. The nanochannel parameters listed in Table IV are chosen to correspond to our experimental validation presented in Sec. IV, and the simulation results are displayed in Fig. 2. Consistent with literature, the modeled conductance of the nanochannel follows a linear relation as does measured bulk conductance at high salt concentrations. Furthermore, the modeled conductance reaches a plateau in the infinite-dilution limit, similar to that found by Refs. [19,24,28,45]. However, as indicated in the log-log plot of Fig. 2(a) by the labels Plateau, Valley, Departure, and Bulk, we find, in contrast to these previous model studies, but in line with Ref. [32] where it went

TABLE IV. List of the nanochannel parameters used in the model calculation of the nanochannel conductance, Fig. 2.

Parameter	Symbol	Value
Height	$2h$	165 nm
Width	w	8.3 μm
Length	L	12.0 mm
Surface site density	Γ_{tot}	5 nm^{-2}
Stern capacitance	C_s	0.2 F m^{-2}
Viscosity of water	η	1.0 mPa s
Permittivity of water	ϵ	690 pF m^{-1}
Temperature	T	298 K

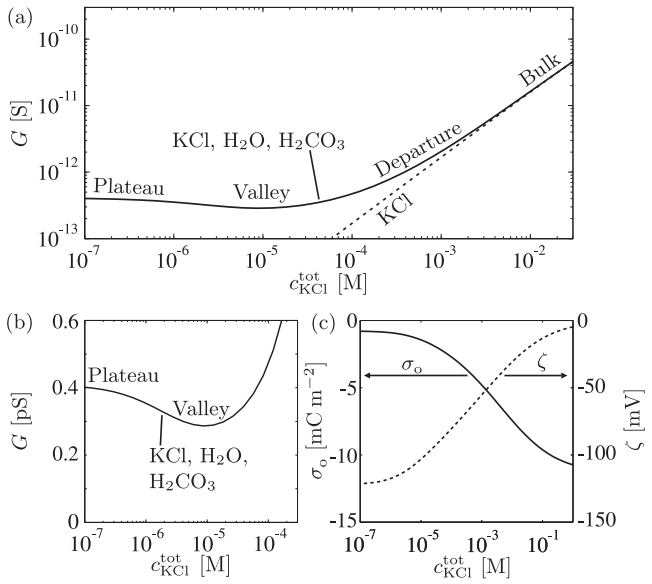

FIG. 2. (Color online) Theoretical predictions for the nanochannel conductance G Eq. (17) vs KCl concentration $c^{\text{tot}}_{\text{KCl}}$ in the reservoirs for the system described in Table IV and Sec. IV. (a) Log-log plot of G vs $c^{\text{tot}}_{\text{KCl}}$ taking KCl, dissolved CO_2, and hydronium ions (full line) into account, and bulk conductance taking only KCl into account (dashed line). Four conductance regimes are marked: bulk, departure, valley (minimum conductance), and plateau. (b) The nonmonotonic conductance from panel (a) in a lin-log plot. (c) The $c^{\text{tot}}_{\text{KCl}}$ dependence of the ζ potential $\zeta = \phi_{\text{d}}$ and the surface charge σ_{o}.

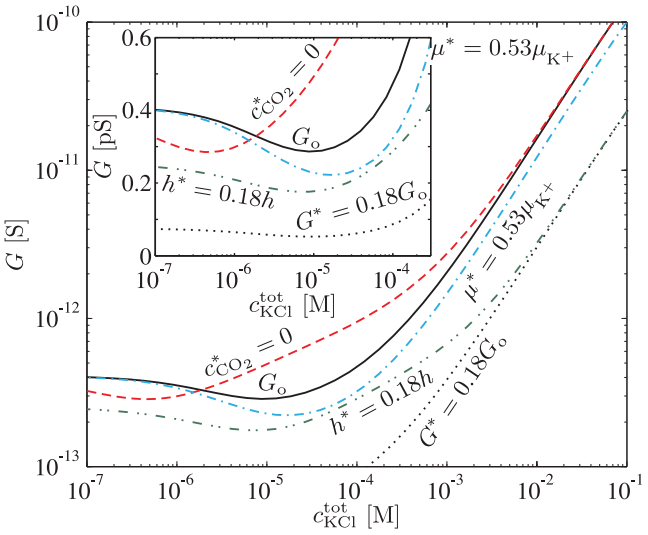

FIG. 3. (Color online) Theoretical prediction for the nanochannel conductance G Eq. (17) vs $c^{\text{tot}}_{\text{KCl}}$ in the reservoirs for the parameters of Fig. 2 (G_{o}, full black curve) and for variations from that: removal of CO_2 ($c^*_{CO_2} = 0$, dashed red curve), decreased mobility of the counterions ($\mu^* = 0.53\mu_{K^+} = \mu_{Li^+}$, dot-dashed blue curve), and decreased nanochannel height ($h^* = 0.18h$, dot-dot-dashed green curve). Also shown is a scaled curve ($G^* = 0.18G_{\text{o}}$, dotted black curve) for aid in comparison to the reduction of nanochannel height. The inset shows the nonmonotonic conductance in a lin-log plot, which enhances the predicted features.

un-noticed, that our model predicts a nonmonotonic behavior: A minimum conductance (the valley) is obtained before reaching the plateau. This conductance minimum positioned at $c^{\text{tot}}_{\text{KCl}} = 10\ \mu$M is more clearly pronounced in the lin-log plot of Fig. 2(b). We quantify the magnitude of the conductance minimum as the ratio δ of the largest conductance G_{max} on the low concentration side of the minimum and the minimum conductance G_{min},

$$\delta = \frac{G_{\text{max}}}{G_{\text{min}}}. \tag{21}$$

For the KCl-based Fig. 2(b), we calculate $\delta_{\text{KCl}} = 1.42$.

In Fig. 2(c), we show how the calculated ζ potential ϕ_{d} and surface charge σ_{o} vary with salt concentration, trends that have been previously observed theoretically and have been validated experimentally [26,44]. Moreover, as the magnitude of the ζ potential is small for our model system, $|\zeta| < 120$ mV $\approx 5k_{\text{B}}T/e$, we have justified our neglecting of ionic crowding effects near the surface [59], and we gain confidence in our model results.

C. Characterization of the conductance minimum

Further results of our model showing nonmonotonic conductance vs the reservoir salt concentration $c^{\text{tot}}_{\text{KCl}}$ are presented in Fig. 3, where parameters of the problem are varied one by one, relative to those of Fig. 2, which here and in the following are denoted G_{o} (full black curve). In particular, when CO_2 is not included in our model (dashed red curve), the conductance changes by up to a factor of 2 relative to G_{o}. Additionally, without CO_2, the position of the conductance minimum shifts from $c^{\text{tot}}_{\text{KCl}} \approx 10\ \mu$M down to $\approx 0.4\ \mu$M governed solely by autoprotolysis of water, again showing the importance of CO_2-induced hydronium ions for the appearance of nonmonotonic conductance.

In Fig. 3, we also plot G of a solution with a lower ion mobility. Specifically, we substitute KCl with LiCl (dot-dashed blue curve), thereby reducing the counterion mobility by a factor of 0.53 from $\mu_{K^+} = 76.2 \times 10^{-9}\ \text{m}^2\,(\text{V s})^{-1}$ to $\mu^* = \mu_{Li^+} = 40.1 \times 10^{-9}\ \text{m}^2\,(\text{V s})^{-1}$. Mobility reduction implies that: (i) In the high $c^{\text{tot}}_{\text{KCl}}$ regime $\sim 10^{-3}$–10^{-1} M, the conductance is lower by a factor of ~ 0.75 consistent with the lower bulk conductivity of the LiCl electrolyte. (ii) In the very dilute $c^{\text{tot}}_{\text{KCl}}$ regime $\sim 10^{-7}$–10^{-6} M, the conductance plateau reaches the same conductance value as KCl, again verifying that nanochannel conductance in this regime is dominated by the contribution from CO_2-induced hydronium. (iii) In the intermediate $c^{\text{tot}}_{\text{KCl}}$ regime $\sim 10^{-6}$–10^{-3} M, the conductance curve has a different shape: The position of the minimum is shifted to a higher value of salt concentration, $c^{\text{tot}}_{\text{KCl}} = 20\ \mu$M, and its magnitude is increased from $\delta_{\text{KCl}} = 1.42$ to $\delta_{\text{LiCl}} = 1.77$. This enhancement of the conductance minimum for the lower-mobility counterion Li^+ is consistent with the intake of counterions and the expulsion of coions in nanochannels with overlapping electric double layers, a situation where the counterions dominate the conductance.

We also show the dependence of nanochannel height on the predominance of a nonmonotonic conductance at low concentrations in Fig. 3. Specifically, we reduce the height of the nanochannel by a factor of 0.18 to $2h^* = 30$ nm (dot-dot-dashed green curve), corresponding to the silica

nanochannels of Ref. [60]. Again, we note that: (i) In the high $c_{\mathrm{KCl}}^{\mathrm{tot}}$ regime $\sim 10^{-3}$–10^{-1} M, the conductance is lower by a factor of ~ 0.18 consistent with the reduced cross-sectional area. (ii) In the intermediate $c_{\mathrm{KCl}}^{\mathrm{tot}}$ regime $\sim 10^{-5}$–10^{-3} M, the conductance curve has a more linear slope and, therefore, a wide regime of minimum conductance. (iii) In the very dilute $c_{\mathrm{KCl}}^{\mathrm{tot}}$ regime $\sim 10^{-7}$–10^{-5} M, the conductance is lower only by a factor of ~ 0.6 and not by the aforementioned factor of 0.18. This relatively higher conductance in smaller channels at low concentrations is due to overlapping electric double layers. For a binary symmetric electrolyte, the conductivity in the electric double layer $\sigma_{\mathrm{el}}^{\mathrm{DL}}$ will be higher than the bulk conductivity if the ζ potential is larger than the thermal voltage $\zeta > k_{\mathrm{B}}T/(ze)$ simply due to an increased ionic concentration. This is indeed the case in our nanochannels, especially at low concentrations, as seen in Fig. 2(c). Hence, in our nanochannels, as the concentration is lowered, the conductivity in the channel gradually changes from $\sigma_{\mathrm{el}}^{\mathrm{b}}$ to $\sigma_{\mathrm{el}}^{\mathrm{DL}}$ concurrently with the electric double layer overlap. The smaller the channel dimensions, the greater the overlap, and, thus, the higher the average conductivity at a given low concentration. Note that, for aid in comparing this low-height curve with the nominal conductance curve, we also have plotted the scaled version $G^* = 0.18G_{\mathrm{o}}$ (dotted black curve) of the original curve.

These theoretical model predictions must now be verified experimentally. To date, log-log plots of conductance vs salt concentration in unbuffered solutions do not readily show the conductance valley, but much of this may be because such a valley is difficult to discern in a log-log plot, as shown in Figs. 2 and 3. However, as listed in Table I, we have found six examples in the literature of an observed (but un-noticed) conductance minimum. To provide further experimental validation of our theoretical predictions, we performed a set of conductance measurements on silica nanochannels described in Sec. IV, varying just one parameter, namely, the hydronium concentration through the addition of HCl, to show that not only does this valley exist, but also our model predicts the behavior of the valley accurately when other ions are added to the system.

IV. EXPERIMENTAL VALIDATION

To test our theoretical predictions, we performed experiments in both bulk solutions and fused-silica nanochannels fabricated in-house at the University of California, Santa Barbara [26]. The nanochannels (165-nm high, 8.3-μm wide, and 12-mm long) were equipped with 1.5-mm-diameter reservoirs of depth 0.5 mm and mounted as shown in Fig. 4(a). We prepared 0.2-μm-filtered KCl concentrations $c_{\mathrm{KCl}}^{\mathrm{tot}} = 0.0001$, 0.0003, 0.001, 0.003, 0.01, 0.025, 0.05, 0.1, 0.5, 1, 5, 10, and 100 mM and another set with 50 μM hydrochloric acid added at the same KCl concentrations and at the additional values $c_{\mathrm{KCl}}^{\mathrm{tot}} = 0.02$, 0.2, 0.6, and 50 mM.

A. Measured bulk conductance

To validate the bulk conductance part of our model, we conducted bulk measurements using a standard technique: The prepared solutions were pipetted into the sample chamber of

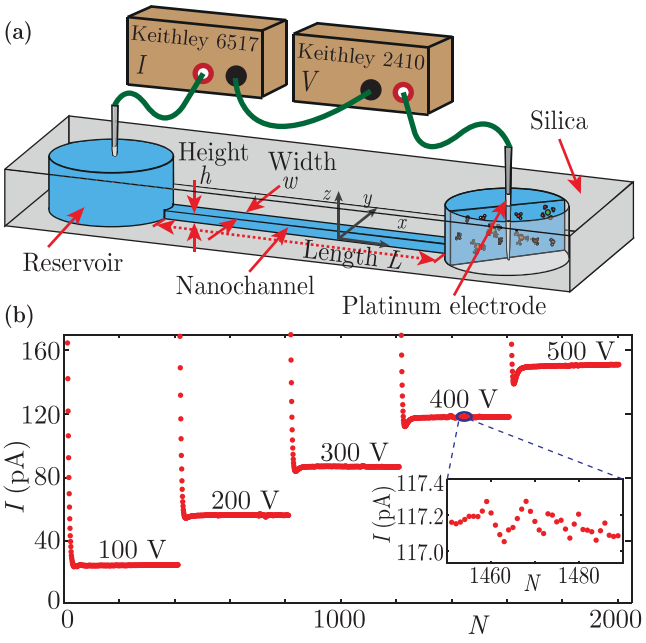

FIG. 4. (Color online) Experimental measurement of current I in silica nanochannels of dimensions $h \times w \times L = 165$ nm $\times$ 8.3 μm $\times$ 12 mm. (a) Our setup. For each experiment, the voltage ΔV (from a Keithley 2410) was applied for 5–10 min to allow I to equilibrate (monitored by a high-sensitive electrometer, Keithley 6517). (b) Raw data (dots) of I vs sample number N for the five values of ΔV indicated. The inset shows detailed variation of I vs N at 8 samples/s.

a commercial pH and conductivity meter (Oakton, Inc), and readouts of the pH and conductivity values were performed after allowing for equilibration to have taken place. These measurements were performed periodically on the prepared solutions to make sure that variations due to temperature and humidity did not exceed 5% of the original value. All solutions were filtered with 0.2-μm PTFE syringe filters prior to use.

Figure 5(a) shows the measured bulk conductivity for the KCl solutions used in our study, together with two model calculations of $\sigma_{\mathrm{el}}^{\mathrm{b}}$ based on Eq. (18) and Table II without any additional adjustable parameters: one (full line) taking into account all ions (H^+, OH^-, HCO_3^-, CO_3^{2-}, K^+, Cl^-), the other (dashed line) only including the salt (K^+, Cl^-). Both measurements and model calculations show the expected monotonic decrease as a function of the bulk KCl concentration $c_{\mathrm{KCl}}^{\mathrm{tot}}$ with a crossover to a constant value at $c_{\mathrm{KCl}}^{\mathrm{tot}} \approx 5 \times 10^{-6}$ M. The inset shows a scatter of the measurements relative to the model with errors within 13%, which, thus, constitutes an estimate of the experimental uncertainty in our paper. To further test the model, we added 50-μM HCl to our KCl solutions; experimental results and model calculation are shown in Fig. 5(b), with the inset indicating the deviation of measurements relative to the model to be within 16%.

B. Measured nanochannel conductance

The nanochannel conductance was measured as follows. After electrokinetically rinsing each channel thoroughly with DI water three times, we applied five voltages to the system

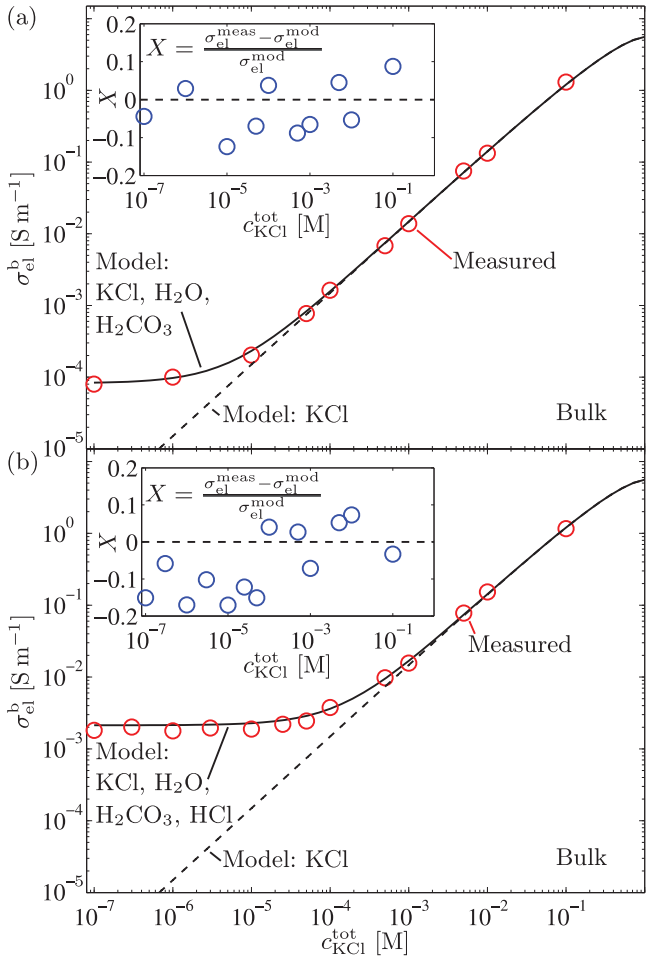

FIG. 5. (Color online) (a) Conductivity σ_{el}^{b} vs KCl concentration c_{KCl}^{tot} for bulk measurements (σ_{el}^{meas}, open red circles) and model calculations for both the full model with KCl, H_2CO_3, and H_2O (σ_{el}^{mod}, full line) and for a partial model with only KCl (dashed line). Model calculations are based on Eq. (18) and Table II without any additional adjustable parameters. The inset shows the relative deviation $X = (\sigma_{el}^{meas} - \sigma_{el}^{mod})/\sigma_{el}^{mod}$ (open blue circles) of the measurements from the model. (b) Same as panel (a) with the addition of 50-μM HCl.

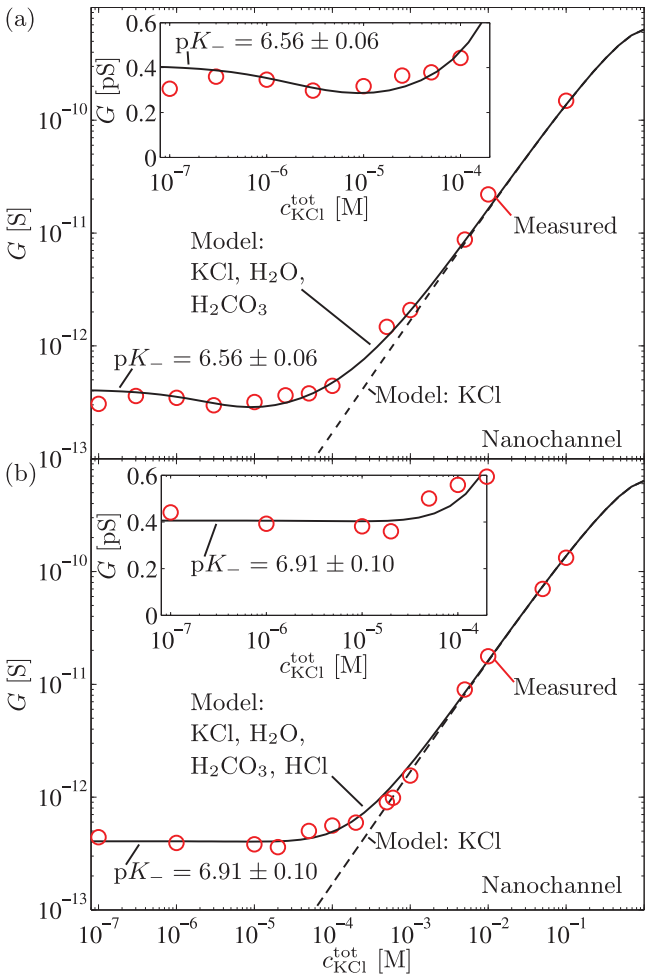

FIG. 6. (Color online) Log-log plot of measured nanochannel conductance G vs KCl concentration c_{KCl}^{tot} (red circles) and curve fits based on Eq. (17) using the logarithmic variables $\log_{10}(G)$ and $\log_{10}(c_{KCl}^{tot})$ for model electrolytes of various compositions (full and dashed curves) employing the parameters of Tables II and IV. (a) No HCl added: Fitting to a model including KCl, H_2O, and H_2CO_3 (full curve) yields $pK_- = 6.56 \pm 0.06$. Also shown is a model calculation including only KCl (dashed line). (b) As before but with 50 μM of HCl added: Fitting to a model including KCl, HCl, H_2O, and H_2CO_3 (full curve) yields $pK_- = 6.91 \pm 0.10$. The insets are lin-log plots of the respective low salt concentration regions.

(100, 200, 300, 400, and 500 V) in succession, each one lasting approximately 40 s. Raw data are shown in Fig. 4(b). To ensure consistent and repeatable data, if the trial did not yield four or five results that were within 10% of each other, we assumed an unsteady current reading, corroded electrodes, external interference, or poor channel preparation, and discarded the data. Solution exchanges were performed in a systematic fashion to avoid introducing bubbles or particulate matter into the channels.

Moreover, for concentrations below 10 μM, we covered the system with a Faraday cage to limit measurement noise. After each day of experiments, we flushed the reservoirs multiple times with DI water to prevent a buildup of salt deposits on the channel during its time in storage, and then stored the chip in a dry Eppendorf tube housed in a nitrogen container. We note that electrolysis does not affect the current measurements in our system: Conservatively, we estimate the pH change of the reservoir to be 7.7×10^{-4} s^{-1} [48]; next, we find the volumetric flow rate to be 4×10^{-15} m^3/s; furthermore, the absorption of CO_2 in the reservoir gives rise to H_2CO_3, which acts as a buffer and would further prevent pH changes, and finally, we replenished the reservoirs every 3 min.

Due to a significant electro-osmotic flow velocity in our 165-nm-high nanochannels, we do not encounter the hour-long equilibration time for conductance measurements encountered in 2-nm-high nanochannels [32].

The most significant contribution of our model is predicting the nanochannel conductance, which is shown together with experimental measurements in Fig. 6. Panel (a) shows results for KCl solutions between infinite dilution (DI water) and 100 mM. Using pK_- as the only fitting parameter, and using $\log_{10}(c_{KCl}^{tot})$ and $\log_{10}(G)$ as variables to ensure an even weighting between low and high concentration values, we

obtain the fit shown for $pK_- = 6.56 \pm 0.06$, corresponding well to the literature value of 6.64 [44]. The inset expands on the low salt concentration region and shows the measured conductance minimum and the theoretical fitting curve. The lowest concentration point is furthest off this curve, but it is also the one most prone to error. Previous models assuming constant surface charge give the plateau but no valley [19,24, 28,45], while relaxing this assumption taking surface chemical reactions into account leads to a monotonically decreasing conductance [61]. Notably, the experimental data of previous studies listed in Table I, have shown the same conductance behavior as our model and data, supporting our claim that the inclusion of hydronium ions in our model is consistent with a broad range of experimental results. In all of these references, the experimentally measured conductance has a minimum that the applied models do not capture. Furthermore, the minimum is located at KCl concentrations around 10^{-5}–10^{-4} M that is consistent with our model predictions.

Another way to validate the predictions of our model is to add an extra amount of hydronium ions. The conductance valley is due to the concentration of K^+ and Cl^- dropping below that of H^+ and HCO_3^- together with the fact that the Debye length and ζ potential increase for decreasing ionic strength (Fig. 2). Therefore, as in Fig. 5, we can test the model by adding HCl and can observe the change in the conductance curve. The result in Fig. 6(b) shows no valley in both experiment and model. The fit now gives $pK_- = 6.91$, indicating that surface reactions are pH dependent.

Finally, as a control experiment, we measured the change in pH and conductance of nanochannels substituting CO_2-saturated by CO_2-oversaturated KCl solutions generated by dry ice vapors. In this case, pH dropped by 22%, and G increased by 27% (data not shown). Clearly, it would be desirable to design experiments with a more controlled content of CO_2 in the atmosphere to further investigate its influence on nanochannel conductance, but this is beyond the scope of this current paper.

V. CONCLUSION

In this paper, we have extended a recent self-consistent theoretical model of nanochannel ion transport [26] to unbuffered solutions with low salt concentration by taking hydronium ions into account, induced by carbonic acid arising from dissolved CO_2 from the atmosphere, through the explicit addition of H^+ and HCO_3^- in our coupled solution/wall chemical-equilibrium dissociation scheme. Using this model, we have predicted the hydronium dependence of the electrical conductance of electrolyte-filled nanochannels, and, in particular, we have identified a conductance minimum in the low salt concentration regime as a function of the reservoir salt concentration c_{KCl}^{tot}. We studied the dependence of the conductance minimum theoretically and have predicted that its magnitude would be reduced dramatically in a CO_2-poor atmosphere and significantly enhanced using low-mobility counterions.

Our theoretical prediction of the conductance minimum is supported by several independent experimental observations in the literature. Furthermore, to validate our theoretical predictions, we have successfully compared our model with direct experimental conductance measurements on a wide range of KCl concentrations with and without the addition of a specific extra amount of hydronium ions from HCl in 165-nm-high silica nanochannels. A more thorough experimental study is underway to fully characterize the nanochannel conductance minimum at low salt concentrations and CO_2-dissolution controlled hydronium concentrations.

Our modeling and experimental results indicate the possibility for developing a sensitive nanochannel-based carbon dioxide sensor. To this end, an in-depth experimental study must be performed in a tightly regulated atmosphere. Combining such measurements with our model could be used to determine which parameter values lead to the most pronounced conductance minimum and what consequences this may have for using nanochannels for unique gas sensors.

[1] T. M. Squires and S. R. Quake, Rev. Mod. Phys. **77**, 977 (2005).
[2] R. Schoch, J. Han, and P. Renaud, Rev. Mod. Phys. **80**, 839 (2008).
[3] W. Sparreboom, A. van den Berg, and J. C. T. Eijkel, Nat. Nanotechnol. **4**, 713 (2009).
[4] L. Bocquet and E. Charlaix, Chem. Soc. Rev. **39**, 1073 (2010).
[5] M. Napoli, J. C. T. Eijkel, and S. Pennathur, Lab Chip **10**, 957 (2010).
[6] J. Han and H. G. Craighead, Science **288**, 1026 (2000).
[7] L. R. Huang, J. O. Tegenfeldt, J. J. Kraeft, J. C. Sturm, R. H. Austin, and E. C. Cox, Nat. Biotechnol. **20**, 1048 (2002).
[8] R. Karnik, K. Castelino, R. Fan, P. Yang, and A. Majumdar, Nano Lett. **5**, 1638 (2005).
[9] R. Karnik, K. Castelino, and A. Majumdar, Appl. Phys. Lett. **88**, 123114 (2006).
[10] J. Fu, R. B. Schoch, A. L. Stevens, S. R. Tannenbaum, and J. Han, Nat. Nanotechnol. **2**, 121 (2007).
[11] N. F. Y. Durand and P. Renaud, Lab Chip **9**, 319 (2009).
[12] W. Reisner, N. B. Larsen, A. Silahtaroglu, A. Kristensen, N. Tommerup, J. O. Tegenfeldt, and H. Flyvbjerg, Proc. Natl. Acad. Sci. USA **107**, 13294 (2010).
[13] H. Daiguji, P. Yang, A. J. Szeri, and A. Majumdar, Nano Lett. **4**, 2315 (2004).
[14] W. Olthuis, B. Schippers, J. Eijkel, and A. van den Berg, Sens. Actuators B **111-112**, 385 (2005).
[15] F. H. J. van der Heyden, D. J. Bonthuis, D. Stein, C. Meyer, and C. Dekker, Nano Lett. **7**, 1022 (2007).
[16] S. Pennathur, J. C. T. Eijkel, and A. van den Berg, Lab Chip **7**, 1234 (2007).
[17] C. Davidson and X. Xuan, Electrophoresis **29**, 1125 (2008).
[18] M. Wang and Q. Kang, Microfluid. Nanofluid. **9**, 181 (2009).
[19] D. Stein, M. Kruithof, and C. Dekker, Phys. Rev. Lett. **93**, 035901 (2004).
[20] S. Pennathur and J. G. Santiago, Anal. Chem. **77**, 6782 (2005).

[21] H. Daiguji, P. Yang, and A. Majumdar, Nano Lett. **4**, 137 (2004).
[22] K. G. H. Janssen, H. T. Hoang, J. Floris, J. de Vries, N. R. Tas, J. C. T. Eijkel, and T. Hankemeier, Anal. Chem. **80**, 8095 (2008).
[23] M. Whitby, L. Cagnon, M. Thanou, and N. Quirke, Nano Lett. **8**, 2632 (2008).
[24] D. Martins, V. Chu, D. M. F. Prazeres, and J. P. Conde, Procedia Chemistry (Weinheim, Germany) **1**, 1095 (2009).
[25] M. Wang, Q. Kang, and E. Ben-Naim, Anal. Chim. Acta **664**, 158 (2010).
[26] M. B. Andersen, J. Frey, S. Pennathur, and H. Bruus, J. Colloid Interface Sci. **353**, 301 (2011).
[27] Q. Pu, J. Yun, H. Temkin, and S. Liu, Nano Lett. **4**, 1099 (2004).
[28] R. Karnik, R. Fan, M. Yue, D. Li, P. Yang, and A. Majumdar, Nano Lett. **5**, 943 (2005).
[29] R. Karnik, C. Duan, K. Castelino, H. Daiguji, and A. Majumdar, Nano Lett. **7**, 547 (2007).
[30] S. J. Kim, Y.-C. Wang, J. H. Lee, H. Jang, and J. Han, Phys. Rev. Lett. **99**, 044501 (2007).
[31] G. Yossifon, P. Mushenheim, Y.-C. Chang, and H.-C. Chang, Phys. Rev. E **79**, 046305 (2009).
[32] C. Duan and A. Majumdar, Nat. Nanotechnol. **5**, 848 (2010).
[33] C. G. Armistead, A. J. Tyler, F. H. Hambleton, S. A. Mitchell, and J. A. Hockey, J. Phys. Chem. **73**, 3947 (1969).
[34] S. Levine and A. L. Smith, Discuss. Faraday Soc. **52**, 290 (1971).
[35] D. E. Yates, S. Levine, and T. W. Healy, J. Chem. Soc., Faraday Trans. 1 **70**, 1807 (1974).
[36] J. A. Davis, R. O. James, and J. O. Leckie, J. Colloid Interface Sci. **63**, 480 (1978).
[37] J. A. Davis and J. O. Leckie, J. Colloid Interface Sci. **67**, 90 (1978).
[38] T. Hiemstra, W. V. Riemsdijk, and G. Bolt, J. Colloid Interface Sci. **133**, 91 (1989).
[39] R. Charmas, W. Piasecki, and W. Rudzinski, Langmuir **11**, 3199 (1995).
[40] N. L. Burns, J. Colloid Interface Sci. **183**, 249 (1996).
[41] J. Lützenkirchen, Environ. Sci. Technol. **32**, 3149 (1998).
[42] S. H. Behrens and D. G. Grier, J. Chem. Phys. **115**, 6716 (2001).
[43] P. M. Biesheuvel, J. Colloid Interface Sci. **275**, 514 (2004).
[44] M. Wang and A. Revil, J. Colloid Interface Sci. **343**, 381 (2010).
[45] R. B. Schoch and P. Renaud, Appl. Phys. Lett. **86**, 253111 (2005).
[46] L. Cheng, Ph.D. thesis, University of Michigan, 2008.
[47] R. F. Probstein, *Physicochemical Hydrodynamics: An Introduction* (Wiley Interscience, 1994).
[48] A. Persat, R. D. Chambers, and J. G. Santiago, Lab Chip **9**, 2437 (2009).
[49] A. Persat, R. D. Chambers, and J. G. Santiago, [http://microfluidics.stanford.edu/download].
[50] This value follows from Henry's law with the coefficient $c_{CO_{2(aq)}}/p_{CO_{2(g)}} = 3.5$ mM/atm [51] for $CO_{2(g)} \rightleftharpoons CO_{2(aq)}$ and the reaction constant $K_{H_2CO_3} = 2.6 \times 10^{-3}$ for carbonic acid $H_2O + CO_{2(aq)} \rightleftharpoons H_2CO_3$ [48].
[51] H. S. Harned and R. Davis, J. Am. Chem. Soc. **65**, 2030 (1943).
[52] A. Persat, M. E. Suss, and J. G. Santiago, Lab Chip **9**, 2454 (2009).
[53] D. R. Lide, *CRC Handbook of Chemistry and Physics*, 91st ed. (Internet Version 2011) (CRC/Taylor and Francis, Boca Raton, FL, 2010).
[54] J. Kielland, J. Am. Chem. Soc. **59**, 1675 (1937).
[55] D. C. Grahame, Chem. Rev. **41**, 441 (1947).
[56] V. G. Levich, *Physicochemical Hydrodynamics* (Prentice-Hall, New York, 1962).
[57] I. Rubinstein, *Physical Electrochemistry* (Dekker, New York, 1995).
[58] H. Bruus, *Theoretical Microfluidics*, Oxford Master Series in Physics No. 18 (Oxford University Press, Oxford, 2008).
[59] M. S. Kilic, M. Z. Bazant, and A. Ajdari, Phys. Rev. E **75**, 021502 (2007).
[60] F. Persson, L. H. Thamdrup, M. B. Mikkelsen, S. E. Jarlgaard, P. Skafte-Pedersen, H. Bruus, and A. Kristensen, Nanotechnology **18**, 245301 (2007).
[61] K. Huang and R. Yang, Nanotechnology **18**, 115701 (2007).

Appendix E

Paper submitted to Phys Rev Lett

M. B. Andersen, M. van Soestbergen, A. Mani, H. Bruus, P. M. Biesheuvel, and M. Z. Bazant, Current-induced membrane discharge (submitted to Phys Rev Lett on 29 Feb 2012 `http://arxiv.org/abs/1202.6448`).

Current-Induced Membrane Discharge

M. B. Andersen,[1,2] M. van Soestbergen,[3,4] A. Mani,[2] H. Bruus,[1] P. M. Biesheuvel,[3,5] and M. Z. Bazant[6]

[1] *Department of Micro- and Nanotechnology, Technical University of Denmark, DTU Nanotech Building 345 East, DK-2800 Kongens Lyngby, Denmark*
[2] *Department of Mechanical Engineering, Stanford University, Stanford, CA, 94305, USA*
[3] *Wetsus, Centre of Excellence for Sustainable Water Technology, Agora 1, 8934 CJ Leeuwarden, The Netherlands*
[4] *Department of Applied Physics, Eindhoven University of Technology, Den Dolech 2, 5612 AZ Eindhoven, The Netherlands*
[5] *Department of Environmental Technology, Wageningen University, Bornse Weilanden 9, 6708 WG Wageningen, The Netherlands*
[6] *Departments of Chemical Engineering and Mathematics, Massachusetts Institute of Technology, Cambridge, MA, 02139, USA.*

(Dated: February 29, 2012)

Possible mechanisms for over-limiting current (OLC) through aqueous ion-exchange membranes (exceeding diffusion limitation) have been debated for half a century. Flows consistent with electro-osmotic instability (EOI) have recently been observed in microfluidic experiments, but the existing theory neglects chemical effects and remains to be quantitatively tested. Here, we show that charge regulation and water self-ionization can lead to OLC by "current-induced membrane discharge" (CIMD), even in the absence of fluid flow. Salt depletion leads to a large electric field which expels water co-ions, causing the membrane to discharge and lose its selectivity. Since salt co-ions and water ions contribute to OLC, CIMD interferes with electrodialysis (salt counter-ion removal) but could be exploited for current-assisted ion exchange and pH control. CIMD also suppresses the extended space charge that leads to EOI, so it should be reconsidered in both models and experiments on OLC.

PACS numbers: 47.57.jd, 87.16.dp, 82.45.Mp, 82.33.Ln

Selective ion transport across charged, water-filled membranes plays a major role in ion exchange and desalination [1, 2], electrophysiology [3], fuel cells [4, 5], and lab-on-a-chip devices [6–10], but is not yet fully understood. A long-standing open question has been to explain experimentally observed overlimiting current (OLC), exceeding classical diffusion limitation [11]. Possible mechanisms include electroosmotic instability (EOI) and water splitting in the bulk solution [12, 13], as well as surface conduction and electro-osmotic flow in microchannels [14]. Vortices consistent with EOI have recently been observed under OLC conditions [7, 15, 16], although the theory of Rubinstein and Zaltzman [17–19] remains to be tested quantitatively. The water splitting mechanism, either catalyzed by membrane surface groups or through the second Wien effect, has not yet been conclusively tied to OLC [13, 20–23].

In this Letter, we propose a chemical mechanism for OLC, "current-induced membrane discharge" (CIMD), resulting from membrane (de)protonation and water self-ionization, even in the absence of fluid flow. The amphoteric nature of the charge of ion-exchange membranes (i.e. sensitivity to pH and other stimuli) is well known [5, 24–29], but not the response to a large applied current. The basic physics of CIMD is illustrated in Fig. 1 for an anion-exchange membrane. During OLC, a large electric field develops on the upstream, salt-depleted side of the membrane, which expels H^+ and attracts OH^-, causing the membrane to deprotonate and lose selectivity, thereby allowing salt co-ions to pass and producing large pH gradients. The upstream solution becomes more acidic (low pH), while the downstream, salt-enriched solution and the membrane become more basic (high pH).

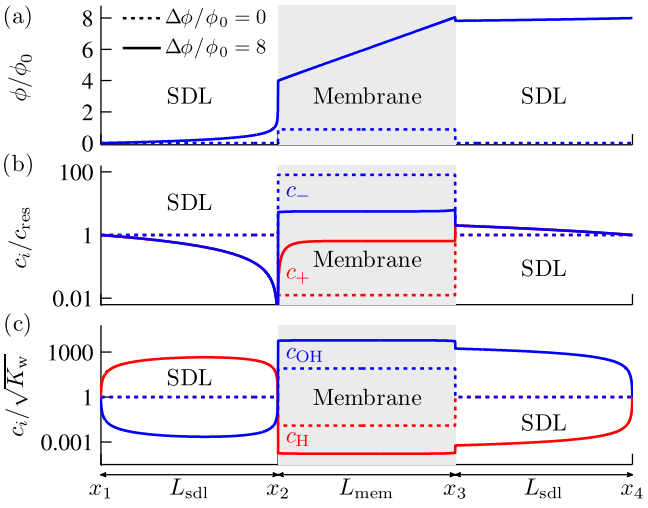

FIG. 1. [Color online] Basic physics of CIMD, illustrated by numerical solutions of Eqs. (2), (5), and (6) for an anion exchange membrane between two stagnant diffusion layers (SDL) for (a) electrostatic potential and concentrations of (b) cations c_+ and anions c_- and (c) protons c_H and hydroxyl ions c_{OH}.

The local charge of an aqueous membrane strongly de-

pends on the local pH. In our examples below, we consider an anion-exchange membrane with fixed surface groups of volumetric concentration $c_{\rm mem}$, which selectively allows negatively charged anions (counter-ions) to pass, while blocking cations (co-ions) [30]. Depending on pH $\approx$ p[H] $= -\log_{10}(c_{\rm H})$, where $c_{\rm H}$ is the proton concentration (H^+ or H_3O^+) in M, the membrane can "discharge" (deprotonate):

$$\mathrm{RH^+} \overset{K}{\rightleftharpoons} \mathrm{R} + \mathrm{H^+}. \tag{1}$$

The ratio of product to reactant concentrations in equilibrium is the dissociation constant K in M (pK $= -\log_{10} K$). Assuming a classical Langmuir adsorption isotherm [24–28, 31, 32], the ionization degree of the membrane,

$$\alpha = \left(1 + \frac{K}{c_{\rm H}}\right)^{-1} = \left(1 + 10^{\rm pH - pK}\right)^{-1}, \tag{2}$$

relates its charge concentration $\alpha\, c_{\rm mem}$ to pH and pK. (For a cation-exchange membrane, the power is p$K-$pH.) To describe the local pH, we cannot assume Boltzmann equilibrium with an external reservoir. Instead, we consider ion transport coupled to membrane discharge Eq. (1) and water self-ionization,

$$\mathrm{H_2O} \overset{K_{\rm w}}{\rightleftharpoons} \mathrm{OH^-} + \mathrm{H^+}, \tag{3}$$

with dissociation constant

$$K_{\rm w} = c_{\rm H} c_{\rm OH} \tag{4}$$

where $K_{\rm w} = 10^{-14}$ M^2 at $T = 25$ °C. Although kinetics can be included [5, 20–22, 33], the reactions (1) and (3) are typically fast, so we assume local quasi-equilibrium.

We now develop a membrane model (seemingly the first) including all of these effects: (i) transport of four ionic species, including co-ions and water ions (H^+ and OH^-) along with majority anions, (ii) water self-ionization, and (iii) pH-dependent membrane charge. We consider the prototypical 1D electrodialysis geometry in Fig. 1, consisting of a planar ion-selective membrane of thickness $L_{\rm mem}$ between two well-stirred reservoir compartments of salt ion concentration $c_{\rm res}$ and pH of pH$_{\rm res}$. We adopt the simplest and most commonly used model of diffusion limitation [11], in which ion concentrations vary across "stagnant diffusion layers" (SDL) of thickness $L_{\rm sdl}$ (of the order 10–100 μm) between the reservoirs and the membrane, e.g. representing convection-diffusion boundary layers or stagnant gel films.

Ionic diffusion, electromigration and reactions are described by four Nernst-Planck equations. Following Refs. [24, 25, 34], we combine the Nernst–Planck equations for H^+ and OH^- using Eq. (4) to eliminate the reaction terms and relate the water-ion current density $J_{\rm w}$ to the water-ion variable $c_{\rm w} = (D_{\rm H} c_{\rm H} - D_{\rm OH} c_{\rm OH})/D_{\rm w}$, in which $D_{\rm w} = \sqrt{D_{\rm H} D_{\rm OH}}$ is the geometric mean of the free H^+ and OH^- diffusivities. We thus arrive at the following set of coupled, nonlinear, differential equations to be solved in both SDLs and the membrane [34]:

$$\frac{\mathrm{d}J_i}{\mathrm{d}x} = 0, \qquad i = +, -, \mathrm{w}, \tag{5a}$$

$$J_\pm = \mp f_{\rm r} D_\pm \Big(\frac{\mathrm{d}c_\pm}{\mathrm{d}x} \pm c_\pm \frac{\mathrm{d}\phi}{\mathrm{d}x} \Big), \tag{5b}$$

$$J_{\rm w} = -f_{\rm r} D_{\rm w} \Big(\frac{\mathrm{d}c_{\rm w}}{\mathrm{d}x} + \left[4K_{\rm w} + c_{\rm w}^2\right]^{\frac{1}{2}} \frac{\mathrm{d}\phi}{\mathrm{d}x} \Big), \tag{5c}$$

where J_i is the ionic current density of species i and $f_{\rm r}$ is a hindrance factor accounting for porosity, tortuosity and constriction ($f_{\rm r} = 1$ in the SDLs). Here, ϕ is the dimensionless mean electrostatic potential scaled to the thermal voltage $V_{\rm T} = k_{\rm B}T/e = 25.7$ mV and satisfying Poisson's equation

$$\frac{\mathrm{d}^2\phi}{\mathrm{d}x^2} = -4\,\pi \lambda_{\rm B} \left(\rho_{\rm ions} + \rho_{\rm mem}\right), \tag{6}$$

where $\lambda_{\rm B} = e^2/(4\,\pi \varepsilon_{{\rm r},j} \varepsilon_0 k_{\rm B} T)$ is the Bjerrum length, and $\rho_{\rm ions} = \epsilon\,(c_+ - c_- + c_{\rm H} - c_{\rm OH})$ and $\rho_{\rm mem} = \alpha\,\epsilon\, c_{\rm mem}$ are charge densities due to the ions and the immobilized charges in the membrane, respectively. The porosity ϵ of the membrane appears because concentrations c_i are defined with respect to the interstitial, not total, volume ($\epsilon = 1$ in the SDLs). In our simulations below, we choose the following typical parameters: $c_{\rm mem} = 5$ M, p$K = 9.5$, $L_{\rm mem} = L_{\rm sdl} = 100$ μm, $\varepsilon_{\rm r,sdl} = 78$, $\varepsilon_{\rm r,mem} = 29$, $\epsilon = 0.4$, $f_{\rm r} = 0.02$ [35], $D_+ = 1.3 \times 10^{-9}$ m^2 s^{-1} and $D_- = 2.0 \times 10^{-9}$ m^2 s^{-1} (corresponding to NaCl), $D_{\rm H} = 9.3 \times 10^{-9}$ m^2 s^{-1}, and $D_{\rm OH} = 5.3 \times 10^{-9}$ m^2 s^{-1}. We also use pH$_{\rm res} = 7$ and $\beta = 2\,c_{\rm res}/c_{\rm mem} = 0.02$, unless otherwise noted. The voltage difference across the system is $\Delta\phi$. At the reservoir/SDL boundaries we set $c_\pm = c_{\rm res}$ and relate $c_{\rm w}$ to pH$_{\rm res}$.

In spite of neglecting fluid flow, the model still predicts OLC, as shown in Fig. 1. The classical ion concentration polarization phenomenon is apparent in panel (b) with salt depletion where counter-ions (anions) enter ($x = x_2$) and enrichment where they leave ($x = x_3$). Within the membrane, however, anion depletion and cation (co-ion) enrichment reveal a significant loss of selectivity due to CIMD. At the same time, panel (c) shows large, order-of-magnitude variations in $c_{\rm H}$, "mirrored" by $c_{\rm OH}$ in equilibrium Eq. (4), with proton enrichment (acidity) in the left SDL and proton depletion (basicity) in both the membrane and the right SDL. The existence of such pH variations has been confirmed experimentally in similar systems [36–39].

Motivated by this observation, we analyze the pH gradients perturbatively in the full CIMD model. We consider under-limiting currents, assume thin, quasi-equilibrium double layers (Donnan approximation) at the SDL/membrane interfaces, and solve the leading-order

problem for c_+, c_- and ϕ with small perturbations in c_H and c_{OH}, valid when $(c_H - c_{OH})/(c_+ - c_-) \ll 1$. The resulting semi-analytical model (to be described in detail elsewhere) suffices to predict CIMD (variations of membrane charge with local pH) via Eq. (2). Numerical calculations show that pH and α are nearly constant across the membrane, so the water charge density is averaged between positions x_2 and x_3 (see below) to calculate the membrane charge and midplane pH [Fig. 2(b)] to be used in Eq. (2) to calculate α.

The final result for the most general model including membrane discharge, arbitrary values for pH_{res} and c_{res}, and the possibility that all diffusion coefficients are different, consists of Eq. (2) together with the set of algebraic equations below (see the Supplemental Material for details). First, we introduce the dimensionless salt flux variable $j_{salt} = (J_- - J_+ D_-/D_+)/J_{lim}$, in which $J_{lim} = -2\,D_- c_{res}/L_{sdl}$ is the "classical" limiting current density [11], and obtain the salt current-voltage relation,

$$\Delta\phi = 4\,\tanh^{-1}(j_{salt}) + \frac{j_{salt}}{\gamma}\frac{\beta}{\alpha}, \qquad (7)$$

in which $\gamma = f_r/l_{mem}$, where $l_{mem} = L_{mem}/L_{sdl}$ is the membrane-to-SDL width ratio. The first term describes concentration polarization in the SDLs, while the second is the Ohmic response of the membrane. Next, we introduce the dimensionless water ion flux $j_w = J_w L_{sdl}/(D_w\sqrt{K_w})$ and water ion variable $\rho_w = c_w/\sqrt{K_w}$ and obtain the following equations, $\rho_w(x_3^{mem}) - \rho_w(x_2^{mem})\exp[j_{salt}\,\beta/(\gamma\,\alpha)] + j_w/\gamma = 0$, $\sinh^{-1}[\rho_w(x_i^{mem})/2] = \sinh^{-1}\left[\rho_w(x_i^{sdl})/2\right] - \sinh^{-1}(\alpha/[\beta\,(1\mp j_{salt})])$, and $\rho_w(x_i^{sdl}) = \rho_w^{res} \mp j_w + \rho_0[1 + 2\,\gamma\,\beta/\alpha]\ln(1 \mp j_{salt})$, (where in these expressions $i = 2$ and 3 corresponds to $-$ and $+$, respectively). Here, ρ_w^{res} is related to pH_{res} and $\rho_0 = [4 + (\rho_w^{res})^2]^{\frac{1}{2}}$. Note that x_i^{mem} and x_i^{sdl} refer to positions on either side of the equilibrium electric double layer at the membrane-SDL interfaces. In the limit of an infinite membrane charge $\beta/\alpha \to 0$ the solution to the leading order problem [Eq. (7)] is simply the "classical" result [40], $j_{salt} = \tanh(\Delta\phi/4)$. We find the characteristic voltage factor ϕ_0 by expanding Eq. (7) for small $j_{salt} \ll 1$ and obtain $j_{salt} = \Delta\phi/\phi_0$ in which $\phi_0 = 4 + \beta/\gamma$ assuming constant $\alpha = 1$.

Results of the semi-analytical model are compared with full numerical calculations in Fig. 2, which shows good agreement in the expected range of validity $\Delta\phi/\phi_0 \lesssim 1$. The pH appears to converge towards a limiting value for $\Delta\phi \to \infty$, and the jump in this limiting pH-value between the left SDL and the membrane is huge, here about 5 pH units at the highest values of $\Delta\phi$ considered. We note that the deviation between the analytical and numerical solution is largest in the left SDL where electroneutrality is most strongly violated. This comparative analysis constitutes a validation of our numerics and provides further support for our conclusions

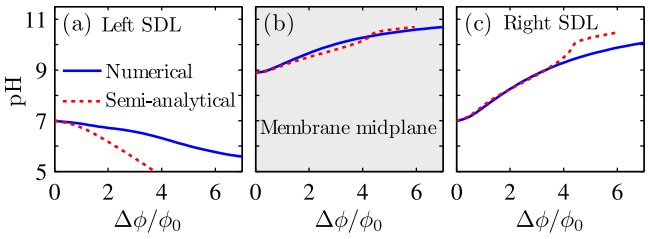

FIG. 2. [Color online] Predicted pH variations from the full numerical model, compared to the semi-analytical approximation, as a function of the applied voltage (a) in the left SDL, just next to the membrane, (b) at the membrane midplane, and (c) in the right SDL, next to the membrane.

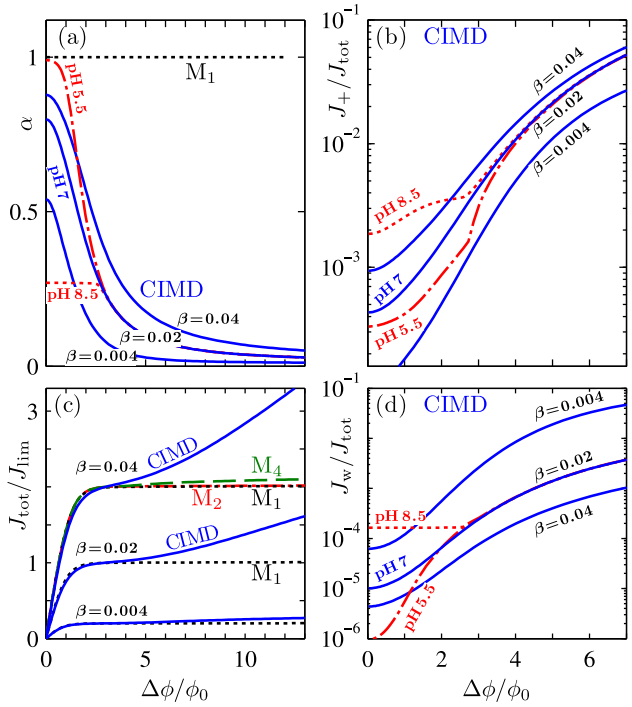

FIG. 3. [Color online] Comparison of the classical M_1 model (only counterions in the membrane) with the full CMID model (label "pH" refers to pH_{res}). (a) Membrane ionization degree α. (b) co-ion current J_+. (c) Total current J_{tot}. (d) Water ion current J_w.

regarding the role of pH as controlling the ionic transport properties of ion-selective membranes.

We now turn to a numerical analysis of the CIMD model Eqs. (2)–(6). For comparison, we also solve the classical model M_1 used in all prior work on EOI [15–19] in which (i) $c_- = 0$ in the membrane, (ii) $c_H = c_{OH} = 0$ everywhere, and (iii) $\alpha = 1$ for all conditions. We also solve two intermediate models which include co-ions in the membrane with $\alpha = 1$ and either *exclude* (M_2) or *include* (M_4) water ions, i.e. taking 2 or 4 ions into account in the membrane, respectively. The total current density is $J_{tot} = J_+ + J_- + J_w$.

Figure 3(a) shows the significant decrease in the ionization degree α predicted by the CIMD model, in contrast to the constant $\alpha = 1$ in the M_1 model. Moreover, α decreases with decreasing β (due to increasing Donnan potential) and decreases with pH_{res} (due to decreasing c_H in the membrane). A striking, and yet unexplained prediction is that for pH_{res} larger than 7 the ionization degree is almost constant until the curve hits that for $pH_{res} = 7$ after which the curves follow each other. In general we find beyond a few times ϕ_0 that reservoir pH has a very small influence on membrane charge, fluxes and currents (see also Fig. 3(b)-(d)). Figure 3(b) shows the significant increase of co-ion flux J_+, thus loss of membrane selectivity, with increasing voltage, as predicted by the CIMD model, for all values of pH and β, while Fig. 3(d) shows likewise the increase in current density J_w due to water ions. Still, these contributions do not sum to the increased current during OLC, as shown in Fig. 3(c), the difference being due to increased counter-ion flux J_-.

Although the current-voltage relation in CIMD is quite complicated, our simulations and analysis suggest two general trends: (i) OLC increases with reservoir salt concentration, roughly as $\beta^{0.65}$ for the parameters of Fig. 3; (ii) OLC is nearly independent of reservoir pH, in spite of the large pH gradients produced across the membrane.

Finally, we analyze the possible effect of CIMD on EOI. In the classical M_1 model, non-equilibrium space charge forms at the limiting current [40–43], and its growing separation from the membrane reduces viscous resistance to electro-osmotic flow and destabilizes the fluid [17–19]. As a measure of the propensity to develop EOI we use the transverse (Helmholtz–Smoluchowski) electroosmotic mobility $\mu_{eo}/\mu_{eo,0}$ at the left SDL-reservoir edge, which is equal to the first moment of the charge density, $-4\,\pi\lambda_B \int_{x_1}^{x_2} x\,\rho_{ions}\,dx$, or the dimensionless potential difference across the left SDL, $\phi(x_1) - \phi(x_2)$.

Figure 4(a) shows that slightly above the limiting current ($J_{tot}/J_{lim} = 1.01$) the M_1 model already predicts a very significant extended space charge layer (the "shoulder" maximum in $\rho_{ions}/\rho_{ions,0} = (\lambda_D\, L_{sdl}/\phi_0)\, d^2\phi/dx^2$ several hundred Debye lengths from the membrane), whereas for an even higher current ($J_{tot}/J_{lim} = 1.03$), using the more realistic CIMD model, the extension of this layer is still very minor. The two intermediate models lie in between. Figure 4(b) shows how the transverse electroosmotic mobility is predicted by the M_1 model to diverge at the limiting current. This divergence is significantly reduced only by the full CIMD model including simultaneously co-ion access, water ion transport, water splitting, and membrane discharge. We note that a proper analysis of EOI would be more involved, since here we have simply focused on the transverse electroosmotic mobility as a way of illustrating the suppression of EOI due to CIMD.

In conclusion, we have theoretically demonstrated that OLC through aqueous ion-exchange membranes

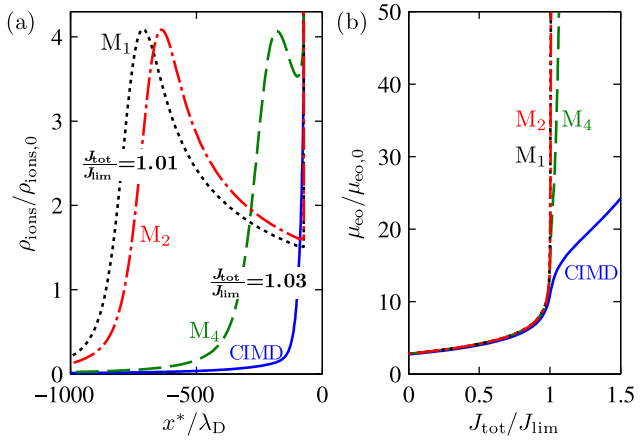

FIG. 4. [Color online] Comparison of three fixed-charge membrane models M_n having $n = 1$, 2, or 4 mobile ionic species and the CIMD model for (a) charge density ρ_{ions} versus distance x^* from the membrane scaled to the reservoir Debye length λ_D, and (b) electroosmotic mobility μ_{eo} as function of total current J_{tot}.

can result from CIMD, or loss ion selectivity due to (de-)protonation coupled to ion transport and water self-ionization. The appearance of OLC carried partially by salt co-ions and water ions reduces separation efficiency in electrodialysis, but the associated large pH gradients and membrane discharge could be exploited for current-assisted ion exchange or pH control. CIMD also suppresses the non-equilibrium space charge responsible for EOI and thus should be considered in both models and experiments on OLC with fluid flow. Although we have developed the theory for ion-exchange membranes in aqueous solutions, CIMD could occur in any nanofluidic system with an electrolyte whose ions regulate the surface charge.

[1] F. G. Helfferich, *Ion exchange* (McGraw-Hill, 1962; Dover 1995).
[2] X. Tongwen, J Membrane Sci **263**, 1 (2005).
[3] T. F. Weiss, *Cellular Biophysics* (MIT Press, 1996).
[4] R. P. O'Hare, S.-W. Cha, W. G. Colella, and F. B. Prinz, *Fuel Cell Fundamentals* (Wiley, 2009).
[5] P. Berg, K. Promislow, J. S. Pierre, J. Stumper, and B. Wetton, J Electrochem Soc **151**, A341 (2004).
[6] Y.-C. Wang, A. L. Stevens, and J. Han, Anal Chem **77**, 4293 (2005).
[7] S. J. Kim, Y.-C. Wang, J. H. Lee, H. Jang, and J. Han, Phys Rev Lett **99**, 044501 (2007).
[8] R. Schoch, J. Han, and P. Renaud, Rev Mod Phys **80**, 839 (2008).
[9] W. Sparreboom, A. van den Berg, and J. C. T. Eijkel, Nat Nanotechnol **4**, 713 (2009).
[10] S. J. Kim, S. H. Ko, K. H. Kang, and J. Han, Nat Nanotechnol **5**, 297 (2010).

[11] V. G. Levich, *Physicochemical Hydrodynamics* (Prentice-Hall, New York, 1962).
[12] V. V. Nikonenko, N. D. Pismenskaya, E. I. Belova, P. Sistat, P. Huguet, G. Pourcelly, and C. Larchet, Adv Colloid Interface Sci **160**, 101 (2010).
[13] L.-J. Cheng and H.-C. Chang, Biomicrofluidics **5**, 046502 (2011).
[14] E. V. Dydek, B. Zaltzman, I. Rubinstein, D. S. Deng, A. Mani, and M. Z. Bazant, Phys Rev Lett **107**, 118301 (2011).
[15] S. M. Rubinstein, G. Manukyan, A. Staicu, I. Rubinstein, B. Zaltzman, R. G. H. Lammertink, F. Mugele, and M. Wessling, Phys Rev Lett **101**, 236101 (2008).
[16] G. Yossifon and H.-C. Chang, Phys Rev Lett **101**, 254501 (2008).
[17] I. Rubinstein and B. Zaltzman, Phys Rev E **62**, 2238 (2000).
[18] I. Rubinstein, B. Zaltzman, J. Pretz, and C. Linder, Russ J Electrochem **38**, 853 (2002).
[19] B. Zaltzman and I. Rubinstein, J Fluid Mech **579**, 173 (2007).
[20] R. Simons, Nature **280**, 824 (1979).
[21] R. Simons, Electrochimica Acta **29**, 151 (1984).
[22] C.-O. Danielsson, A. Dahlkild, A. Velin, and M. Behm, Electrochimica Acta **54**, 2983 (2009).
[23] Y. Tanaka, J Membrane Sci **350**, 347 (2010).
[24] P. Ramirez, A. Alcaraz, and S. Mafe, J Electroanal Chem **436**, 119 (1997).
[25] P. Ramirez, S. Mafe, A. Tanioka, and K. Saito, Polymer **38**, 4931 (1997).
[26] W. B. S. de Lint, P. M. Biesheuvel, and H. Verweij, J Colloid Interface Sci **251**, 131 (2002).
[27] R. Takagi and M. Nakagaki, Sep Purif Technol **32**, 65 (2003).
[28] S. Bandini, J Membrane Sci **264**, 75 (2005).
[29] K. L. Jensen, J. T. Kristensen, A. M. Crumrine, M. B. Andersen, H. Bruus, and S. Pennathur, Phys Rev E **83**, 056307 (2011).
[30] A. Yaroshchuk, J Membrane Sci **396**, 43 (2012).
[31] K. Köhler, P. M. Biesheuvel, R. Weinkamer, H. Möhwald, and G. B. Sukhorukov, Phys Rev Lett **97**, 188301 (2006).
[32] P. M. Biesheuvel, T. Mauser, G. B. Sukhorukov, and H. Möhwald, Macromolecules **39**, 8480 (2006).
[33] P. M. Biesheuvel, Langmuir **18**, 5566 (2002).
[34] M. Van Soestbergen, A. Mavinkurve, R. T. H. Rongen, K. M. B. Jansen, L. J. Ernst, and G. Q. Zhang, Electrochimica Acta **55**, 5459 (2010).
[35] A. Elattar, A. Elmidaoui, N. Pismenskaia, C. Gavach, and G. Pourcelly, J Membrane Sci **143**, 249 (1998).
[36] A. P. Thoma, A. Viviani-Nauer, S. Arvanitis, W. E. Morf, and W. Simon, Anal Chem **49**, 1567 (1977).
[37] L. Jialin, W. Yazhen, Y. Changying, L. Guangdou, and S. Hong, J Membrane Sci **147**, 247 (1998).
[38] J. J. Krol, M. Wessling, and H. Strathmann, J Membrane Sci **162**, 145 (1999).
[39] J.-H. Choi, H.-J. Lee, and S.-H. Moon, J Colloid Interface Sci **238**, 188 (2001).
[40] M. Z. Bazant, K. T. Chu, and B. J. Bayly, SIAM J Appl Math **65**, 1463 (2005).
[41] I. Rubinstein and L. Shtilman, J Chem Soc, Faraday Trans 2 **75**, 231 (1979).
[42] K. T. Chu and M. Z. Bazant, SIAM J Appl Math **65**, 1485 (2005).
[43] P. M. Biesheuvel, M. van Soestbergen, and M. Z. Bazant, Electrochimica Acta **54**, 4857 (2009).

Appendix F

Paper published in Phys Rev E

M. M. Gregersen, M. B. Andersen, G. Soni, C. Meinhart, and H. Bruus, Numerical analysis of finite debye-length effects in induced-charge electro-osmosis, Phys Rev E 79, 066316 (2009).

Numerical analysis of finite Debye-length effects in induced-charge electro-osmosis

Misha Marie Gregersen,[1] Mathias Bækbo Andersen,[1] Gaurav Soni,[2] Carl Meinhart,[2] and Henrik Bruus[1]
[1]*Department of Micro- and Nanotechnology, Technical University of Denmark, DTU Nanotech, Building 345 East, DK-2800 Kongens Lyngby, Denmark*
[2]*Department of Mechanical Engineering, University of California, Engineering II Building, Santa Barbara, California 93106, USA*
(Received 23 February 2009; published 26 June 2009)

For a microchamber filled with a binary electrolyte and containing a flat unbiased center electrode at one wall, we employ three numerical models to study the strength of the resulting induced-charge electro-osmotic (ICEO) flow rolls: (i) a full nonlinear continuum model resolving the double layer, (ii) a linear slip-velocity model not resolving the double layer and without tangential charge transport inside this layer, and (iii) a nonlinear slip-velocity model extending the linear model by including the tangential charge transport inside the double layer. We show that, compared to the full model, the slip-velocity models significantly overestimate the ICEO flow. This provides a partial explanation of the quantitative discrepancy between observed and calculated ICEO velocities reported in the literature. The discrepancy increases significantly for increasing Debye length relative to the electrode size, i.e., for nanofluidic systems. However, even for electrode dimensions in the micrometer range, the discrepancies in velocity due to the finite Debye length can be more than 10% for an electrode of zero height and more than 100% for electrode heights comparable to the Debye length.

DOI: 10.1103/PhysRevE.79.066316 PACS number(s): 47.57.jd, 47.61.−k, 47.11.Fg

I. INTRODUCTION

Within the last decade the interest in electrokinetic phenomena in general and induced-charge electro-osmosis (ICEO) in particular has increased significantly as the field of lab-on-a-chip technology has developed. Previously, the research in ICEO has primarily been conducted in the context of colloids, where experimental and theoretical studies have been carried out on the electric double layer and induced dipole moments around spheres in electric fields, as reviewed by Dukhin [1] and Murtsovkin [2]. In microfluidic systems, electrokinetically driven fluid motion has been used for fluid manipulation, e.g., mixing and pumping. From a microfabrication perspective planar electrodes are easy to fabricate and relatively easy to integrate in existing systems. For this reason much research has been focused on the motion of fluids above planar electrodes. ac electrokinetic micropumps based on ac electro-osmosis have been thoroughly investigated as a possible pumping and mixing device. Experimental observations and theoretical models were initially reported around year 2000 [3–6], and further investigations and theoretical extensions of the models have been published by numerous groups since [7–12]. Recently, ICEO flows around inert polarizable objects have been observed and investigated theoretically [13–18]. For a thorough historical review of research leading up to these results, we refer the reader to Squires *et al.* [13] and references therein.

In spite of the growing interest in the literature, not all aspects of the flow-generating mechanisms have been explained so far. While qualitative agreement is seen between theory and experiment, quantitative agreement is often lacking as reported by Gregersen *et al.* [11], Harnett *et al.* [16], and Soni *et al.* [19]. Specifically, the latter experiments show two-order-of-magnitude lower velocity scales when compared to velocities predicted by linear slip-velocity (LS) simulations (see Sec. IV A). A nonlinear slip-velocity (NLS) model (see Sec. IV B) captures more (but not all) of the relevant physics and agrees to within approximately one order of magnitude with the experimental data. In the present work we seek to illuminate some of the possible reasons underlying these observed discrepancies.

ICEO flow is generated when an external electric field polarizes an object in an electrolytic solution. Counter ions in the electrolyte screen out the induced dipole, having a potential difference ζ relative to the bulk electrolyte, by forming an electric double layer of width λ_D at the surface of the object. The ions in the diffuse part of the double layer then electromigrate in the external electric field and drag the entire liquid by viscous forces. At the outer surface of the double layer a resulting effective slip velocity $\boldsymbol{v}_{\mathrm{slip}}$ is thus established. Many numerical models of ICEO problems exploit this characteristic by applying the so-called Helmholtz-Smoluchowski slip condition on the velocity field at the electrode surface [20–24]. Generally, the slip-condition based model remains valid as long as

$$\frac{\lambda_D}{a_c}\exp\left(\frac{Ze\zeta}{2k_BT}\right) \ll 1, \tag{1}$$

where $k_BT/(Ze)$ is the thermal voltage and a_c denotes the radius of curvature of the surface [13]. The slip-velocity condition may be applied when the double layer is infinitely thin compared to the geometrical length scale of the object; however, for planar electrodes, condition (1) is not well defined. In the present work we investigate to what extent the slip condition remains valid.

Squires *et al.* [13] have presented an analytical solution to the ICEO flow problem around a metallic cylinder with radius a_c using a linear slip-velocity model in the two-dimensional (2D) plane perpendicular to the cylinder axis. In this model with its infinitely thin double layer, the surrounding electrolyte is charge neutral, and hence the strength of the ICEO flow can be defined solely in terms of the hydrodynamic stress tensor $\boldsymbol{\sigma}$, as the mechanical power

$P_{\mathrm{mech}}=\oint_{|\boldsymbol{r}|=a_c}\hat{\boldsymbol{n}}\cdot\boldsymbol{\sigma}\cdot\boldsymbol{v}_{\mathrm{slip}}da$ exerted on the electrolyte by the tangential slip velocity $\boldsymbol{v}_{\mathrm{slip}}=u_{\mathrm{eo}}\hat{\boldsymbol{t}}$, where $\hat{\boldsymbol{n}}$ and $\hat{\boldsymbol{t}}$ is the normal and tangential vectors to the cylinder surface, respectively. In steady flow, this power is equal to the total kinetic-energy dissipation $P_{\mathrm{kin}}=\frac{1}{2}\eta\int_{a_c<|\boldsymbol{r}|}(\partial_i v_j+\partial_j v_i)^2 d\boldsymbol{r}$ of the resulting quadrupolar velocity field in the electrolyte.

When comparing the results for the strength of the ICEO flow around the cylinder obtained by the analytical model with those obtained by a numerical solution of the full equation system, where the double layer is fully resolved, we have noted significant discrepancies. These discrepancies, which are described in the following, have become the primary motivation for the study presented in this paper.

First, in the full double-layer resolving simulation we determined the value $P^*_{\mathrm{mech}}(R_0)=\oint_{|\boldsymbol{r}|=R_0}\hat{\boldsymbol{n}}\cdot\boldsymbol{\sigma}\cdot\boldsymbol{v}da$ of the mechanical input power, where R_0 is the radius of a cylinder surface placed coaxially with the metallic cylinder. Then, as expected due to the electrical forces acting on the net charge in the double layer, we found that $P^*_{\mathrm{mech}}(R_0)$ varied substantially as long as the integration cylinder surface was inside the double layer. For $R_0\approx a_c+6\lambda_{\mathrm{D}}$ the mechanical input power stabilized at a certain value. However, this value is significantly lower than the analytical value while the discrepancy decreased for decreasing values of λ_{D}. Remarkably, even for a quite thin Debye layer, $\lambda_{\mathrm{D}}=0.01a_c$, the value of the full numerical simulation was about 40% lower than the analytical value. Clearly, the analytical model overestimates the ICEO effect, and the double-layer width must be extremely thin before the simple analytical model agrees well with the full model.

A partial explanation of the quantitative failure of the analytical slip-velocity model is the radial dependence of the tangential field $E_{\parallel}$ combined with the spatial extent of the charge density ρ_{el} of the double layer. In the Debye-Hückel approximation $E_{\parallel}$ and ρ_{el} around the metallic cylinder of radius a_c become

$$E_{\parallel}(r,\theta)=E_0\left[1+\frac{a_c^2}{r^2}-2\frac{a_c}{r}\frac{K_1\left(\frac{r}{\lambda_{\mathrm{D}}}\right)}{K_1\left(\frac{a_c}{\lambda_{\mathrm{D}}}\right)}\right]\sin\theta, \tag{2a}$$

$$\rho_{\mathrm{el}}(r,\theta)=2\frac{\epsilon E_0 a_c}{\lambda_{\mathrm{D}}^2}\frac{K_1\left(\frac{r}{\lambda_{\mathrm{D}}}\right)}{K_1\left(\frac{a_c}{\lambda_{\mathrm{D}}}\right)}\cos\theta, \tag{2b}$$

where K_1 is the decaying modified Bessel function of order 1. The slowly varying part of $E_{\parallel}$ is given by $E_0[1+(a_c/r)^2]\sin\theta$. For very thin double layers it is well approximated by the r-independent expression $2E_0\sin\theta$, while for wider double layers, the screening charges sample the decrease in $E_{\parallel}$ as a function of the distance from the cylinder. Also tangential hydrodynamic and osmotic-pressure gradients developing in the double layer may contribute to the lower ICEO strength when taking the finite width of the double layer into account.

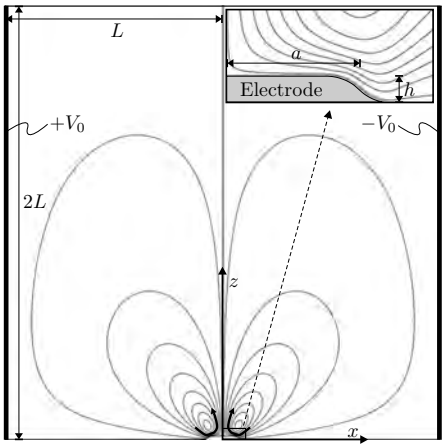

FIG. 1. A sketch of the square $2L\times 2L$ electrolytic microchamber in the xz plane. The external voltage $\pm V_0$ is applied to the two electrodes (thick black lines) at $x=\pm L$, respectively. It induces two counter-rotating flow rolls (curved black arrows) by electro-osmosis over the unbiased metallic center electrode of length $2a$ and height h placed at the bottom wall around $(x,z)=(0,0)$. The spatial extent of the flow rolls is represented by the streamline plot (thin black curves) drawn as equidistant contours of the flow rate. The inset is a zoom in on the right half, $0<x<a$, of the unbiased center electrode and the nearby streamlines.

In this work we analyze quantitatively the impact of a finite Debye length on the kinetic energy of the flow rolls generated by ICEO for three different models: (i) the full nonlinear (FN) electrokinetic model with a fully resolved double layer, (ii) the LS model, where electrostatics and hydrodynamics are completely decoupled, and (iii) a NLS model including the double layer charging through Ohmic currents from the bulk electrolyte and the surface conduction in the Debye layer. The latter two models are only strictly valid for infinitely thin double layers, and we emphasize that the aim of our analysis is to determine the errors introduced by these models neglecting the finite width of the double layers compared to the full nonlinear model resolving the double layer. We do not seek to provide a more accurate description of the physics in terms of extending the modeling by adding, say, the Stern layer (not present in the model) or the steric effects of finite-sized ions (not taken into account).

II. MODEL SYSTEM

To keep our analysis simple, we consider a single unbiased metallic electrode in a uniform external electric field. The electrode of width $2a$ and height h is placed at the bottom center, $-a<x<a$ and $z=0$, of a square $2L\times 2L$ domain in the xz plane filled with an electrolyte, see Fig. 1. The system is unbounded and translational invariant in the perpendicular y direction. The uniform electric field, parallel to the surface of the center electrode, is provided by biasing the driving electrodes placed at the edges $x=\pm L$ with the dc voltages $\pm V_0$, respectively. This antisymmetry in the bias voltage ensures that the constant potential of the center electrode is zero. A double layer, or a Debye screening layer, is induced above the center electrode, and an ICEO flow is

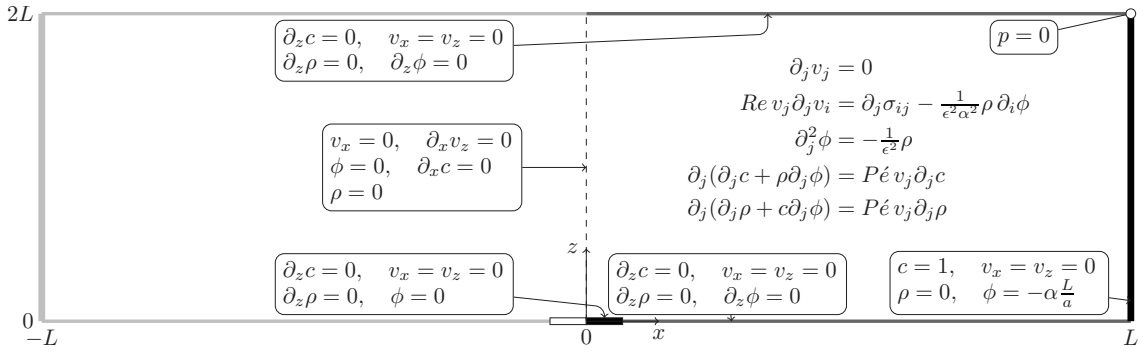

FIG. 2. The governing equations (without box) and boundary conditions (with boxes, arrows point to specific boundaries) in dimensionless form (the tilde is omitted for clarity) for the entire quadratic $2L \times 2L$ domain (not shown in correct aspect ratio) bisected into two symmetric halves. Only the right half ($x > 0$) of the domain is included in the simulations. The boundaries are the surface of the unbiased center electrode (black rectangle), the solid insulating walls (dark gray lines), the external electrode (black line), and the symmetry line (dashed black line).

generated consisting of two counter-rotating flow rolls. Electric insulating walls at $z=0$ (for $|x|>a$) and at $z=2L$ confine the domain in the z direction. The symmetry of the system around $x=0$ is exploited in the numerical calculations.

III. FN MODEL

We follow the usual continuum approach to the electrokinetic modeling of the electrolytic microchamber and treat only steady-state problems. For simplicity we consider a symmetric binary electrolyte, where the positive and negative ions with concentrations c_+ and c_-, respectively, have the same diffusivity D and charge number Z. Using the ideal-gas model for the ions, an ion is affected by the sum of an electrical and an osmotic force given by $\boldsymbol{F}_\pm = \mp Ze \boldsymbol{\nabla} \phi - (k_B T / c_\pm) \boldsymbol{\nabla} c_\pm$. Here e is the elementary charge, T is the absolute temperature, and k_B is Boltzmann's constant. Assuming a complete force balance between each ion and the surrounding electrolyte, the resulting body force density $\boldsymbol{f}_{\text{ion}} = \Sigma_{i=\pm} c_i \boldsymbol{F}_i$, appearing in the Navier-Stokes equation for the electrolyte due to the forces acting on the ions, is

$$\boldsymbol{f}_{\text{ion}} = -Ze(c_+ - c_-) \boldsymbol{\nabla} \phi - k_B T \boldsymbol{\nabla} (c_+ + c_-). \tag{3}$$

As the second term is a gradient, namely, the gradient of the osmotic pressure of the ions, it can in the Navier-Stokes equation be absorbed into the pressure gradient $\boldsymbol{\nabla} p = \boldsymbol{\nabla} p_{\text{dyn}} + \boldsymbol{\nabla} p_{\text{os}}$, which is the gradient of the sum of hydrodynamic pressure and the osmotic pressure. Only the electric force is then kept as an explicit body force.

A. Bulk equations

Neglecting bulk reactions in the electrolyte, the ionic transport is governed by the particle conservation

$$\boldsymbol{\nabla} \cdot \boldsymbol{J}_\pm = 0, \tag{4}$$

where $\boldsymbol{J}_\pm$ is the flux density of the two ionic species. Assuming the electrolytic solution to be dilute, the ion flux densities are governed by the Nernst-Planck equation

$$\boldsymbol{J}_\pm = -D \left(\boldsymbol{\nabla} c_\pm + \frac{\pm Ze}{k_B T} c_\pm \boldsymbol{\nabla} \phi \right) + c_\pm \boldsymbol{v}, \tag{5}$$

where the first term expresses ionic diffusion and the second term expresses ionic electromigration due to the electrostatic potential ϕ. The last term expresses the convective transport of ions by the fluid velocity field $\boldsymbol{v}$.

The electrostatic potential is determined by the charge density $\rho_{\text{el}} = Ze(c_+ - c_-)$ through Poisson's equation

$$\boldsymbol{\nabla} \cdot (\epsilon \boldsymbol{\nabla} \phi) = -\rho_{\text{el}}, \tag{6}$$

where ε is the fluid permittivity, which is assumed constant. The fluid velocity field $\boldsymbol{v}$ and pressure field p are governed by the continuity equation and the Navier-Stokes equation for incompressible fluids,

$$\boldsymbol{\nabla} \cdot \boldsymbol{v} = 0, \tag{7a}$$

$$\rho_m (\boldsymbol{v} \cdot \boldsymbol{\nabla}) \boldsymbol{v} = -\boldsymbol{\nabla} p + \eta \nabla^2 \boldsymbol{v} - \rho_{\text{el}} \boldsymbol{\nabla} \phi, \tag{7b}$$

where ρ_m and η are the fluid mass density and viscosity, respectively, both assumed constant.

B. Dimensionless form

To simplify the numerical implementation, the governing equations are rewritten in dimensionless form, as summarized in Fig. 2, using the characteristic parameters of the system: the geometric half length a of the electrode, the ionic concentration c_0 of the bulk electrolyte, and the thermal voltage $\phi_0 = k_B T / (Ze)$. The characteristic zeta potential ζ of the center electrode, i.e., its induced voltage, is given as the voltage drop along half of the electrode, $\zeta = (a/L) V_0$, and we introduce the dimensionless zeta potential α as $\zeta \equiv \alpha \phi_0$, or $\alpha = (a V_0)/(L \phi_0)$. The characteristic velocity u_0 is chosen as the Helmholtz-Smoluchowski slip velocity induced by the local electric field $E = \zeta / a$, and finally the pressure scale is set by the characteristic microfluidic pressure scale $p_0 = \eta u_0 / a$. In summary,

$$\phi_0 = \frac{k_B T}{Ze}, \quad u_0 = \frac{\varepsilon \zeta}{\eta} \frac{\zeta}{a} = \frac{\varepsilon \phi_0^2}{\eta a} \alpha^2, \quad p_0 = \frac{\eta u_0}{a}. \tag{8}$$

The new dimensionless variables (denoted by a tilde) thus become

$$\tilde{\boldsymbol{r}} = \frac{\boldsymbol{r}}{a}, \quad \tilde{c}_i = \frac{c_i}{c_0}, \quad \tilde{\phi} = \frac{\phi}{\phi_0}, \quad \tilde{\boldsymbol{v}} = \frac{\boldsymbol{v}}{u_0}, \quad \tilde{p} = \frac{p}{p_0}. \tag{9}$$

To exploit the symmetry of the system and the binary electrolyte, the governing equations are reformulated in terms of the average ion concentration $c \equiv (c_+ + c_-)/2$ and half the charge density $\rho \equiv (c_+ - c_-)/2$. Correspondingly, the average ion flux density $\boldsymbol{J}_c = (\boldsymbol{J}_+ + \boldsymbol{J}_-)/2$ and half the current density $\boldsymbol{J}_\rho = (\boldsymbol{J}_+ - \boldsymbol{J}_-)/2$ are introduced. Thus, the resulting full system of coupled nonlinear equations takes the following form for the ionic fields

$$\tilde{\boldsymbol{\nabla}} \cdot \tilde{\boldsymbol{J}}_c = \tilde{\boldsymbol{\nabla}} \cdot \tilde{\boldsymbol{J}}_\rho = 0, \tag{10a}$$

$$\tilde{\boldsymbol{J}}_c = -\tilde{\rho} \tilde{\boldsymbol{\nabla}} \tilde{\phi} - \tilde{\boldsymbol{\nabla}} \tilde{c} + \mathrm{Pe}\, \tilde{c} \tilde{\boldsymbol{v}}, \tag{10b}$$

$$\tilde{\boldsymbol{J}}_\rho = -\tilde{c} \tilde{\boldsymbol{\nabla}} \tilde{\phi} - \tilde{\boldsymbol{\nabla}} \tilde{\rho} + \mathrm{Pe}\, \tilde{\rho} \tilde{\boldsymbol{v}}, \tag{10c}$$

$$\mathrm{Pe} = \frac{u_0 a}{D}, \tag{10d}$$

while the electric potential obeys

$$\tilde{\boldsymbol{\nabla}}^2 \tilde{\phi} = -\frac{1}{\epsilon^2} \tilde{\rho}, \tag{11}$$

and finally the fluid fields satisfy

$$\tilde{\boldsymbol{\nabla}} \cdot \tilde{\boldsymbol{v}} = 0, \tag{12a}$$

$$\mathrm{Re}(\tilde{\boldsymbol{v}} \cdot \tilde{\boldsymbol{\nabla}}) \tilde{\boldsymbol{v}} = -\tilde{\boldsymbol{\nabla}} \tilde{p} + \tilde{\boldsymbol{\nabla}}^2 \tilde{\boldsymbol{v}} - \frac{\tilde{\rho}}{\epsilon^2 \alpha^2} \tilde{\boldsymbol{\nabla}} \tilde{\phi}, \tag{12b}$$

$$\mathrm{Re} = \frac{\rho u_0 a}{\eta}. \tag{12c}$$

Here the small dimensionless parameter $\epsilon = \lambda_D / a$ has been introduced, where λ_D is the Debye length,

$$\epsilon = \frac{\lambda_D}{a} = \frac{1}{a} \sqrt{\frac{\varepsilon k_B T}{2(Ze)^2 c_0}}. \tag{13}$$

We note that the dimensionless form of the osmotic force, the second term in Eq. (3), is $\tilde{\boldsymbol{f}}_{\mathrm{ion}}^{\mathrm{os}} = -(1/\epsilon^2 \alpha^2) \boldsymbol{\nabla} \tilde{c}$.

C. Boundary conditions

We exploit the symmetry around $x=0$ and consider only the right half $(0 < x < L)$ of the domain, see Fig. 2. As boundary conditions on the driving electrode, we take both ion concentrations to be constant and equal to the bulk charge neutral concentration. Correspondingly, the charge density is set to zero. Consequently, we ignore all dynamics taking place on the driving electrode and simply treat it as an equipotential surface with the value V_0. We set a no-slip condition for the fluid velocity, and thus at $x=L$ we have

$$\tilde{c} = 1, \quad \tilde{\rho} = 0, \quad \tilde{\phi} = \frac{V_0}{\phi_0} = \alpha \frac{L}{a}, \quad \tilde{\boldsymbol{v}} = \boldsymbol{0}. \tag{14}$$

On the symmetry axis $(x=0)$ the potential and the charge density must be zero due to the antisymmetry of the applied potential. Moreover, there is neither a fluid flux nor a net ion flux in the normal direction and the shear stresses vanish. So at $x=0$ we have

$$\tilde{\phi} = 0, \quad \hat{\boldsymbol{n}} \cdot \tilde{\boldsymbol{J}}_c = 0, \quad \tilde{\rho} = 0, \tag{15a}$$

$$\hat{\boldsymbol{t}} \cdot \tilde{\boldsymbol{\sigma}} \cdot \hat{\boldsymbol{n}} = 0, \quad \hat{\boldsymbol{n}} \cdot \tilde{\boldsymbol{v}} = 0, \tag{15b}$$

where the stress tensor is $(\boldsymbol{\sigma})_{ik} = -p \delta_{ik} + \eta(\partial_i u_k + \partial_k u_i)$, and $\hat{\boldsymbol{n}}$ and $\hat{\boldsymbol{t}}$ are the normal and tangential unit vectors, respectively, which in two dimensions, contrary to three dimensions, are uniquely defined. The constant potential on the unbiased metallic electrode is zero due to symmetry, and on the electrode surface we apply a no-slip condition on the fluid velocity and no-current condition in the normal direction. So on the electrode surface we have

$$\hat{\boldsymbol{n}} \cdot \tilde{\boldsymbol{J}}_c = 0, \quad \hat{\boldsymbol{n}} \cdot \tilde{\boldsymbol{J}}_\rho = 0, \quad \tilde{\phi} = 0, \quad \tilde{\boldsymbol{v}} = \boldsymbol{0}. \tag{16}$$

On the solid insulating walls there are no fluxes in the normal direction, the normal component of the electric field vanishes, and there are no slip on the fluid velocity,

$$\hat{\boldsymbol{n}} \cdot \tilde{\boldsymbol{J}}_c = 0, \quad \hat{\boldsymbol{n}} \cdot \tilde{\boldsymbol{J}}_\rho = 0, \quad \hat{\boldsymbol{n}} \cdot \boldsymbol{\nabla} \tilde{\phi} = 0, \quad \tilde{\boldsymbol{v}} = \boldsymbol{0}. \tag{17}$$

A complete overview of the governing equations and boundary conditions is given in Fig. 2.

D. Strongly nonlinear regime

At high values of the induced ζ potential, the concentrations of counter- and co-ions acquire very large and very small values, respectively, near the center electrode. Numerically this is problematic. The concentration ratio becomes extremely large and the vanishingly small concentration of co-ions is comparable to the round-off error and may even become negative. However, this numerical problem can be circumvented by working with the logarithms (marked by a breve accent) of the concentration fields, $\breve{c}_\pm = \log(c_\pm / c_0)$. By inserting

$$c_\pm = c_0 \exp(\breve{c}_\pm) \tag{18}$$

in governing equations (5), (6), and (7b), a new equivalent set of governing equations is derived. The symmetry is exploited by defining the symmetric $\breve{c} = \breve{c}_+ + \breve{c}_-$ and antisymmetric $\breve{\rho} = \breve{c}_+ - \breve{c}_-$ combinations of the logarithmic fields, and the corresponding formulation of the governing equations is

$$\tilde{\nabla}^2 \breve{c} = \mathrm{Pe}\, \tilde{\boldsymbol{v}} \cdot \tilde{\boldsymbol{\nabla}} \breve{c} - \frac{(\tilde{\boldsymbol{\nabla}} \breve{c})^2 + (\tilde{\boldsymbol{\nabla}} \breve{\rho})^2}{2} - \tilde{\boldsymbol{\nabla}} \tilde{\phi} \cdot \tilde{\boldsymbol{\nabla}} \breve{\rho}, \tag{19a}$$

$$\tilde{\nabla}^2 (\breve{\rho} + 2\tilde{\phi}) = \mathrm{Pe}\, \tilde{\boldsymbol{v}} \cdot \tilde{\boldsymbol{\nabla}} \breve{\rho} - \tilde{\boldsymbol{\nabla}} \breve{c} \cdot \tilde{\boldsymbol{\nabla}} \breve{\rho} - \tilde{\boldsymbol{\nabla}} \tilde{\phi} \cdot \tilde{\boldsymbol{\nabla}} \breve{\rho}, \tag{19b}$$

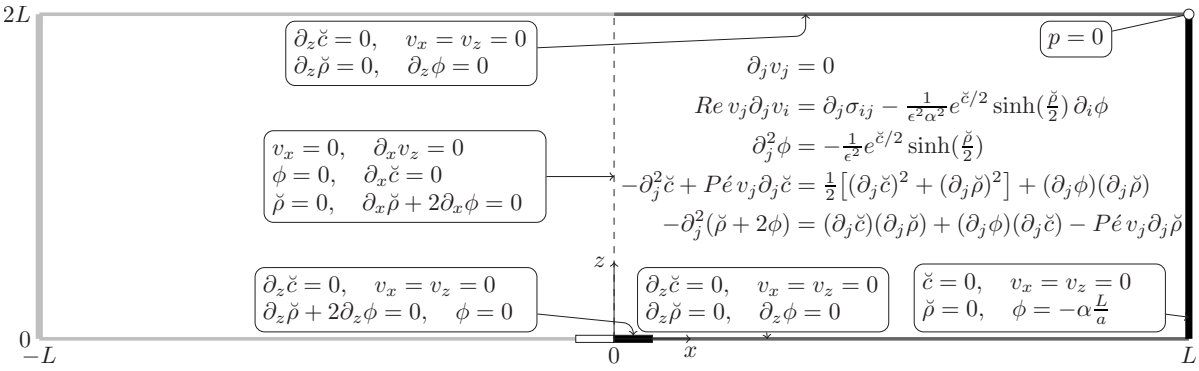

FIG. 3. The governing equations (without box) and boundary conditions (with boxes) in dimensionless form (the tilde is omitted) using the logarithmic concentrations (denoted by a breve) of Eq. (18). Otherwise the figure is identical to Fig. 2.

$$\tilde{\nabla}^2\tilde{\phi}=-\frac{1}{\epsilon^2}e^{\check{c}/2}\sinh\left(\frac{\check{\rho}}{2}\right), \tag{19c}$$

$$\mathrm{Re}(\tilde{\boldsymbol{v}}\cdot\tilde{\boldsymbol{\nabla}})\tilde{\boldsymbol{v}}=-\tilde{\boldsymbol{\nabla}}\tilde{p}+\tilde{\nabla}^2\tilde{\boldsymbol{v}}-\frac{1}{\epsilon^2\alpha^2}e^{\check{c}/2}\sinh\left(\frac{\check{\rho}}{2}\right)\tilde{\boldsymbol{\nabla}}\tilde{\phi}, \tag{19d}$$

while the continuity equation remains the same as in Eq. (12a). The governing equations and boundary conditions for the logarithmic fields (breve notation) are summarized in Fig. 3. This transformation serves to help linearize solutions of the dependent variables, $\check{c}$ and $\check{\rho}$, at the expense of introducing more nonlinearity into the governing equations.

IV. SLIP-VELOCITY MODELS

The numerical calculation of ICEO flows in microfluidic systems is generally connected with computational limitations due to the large difference of the inherent length scales. Typically, the Debye length is much smaller than the geometric length scale, $\lambda_D \ll a$, making it difficult to resolve both the dynamics of the Debye layer and the entire microscale geometry with the available computer capacity. Therefore, it is customary to use slip-velocity models, where it is assumed that the electrodes are screened completely by the Debye layer leaving the bulk electrolyte charge neutral. The dynamics of the Debye layer is modeled separately and applied to the bulk fluid velocity through an effective so-called Helmholtz-Smoluchowski slip-velocity condition at the electrode surface,

$$\boldsymbol{v}_{\mathrm{HS}}=-\frac{\varepsilon}{\eta}\zeta\boldsymbol{E}_{\parallel}, \tag{20}$$

where ζ is the zeta potential at the electrode surface, and $\boldsymbol{E}_{\parallel}$ is the electric field parallel to the surface. Regardless of the modeled dynamics in the double layer the slip-velocity models are only strictly valid in the limit of infinitely thin double layers $\lambda_D \ll a$.

A. LS model

The double-layer screening of the electrodes leaves the bulk electrolyte charge neutral, and hence the governing equations only include the potential ϕ, the pressure field p, and the flow velocity field $\boldsymbol{v}$. In dimensionless form they become

$$\tilde{\boldsymbol{\nabla}}^2\tilde{\phi}=0, \tag{21a}$$

$$\mathrm{Re}(\tilde{\boldsymbol{v}}\cdot\tilde{\boldsymbol{\nabla}})\tilde{\boldsymbol{v}}=-\tilde{\boldsymbol{\nabla}}\tilde{p}+\tilde{\boldsymbol{\nabla}}^2\tilde{\boldsymbol{v}}, \tag{21b}$$

$$\tilde{\boldsymbol{\nabla}}\cdot\tilde{\boldsymbol{v}}=0. \tag{21c}$$

The electrostatic problem is solved independently of the hydrodynamics, and the potential is used to calculate the effective slip velocity applied to the fluid at the unbiased electrode surface. The boundary conditions of the potential and fluid velocity are equivalent to the conditions applied to the full nonlinear system, except at the surface of the unbiased electrode. Here, the normal component of the electric field vanishes, and the effective slip velocity of the fluid is calculated from the electrostatic potential using $\zeta=-\phi$ and $\boldsymbol{E}_{\parallel}=-[(\hat{\boldsymbol{t}}\cdot\tilde{\boldsymbol{\nabla}})\tilde{\phi}]\hat{\boldsymbol{t}}$,

$$\hat{\boldsymbol{n}}\cdot\boldsymbol{\nabla}\tilde{\phi}=0, \tag{22a}$$

$$\tilde{\boldsymbol{v}}_{\mathrm{HS}}=\frac{1}{\alpha^2}\tilde{\phi}[(\hat{\boldsymbol{t}}\cdot\tilde{\boldsymbol{\nabla}})\tilde{\phi}]\hat{\boldsymbol{t}}. \tag{22b}$$

This represents the simplest possible so-called linear slip-velocity model; a model that is widely applied as a starting point for numerical simulations of actual microfluidic systems [20,21]. In this simple model all the dynamics of the double layer has been neglected, an assumption known to be problematic when the voltage across the electrode exceeds the thermal voltage.

B. NLS model

The linear slip-velocity model can be improved by taking into account the nonlinear charge dynamics of the double layer. This is done in the so-called nonlinear slip-velocity model, where, although still treated as being infinitely thin, the double layer has a nontrivial charge dynamics with currents from the bulk in the normal direction and currents flowing tangential to the electrode inside the double layer.

For simplicity we assume in the present nonlinear model that the neutral salt concentration c_0 is uniform. This assumption breaks down at high zeta potentials, where surface transport of ionic species can set up gradients in the salt concentrations leading to chemiosmotic flow. In future more complete studies of double-layer charge dynamics, these effects should be included.

The charging of the double layer by the Ohmic bulk current is assumed to happen in quasiequilibrium characterized by a nonlinear differential capacitance C_{dl} given by the Gouy-Chapmann model, $C_{\mathrm{dl}}=\varepsilon\cosh[ze\zeta/(2k_{\mathrm{B}}T)]/\lambda_{\mathrm{D}}$, which in the low-voltage linear Debye-Hückel regime reduces to $C_{\mathrm{dl}}=\varepsilon/\lambda_{\mathrm{D}}$. Ignoring the Stern layer, the zeta potential is directly proportional to the bulk potential right outside the double layer, $\zeta=-\phi$.

The current along the electrode inside the Debye layer is described by a 2D surface conductance σ_s, which for a binary symmetric electrolyte is given by [1]

$$\sigma_s = 4\lambda_{\mathrm{D}}\sigma(1+m)\sinh^2\left(\frac{Ze\zeta}{4k_{\mathrm{B}}T}\right), \tag{23}$$

where σ is the bulk three-dimensional conductivity and

$$m = 2\frac{\varepsilon}{\eta D}\left(\frac{k_{\mathrm{B}}T}{Ze}\right)^2 \tag{24}$$

is a dimensionless parameter indicating the relative contribution of electro-osmosis to surface conduction. In steady state the conservation of charge then yields [25]

$$0 = \hat{\boldsymbol{n}}\cdot(\sigma\nabla\phi) + \nabla_s\cdot[\sigma_s\nabla_s\phi], \tag{25}$$

where the operator $\nabla_s=\hat{\boldsymbol{t}}(\hat{\boldsymbol{t}}\cdot\nabla)$ is the gradient in the tangential direction of the surface.

Given the length scale a of the electrode, the strength of the surface conductance can by characterized by the dimensionless Dukhin number Du defined by

$$\mathrm{Du} = \frac{\sigma_s}{a\sigma} = \frac{4\lambda_{\mathrm{D}}}{a}(1+m)\sinh^2\left(\frac{Ze\zeta}{k_{\mathrm{B}}T}\right). \tag{26}$$

Conservation of charge then takes the dimensionless form

$$0 = \hat{\boldsymbol{n}}\cdot(\tilde{\nabla}\tilde{\phi}) + \tilde{\nabla}_s\cdot[\mathrm{Du}\tilde{\nabla}_s\cdot\tilde{\phi}], \tag{27}$$

and this effective boundary condition for the potential on the flat electrode constitutes a one-dimensional (1D) partial differential equation and as such needs accompanying boundary conditions. As a boundary condition the surface flux is assumed to be zero at the edges of the electrode,

$$\sigma_s(\hat{\boldsymbol{t}}\cdot\nabla)\phi|_{x=\pm a} = 0, \tag{28}$$

which is well suited for the weak formulation we employ in our numerical simulation as seen in Eq. (34).

V. NUMERICS IN COMSOL

The numerical calculations are performed using the commercial finite-element-method software COMSOL with second-order Lagrange elements for all the fields except the pressure, for which first-order elements suffice. We have applied the so-called weak formulation mainly to be able to control the coupling between the bulk equations and the boundary constraints, such as Eqs. (22b) and (25), in the implementation of the slip-velocity models in script form.

The Helmholtz-Smoluchowski slip condition poses a numerical challenge because it is a Dirichlet condition including not one but up to three variables, for which we want a one-directional coupling from the electrostatic field ϕ to the hydrodynamic fields $\boldsymbol{v}$ and p. We use the weak formulation to unambiguously enforce the boundary condition with the explicit introduction of the required hydrodynamic reaction force $\boldsymbol{f}$ on the unbiased electrode

$$\boldsymbol{f} = \boldsymbol{\sigma}\cdot\hat{\boldsymbol{n}}. \tag{29}$$

The x and z components of Navier-Stokes equation are multiplied with test functions u_x and u_z, respectively, and subsequently integrated over the whole domain Ω. Partial integration is then used to move the stress tensor contribution to the boundaries $\partial\Omega$,

$$0 = \int_{\partial\Omega} u_i\sigma_{ij}n_j ds - \int_{\Omega}[(\partial_j u_i)\sigma_{ij} + u_i B_i]da, \tag{30}$$

where $B_i=\mathrm{Re}(v_j\partial_j)v_i+\rho(\partial_i\phi)/(\epsilon^2\alpha^2)$. The boundary integral on the unbiased electrode $\partial\Omega_{\mathrm{ue}}$ is rewritten as

$$\int_{\partial\Omega_{\mathrm{ue}}} u_i\sigma_{ij}n_j ds = \int_{\partial\Omega_{\mathrm{ue}}}[u_i f_i + F_i(v_i - v_{\mathrm{HS},i})]ds, \tag{31}$$

where F_i are the test functions belonging to the components f_i of the reaction force $\boldsymbol{f}$. These test functions are used to enforce the Helmholtz-Smoluchowski slip boundary condition consistently. This formulation is used for both slip-velocity models.

In the nonlinear slip-velocity model, the Laplace equation (21a) is multiplied with the electrostatic test function Φ, and partially integrated to get a boundary term and a bulk term

$$0 = \int_{\partial\Omega}\Phi(\partial_i\phi)n_i ds - \int_{\Omega}(\partial_i\Phi)(\partial_i\phi)da. \tag{32}$$

The boundary integration term on the electrode is simplified by substitution of Eq. (25), which results in

$$\int_{\partial\Omega_{\mathrm{ue}}}\Phi(\partial_i\phi)n_i ds = -\int_{\partial\Omega_{\mathrm{ue}}}\Phi[\hat{t}_i\partial_i(\mathrm{Du}\,\hat{t}_j\partial_j\phi)]ds. \tag{33}$$

Again, the resulting boundary integral is partially integrated, which gives us explicit access to the end points of the unbiased electrode. This is necessary for applying the boundary conditions on this 1D electrode,

$$\int_{\partial\Omega_{\mathrm{ue}}}\Phi[\hat{t}_i\partial_i(\mathrm{Du}\,\hat{t}_j\partial_j\phi)]ds = [\Phi\mathrm{Du}(\hat{t}_i\partial_i\phi)]_{x=-a}^{x=+a} - \int_{\partial\Omega_{\mathrm{ue}}}(\hat{t}_i\partial_i\Phi)\mathrm{Du}(\hat{t}_j\partial_j\phi)ds, \tag{34}$$

The no-flux boundary condition can be explicitly included with this formulation. Note that in both slip-velocity models

the zeta potential is given by the potential just outside the Debye layer, $\zeta=-\phi$, and it is therefore not necessary to include it as a separate variable.

The accuracy and the mesh dependence of the simulation have been investigated as follows. The comparison between the three models quantifies relative differences of orders down to 10^{-3}, and the convergence of the numerical results is ensured in the following way. COMSOL has a build-in adaptive mesh generation technique that is able to refine a given mesh so as to minimize the error in the solution. The adaptive mesh generator increases the mesh density in the immediate region around the electrode to capture the dynamics of the ICEO in the most optimal way under the constraint of a maximum number of degrees of freedom (DOFs). For a given set of physical parameters, the problem is solved each time by increasing the number of DOFs and comparing consecutive solutions. As a convergence criterium we demand that the standard deviation of the kinetic energy relative to the mean value should be less than a given threshold value typically chosen to be around 10^{-5}. All of the simulations ended with more than 10^6 DOFs, and the ICEO flow is therefore sufficiently resolved even for the thinnest double layers in our study for which $\epsilon=10^{-4}$.

VI. RESULTS

Our comparison of the three numerical models is primarily focused on variations in the three dimensionless parameters ϵ, α, and β relating to the Debye length λ_D, the applied voltage V_0, and the height h of the electrode, respectively,

$$\epsilon=\frac{\lambda_D}{a},\quad \alpha=\frac{aV_0}{L\phi_0},\quad \beta=\frac{h}{a}. \tag{35}$$

As mentioned in Sec. I, the strength of the generated ICEO flow can be measured as the mechanical power input P_{mech} exerted on the electrolyte by the slip velocity just outside the Debye layer or equivalently by the kinetic-energy dissipation P_{kin} in the bulk of the electrolyte. However, both these methods suffer from numerical inaccuracies due to the dependence of both the position of the integration path and of the less accurately determined velocity gradients in the stress tensor $\boldsymbol{\sigma}$. To obtain a numerically more stable and accurate measure, we have chosen in the following analysis to characterize the strength of the ICEO flow by the kinetic energy E_{kin} of the induced flow field $\boldsymbol{v}$,

$$E_{kin}=\frac{1}{2}\rho_m\int_\Omega v^2 dxdz, \tag{36}$$

which depends on the velocity field and not its gradients, and which furthermore is a bulk integral of good numerical stability.

A. Zero height of the unbiased center electrode

We assume the height h of the unbiased center electrode to be zero, i.e., $\beta=0$, while varying the Debye length and the applied voltage through the parameters ϵ and α. We note that linear slip-velocity model equations (21) and (22) are independent of the dimensionless Debye length ϵ. It is therefore natural to use the kinetic energy E_{kin}^{LS} of this model as a normalization factor.

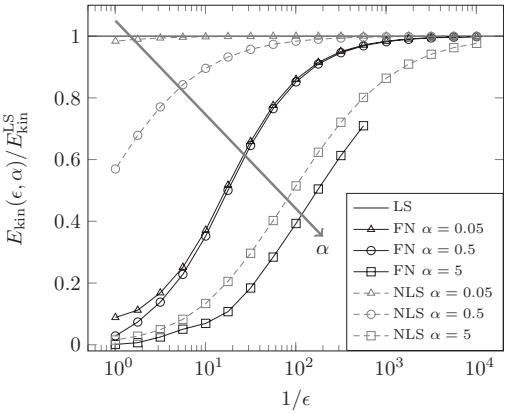

FIG. 4. The total induced kinetic energy E_{kin}^{NLS} (gray dashed) and E_{kin}^{FN} (black) for the nonlinear slip-velocity model and the full model, respectively, relative to E_{kin}^{LS} (horizontal black line) of the linear slip-velocity model as a function of dimensionless inverse Debye length $1/\epsilon$. Each are shown for three values of the dimensionless applied voltage $\alpha=0.05$, 0.5, and 5. The value of ϵ decreases from 1 to 10^{-4} going from left to right.

In the lin-log plot of Fig. 4 we show the kinetic energy E_{kin}^{NLS} and E_{kin}^{FN} normalized by E_{kin}^{LS} as a function of the inverse Debye length $1/\epsilon$ for three different values of the applied voltage, $\alpha=0.05$, 0.5, and 5, ranging from the linear to the strongly nonlinear voltage regime.

We first note that in the limit of vanishing Debye length (to the right in the graph) all models converge toward the same value for all values of the applied voltage α. For small values of α the advanced slip-velocity model E_{kin}^{NLS} is fairly close to the linear slip-velocity model E_{kin}^{LS}, but as α increases, it requires smaller and smaller values of ϵ to obtain the same results in the two models. In the linear regime $\alpha=0.05$ a deviation less than 5% is obtained already for $\epsilon<1$. In the nonlinear regime $\alpha=0.5$ the same deviation requires $\epsilon<10^{-2}$ while in the strongly nonlinear regime $\epsilon<10^{-4}$ is needed to obtain a deviation lower than 5%.

In contrast, it is noted how the more realistic full model E_{kin}^{FN} deviates strongly from E_{kin}^{LS} for most of the displayed values of ϵ and α. To obtain a relative deviation less than 5% in the linear ($\alpha=0.05$) and nonlinear ($\alpha=0.5$) regimes, a minute Debye length of $\epsilon<10^{-3}$ is required, and in the strongly nonlinear regime the 5% level is not reached at all.

The deviations are surprisingly large. The Debye length in typical electrokinetic experiments is $\lambda_D=30$ nm. For a value of $\epsilon=0.01$ this corresponds to an electrode of width 2×3 μm$=6$ μm, comparable to those used in Refs. [7,10,11]. In Fig. 4 we see that, for $\alpha=5$, corresponding to a moderate voltage drop of 0.26 V across the electrode, the linear slip-velocity model overestimates the ICEO strength by a factor $1/0.4=2.5$. The nonlinear slip model does a better job. For the same parameters it only overestimates the ICEO strength by a factor $0.5/0.4=1.2$.

For more detailed comparisons between the three models, the data of Fig. 4 are plotted in a different way in Fig. 5.

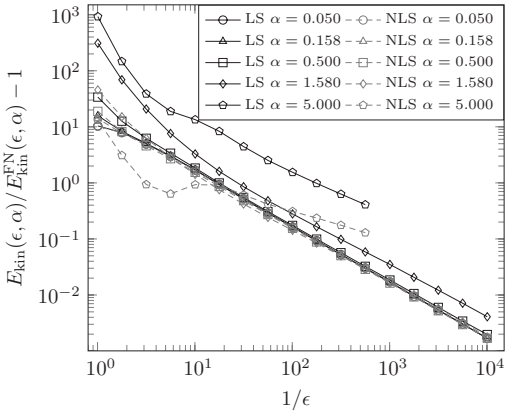

FIG. 5. The difference between the induced kinetic energies $E_{\mathrm{kin}}^{\mathrm{LS}}$ and $E_{\mathrm{kin}}^{\mathrm{NLS}}$ of the linear and nonlinear slip-velocity models, respectively, relative to the full model $E_{\mathrm{kin}}^{\mathrm{FN}}$ as a function of the inverse Debye length $1/\epsilon$ for five different applied voltages $\alpha = 0.050, 0.158, 0.500, 1.580, 5.000$.

Here the overestimates $(E_{\mathrm{kin}}^{\mathrm{LS}}/E_{\mathrm{kin}}^{\mathrm{FN}})-1$ and $(E_{\mathrm{kin}}^{\mathrm{NLS}}/E_{\mathrm{kin}}^{\mathrm{FN}})-1$ of the two slip-velocity models relative to the more correct full model are plotted in a log-log plot as a function of the inverse Debye length $1/\epsilon$ for three different values of the applied voltage. It is clearly seen how the relative deviation decreases proportional to ϵ as ϵ approaches zero.

Finally, in Fig. 6 the relative deviations $(E_{\mathrm{kin}}^{\mathrm{LS}}/E_{\mathrm{kin}}^{\mathrm{FN}})-1$ and $(E_{\mathrm{kin}}^{\mathrm{NLS}}/E_{\mathrm{kin}}^{\mathrm{FN}})-1$ are plotted versus the voltage α in a log-log plot. For any value of the applied voltage α, both slip-velocity models overestimates by more than 100% for large Debye lengths $\epsilon = 10^{-1}$ and by more than 10% for $\epsilon = 10^{-2}$. For the minute Debye length $\lambda_{\mathrm{D}} = 1.8 \times 10^{-3}$ the overestimates are about 3% in the linear and weakly nonlinear regime $\alpha < 1$; however, as we enter the strongly nonlinear regime with $\alpha = 5$ the overestimation increases to a level above 10%.

B. Finite height of the unbiased electrode

Compared to the full numerical model, the slip-velocity models are convenient to use but even for small Debye lengths, say $\lambda_{\mathrm{D}} = 0.01a$, they are prone to significant quantitative errors as shown above. Similarly, it is of relevance to study how the height of the unbiased electrode influences the strength of the ICEO flow rolls. In experiments the thinnest electrodes are made by evaporation techniques. The resulting electrode heights are of the order of 50–200 nm, which relative to the typical electrode widths $a \approx 5$ μm results in dimensionless heights $10^{-3} < \beta < 10^{-1}$.

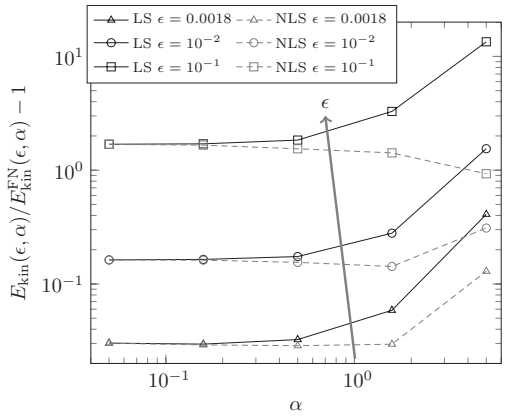

FIG. 6. The difference between the induced kinetic energies $E_{\mathrm{kin}}^{\mathrm{LS}}$ and $E_{\mathrm{kin}}^{\mathrm{NLS}}$ of the linear and nonlinear slip-velocity models, respectively, relative to the full model $E_{\mathrm{kin}}^{\mathrm{FN}}$ as a function of the voltage bias α for three different Debye layer thicknesses $\epsilon = 1.8 \times 10^{-3}, 10^{-2}, 10^{-1}$.

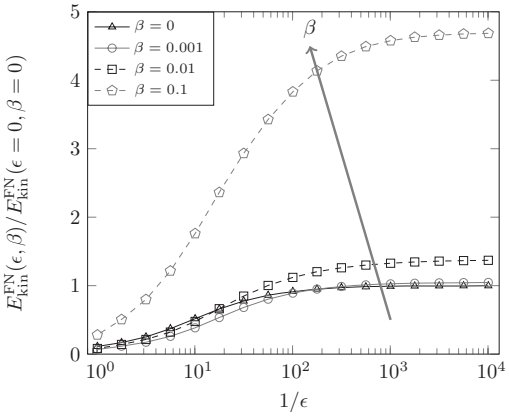

FIG. 7. The difference between the induced kinetic energies $E_{\mathrm{kin}}^{\mathrm{FN}}(\epsilon,\beta)$ of the full model at finite Debye length and electrode height relative to the full model $E_{\mathrm{kin}}^{\mathrm{FN}}(0,0)$ at zero Debye length and zero electrode height as a function of the inverse Debye length $1/\epsilon$ for four electrode heights $\beta = 0, 10^{-3}, 10^{-2}, 10^{-1}$.

In Fig. 7 is shown the results for the numerical calculation of the kinetic energy $E_{\mathrm{kin}}^{\mathrm{FN}}(\epsilon,\beta)$ using the full numerical model. The dependence on the kinetic energy of the dimensionless Debye length $\epsilon = \lambda_{\mathrm{D}}/a$ and the dimensionless electrode height $\beta = h/a$ is measured relative to the value $E_{\mathrm{kin}}^{\mathrm{FN}}(\epsilon,\beta)$ of the infinitely small Debye length for an electrode of zero height. For small values of the height no major deviations are seen. The curve for $\beta = 0$ and $\beta = 0.001$ are close. As the height is increased to $\beta = 10^{-2}$ we note that the strength of the ICEO is increased by 20–25 % as $\beta > \epsilon$. This tendency is even stronger pronounced for the higher electrode $\beta = 10^{-1}$. Here the ICEO strength is increased by approximately 400% for a large range of Debye lengths. We speculate that this strong β dependence may be due to the fact that there is an increased electric field in the region of high curvature of the raised electrode as compared to the flat electrode.

C. Thermodynamic efficiency of the ICEO system

Conventional electro-osmosis is known to have a low thermodynamic efficiency defined as the delivered mechanical pumping power relative to the total power delivered by the driving voltage. Typical efficiencies are of the order of 1% [26] while in special cases an efficiency of 5.6% has been reported [27]. In the following we provide estimates and numerical calculations of the corresponding thermodynamic efficiency of the ICEO system.

The applied voltage drop $2V_0 = 2E_0 L$ across the system in the x direction is written as the average electrical field E_0 times the length $2L$ while the electrical current is given by

$I=WH\sigma E_0$, where W and H is the width and height in the y and z directions, respectively, and $\sigma=D\varepsilon/\lambda_D^2=\varepsilon/\tau_D$ is the conductivity written in terms of the Debye time $\tau_D=\lambda_D^2/D$. The total power consumption to run the ICEO system is thus

$$P_{\text{tot}}=2V_0I=\frac{4}{\tau_D}\left(\frac{1}{2}\varepsilon E_0^2\right)LWH. \tag{37}$$

This expression can be interpreted as the total energy, $\frac{1}{2}\varepsilon E_0^2 LWH$, stored in the average electrical field of the system with volume LWH multiplied by the characteristic electrokinetic rate $4/\tau_D$.

The velocity-gradient part of the hydrodynamic stress tensor is denoted $\tilde{\boldsymbol{\sigma}}$, i.e., $(\tilde{\boldsymbol{\sigma}})_{ij}=\eta(\partial_i v_j+\partial_j v_i)$. In terms of $\tilde{\boldsymbol{\sigma}}$, the kinetic-energy dissipation P_{kin} necessary to sustain the steady-state flow rolls is given by $P_{\text{kin}}=\frac{W}{2\eta}\int_0^L dx\int_0^H dz\ \text{Tr}(\tilde{\boldsymbol{\sigma}}^2)$. In the following estimate we work in the Debye-Hückel limit for an electrode of length $2a$, where the induced zeta potential is given by $\zeta_{\text{ind}}=aE_0$ and the radius of each flow roll is approximately a. In this limit the electro-osmotic slip velocity u_{eo} and the typical size of the velocity gradient $|\partial_i v_j|$ are

$$u_{\text{eo}}=\frac{\varepsilon\zeta_{\text{ind}}}{\eta}E_0=\frac{\varepsilon a}{\eta}E_0^2, \tag{38a}$$

$$|\partial_i v_j|\approx\frac{u_{\text{eo}}}{a}=\frac{\varepsilon}{\eta}E_0^2. \tag{38b}$$

Thus, since the typical area covered by each flow roll is πa^2, we obtain the following estimate of P_{kin},

$$P_{\text{kin}}\approx 2\frac{W}{2\eta}\pi a^2 4\left[\eta\frac{u_{\text{eo}}}{a}\right]^2=8\frac{\varepsilon E_0^2}{\eta}\left(\frac{1}{2}\varepsilon E_0\right)^2\pi a^2 W. \tag{39}$$

Here the power dissipation can be interpreted as the energy of the electrical field in the volume $\pi a^2 W$ occupied by each flow roll multiplied by an ICEO rate given by the electric energy density εE_0^2 divided by the rate of viscous energy dissipation per volume given by η.

The thermodynamic efficiency can now be calculated as the ratio $P_{\text{kin}}/P_{\text{tot}}$ using Eqs. (37) and (39),

$$\frac{P_{\text{kin}}}{P_{\text{tot}}}\approx\frac{2\pi a^2}{LH}\frac{\varepsilon E_0^2}{\eta/\tau_D}\approx 2.4\times 10^{-8}. \tag{40}$$

This efficiency is the product of the ratio between the volumes of the flow rolls and the entire volume multiplied, and the ratio of the electric energy density in the viscous energy density η/τ_D. The value is found using $L=H=15a=0.15$ mm, $E_0=2.5$ kV/m, and $\lambda_D=20$ nm, which is in agreement with the conventional efficiencies for conventional electro-osmotic systems quoted above.

VII. CONCLUSION

We have shown that the ICEO velocities calculated using the simple zero-width models significantly overestimates those calculated in more realistic models taking the finite size of the Debye screening length into account. This may provide a partial explanation of the observed quantitative discrepancy between observed and calculated ICEO velocities. The discrepancy increases substantially for increasing ϵ, i.e., in nanofluidic systems.

Even larger deviations of the ICEO strength is calculated in the full numerical model when a small but finite height of the unbiased electrode is taken into account.

A partial explanation of the quantitative failure of the analytical slip-velocity model is the decrease in the tangential electric field as a function of the distance to the surface of the polarized ICEO object combined with the spatial extent of the charge density of the double layer. Also tangential hydrodynamic and osmotic-pressure gradients developing inside the double layer may contribute to the lowering ICEO strength when taking the finite width of the double layer into account. The latter may be related to the modification of the classical Helmholtz-Smoluchowski expression of the slip velocity obtained by adding a term proportional to the gradient of the salt concentration c [28].

Our work shows that for systems with a small but nonzero Debye length of 0.001–0.01 times the size of the electrode, and even when the Debye-Hückel approximation is valid, a poor quantitative agreement between experiments and model calculations must be expected when applying the linear slip-velocity model based on a zero Debye length. It is advised to employ the full numerical model of ICEO, when comparing simulations with experiments.

ACKNOWLEDGMENTS

We thank Sumita Pennathur and Martin Bazant for illuminating discussions, and we are particularly grateful to Todd Squires for a number of valuable comments and suggestions. This work is supported in part by the Institute for Collaborative Biotechnologies through Contract No. W911NF-09-D-0001 from the U.S. Army Research Office.

[1] S. S. Dukhin, Adv. Colloid Interface Sci. **44**, 1 (1993).
[2] V. A. Murtsovkin, Colloid J. **58**, 341 (1996).
[3] A. Gonzalez, A. Ramos, N. G. Green, A. Castellanos, and H. Morgan, Phys. Rev. E **61**, 4019 (2000).
[4] N. G. Green, A. Ramos, A. Gonzalez, H. Morgan, and A. Castellanos, Phys. Rev. E **66**, 026305 (2002).
[5] A. Ajdari, Phys. Rev. E **61**, R45 (2000).
[6] A. B. D. Brown, C. G. Smith, and A. R. Rennie, Phys. Rev. E **63**, 016305 (2000).
[7] V. Studer, A. Pépin, Y. Chen, and A. Ajdari, Analyst (Cambridge, U.K.) **129**, 944 (2004).
[8] D. Lastochkin, R. Zhou, P. Whang, Y. Ben, and H.-C. Chang, J. Appl. Phys. **96**, 1730 (2004).
[9] S. Debesset, C. J. Hayden, C. Dalton, J. C. T. Eijkel, and A. Manz, Lab Chip **4**, 396 (2004).
[10] B. P. Cahill, L. J. Heyderman, J. Gobrecht, and A. Stemmer,

Phys. Rev. E **70**, 036305 (2004).
[11] M. M. Gregersen, L. H. Olesen, A. Brask, M. F. Hansen, and H. Bruus, Phys. Rev. E **76**, 056305 (2007).
[12] L. H. Olesen, H. Bruus, and A. Ajdari, Phys. Rev. E **73**, 056313 (2006).
[13] T. M. Squires and M. Z. Bazant, J. Fluid Mech. **509**, 217 (2004).
[14] J. A. Levitan, S. Devasenathipathy, V. Studer, Y. Ben, T. Thorsen, T. M. Squires, and M. Z. Bazant, Colloids Surf., A **267**, 122 (2005).
[15] T. M. Squires and M. Z. Bazant, J. Fluid Mech. **560**, 65 (2006).
[16] C. K. Harnett, J. Templeton, K. Dunphy-Guzman, Y. M. Senousy, and M. P. Kanouff, Lab Chip **8**, 565 (2008).
[17] A. S. Khair and T. M. Squires, J. Fluid Mech. **615**, 323 (2008).
[18] M. Gregersen, F. Okkels, M. Bazant, and H. Bruus, New J. Phys., Focus Issue (to be published), e-print arXiv:0901.1788.
[19] G. Soni, T. M. Squires, and C. D. Meinhart, Proceedings of 2007 ASME International Mechanical Engineering Congress and Exposition, 2007 (unpublished).
[20] R. F. Probstein, *Physicochemical Hydrodynamics* (John Wiley & Sons, New York, 1994).
[21] H. Bruus, *Theoretical Microfluidics* (Oxford University Press, Oxford, 2008).
[22] S. S. Dukhin, R. Zimmermann, and C. Werner, Colloids Surf., A **195**, 103 (2001).
[23] J. Lyklema, J. Phys.: Condens. Matter **13**, 5027 (2001).
[24] K. T. Chu and M. Z. Bazant, J. Colloid Interface Sci. **315**, 319 (2007).
[25] G. Soni, M. B. Andersen, H. Bruus, T. Squires, and C. Meinhart, Phys. Rev. E (to be published).
[26] D. J. Laser and J. G. Santiago, J. Micromech. Microeng. **14**, R35 (2004).
[27] D. S. Reichmuth, G. S. Chirica, and B. J. Kirby, Sens. Actuators B **92**, 37 (2003).
[28] A. S. Khair and T. M. Squires, Phys. Fluids **20**, 087102 (2008).

Bibliography

[1] J. N. Israelachvili, *Intermolecular and Surface Forces*, 2nd ed. (Academic Press, London, 1992).

[2] S. S. Dukhin, "Non-equilibrium electric surface phenomena," Adv Colloid Interface Sci **44**, 1 (1993).

[3] J. Lyklema, *Fundamentals of Interface and Colloid Science—Solid-liquid interfaces*, Vol. 2 (Academic Press, London, 1995).

[4] R. J. Hunter, L. R. White, and D. Y. C. Chan, *Foundations of colloid science*, 2nd ed. (Oxford University Press, Oxford, 2001).

[5] N. Lakshminarayanaiah, *Transport phenomena in membranes* (Academic Press New York, 1969).

[6] E. Sélégny, *Charged gels and membranes* (Reidel, Dordrecht, 1976).

[7] F. Helfferich, *Ion exchange* (Dover, 1995).

[8] P. Gravesen, J. Branebjerg, and O. S. Jensen, "Microfluidics-a review," J Micromech Microeng **3**, 168 (1993).

[9] H. A. Stone, A. D. Stroock, and A. Ajdari, "Engineering flows in small devices," Annu Rev Fluid Mech **36**, 381 (2004).

[10] J. C. T. Eijkel and A. van den Berg, "Nanofluidics: what is it and what can we expect from it?" Microfluid Nanofluidics **1**, 249 (2005).

[11] T. M. Squires and S. R. Quake, "Microfluidics: Fluid physics at the nanoliter scale," Rev Mod Phys **77**, 977 (2005).

[12] G. M. Whitesides, "The origins and the future of microfluidics," Nature **442**, 368 (2006).

[13] S. Pennathur, C. D. Meinhart, and H. T. Soh, "How to exploit the features of microfluidics technology," Lab Chip **8**, 20 (2007).

[14] H. Bruus, *Theoretical microfluidics*, Oxford master series in physics No. 18 (Oxford University Press, Oxford, 2008).

[15] B. J. Kirby, *Micro-and nanoscale fluid mechanics: transport in microfluidic devices* (Cambridge University Press, 2010).

[16] D. Mijatovic, J. C. T. Eijkel, and A. van den Berg, "Technologies for nanofluidic systems: top-down vs. bottom-up—a review," Lab Chip **5**, 492 (2005).

[17] R. Schoch, J. Han, and P. Renaud, "Transport phenomena in nanofluidics," Rev Mod Phys **80**, 839 (2008).

[18] W. Sparreboom, A. van den Berg, and J. C. T. Eijkel, "Principles and applica-

tions of nanofluidic transport," Nat Nanotechnol **4**, 713 (2009).

[19] M. Napoli, J. C. T. Eijkel, and S. Pennathur, "Nanofluidic technology for biomolecule applications: a critical review," Lab Chip **10**, 957 (2010).

[20] W. Sparreboom, A. van den Berg, and J. C. T. Eijkel, "Transport in nanofluidic systems: a review of theory and applications," New J Phys **12**, 015004 (2010).

[21] L. Bocquet and E. Charlaix, "Nanofluidics, from bulk to interfaces," Chem Soc Rev **39**, 1073 (2010).

[22] H. Daiguji, P. Yang, A. J. Szeri, and A. Majumdar, "Electrochemomechanical energy conversion in nanofluidic channels," Nano Lett **4**, 2315 (2004).

[23] S. Pennathur, J. C. T. Eijkel, and A. van den Berg, "Energy conversion in microsystems: is there a role for micro/nanofluidics," Lab Chip **7**, 1234 (2007).

[24] F. H. J. van der Heyden, D. J. Bonthuis, D. Stein, C. Meyer, and C. Dekker, "Electrokinetic energy conversion efficiency in nanofluidic channels," Nano Lett **6**, 2232 (2006).

[25] F. H. J. van der Heyden, D. J. Bonthuis, D. Stein, C. Meyer, and C. Dekker, "Power generation by Pressure-Driven transport of ions in nanofluidic channels," Nano Lett **7**, 1022 (2007).

[26] M. Wang and Q. Kang, "Electrochemomechanical energy conversion efficiency in silica nanochannels," Microfluid Nanofluidics **9**, 181 (2009).

[27] D.-K. Kim, C. Duan, Y.-F. Chen, and A. Majumdar, "Power generation from concentration gradient by reverse electrodialysis in ion-selective nanochannels," Microfluid Nanofluidics **9**, 1215 (2010).

[28] W. Guo, L. Cao, J. Xia, F. Nie, W. Ma, J. Xue, Y. Song, D. Zhu, Y. Wang, and L. Jiang, "Energy harvesting with Single-Ion-Selective nanopores: A Concentration-Gradient-Driven nanofluidic power source," Adv Funct Mater **20**, 1339 (2010).

[29] D. Stein, M. Kruithof, and C. Dekker, "Surface-Charge-Governed ion transport in nanofluidic channels," Phys Rev Lett **93**, 035901 (2004).

[30] R. Karnik, K. Castelino, R. Fan, P. Yang, and A. Majumdar, "Effects of biological reactions and modifications on conductance of nanofluidic channels," Nano Lett **5**, 1638 (2005).

[31] A. Höltzel and U. Tallarek, "Ionic conductance of nanopores in microscale analysis systems: Where microfluidics meets nanofluidics," J Sep Sci **30**, 1398 (2007).

[32] D. P. Hoogerheide, S. Garaj, and J. A. Golovchenko, "Probing surface charge fluctuations with Solid-State nanopores," Phys Rev Lett **102**, 256804 (2009).

[33] D. Martins, V. Chu, D. M. F. Prazeres, and J. P. Conde, "Ionic conductivity measurements in a SiO2 nanochannel with PDMS interconnects," Procedia Chemistry **1**, 1095 (2009).

[34] C. Duan and A. Majumdar, "Anomalous ion transport in 2-nm hydrophilic nanochannels," Nat Nano **5**, 848 (2010).

[35] K. L. Jensen, J. T. Kristensen, A. M. Crumrine, M. B. Andersen, H. Bruus, and S. Pennathur, "Hydronium-dominated ion transport in carbon-dioxide-saturated electrolytes at low salt concentrations in nanochannels," Phys Rev E **83**, 056307 (2011).

[36] J. Han and H. G. Craighead, "Entropic trapping and sieving of long DNA molecules in a nanofluidic channel," J Vac Sci Technol A **17**, 2142 (1999).

[37] J. T. Mannion, C. H. Reccius, J. D. Cross, and H. G. Craighead, "Conformational analysis of single DNA molecules undergoing entropically induced motion in nanochannels," Biophys J **90**, 4538 (2006).

[38] R. M. M. Smeets, U. F. Keyser, D. Krapf, M.-Y. Wu, N. H. Dekker, and C. Dekker, "Salt dependence of ion transport and DNA translocation through Solid-State nanopores," Nano Lett **6**, 89 (2006).

[39] C. Dekker, "Solid-state nanopores," Nat Nanotechnol **2**, 209 (2007).

[40] J. D. Cross, E. A. Strychalski, and H. G. Craighead, "Size-dependent DNA mobility in nanochannels," J Appl Phys **102**, 024701 (2007).

[41] J. Fu, R. B. Schoch, A. L. Stevens, S. R. Tannenbaum, and J. Han, "A patterned anisotropic nanofluidic sieving structure for continuous-flow separation of DNA and proteins," Nat Nanotechnol **2**, 121 (2007).

[42] W. Reisner, N. B. Larsen, A. Silahtaroglu, A. Kristensen, N. Tommerup, J. O. Tegenfeldt, and H. Flyvbjerg, "Single-molecule denaturation mapping of DNA in nanofluidic channels," P Natl Acad Sci **107**, 13294 (2010).

[43] Q. Pu, J. Yun, H. Temkin, and S. Liu, "Ion-enrichment and ion-depletion effect of nanochannel structures," Nano Lett **4**, 1099 (2004).

[44] A. Plecis, R. Schoch, and P. Renaud, "Ionic transport phenomena in nanofluidics: Experimental and theoretical study of the exclusion-enrichment effect on a chip," Nano Lett **5**, 1147 (2005).

[45] Y.-C. Wang, A. L. Stevens, and J. Han, "Million-fold preconcentration of proteins and peptides by nanofluidic filter," Anal Chem **77**, 4293 (2005).

[46] S. J. Kim, Y.-C. Wang, J. H. Lee, H. Jang, and J. Han, "Concentration polarization and nonlinear electrokinetic flow near a nanofluidic channel," Phys Rev Lett **99**, 044501 (2007).

[47] K. Zhou, M. L. Kovarik, and S. C. Jacobson, "Surface-Charge induced ion depletion and sample stacking near single nanopores in microfluidic devices," J Am Chem Soc **130**, 8614 (2008).

[48] A. Mani, T. A. Zangle, and J. G. Santiago, "On the propagation of concentration polarization from Microchannel-Nanochannel interfaces part i: Analytical model and characteristic analysis," Langmuir **25**, 3898 (2009).

[49] T. A. Zangle, A. Mani, and J. G. Santiago, "On the propagation of concentration polarization from Microchannel-Nanochannel interfaces part II: numerical and experimental study," Langmuir **25**, 3909 (2009).

[50] S. J. Kim, L. D. Li, and J. Han, "Amplified electrokinetic response by concentration polarization near nanofluidic channel," Langmuir **25**, 7759 (2009).

[51] T. A. Zangle, A. Mani, and J. G. Santiago, "Theory and experiments of concentration polarization and ion focusing at microchannel and nanochannel interfaces," Chem Soc Rev **39**, 1014 (2010).

[52] P. M. Biesheuvel and M. Z. Bazant, "Nonlinear dynamics of capacitive charging and desalination by porous electrodes," Phys Rev E **81**, 031502 (2010).

[53] P. M. Biesheuvel, R. Zhao, S. Porada, and A. van der Wal, "Theory of membrane capacitive deionization including the effect of the electrode pore space," J Colloid Interface Sci **360**, 239 (2011).

[54] G. Yossifon, P. Mushenheim, Y.-C. Chang, and H.-C. Chang, "Nonlinear current-voltage characteristics of nanochannels," Phys Rev E **79**, 046305 (2009).

[55] G. Wang, B. Zhang, J. R. Wayment, J. M. Harris, and H. S. White, "Electrostatic-Gated transport in chemically modified glass nanopore electrodes," J Am Chem Soc **128**, 7679 (2006).

[56] J. Cervera, B. Schiedt, R. Neumann, S. Mafé, and P. Ramírez, "Ionic conduction, rectification, and selectivity in single conical nanopores," J Chem Phys **124**, 104706 (2006).

[57] R. Karnik, K. Castelino, and A. Majumdar, "Field-effect control of protein transport in a nanofluidic transistor circuit," Appl Phys Lett **88**, 123114 (2006).

[58] D. Constantin and Z. S. Siwy, "Poisson-Nernst-Planck model of ion current rectification through a nanofluidic diode," Phys Rev E **76**, 041202 (2007).

[59] R. Karnik, C. Duan, K. Castelino, H. Daiguji, and A. Majumdar, "Rectification of ionic current in a nanofluidic diode," Nano Lett **7**, 547 (2007).

[60] X. Wang, J. Xue, L. Wang, W. Guo, W. Zhang, Y. Wang, Q. Liu, H. Ji, and Q. Ouyang, "How the geometric configuration and the surface charge distribution influence the ionic current rectification in nanopores," J Phys D: Appl Phys **40**, 7077 (2007).

[61] M. Davenport, A. Rodriguez, K. J. Shea, and Z. S. Siwy, "Squeezing ionic liquids through nanopores," Nano Lett **9**, 2125 (2009).

[62] Y. He, D. Gillespie, D. Boda, I. Vlassiouk, R. S. Eisenberg, and Z. S. Siwy, "Tuning transport properties of nanofluidic devices with local charge inversion," J Am Chem Soc **131**, 5194 (2009).

[63] L.-J. Cheng and L. J. Guo, "Ionic current rectification, breakdown, and switching in heterogeneous oxide nanofluidic devices," ACS Nano **3**, 575 (2009).

[64] L.-J. Cheng and L. Guo, "Entrance effect on ion transport in nanochannels," Microfluid Nanofluidics **9**, 1033 (2010).

[65] L.-J. Cheng and L. J. Guo, "Nanofluidic diodes," Chem Soc Rev **39**, 923 (2010).

[66] S. Pennathur and J. G. Santiago, "Electrokinetic transport in nanochannels. 2. experiments," Anal Chem **77**, 6782 (2005).

[67] S. Pennathur and J. G. Santiago, "Electrokinetic transport in nanochannels. 1. theory," Anal Chem **77**, 6772 (2005).

[68] Y. Zeng and D. J. Harrison, "Self-Assembled colloidal arrays as Three-Dimensional nanofluidic sieves for separation of biomolecules on microchips," Anal Chem **79**, 2289 (2007).

[69] M. Napoli, P. Atzberger, and S. Pennathur, "Experimental study of the separation behavior of nanoparticles in micro- and nanochannels," Microfluid Nanofluidics **10**, 69 (2010).

[70] T. M. Wynne, A. H. Dixon, and S. Pennathur, "Electrokinetic characterization of individual nanoparticles in nanofluidic channels," Microfluid Nanofluidics **12**, 411 (2011).

[71] J. Eijkel, "Liquid slip in micro- and nanofluidics: recent research and its possible implications," Lab On A Chip **7**, 299 (2007).

[72] C. I. Bouzigues, P. Tabeling, and L. Bocquet, "Nanofluidics in the debye layer at hydrophilic and hydrophobic surfaces," Phys Rev Lett **101**, 114503 (2008).

[73] Y. Ren and D. Stein, "Slip-enhanced electrokinetic energy conversion in nanofluidic channels," Nanotechnology **19**, 195707 (2008).

[74] K. G. H. Janssen, H. T. Hoang, J. Floris, J. de Vries, N. R. Tas, J. C. T. Eijkel,

and T. Hankemeier, "Solution titration by wall deprotonation during capillary filling of silicon oxide nanochannels," Anal Chem **80**, 8095 (2008).

[75] D. Bottenus, Y.-J. Oh, S. M. Han, and C. F. Ivory, "Experimentally and theoretically observed native pH shifts in a nanochannel array," Lab Chip **9**, 219 (2009).

[76] M. B. Andersen, J. Frey, S. Pennathur, and H. Bruus, "Surface-dependent chemical equilibrium constants and capacitances in bare and 3-cyanopropyldimethylchlorosilane coated silica nanochannels," J Colloid Interface Sci **353**, 301 (2011).

[77] F. van der Heyden, D. Stein, and C. Dekker, "Streaming currents in a single nanofluidic channel," Phys Rev Lett **95**, 116104 (2005).

[78] F. H. J. van der Heyden, D. Stein, K. Besteman, S. G. Lemay, and C. Dekker, "Charge inversion at high ionic strength studied by streaming currents," Phys Rev Lett **96**, 224502 (2006).

[79] M. B. Andersen, H. Bruus, J. P. Bardhan, and S. Pennathur, "Streaming current and wall dissolution over 48 h in silica nanochannels," J Colloid Interface Sci **360**, 262 (2011).

[80] N. R. Tas, P. Mela, T. Kramer, J. W. Berenschot, and A. van den Berg, "Capillarity induced negative pressure of water plugs in nanochannels," Nano Lett **3**, 1537 (2003).

[81] V.-N. Phan, C. Yang, and N.-T. Nguyen, "Analysis of capillary filling in nanochannels with electroviscous effects," Microfluid Nanofluidics **7**, 519 (2009).

[82] D. Gillespie, A. S. Khair, J. P. Bardhan, and S. Pennathur, "Efficiently accounting for ion correlations in electrokinetic nanofluidic devices using density functional theory," J Colloid Interface Sci **359**, 520 (2011).

[83] H. T. Hoang, I. M. Segers-Nolten, J. W. Berenschot, M. J. de Boer, N. R. Tas, J. Haneveld, and M. C. Elwenspoek, "Fabrication and interfacing of nanochannel devices for single-molecule studies," J Micromech Microeng **19**, 065017 (2009).

[84] I. Vlassiouk, T. R. Kozel, and Z. S. Siwy, "Biosensing with nanofluidic diodes," J Am Chem Soc **131**, 8211 (2009).

[85] X. Tongwen, "Ion exchange membranes: State of their development and perspective," J Membrane Sci **263**, 1 (2005).

[86] T. F. Weiss, *Cellular Biophysics* (MIT Press, 1996).

[87] R. P. O'Hare, S.-W. Cha, W. G. Colella, and F. B. Prinz, *Fuel Cell Fundamentals* (Wiley, 2009).

[88] P. Berg, K. Promislow, J. S. Pierre, J. Stumper, and B. Wetton, "Water management in PEM fuel cells," J Electrochem Soc **151**, A341 (2004).

[89] L. D. Landau and E. M. Lifshits, *Electrodynamics of continuous media*, 2nd ed., Vol. 8 (Pergamon, Oxford, 1984).

[90] D. J. Griffiths and R. College, *Introduction to electrodynamics*, 3rd ed. (Prentice Hall, New Jersey, 1999).

[91] H. Strathmann, *Ion-exchange membrane separation processes* (Elsevier, Amsterdam, 2004).

[92] R. W. O'Brien and L. R. White, "Electrophoretic mobility of a spherical colloidal particle," J Chem Soc, Faraday Trans 2 **74**, 1607 (1978).

[93] R. F. Probstein, *Physicochemical hydrodynamics*, 2nd ed. (Wiley, New York,

1994).

[94] M. Z. Bazant and T. M. Squires, "Induced-charge electrokinetic phenomena: Theory and microfluidic applications," Phys Rev Lett **92**, 066101 (2004).

[95] J. S. Newman and K. E. Thomas-Alyea, *Electrochemical systems*, 3rd ed. (Wiley-Interscience, Hoboken, New Jersey, 2004).

[96] P. M. Biesheuvel, "Two-fluid model for the simultaneous flow of colloids and fluids in porous media," J Colloid Interface Sci **355**, 389 (2011).

[97] A. Persat, R. D. Chambers, and J. G. Santiago, "Basic principles of electrolyte chemistry for microfluidic electrokinetics. part i: Acid-base equilibria and pH buffers," Lab Chip **9**, 2437 (2009).

[98] A. Einstein, "Über die von der molekularkinetischen theorie der wärme geforderte bewegung von in ruhenden flüssigkeiten suspendierten teilchen," Ann Phys **322**, 549 (1905).

[99] D. C. Grahame, "The electrical double layer and the theory of electrocapillarity." Chem Rev **41**, 441 (1947).

[100] L. D. Landau and E. M. Lifshitz, *Fluid Mechanics*, 2nd ed. (Pergamon, Oxford, 1987).

[101] D. A. Saville, "Electrohydrodynamics: The taylor-melcher leaky dielectric model," Annu Rev Fluid Mech **29**, 27 (1997).

[102] H. Morgan and N. G. Green, *AC electrokinetics: colloids and nanoparticles* (Research Studies Press, Baldock, Hertfordshire, 2003).

[103] T. M. Squires and M. Z. Bazant, "Induced-charge electro-osmosis," J Fluid Mech **509**, 217 (2004).

[104] M. Štědrý, M. Jaroš, V. Hruška, and B. Gaš, "Eigenmobilities in background electrolytes for capillary zone electrophoresis: III. linear theory of electromigration," Electrophoresis **25**, 3071 (2004).

[105] A. Persat, M. E. Suss, and J. G. Santiago, "Basic principles of electrolyte chemistry for microfluidic electrokinetics. part II: coupling between ion mobility, electrolysis, and acid-base equilibria," Lab Chip **9**, 2454 (2009).

[106] D. A. Saville and O. A. Palusinski, "Theory of electrophoretic separations. part i: Formulation of a mathematical model," AIChE Journal **32**, 207 (1986).

[107] M. Bercovici, S. K. Lele, and J. G. Santiago, "Open source simulation tool for electrophoretic stacking, focusing, and separation," J Chromatogr A **1216**, 1008 (2009).

[108] M. Bercovici, S. K. Lele, and J. G. Santiago, "Compact adaptive-grid scheme for high numerical resolution simulations of isotachophoresis," J Chromatogr A **1217**, 588 (2010).

[109] P. Schindler and H. R. Kamber, "Die acidität von silanolgruppen. vorläufige mitteillung," Helv Chim Acta **51**, 1781 (1968).

[110] T. Hiemstra, W. H. V. Riemsdijk, and G. H. Bolt, "Multisite proton adsorption modeling at the solid/solution interface of (hydr)oxides: A new approach: I. model description and evaluation of intrinsic reaction constants," J Colloid Interface Sci **133**, 91 (1989).

[111] D. E. Yates, S. Levine, and T. W. Healy, "Site-binding model of the electrical double layer at the oxide/water interface," J Chem Soc, Faraday Trans 1 **70**, 1807 (1974).

[112] J. A. Davis, R. O. James, and J. O. Leckie, "Surface ionization and complexation at the oxide/water interface: I. computation of electrical double layer properties in simple electrolytes," J Colloid Interface Sci **63**, 480 (1978).

[113] R. Charmas, W. Piasecki, and W. Rudzinski, "Four layer complexation model for ion adsorption at Electrolyte/Oxide interface: Theoretical foundations," Langmuir **11**, 3199 (1995).

[114] S. Bandini, "Modelling the mechanism of charge formation in NF membranes: Theory and application," J Membrane Sci **264**, 75 (2005).

[115] C. Mazzoni, L. Bruni, and S. Bandini, "Nanofiltration: Role of the electrolyte and pH on desal DK performances," Ind Eng Chem Res **46**, 2254 (2007).

[116] L. Bruni and S. Bandini, "The role of the electrolyte on the mechanism of charge formation in polyamide nanofiltration membranes," J Membrane Sci **308**, 136 (2008).

[117] A. Szymczyk, P. Fievet, and S. Bandini, "On the amphoteric behavior of desal DK nanofiltration membranes at low salt concentrations," J Membrane Sci **355**, 60 (2010).

[118] R. D. Cook, D. S. Malkus, M. E. Plesha, and R. J. Witt, *Concepts and Applications of Finite Element Analysis*, 4th ed. (Wiley, Hoboken, NJ, 2002).

[119] J. Fish and T. Belytschko, *A First Course in Finite Elements* (Wiley, Chichester, 2007).

[120] "Comsol multiphysics reference guide," (2011), ver. 4.2a.

[121] L. H. Olesen, *Computational fluid dynamics in microfluidic systems*, Master's thesis, Technical University of Denmark (2003).

[122] H.-C. Chang and G. Yossifon, "Understanding electrokinetics at the nanoscale: A perspective," Biomicrofluidics **3**, 012001 (2009).

[123] M. Z. Bazant, M. S. Kilic, B. D. Storey, and A. Ajdari, "Towards an understanding of induced-charge electrokinetics at large applied voltages in concentrated solutions," Adv Colloid Interface Sci **152**, 48 (2009).

[124] "Gelest inc. phase news," (**1**), no. 2.

[125] R. J. White, E. N. Ervin, T. Yang, X. Chen, S. Daniel, P. S. Cremer, and H. S. White, "Single Ion-Channel recordings using glass nanopore membranes," J Am Chem Soc **129**, 11766 (2007).

[126] S. J. Oh, S. J. Cho, C. O. Kim, and J. W. Park, "Characteristics of DNA microarrays fabricated on various aminosilane layers," Langmuir **18**, 1764 (2002).

[127] D. R. Lide, *CRC Handbook of Chemistry and Physics*, 91st ed., edited by W. M. Haynes, (Internet Version 2011) (CRC Press/Taylor and Francis, Boca Raton, FL, 2010).

[128] S. A. Smith and W. A. Pretorius, "Spectrophotometric determination of pK(a) values for fluorescein using activity coefficient corrections," Water SA **28**, 395 (2002).

[129] M. Wang and A. Revil, "Electrochemical charge of silica surfaces at high ionic strength in narrow channels," J Colloid Interface Sci **343**, 381 (2010).

[130] N. R. Tas, J. Haneveld, H. V. Jansen, M. Elwenspoek, and A. van den Berg, "Capillary filling speed of water in nanochannels," Appl Phys Lett **85**, 3274 (2004).

[131] F. Persson, L. H. Thamdrup, M. B. Mikkelsen, S. E. Jarlgaard, P. Skafte-

Pedersen, H. Bruus, and A. Kristensen, "Double thermal oxidation scheme for the fabrication of SiO2 nanochannels," Nanotechnology **18**, 245301 (2007).

[132] A. Sze, D. Erickson, L. Ren, and D. Li, "Zeta-potential measurement using the smoluchowski equation and the slope of the current-time relationship in electroosmotic flow," J Colloid Interface Sci **261**, 402 (2003).

[133] B. J. Kirby and E. F. Hasselbrink, "Zeta potential of microfluidic substrates: 1. theory, experimental techniques, and effects on separations," Electrophoresis **25**, 187 (2004).

[134] E. W. Washburn, "The dynamics of capillary flow," Phys Rev **17**, 273 (1921).

[135] C. G. Armistead, A. J. Tyler, F. H. Hambleton, S. A. Mitchell, and J. A. Hockey, "The surface hydroxylation of silica," J Phys Chem **73**, 3947 (1969).

[136] T. Hiemstra, J. C. M. D. Wit, and W. H. V. Riemsdijk, "Multisite proton adsorption modeling at the solid/solution interface of (hydr)oxides: A new approach: II. application to various important (hydr)oxides," J Colloid Interface Sci **133**, 105 (1989).

[137] Y. Gushikem and J. Moreira, "Adsorption of MX2 (M = mn, ni, cu, zn, and cd; x = cl, br, and i) and FeCl3 by modified silica surface with imidazolylpropyl group," J Colloid Interface Sci **107**, 70 (1985).

[138] L. T. Kubota, J. C. Moreira, and Y. Gushikem, "Adsorption of metal ions from ethanol on an iminosalicyl-modified silica gel," Analyst **114**, 1385 (1989).

[139] R. B. Schoch and P. Renaud, "Ion transport through nanoslits dominated by the effective surface charge," Appl Phys Lett **86**, 253111 (2005).

[140] P. M. Dove, "The dissolution kinetics of quartz in aqueous mixed cation solutions," Geochim Cosmochim Acta **63**, 3715 (1999).

[141] P. M. Dove, N. Han, and J. J. D. Yoreo, "Mechanisms of classical crystal growth theory explain quartz and silicate dissolution behavior," P Natl Acad Sci **102**, 15357 (2005).

[142] P. M. Dove, N. Han, A. F. Wallace, and J. J. D. Yoreo, "Kinetics of amorphous silica dissolution and the paradox of the silica polymorphs," P Natl Acad Sci **105**, 9903 (2008).

[143] G. W. Greene, K. Kristiansen, E. E. Meyer, J. R. Boles, and J. N. Israelachvili, "Role of electrochemical reactions in pressure solution," Geochim Cosmochim Acta **73**, 2862 (2009).

[144] N. R. Tas, J. W. Berenschot, P. Mela, H. V. Jansen, M. Elwenspoek, and A. van den Berg, "2D-Confined nanochannels fabricated by conventional micromachining," Nano Lett **2**, 1031 (2002).

[145] Q. Xia, K. J. Morton, R. H. Austin, and S. Y. Chou, "Sub-10 nm Self-Enclosed Self-Limited nanofluidic channel arrays," Nano Lett **8**, 3830 (2008).

[146] Y. Zhao, E. Berenschot, H. Jansen, N. Tas, J. Huskens, and M. Elwenspoek, "Sub-10 nm silicon ridge nanofabrication by advanced edge lithography for NIL applications," Microelectron Eng **86**, 832 (2009).

[147] S.-W. Nam, M.-H. Lee, S.-H. Lee, D.-J. Lee, S. M. Rossnagel, and K.-B. Kim, "Sub-10-nm nanochannels by Self-Sealing and Self-Limiting atomic layer deposition," Nano Lett **10**, 3324 (2010).

[148] R. B. H. Veenhuis, E. J. van der Wouden, J. W. van Nieuwkasteele, A. van den Berg, and J. C. T. Eijkel, "Field-effect based attomole titrations in nanoconfine-

ment," Lab Chip **9**, 3472 (2009).

[149] R. E. G. van Hal, J. C. T. Eijkel, and P. Bergveld, "A general model to describe the electrostatic potential at electrolyte oxide interfaces," Adv Colloid Interface Sci **69**, 31 (1996).

[150] S. H. Behrens and D. G. Grier, "The charge of glass and silica surfaces," J Chem Phys **115**, 6716 (2001).

[151] R. K. Iler, *The chemistry of silica : solubility, polymerization, colloid and surface properties, and biochemistry* (Wiley, New York, 1979).

[152] R. Karnik, R. Fan, M. Yue, D. Li, P. Yang, and A. Majumdar, "Electrostatic control of ions and molecules in nanofluidic transistors," Nano Lett **5**, 943 (2005).

[153] N. F. Y. Durand and P. Renaud, "Label-free determination of protein-surface interaction kinetics by ionic conductance inside a nanochannel," Lab Chip **9**, 319 (2009).

[154] E. V. Dydek, B. Zaltzman, I. Rubinstein, D. S. Deng, A. Mani, and M. Z. Bazant, "Overlimiting current in a microchannel," Phys Rev Lett **107**, 118301 (2011).

[155] L.-J. Cheng, *Ion and Molecule Transport in Nanochannels*, PhD thesis, University of Michigan (2008).

[156] H. S. Harned and R. Davis, "The ionization constant of carbonic acid in water and the solubility of carbon dioxide in water and aqueous salt solutions from 0 to 50," J Am Chem Soc **65**, 2030 (1943).

[157] A. F. B. R F Keeling, S C Piper and J. S. Walker, "Atmospheric CO2 records from sites in the SIO air sampling network," In Trends: A Compendium of Data on Global Change (2009).

[158] J. Kielland, "Individual activity coefficients of ions in aqueous solutions," J Am Chem Soc **59**, 1675 (1937).

[159] S. J. Kim, S. H. Ko, K. H. Kang, and J. Han, "Direct seawater desalination by ion concentration polarization," Nat Nanotechnol **5**, 297 (2010).

[160] V. G. Levich, *Physicochemical Hydrodynamics* (Prentice-Hall, New York, 1962).

[161] I. Rubinstein and L. Shtilman, "Voltage against current curves of cation exchange membranes," J Chem Soc, Faraday Trans 2 **75**, 231 (1979).

[162] F. Maletzki, H. W. Rösler, and E. Staude, "Ion transfer across electrodialysis membranes in the overlimiting current range: stationary voltage current characteristics and current noise power spectra under different conditions of free convection," J Membrane Sci **71**, 105 (1992).

[163] I. Rubinstein and B. Zaltzman, "Electro-osmotically induced convection at a permselective membrane," Phys Rev E **62**, 2238 (2000).

[164] I. Rubinshtein, B. Zaltzman, J. Pretz, and C. Linder, "Experimental verification of the electroosmotic mechanism of overlimiting conductance through a cation exchange electrodialysis membrane," Russ J Electrochem **38**, 853 (2002).

[165] B. Zaltzman and I. Rubinstein, "Electro-Osmotic slip and electroconvective instability," J Fluid Mech **579**, 173 (2007).

[166] S. M. Rubinstein, G. Manukyan, A. Staicu, I. Rubinstein, B. Zaltzman, R. G. H. Lammertink, F. Mugele, and M. Wessling, "Direct observation of a nonequilibrium Electro-Osmotic instability," Phys Rev Lett **101**, 236101 (2008).

[167] G. Yossifon and H.-C. Chang, "Selection of nonequilibrium overlimiting currents: Universal depletion layer formation dynamics and vortex instability," Phys Rev

Lett **101**, 254501 (2008).

[168] R. Ibanez, D. F. Stamatialis, and M. Wessling, "Role of membrane surface in concentration polarization at cation exchange membranes," J Membrane Sci **239**, 119 (2004).

[169] E. Volodina, N. Pismenskaya, V. Nikonenko, C. Larchet, and G. Pourcelly, "Ion transfer across ion-exchange membranes with homogeneous and heterogeneous surfaces," J Colloid Interface Sci **285**, 247 (2005).

[170] E. I. Belova, G. Y. Lopatkova, N. D. Pismenskaya, V. V. Nikonenko, C. Larchet, and G. Pourcelly, "Effect of anion-exchange membrane surface properties on mechanisms of overlimiting mass transfer," J Phys Chem B **110**, 13458 (2006).

[171] T. A. Zangle, A. Mani, and J. G. Santiago, "Effects of constant voltage on time evolution of propagating concentration polarization," Anal Chem **82**, 3114 (2010).

[172] A. Mani and M. Z. Bazant, "Deionization shocks in microstructures," Phys Rev E **84**, 061504 (2011).

[173] R. Simons, "The origin and elimination of water splitting in ion exchange membranes during water demineralisation by electrodialysis," Desalination **28**, 41 (1979).

[174] R. Simons, "Water splitting in ion exchange membranes," Electrochimica Acta **30**, 275 (1985).

[175] V. I. Zabolotskii, N. V. Shel'deshov, and N. P. Gnusin, "Dissociation of water molecules in systems with ion-exchange membranes," Russ Chem Rev **57**, 801 (1988).

[176] J.-H. Choi, H.-J. Lee, and S.-H. Moon, "Effects of electrolytes on the transport phenomena in a Cation-Exchange membrane," J Colloid Interface Sci **238**, 188 (2001).

[177] J.-H. Choi and S.-H. Moon, "Structural change of ion-exchange membrane surfaces under high electric fields and its effects on membrane properties," J Colloid Interface Sci **265**, 93 (2003).

[178] M. Kang, Y. Choi, and S. Moon, "Effects of charge density on water splitting at cation-exchange membrane surface in the over-limiting current region," Korean J Chem Eng **21**, 221 (2004).

[179] L.-J. Cheng and H.-C. Chang, "Microscale pH regulation by splitting water," Biomicrofluidics **5**, 046502 (2011).

[180] Y. I. Kharkats, "Theory of the exaltation effect and the effect of correlation exaltation of migration current," J Electroanal Chem Interfacial Electrochem **105**, 97 (1979).

[181] R. Simons, "Electric field effects on proton transfer between ionizable groups and water in ion exchange membranes," Electrochimica Acta **29**, 151 (1984).

[182] R. Simons, "Strong electric field effects on proton transfer between membrane-bound amines and water," Nature **280**, 824 (1979).

[183] C.-O. Danielsson, A. Dahlkild, A. Velin, and M. Behm, "A model for the enhanced water dissociation on monopolar membranes," Electrochimica Acta **54**, 2983 (2009).

[184] C.-O. Danielsson, A. Dahlkild, A. Velin, and M. Behm, "Modeling continuous electropermutation with effects of water dissociation included," AIChE Journal

56, 2455 (2010).

[185] K. T. Chu and M. Z. Bazant, "Electrochemical thin films at and above the classical limiting current," SIAM J Appl Math **65**, 1485 (2005).

[186] M. Z. Bazant, K. T. Chu, and B. J. Bayly, "Current-Voltage relations for electrochemical thin films," SIAM J Appl Math **65**, 1463 (2005).

[187] E. Yariv, "Asymptotic current-voltage relations for currents exceeding the diffusion limit," Phys Rev E **80**, 051201 (2009).

[188] E. Yariv and Y. Almog, "Ionic currents in the presence of supporting electrolytes," Phys Rev Lett **105**, 176101 (2010).

[189] E. Yariv, "Improved current-voltage approximations for currents exceeding the diffusion limit," SIAM J Appl Math **71**, 2131 (2011).

[190] Y. Almog and E. Yariv, "One-dimensional conduction through supporting electrolytes: Two-scale cathodic debye layer," Phys Rev E **84**, 041204 (2011).

[191] V. V. Nikonenko, N. D. Pismenskaya, E. I. Belova, P. Sistat, P. Huguet, G. Pourcelly, and C. Larchet, "Intensive current transfer in membrane systems: Modelling, mechanisms and application in electrodialysis," Adv Colloid Interface Sci **160**, 101 (2010).

[192] A. Elattar, A. Elmidaoui, N. Pismenskaia, C. Gavach, and G. Pourcelly, "Comparison of transport properties of monovalent anions through anion-exchange membranes," J Membrane Sci **143**, 249 (1998).

[193] A. Brovelli and G. Cassiani, "Effective permittivity of porous media: A critical analysis of the complex refractive index model," Geophys Prospect **56**, 715 (2008).

[194] M. Van Soestbergen, A. Mavinkurve, R. T. H. Rongen, K. M. B. Jansen, L. J. Ernst, and G. Q. Zhang, "Theory of aluminum metallization corrosion in microelectronics," Electrochimica Acta **55**, 5459 (2010).

[195] M. B. Andersen, M. van Soestbergen, A. Mani, H. Bruus, P. M. Biesheuvel, and M. Z. Bazant, "Current-induced membrane discharge," (submitted Feb 2012).

[196] A. P. Thoma, A. Viviani-Nauer, S. Arvanitis, W. E. Morf, and W. Simon, "Mechanism of neutral carrier mediated ion transport through ion-selective bulk membranes," Anal Chem **49**, 1567 (1977).

[197] L. Jialin, W. Yazhen, Y. Changying, L. Guangdou, and S. Hong, "Membrane catalytic deprotonation effects," J Membrane Sci **147**, 247 (1998).

[198] J. J. Krol, M. Wessling, and H. Strathmann, "Concentration polarization with monopolar ion exchange membranes: current-voltage curves and water dissociation," J Membrane Sci **162**, 145 (1999).

[199] M. M. Gregersen, L. H. Olesen, A. Brask, M. F. Hansen, and H. Bruus, "Flow reversal at low voltage and low frequency in a microfabricated ac electrokinetic pump," Phys Rev E **76**, 056305 (2007).

[200] G. Soni, T. M. Squires, and C. Meinhart, "Nonlinear phenomena in induced charge electroosmosis," in *2007 ASME International Mechanical Engineering Congress and Exposition* (2007).

[201] C. K. Harnett, J. Templeton, K. A. Dunphy-Guzman, Y. M. Senousy, and M. P. Kanouff, "Model based design of a microfluidic mixer driven by induced charge electroosmosis," Lab Chip **8**, 565 (2008).

[202] M. M. Gregersen, M. B. Andersen, G. Soni, C. Meinhart, and H. Bruus, "Numerical analysis of finite debye-length effects in induced-charge electro-osmosis,"

Phys Rev E **79**, 066316 (2009).

[203] A. S. Khair and T. M. Squires, "Fundamental aspects of concentration polarization arising from nonuniform electrokinetic transport," Phys Fluids **20**, 087102 (2008).

[204] A. S. Khair and T. M. Squires, "Surprising consequences of ion conservation in Electro-Osmosis over a surface charge discontinuity," J Fluid Mech **615**, 323 (2008).

[205] B. P. Cahill, L. J. Heyderman, J. Gobrecht, and A. Stemmer, "Electro-osmotic streaming on application of traveling-wave electric fields," Phys Rev E **70**, 036305 (2004).

[206] V. Studer, A. Pépin, Y. Chen, and A. Ajdari, "An integrated AC electrokinetic pump in a microfluidic loop for fast and tunable flow control," Analyst **129**, 944 (2004).